BIOMIMETIC AND SYNTHETIC SYNTHESES OF NANOSTRUCTURED ELECTRODE MATERIALS

A Dissertation
Presented to
The Academic Faculty

by

John Daniel Berrigan

In Partial Fulfillment
of the Requirements for the Degree
Doctor of Philosophy in the
School of Materials Science and Engineering

Georgia Institute of Technology
December 2012

Biomimetic and Synthetic Syntheses of Nanostructured Electrode Materials

Approved by:

Dr. Kenneth H. Sandhage, Adviser
School of Materials Science & Engineering
Georgia Institute of Technology

Dr. Bernard Kippelen
School of Electrical and Computer Engineering
Georgia Institute of Technology

Dr. Michael F. Durstock
Materials and Manufacturing Directorate
Wright-Patterson Air Force Base

Dr. Seth Marder
School of Chemistry & Biochemistry
Georgia Institute of Technology

Dr. Meilin Liu
School of Materials Science & Engineering
Georgia Institute of Technology

Dr. David Bucknall
School of Materials Science & Engineering
Georgia Institute of Technology

To my family, friends, and all of those who have come before me.

ACKNOWLEDGEMENTS

Certainly it is possible to finish the work required for a dissertation without the love and support of family and friends, but graduation would without a doubt be held in a padded room. My parents deserve much credit for their patience and faith that this day would one day come during their lifetimes. I do not think I will ever be able to thank them enough. I have found that I am fortunate to have been raised in a family that believes strongly in the value of higher education, a belief that began with my grandmother. She was a public school teacher herself and graciously supported the educations of both her children and grandchildren. If not for her values and guidance, I would not be where I am today. I also am grateful to my sister, her family, and my brother for their love and support, even if it came as good-natured ribbing.

I have been lucky in many ways, but nothing can compare with how lucky I have been to have the unconditional love of Mary. She understood when I needed to leave and go into the lab at odd hours, believed in me when I didn't, and has stayed with me even though she could certainly do better. Her unselfish support of my dreams and ambitions cannot be exaggerated, and I can only hope that I am able to repay her over time.

Professionally, this work would not have been possible without the efforts of my advisor, Professor Ken Sandhage. His tireless writing of proposals provided me with the opportunity to conduct research without significant concern over lost funding or lack of supplies. He is one of the hardest working people in the department, and I never once regretted joining the group. I'd also like to thank Dr. Seth Marder, Dr. Bernard Kippelen, Dr. Meilin Liu, and Dr. David Bucknall for taking the time out to guide my research and

provide me feedback and advice. I also must thank Dr. Jonathan Vernon for his brutal honesty, friendship, quick-wit, and uncanny attention to detail. He was a tremendous role model for me during my time at Georgia Tech. I would especially like to thank Nick Haase and Taylor McLachlan, who were incredibly open and willing to work with me on two crazy ideas. Their hard work made the enzymatic biofuel cell and multi-wall titania nanotube projects a reality. I also must thank my lab mates Dr. Yunnan Fang, Dr. Yunshu Zhang, Dr. Ye Cai, Dr. Jonathan Vernon, Dr. Dave Lipke, Dr. Sam Shian, Brandon Goodwin, Ari Gordin, Craig Cameron, Yihong Li, Phil Brooke, and Stan Davis for their technical expertise, scientific advice, and willingness to discuss ideas. I also must thank Dr. Mike Weatherspoon and Dr. Matt Dickerson for providing the foundations for which my work was built.

I have also been very fortunate to work with some of the best and brightest people at the Air Force Research Lab (AFRL) at Wright-Patterson Air Force Base and Tyndall Air Force Base. I hope I was not too much of a burden to Dr. Michael Durstock, Dr. Tae-Sik Kang, Dr. Giorgio Bazzan, Dr. Ben Leever, Dr. Glenn Johnson, Dr. Guin Strack, Dr. Heather Luckarift, Dr. Rajesh Naik, Jim Deneault, and Susan Sizemore. It was a wonderful experience to visit both Air Force Bases and demonstrated that scientific research can indeed be an open, collaborative effort. Everyone I met at AFRL was willing to take time from their own projects to discuss mine, and I am very grateful for all of their help.

This research was conducted as part of an Air Force Center of Excellence on Bio-nano-enabled Inorganic/Organic Nanocomposites and Improved Cognition (BIONIC)

which was supported by the Air Force Office of Scientific Research (Award No. FA9550-09-1-0162) with Dr. Charles Lee as program manager.

TABLE OF CONTENTS

LIST OF TABLES

LIST OF FIGURES

LIST OF SYMBOLS AND ABBREVIATIONS

(in order of appearance)

TiBALDH	Titanium(IV) bisammoniumlactato dihydroxide
N719	cis-di(thiocyanato)-N-N'-bis(2,2'-bipyridyl-4-carboxylic acid-4'-tetrabutylammonium carboxylate) ruthenium (II)
LbL	layer-by-layer
3D	three dimensional
DSSC	dye-sensitized solar cell
AM 1.5G	air mass 1.5 global
TP-AAO	through-pore anodic aluminum oxide
DI	deionized
h	hour
Tris	tris(hydroxymethyl)aminomethane
FTO	fluorine-doped tin oxide
UV-Vis	ultraviolet-visible
FEG	field emission gun
SEM	scanning electron microscopy
TEM	transmission electron microscopy
XRD	X-ray diffraction
XPS	X-ray photoelectron spectroscopy
TGA	thermogravimetric analysis
J-V	current density-voltage
V_{oc}	open-circuit voltage
J_{sc}	short-circuit current
FF	fill factor
η_{eff}	power conversion efficiency
I_s	spectral irradiance
MWTNT	multi-wall titania nanotube
SWTNT	single-wall titania nanotube
AAO	anodic aluminum oxide
min	minutes
f_r	roughness factor (rugosity)

A_r	real surface area
A_p	projected surface area
PEI	polyethyleneimine
QCM-D	quartz crystal microbalance with dissipation monitoring
AFM	atomic force microscopy
BET	Brunauer-Emmett-Teller
PAH	poly(allylamine hydrochloride)
PSS	poly(styrene sulfonate)
PLL	poly(L-lysine)
PDDA	poly(diallyldimethylammonium chloride
PGA	poly(L-glutamic acid)
HA	hyaluronic acid
n	number of deposited bilayers
PEI600	600 M_w polyethyleneimine
PEI750K	750,000 M_w polyethyleneimine
L-PEI2500	linear polyethyleneimine, 2,500 M_w
Δd	added thickness after one deposition cycle
K	proportionality constant
q_o	polyelectrolyte adsorbed to the outer surface of the film
SDS	sodium dodecyl sulfate
ΔF	change in frequency
ΔD	change in energy dissipation
M_w	molecular weight
FITC	fluorescein isothiocyanate
t	film thickness
RMS	root-mean-squared
CNT-BP	carbon nanotube “buckypaper”
Lac-PA	protamine-modified laccase
PBSE	1-pyrenebutanoic acid, succinimidyl ester
E^0	thermodynamic driving force
ORR	oxygen reduction reaction
η	overvoltage

E_{eq}	equilibrium voltage
E	electrode voltage
PDB	protein database
DET	direct electron transfer
MET	mediated electron transfer
CNT	carbon nanotube
BS3	bis(sulfosuccinimidyl) suberate
NaAc	sodium acetate
HEPES	4-(2-hydroxyethyl)-1-piperazineethanesulfonic acid
ABTS	2,2′-azino-bis(3-ethylbenzothiazoline-6-sulphonic acid)
DMSO	dimethyl sulfoxide
CV	cyclic voltammetry
Lac-RRRR	RRRR-modified laccase
Lac-RRRTTR	RRRTTR-modified laccase
Lac-HPA	RRRTTRRRRAGRRRR-modified laccase
r_1	nanotube outer radius
r_2	nanotube inner radius
l	nanotube length
t_{space}	channel-center-to-channel center spacing
n_{tubes}	number of nanotubes per hexagon
W_t	nanotube wall thickness

SUMMARY

The scalable syntheses of functional, porous nanostructures with tunable three-dimensional morphologies is a significant challenge with potential applications in chemical, electrical, electrochemical, optical, photochemical, and biochemical devices. As a result, several bio-enabled and synthetic approaches are explored in this work for the generation of aligned nanotubes of nanostructured titania and functional carbon nanotube/enzyme biocomposites, with an emphasis on peptide-enabled deposition.

Peptide-enabled deposition utilizes the ability of certain readily-available arginine-rich peptides (e.g., protamine) to both bind-to and induce the precipitation of TiO_2 from aqueous solution under ambient conditions and near-neutral pH. The coatings deposited by peptide-enabled deposition inherently were an inorganic/bioorganic composite that, upon heat treatment, became porous due to organic pyrolysis. As part of this work, peptide-enabled deposition is used to deposit conformal TiO_2 coatings onto porous anodic alumina templates to generate aligned, porous-wall TiO_2 nanotube arrays that can be integrated into dye-sensitized solar cells where the arrays displayed improved functional dye loading compared to sol-gel-derived nanotubes.

Once TiO_2 nanotube arrays were developed, it became important to improve the areal density of TiO_2 nanotubes, while maintaining the aligned nanotube geometry. To further increase functional dye-loading and photovoltaic performance, a new synthetic method was developed to create aligned, multi-walled TiO_2 nanotube arrays that combined sol-gel deposition with gas/solid reactive conversion techniques. These multi-

walled TiO_2 nanotubes exhibited improved efficiencies (5.5 ± 0.8% to 3.0 ± 1.0%), roughness factors (282 to 75), and dye loading (195 ± 31 nmol cm^{-2} to 87 ± 28 nmol cm^{-2}) compared to single-wall TiO_2 nanotube arrays synthesized by sol-gel techniques alone.

Long-chain polyamines (e.g., protamine and polyethyleneimine) have been shown to precipitate TiO-bearing layers from aqueous precursor-containing solutions (e.g., titanium(IV) bisammoniumlactato dihydroxide), and a detailed comparison between synthetic and bioorganic polyamines regarding film deposition rates and properties can provide information beneficial for future TiO_2 coating experimental design given specific applications. This study aims to provide insight into the effect of polyamine on TiO-bearing coating properties, and advance peptide-enabled deposition further by providing a basic understanding of the molecular mechanism for peptide-enabled deposition.

Lastly, peptide-enabled deposition methods are extended beyond inorganic mineral and used for enzyme immobilization by cross-linking protamine with the multicopper oxidase laccase. Laccase is known to catalyze the oxygen reduction reaction at relatively low overvoltages in mild aqueous conditions, making it an attractive alternative to traditional platinum-based electrodes. Protamine-laccase hybrid enzymes are shown to improve both the amount of enzyme adsorbed onto carbon nanotube "buckypaper" and help the enzyme retain more activity upon immobilization onto the surface. This method also led to an almost twofold improvement in maximum current density relative to unmodified laccase (137 μA cm^{-2} to 271 μA cm^{-2}), when employed as an electrode in an electrochemical half-cell. Changing the length of the cross-linked

peptide based on fragments of protamine illustrated the importance of threonine and serine residues with respect to immobilization, but laccase modified by these fragments did not further improve electrode performance.

CHAPTER 1: SUMMARY AND MOTIVATION

1.1 Summary and Motivation

Scientific interest in biomimetic or biomolecule-enabled synthesis of materials is burgeoning in the materials science community because nature provides spectacular examples of hierarchical control of three-dimensional (3D) inorganic, organic, and/or inorganic/organic composite materials under ambient conditions.[1-7] Moreover, biomimetic approaches provide a pathway towards energy-efficient (e.g., low temperature) and environmentally friendly (e.g., near-neutral pH, non-hazardous chemical) materials synthesis. Peptide-enabled deposition uses the ability of readily-available arginine-rich peptides (e.g., protamine) to both bind-to and induce the precipitation of TiO_2 from *aqueous solution* under *ambient conditions* and *near-neutral pH*. Thus far, peptide-enabled deposition has been used to create 3D, freestanding replicas of biogenic templates for use as hydrogen gas sensors.[8]

Aligned metal oxide nanotube or nanorod arrays have demonstrated utility in a number of chemical, electrical, electrochemical, optical, photochemical, and biochemical devices.[9-14] In dye-sensitized solar cells (DSSCs), nanotube arrays have been shown to reduce electron recombination, improve light scattering, facilitate electrolyte access to the nanotube array surface, and provide better control over the oxide/electrolyte interface.[15] Such arrays have been synthesized using anodic oxidation,[13] electrochemical lithography,[16] photoelectrochemical etching,[17] sol-gel processing,[18] hydrothermal,[19] and template-based synthesis methodologies.[20] Specifically, template-based syntheses entail applying an oxide coating to a template material that possesses well-aligned nanopore channels

(e.g., porous anodic alumina[21] or a track-etch polymer membrane[22]), which can be selectively removed to yield nanotube arrays.[23-25] Gas-phase atomic layer deposition[26-28] liquid-phase sol-gel,[20, 29, 30] and surface sol-gel deposition[31] processes have been used by a number of authors to apply continuous and conformal coatings to such aligned-pore templates. Despite these advantages, aligned electrode architectures display efficiencies between ~3% and ~7%, and have yet to supplant mesoporous titania as the best performing DSSCs.[32, 33] The reduced photovoltaic performance of aligned, TiO_2 nanotube arrays relative to mesoporous films may be the result of reduced surface area for dye adsorption due to the processing methods employed to synthesize the arrays.

The coatings generated by the peptide-enabled approach were thought to be comprised of an inorganic/bioorganic composite that, upon heat treatment, could become porous due to organic pyrolysis. As a result, peptide-enabled deposition was used to deposit conformal TiO_2 coatings onto synthetic porous anodic alumina (AAO) templates and generate aligned TiO_2 nanotube arrays. The porosity of the nanotube walls due to organic pyrolysis, and the benefits of such internal porosity when integrated into DSSCs were investigated in this work.

Once porous-wall TiO_2 nanotube arrays were developed, it was hypothesized that photovoltaic performance could be improved further by generating multi-walled TiO_2 nanotube arrays that increase the areal density of TiO_2 while maintaining the aligned nanotube geometry. MWTNTs have previously been synthesized using gas-phase ALD, liquid-phase sol-gel, or electrochemical anodization methods.[34-36] However, no report has developed a method to synthesize aligned, high-aspect-ratio MWTNT arrays and

compared the performance of SWTNT to MWTNT in DSSCs.[34, 35] Furthermore, by combining the sol-gel infiltration of an AAO template with a shape-preserving gas-solid reaction technique, it may be possible to overcome aspect-ratio limitations encountered when MWTNTs are synthesized via electrochemical anodization of Ti foil.[36] Therefore, a new synthetic method that combined sol-gel deposition with the gas/solid reactive conversion of anodic Al_2O_3 is developed in this work, and the benefits of using this alternative method in DSSCs were investigated.

The alternating exposure of a negatively-charged surface to suitable synthetic or biologically-derived long-chain polyamines (e.g., protamine or polyethyleneimine) and a reactive metal oxide precursor (e.g., tetramethoxysilane or titanium(IV) bis(ammoniumlactato) dihydroxide) has been utilized to deposit either SiO- or TiO-bearing coatings in a layer-by-layer fashion.[8, 37-39] Such reactive deposition has been used to generate three-dimensional replicas comprised of microscale titania structures,[8] high-aspect-ratio aligned titania nanotube arrays,[40] and enzyme functionalized SiO_2 and TiO_2 coatings on SiO_2 microspheres.[41] Additionally, these coating methods have been used to develop components of hydrogen gas sensors and DSSCs, as well as materials for biocatalysis and anti-microbial agents.[8, 40-43]

As such, a study was conducted to provide insight into the affects of various polyamines (e.g., protamine and polyethyleneimine) on TiO-bearing coating properties (e.g., deposition rates, specific surface area, pore size), and develop a basic understanding of the molecular mechanism for peptide-enabled deposition. The relationship between the choice of polyamine (i.e., synthetic or bioorganic) to the TiO-bearing film deposition

rate and properties (e.g., film thickness, roughness, surface area) was examined for the first time. Each of these film characteristics are of critical importance for designing future polyamine/TiO_2 layer-by-layer deposition methods for various electrical, biochemical, photochemical, and optical applications. In this study, the deposition rate and film characteristics of TiO-bearing films deposited by either synthetic polyethyleneimine (PEI, 600 and 750,000 M_w branched and 2,500 M_w linear) or bioorganic protamine (~4.1 kDa).

Peptides, such as protamine, provide readily-available polyamines with functional groups at the N- and C-termini through which other proteins can be cross-linked to create functional bioorganic coatings. Protamine was cross-linked to the enzyme laccase (*Trametes versicolor*) and immobilized onto the surfaces of multi-walled carbon nanotubes. Laccase is an enzyme known to catalyze the oxygen reduction to water at relatively low overvoltages under mildly acidic (pH 5.1) conditions, making it an attractive, renewable alternative to traditional platinum-based electrodes. However, changes in enzyme conformation upon tethering to a carbon nanotube surface were thought to reduce the relative and electrochemical activity. A study was conducted to investigate whether the addition of protamine to the enzyme could absorb the conformational changes necessary for enzyme immobilization and improve the relative and electrochemical activities of laccase on the electrode surface.

In total, this work developed techniques for the syntheses of functional, ordered, porous nanostructures using several novel bio-enabled and synthetic approaches. These approaches yielded aligned nanotubes of nanostructured titania and carbon nanotube/

enzyme biocomposites that imparted beneficial properties to the electrodes. The methodologies described in subsequent chapters have broad applicability for functional, inorganic/(bio)organic coatings that can be deposited on various 3-D template materials.

1.2 References

1. S. Mann, *Biomineralization: Principles and Concepts in Bioinorganic Materials Chemistry*, Oxford University Press, Oxford, NY, 2001.

2. E. Bäuerlein, *Biomineralization: Progress in Biology, Molecular Biology, and Application*, Wiley-VCH, Weinheim, Germany, 2004.

3. M. Sarikaya, C. Tamerler, A. K. Y. Jen, K. Schulten and F. Baneyx, *Nature Materials*, 2003, **2**, 577-585.

4. C. E. Flynn, S. Lee, B. R. Peelle and A. M. Belcher, *Acta Materiala*, 2003, **51**, 5867-5880.

5. R. R. Naik and M. O. Stone, *Materials Today*, 2005, **8**, 18-25.

6. A.-W. Xu, Y. Ma and C. Helmut, *Journal Materials Chemistry*, 2007, **17**, 415-449.

7. M. B. Dickerson, K. H. Sandhage and R. R. Naik, *Chemical Reviews*, 2008, **108**, 4935-4978.

8. Y. Fang, Q. Wu, M. B. Dickerson, Y. Cai, S. Shian, J. D. Berrigan, N. Poulsen, N. Kröger and K. H. Sandhage, *Chemistry of Materials*, 2009, **21**, 5704-5710.

9. J.-H. Park, S. Kim and A. J. Bard, *Nano Letters*, 2006, **6**, 24-28.

10. G. K. Mor, K. Shankar, M. Paulose, O. K. Varghese and C. A. Grimes, *Nano Letters*, 2006, **6**, 215-218.

11. O. K. Varghese, M. Paulose, T. J. LaTempa and C. A. Grimes, *Nano Letters*, 2009, **9**, 731-737.

12. Y.-Y. Song, F. Schmidt-Stein, S. Bauer and P. Schmuki, *Journal of the American Chemical Society*, 2009, **131**, 4230-4232.

13. M. Paulose, H. E. Prakasam, O. K. Varghese, L. Peng, K. C. Popat, G. K. Mor, T. A. Desai and C. A. Grimes, *The Journal of Physical Chemistry C*, 2007, **111**, 14992-14997.

14. S. P. Albu, A. Ghicov, J. M. Macak, R. Hahn and P. Schmuki, *Nano Letters*, 2007, **7**, 1286-1289.

15. K. Zhu, N. R. Neale, A. Miedaner and A. J. Frank, *Nano Letters*, 2006, **7**, 69-74.

16. S. Z. Chu, S. Inoue, K. Wada, S. Hishita and K. Kurashima, *Journal of the Electrochemical Society*, 2005, **152**, B116-B124.

17. H. Masuda, K. Kanezawa, M. Nakao, A. Yokoo, T. Tamamura, T. Sugiura, H. Minoura and K. Nishio, *Advanced Materials*, 2003, **15**, 159-161.

18. J. E. Wijnhoven and V. W., *Science*, 1998, **281**, 802-804.

19. D. V. Bavykin, V. N. Parmon, A. A. Lapkin and F. C. Walsh, *Journal of Materials Chemistry*, 2004, **14**, 3370-3377.

20. T.-S. Kang, A. P. Smith, B. E. Taylor and M. F. Durstock, *Nano Letters*, 2009, **9**, 601-606.

21. R. C. Furneaux, W. R. Rigby and A. P. Davidson, *Nature*, 1989, **337**, 147-149.

22. R. Spohr, *Ion Tracks and Microtechnology: Basic Principles and Applications*, Vieweg, Wiesbaden, Germany, 1990.

23. C. R. Martin, *Science*, 1994, **266**, 1961-1966.

24. J. C. Hulteen and C. R. Martin, *Journal of Materials Chemistry*, 1997, **7**, 1075-1087.

25. X. Zhu, Z. Liu and N. Ming, *Journal of Materials Chemistry*, 2010, **20**, 4015-4030.

26. M. S. Sander, M. J. Côté, W. Gu, B. M. Kile and C. P. Tripp, *Advanced Materials*, 2004, **16**, 2052-2057.

27. H. Shin, D. K. Jeong, J. Lee, M. M. Sung and J. Kim, *Advanced Materials*, 2004, **16**, 1197-1200.

28. M. Kemell, V. Pore, J. Tupala, M. Ritala and M. Leskelä, *Chemistry of Materials*, 2007, **19**, 1816-1820.

29. P. Hoyer, *Advanced Materials*, 1996, **8**, 857-859.

30. B. B. Lakshmi, C. J. Patrissi and C. R. Martin, *Chemistry of Materials*, 1997, **9**, 2544-2550.

31. J. Huang and T. Kunitake, *Chemical Communications*, 2005, **21**, 2680-2682.

32. D. Kim, A. Ghicov, S. P. Albu and P. Schmuki, *Journal of the American Chemical Society*, 2008, **130**, 16454-16455.

33. O. K. Varghese, M. Paulose and C. A. Grimes, *Nature Nanotechnology*, 2009, **4**, 592-597.

34. C. Bae, Y. Yoon, H. Yoo, D. Han, J. Cho, B. H. Lee, M. M. Sung, M. Lee, J. Kim and H. Shin, *Chemistry of Materials*, 2009, **21**, 2574-2576.

35. I.-S. Park, S.-R. Jang, J. S. Hong, R. Vittal and K.-J. Kim, *Chemistry of Materials*, 2003, **15**, 4633-4636.

36. S. E. John, S. K. Mohapatra and M. Misra, *Langmuir*, 2009, **25**, 8240-8247.

37. Y. Jiang, D. Yang, L. Zhang, Q. Sun, X. Sun, J. Li and Z. Jiang, *Advanced Functional Materials*, 2009, **19**, 150-156.

38. Y. Zhang, H. Wu, J. Li, L. Li, Y. Jiang, Y. Jiang and Z. Jiang, *Chemistry of Materials*, 2008, **20**, 1041-1048.

39. V. Ball, L. Dahéron, C. Arnoult, V. Toniazzo and D. Ruch, *Langmuir*, 2011, **27**, 1859-1866.

40. J. D. Berrigan, T. S. Kang, Y. Cai, J. R. Deneault, M. F. Durstock and K. H. Sandhage, *Advanced Functional Materials*, 2011, **21**, 1693-1700.

41. N. R. Haase, S. Shian, K. H. Sandhage and N. Kröger, *Advanced Functional Materials*, 2011, **21**, 4243-4251.

42. M. B. Dickerson, C. L. Knight, M. K. Gupta, H. R. Luckarift, L. F. Drummy, M. L. Jespersen, G. R. Johnson and R. R. Naik, *Materials Science and Engineering: C*, 2011, **31**, 1748-1758.

43. H. R. Luckarift, M. B. Dickerson, K. H. Sandhage and J. C. Spain, *Small*, 2006, **2**, 640-643.

CHAPTER 2: BIO-ENABLED SYNTHESIS OF HIGH-ASPECT-RATIO, POROUS, ALIGNED NANOTUBE ARRAYS FOR DYE-SENSITIZED SOLAR CELLS

The research presented in this chapter has been reported in the following publication:

J. D. Berrigan, T.-S. Kang, Y. Cai, J. Deneault, M. F. Durstock, K. H. Sandhage, Adv. Funct. Mater., 21, 1693-1700, (2011).

2.1 Summary

For the first time, an aqueous, bio-enabled layer-by-layer titania deposition process was utilized to convert aligned nanochannel anodic alumina templates into porous aligned nanotube arrays of anatase titania with thin walls (34 nm). The alumina template was exposed, in alternating fashion, to aqueous protamine- and titania precursor-bearing (Ti(IV) bis-ammoniumlactato-dihydroxide, TiBALDH) solutions. Protamine is a naturally occurring polycationic protein derived from a variety of fish (e.g., salmon, herring, tuna, or trout) able to electrostatically bind to alumina and titania, and induce the formation of Ti-O precipitates upon exposure to TiBALDH. Such behavior has been harnessed to deposit, in layer-by-layer fashion, a conformal protamine/Ti-O-bearing composite coating along the surfaces of an anodic alumina template. Subsequent protamine pyrolysis yielded a coating composed of co-continuous networks of interconnected pores and titania nanoparticles. Dissolution of the underlying alumina template produced high-aspect-ratio, aligned, porous-wall titania nanotube arrays with enhanced loading of functional dye molecules (Ru-based N719 dye). The porous-wall titania nanotube arrays synthesized using this new methodology were integrated into dye-sensitized solar cells with light harvesting efficiencies of 5.2 ± 0.4%.

2.2 Introduction

In this chapter, the template-assisted growth of porous-wall titania nanotube arrays by peptide-enabled layer-by-layer (LbL) deposition is presented. The utility of such nanotube arrays is demonstrated in dye-sensitized cells (DSSCs) with enhanced functional dye loading.

2.2.1 Introduction to Peptide-Enabled Layer-by-Layer Deposition

Scientific interest in biomimetic or biomolecule-enabled synthesis of materials is burgeoning in the materials science community because nature provides spectacular examples of hierarchical control of three-dimensional inorganic, organic, and/or inorganic/organic composite materials under ambient conditions.[1-7] Moreover, such approaches provide a pathway towards energy-efficient (e.g., low temperature) and environmentally friendly (e.g., near-neutral pH, non-hazardous chemical) production.[1-7] Many peptides and proteins (e.g., silaffins, silicateins, ferritins, lysosyme) have demonstrated the ability to produce inorganic materials (e.g., SiO_2, TiO_2, GeO_2, Co_3O_4, Ga_2O_3, $BaTiO_3$) that are useful in scientific and engineering applications.[8-16] Prior work by Dickerson, *et al*. involving the use of combinatorial bacteriophage display (i.e., biopanning) identified 20 unique amino acid sequences able to bind to single-crystal rutile titania.[17] Dickerson, *et al*. also revealed the ability of an aptamer to bind to titania did not guarantee an ability to precipitate TiO_2 from a precursor solution. Of the 20 binding peptides identified, only four were able to generate TiO-bearing precipitates when mixed with an aqueous solution of Ti(IV) bis-ammoniumlactato-dihydroxide (TiBALDH).[17] The amino acid sequences of the four binding peptides capable precipitating titania from aqueous solution are listed in **Table 2.1** and designated as Ti-1,

Ti-2, Ti-3, and Ti-4.[17] Each of the peptides were basic (pI > 7.0) and titania yields scaled with the number of basic amino acid residues (arginine, lysine, histidine) with Ti-1 being the most effective peptide for precipitation.

Table 2.1: Titania Precipitation Activities of Peptides.[17]

Designation	Amino Acid Sequence	pI	# Positive Charges	mol TiO_2/ mol peptide
dTi-1 (RKK)	**R K K R K K R K K R K K** G G G W	12.8	**12**	**46.7±2.0**
Ti-1	**R K K R** T **K** N P T **H K** L G G G W	12.4	**6.3**	**38.7±1.6**
dTi-1(H/R)	**R K K R** T **K** N P T **R K** L G G G W	12.6	**7**	**34.9±0.7**
Ti-3	**K** S L S **R H** D **H** I **H H H** G G G W	10.1	**3.7**	**29.1±1.1**
Ti-2	M **R** M I **R R** F P S S L **K** G G G W	12.3	**4**	**21.2±1.0**
Ti-4	T Q **H** L S **H** P **R** Y A T **K** G G G W	10.0	**2.7**	**8.1±1.1**
Protamine	A**RRRR**SSS**R**PI**RRRR**P**RRR**TT**RRRR**AG**RRRR**	13.5	**20**	—

Note: Protamine yield was not examined in ref. 17.

For an electrostatic LbL deposition process to be widely applicable to various templates (i.e., templates with a wide range of isoelectric points), it was important to ensure titania yield remained invariant within a wide-range of pH values. By exchanging the lone-histidine residue (pK_a 6) in Ti-1 with arginine (pK_a 10), the pH dependence on TiO-bearing precipitate yield was reduced (dTi-1(H/R) compared to Ti-1 in **Table 2.1**).[17] A peptide designated dTi-1 (RKK) was synthesized consisting of four repeat units of arginine-lysine-lysine.[17] This amino acid sequence had the largest number of positive

charges and highest yield of all peptides tested. Most importantly, the yield was largely unchanged within a pH range of 4.5 to 8.5.[17]

The discovery that arginine/lysine-rich peptides were capable of binding to and precipitating titania from aqueous solution at room temperature over a wide-range of pH values led to the use of the biomolecule protamine for electrostatic LbL development. Protamine is an inexpensive (< $0.01 per milligram), readily available, arginine-rich (64.5%, see **Table 2.1**), polycationic (pI 13.5) peptide harvested from a variety of fish (e.g., salmon, herring trout, and tuna).[18, 19] Thus, protamine is a convenient analog to the synthetic peptides (cost ~$20 per mg) investigated by Dickerson, *et al*.[17] For years, protamine has often been used to for medicinal purposes to extend lifetime of insulin injections or to neutralize anti-coagulants in bloodstream after cardiac catheterization, cardiothoracic, and vascular surgical procedures.[20-22] Recently protamine has demonstrated additional utility in materials science as a biomolecule with the ability to both electrostatically bind to acidic oxides (e.g., SiO_2, TiO_2) and precipitate such oxides from an aqueous precursor at near-neutral pH, just like the peptide Ti-1.[23-25]

Fang, *et al.* demonstrated the ability of protamine to deposit 180 nm of anatase titania in a LbL fashion onto the surface of a biogenic silica template (*Aulacoseira* diatom frustules).[26] A schematic of the peptide-enabled deposition procedure using protamine is shown in **Figure 2.1**. This process begins with a negatively-charged template surface, which is generally achieved by carrying out the deposition process at a pH above the isoelectric point of the template material. The template is then incubated in a solution of polycationic protamine, which electrostatically binds to the template surface. After

washing with buffer of the same pH to remove excess peptide, the template is exposed to TiBALDH, which reacts with the peptide to form a TiO-bearing coating on surfaces coated with protamine. At this point, the as-deposited coating is composed of an inorganic Ti-O/organic (protamine) composite. Note, titania is an acidic oxide (pI ~5), making it negatively-charged, which allowed the process to be repeated indefinitely in a LbL fashion.

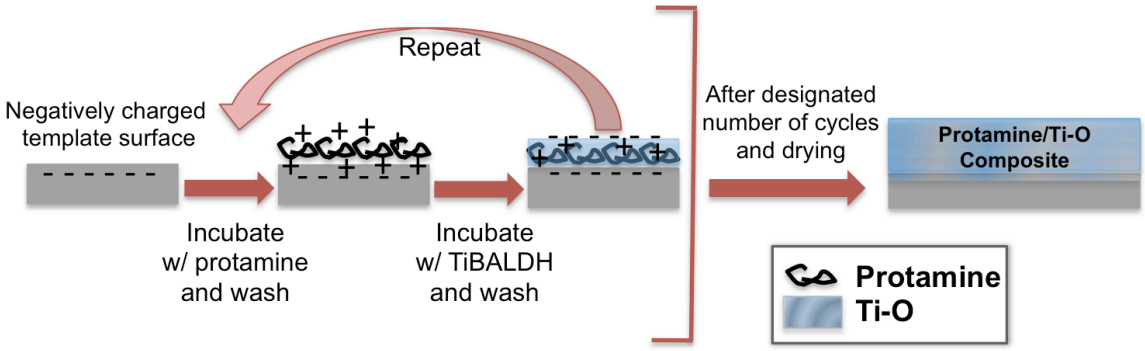

Figure 2.1: A schematic of the peptide-enabled layer-by-layer coating process.

As this work will demonstrate, the careful consideration of template and synthesis conditions (i.e., the solution pH was below the isoelectric point of protamine but above the isoelectric point of both the initial surface and the deposited mineral) enabled protamine to be used to reactively deposit conformal coatings of inorganic materials onto other three-dimensional (3D) templates (e.g., synthetic anodic aluminum oxide). Moreover, this work will highlight the advantages of the incorporation of a significant amount of protamine during deposition introduces porosity into the oxide coating upon pyrolysis of the organic content. In addition to the extension of biologically-enabled

LbL to a new template variety and chemistry and demonstration of nanoscale porosity, the process is exceptionally simple and scalable.

Unlike gas-phase atomic layer deposition, the peptide-based process does not require the use of vapor precursors, controlled atmospheres, or vapor-generating equipment.[27-29] Furthermore, this biomimetic mineralization process does not use moisture-sensitive precursors (e.g., alkoxides used in sol-gel processing) nor does it require hydroxyl-rich templates or multistep surface functionalization treatments (for enriching templates with hydroxyl groups) needed for surface sol-gel-based deposition of continuous and conformal coatings.[28-30]

2.2.2 Titania Dye-Sensitized Solar Cells Utilizing Aligned Nanostructures

Aligned metal oxide nanotube or nanorod arrays have shown utility in a number of chemical, electrical, electrochemical, optical, photochemical, and biochemical devices.[31-36] Such arrays have been synthesized using anodic oxidation,[35] electrochemical lithography,[37] photoelectrochemical etching,[38] sol-gel processing,[39] hydrothermal,[40] and template-based synthesis methodologies.[41] Specifically, template-based syntheses entail applying an oxide coating to a template material that possesses well-aligned nanopore channels (e.g., porous anodic alumina[42] or a track-etch polymer membrane[43]), which is then selectively removed to yield freestanding nanotubes or nanotube arrays.[44-46] Gas-phase atomic layer deposition[47-49] liquid-phase sol-gel,[41, 50, 51] and surface sol-gel deposition[28] processes have been used by a number of authors to apply continuous and conformal coatings to such aligned-pore templates. In this work, the peptide-enabled deposition method has been applied to anodic alumina templates to synthesize high-

aspect-ratio, aligned nanotube arrays with walls composed of co-continuous networks of pores and titania nanocrystals. Dye-sensitized solar cells (DSSCs) were chosen as a platform to demonstrate the applicability of such porous-wall electrode materials because of the potential for higher surface areas intrinsic to porous materials to adsorb more light harvesting dye (Ru-based N719) than sol-gel-based titania nanotube arrays.[41]

DSSCs, first reported by Grätzel 1991, consist of a thin film of mesoporous titania nanoparticles, coated in a layer of photosensitive dye, surrounded by electrolyte and sandwiched between two transparent conducting oxide electrodes.[52] Exposure of a DSSC to visible light begins a sequence of reactions within the device illustrated schematically in **Figure 2.2**.[53] Absorption of light by the photosensitive dye (S) leads to the formation of an excited state (S^*). Once excited, the sensitizer can either decay back to the ground state, undergo oxidative quenching, or inject an electron into the conduction band of titania. For efficient electron injection to occur, the excited state oxidation potential must be more negative than the conduction band-edge of titania.[54] In a typical high-efficiency device, electron flux can exceed 20 mA cm^{-2} and under such high ionic concentrations any macroscopic electric fields are effectively screened.[54] This removes any significant drift component, and therefore, the movement of both electrons and redox ions is governed by diffusion.[54, 55] After injecting an electron into titania, the oxidized dye is rapidly (~ 1 μs) reduced back to the ground state by the redox electrolyte (typically idiodide-triiodide in acetonitrile/valeronitrile for liquid-based cells).[56] Electrons at the platinum-coated cathode reduce the oxidized electrolyte to complete the circuit. The most efficient DSSCs have reached photon-to-electron conversion efficiencies between

11% and 12.3% at AM 1.5 solar irradiance using electrodes of a three-dimensional porous network of nanocrystalline TiO_2 (15 - 20 nm).[52, 57, 58]

In terms of titania electrode design, random networks of mesoporous titania have high surface area (~90 m^2 g^{-1}) and porosity (50 - 65%) which is beneficial for adsorbing photosensitive dye and electrolyte infiltration.[59] However, the random nature of the oxide network is not ideal given that electron transport has been shown to be governed by the multiple trapping model.[55, 60, 61] This model has been developed to explain the observation that electron transport in DSSCs depends strongly on light intensity, and the dependence of the diffusion coefficient on the photocarrier density has been found to follow a power law with an exponent ranging between 1 and 17.[62] The multiple-trapping model attempts to explain this power law dependence of the electron diffusion coefficient in terms of electrons performing a random walk between a lattice of localized "trap states" that lie below the conduction band.[63, 64] Once an electron enters a trap state, the electron is immobilized until it is either excited thermally back to the conduction band or tunnels to another localized trap state.[65-67] An exponential density of trap states is assumed, which implies a power law distribution of waiting times for electrons, and a strong dependence of the effective electron diffusion coefficient on the injected electron density consistent with experimental evidence.[63, 67, 68]

Injected electrons may be localized near the surface or in the bulk of titania. During transport electrons may recombine with triiodide ions in the electrolyte at the solid/liquid interface.[64] The collection of the injected electrons, which is a critical factor in device performance, is determined by competition between electron transport to the

anode and electron transfer to triiodide ions in the electrolyte. Therefore, each encounter with a new TiO_2 particle or trap state increases the likelihood of electron recombination and reduces light harvesting efficiencies.

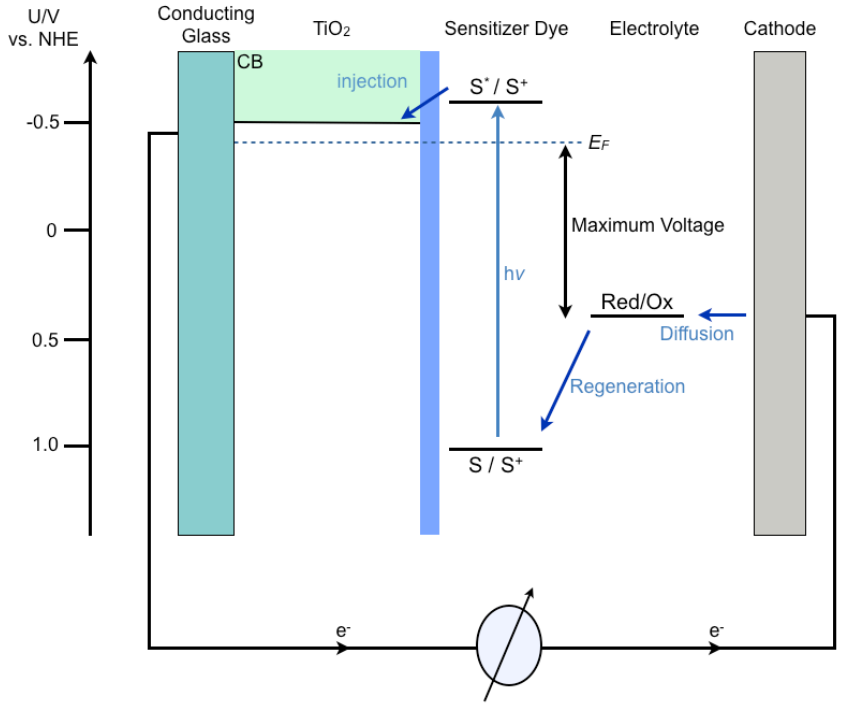

Figure 2.2. An energy schematic of a DSSC device illustrating the energetics of the various reactions that take place upon illumination.[53]

The development of aligned, titania nanostructures (i.e., nanorod and nanotube arrays) may reduce electron recombination by decreasing the dimensionality through which electrons can diffuse thereby providing a more direct electron path toward the current collecting electrode.[69] The enhancement in electron transport can theoretically allow for thicker films that increase the optical density, leading to an improvement in the absorption of low-energy photons. Nanotube array architectures could also improve light scattering, facilitate access to the nanotube array surface, and provide better control over

the oxide/electrolyte interface.[69] Despite these advantages, aligned electrode architectures display efficiencies between ~3% and ~7%, and have yet to supplant mesoporous titania as the best performing DSSCs.[70, 71] The reduced photovoltaic performance of aligned, titania nanotube arrays relative to mesoporous films may be the result of reduced surface area for dye adsorption due to the geometric structure and processing methods used.

The ongoing effort to further develop nanostructured electrodes for DSSCs provided the impetus to develop a novel peptide-enabled method for synthesizing aligned titania nanotube electrodes with unique properties. For the first time, an aqueous peptide-enabled LbL oxide deposition process was used to buildup conformal peptide/oxide composite coatings on aligned-nanochannel templates. Upon organic pyrolysis, a coating composed of a co-continuous network of pores and oxide nanoparticles was formed. After selective dissolution of the template through the interconnected pore network a freestanding, high-aspect-ratio, porous-wall nanotube array was created and integrated into DSSCs that displayed enhanced dye loading with respect to sol-gel derived nanotube arrays.

2.3 Experimental Procedure

2.3.1 Synthesis of Through-Pore Anodic Alumina Templates

A galvanostatic anodization and controlled etching process was used to convert high-purity aluminum foil (99.999% purity, 0.1 cm thick, Goodfellow, Co., Oakdale, PA) into alumina membranes with highly aligned and continuous (through membrane) pore

channels of sub-micrometer diameter. A two-step galvanostatic anodization procedure reported by Kang, *et al.* was first used to convert the aluminum foil into porous alumina films (9.9 ± 0.4 μm thickness) with aligned, one-end-closed pore channels on top of an aluminum backing.[41] The aluminum backing and the alumina barrier layer formed during such anodization must be removed to convert these porous alumina films into alumina membranes with open pore channels running through the membrane thickness. To fabricate these through-pore anodic aluminum oxide (TP-AAO) templates, the aluminum oxide was first coated with a thin nitrocellulose-based film (Double Duty nail polish, Sally Hansen®, Coty, Inc., New York, NY, USA) using a brush. The aluminum backing was then selectively dissolved in an aqueous solution of 0.25 M copper (II) chloride dihydrate (Sigma Aldrich, St. Louis, MO, USA) in 6.0 M HCl at room temperature for 15 min.[72] Aluminum removal exposed the alumina barrier layer that was formed during anodization and capped at one end of the pore channels. The alumina barrier layer was then dissolved by immersion in 3 M NaOH for 16 min at room temperature, which opened the pore channels and created a TP-AAO membrane. The nitrocellulose-based film that had coated and protected the alumina membrane located above the alumina barrier layer during the NaOH treatment was then removed by dissolution in acetone.

2.3.2 Syntheses of Titania Nanotube Arrays

A LbL, peptide-enabled deposition process was used to apply continuous and conformal Ti-O-bearing coatings to the TP-AAO templates. After placement on a porous ceramic frit, the TP-AAO template was exposed to a series of deposition cycles involving alternating exposure to protamine-bearing and titania precursor-bearing solutions. A

schematic of the experimental used is shown in **Figure 2.3**. All solutions were prepared using deionized (DI) water (18.2 MΩ·cm).

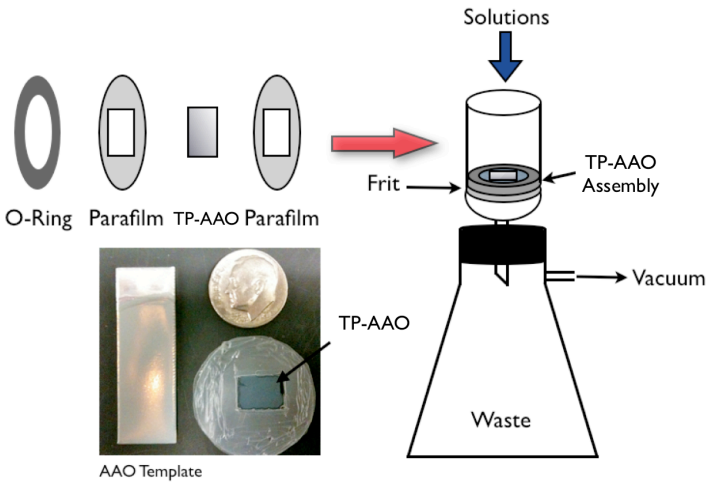

Figure 2.3: A schematic of the experimental apparatus used to coat through-pore anodic aluminum oxide (TP-AAO) shown in the bottom-left.

The first step of each cycle consisted of vacuum infiltration into the TP-AAO template for 1 h with protamine solution (2.5 mg mL^{-1} protamine sulfate in 20 mM tris(hydroxymethyl)aminomethane (Tris) titrated to pH 8.5 with HCl (Tris-HCl buffer)). Vacuum suction was then used to remove the protamine solution, and the template was washed by passing 20 mL of buffer solution (20 mM Tris-HCl, pH 8.5) through the TP-AAO membrane three times. Next, 10 mL of titania precursor solution comprised of 50 mM TiBALDH (Ti(IV) bis-ammoniumlactato-dihydroxide, Sigma-Aldrich, St. Louis, MO) in the same Tris-HCl buffer was then vacuum infiltrated into the template and incubated for 0.5 h. The precursor was then removed by pulling vacuum through the template and then rinsing three times with the buffer solution. The template was then dried under N_2 flow, and this protamine/rinse/TiBALDH/rinse/dry cycle was repeated for

a predetermined number of cycles. The coated TP-AAO template was dried and heat treated at 650 ºC for 3 h in air to pyrolyze organics and crystallize the oxide coating.

2.3.3 Photovoltaic Device Fabrication

After heat treatment, the resulting porous-titania-coated TP-AAO structure was converted into freestanding porous-wall titania nanotube arrays by selective dissolution of the TP-AAO template. After attaching the titania-coated TP-AAO structure to a glass slide with a thin nitrocellulose-based layer (Double Duty nail polish, Sally Hansen), the structure was immersed in an aqueous 3 M NaOH solution for 1.5 h to selectively dissolve the alumina template. After rinsing, the resulting titania nanotube array was removed from the glass slide by pyrolysis of the nitrocellulose-based film at 450 ºC for 0.5 h in air.

To prepare the DSSC working electrode, a fluorine-doped tin oxide (FTO) coated glass slide (2.54 × 1.27 cm × 2 mm thick, 13 Ω/□, Hartford Glass Company) was cleaned by ultrasonication for 20 min in a solution of 2.5 mg mL^{-1} detergent (Alconox Powder Detergent, VWR, West Chester, PA) dissolved in an aqueous solution of 50 vol% ethanol. After rinsing with water and ethanol, the FTO-coated glass was exposed to an aqueous solution of 20 mM $TiCl_4$ (99 % purity, Alfa Aesar, Ward Hill, MA) at 70 ºC for 0.5 h. After washing with water and ethanol, the treated glass surface was partially masked by attaching a piece of Scotch® tape through which a 0.79 cm diameter hole was punched. A titania-bearing paste, composed of titania nanoparticles (20 nm average diameter, Ti-Nanoxide, T20/SP, Solaronix SA, Aubonne, Switzerland), was mixed in a 1:1 weight ratio with ethanol. After placing 10 μL of this mixture in and over the 0.79 cm

diameter hole in the tape, a doctor blade was wiped across the tape to remove excess titania paste located above the hole. The titania nanotube array (0.49 cm^2) was then placed on this layer of TiO_2 paste and the assembly was fired at 500 ºC for 1 h to burn off the tape and to sinter-bond the array to the titania-coated FTO-bearing glass. Afterwards, the electrode was exposed to a 0.2 M $TiCl_4$ solution at 70 ºC for 1 h, and then heated again to 500 ºC for 0.5 h. After an oxygen plasma treatment of the assembly for 10 min at 10.1 W (PDC-002, Harrick Plasma, Ithaca, NY), the working electrode was submerged in light-harvesting solution (0.3 mM t-butanol/acetonitrile solution, 1:1 volume ratio) of N719 dye (cis-di(thiocyanato)-N-N'-bis(2,2'-bipyridyl-4-carboxylic acid-4'-tetrabutylammonium carboxylate) ruthenium (II), Solaronix, Aubonne, Switzerland) for 24 h at room temperature. A counter electrode was prepared by sandblasting a 1 mm diameter hole in an FTO-bearing glass slide, and then depositing an ethanolic solution of 2 mg mL^{-1} H_2PtCl_6 (Alfa Aesar) on the FTO followed by firing at 450 ºC for 15 min.

A 25 μm thick disk-shaped thermoplast spacer (Meltronix 1170-25, Surlyn, Solaronix, Aubonne, Switzerland) was used to separate the working electrode (the titania nanotube-bearing FTO) from the counter electrode (the Pt-coated FTO). A 0.79 cm diameter hole was cut into the spacer so that the titania nanotube array on the working electrode could be positioned within the hole. The redox electrolyte solution, which was composed of 0.6 M 1-butyl-3-methyl imidazolium iodide, 0.1 M guanidinium thiocyanate, 0.03 M I_2 and 0.5 M tert-butylpyridine dissolved in a mixture of 85 vol% acetonitrile and 15 vol% valeronitrile, was infiltrated under vacuum through the hole in the FTO-bearing glass of the counter electrode into the space between the counter and

working electrodes and into the titania nanotube array. The hole in the counter electrode was then sealed using a 60 μm thick thermoplast film (Meltronix 1162-60, Solaronix SA, Aubonne, Switzerland) and a cover glass slide. A completed device is shown in **Figure 2.4(a)** along with a schematic (**Figure 2.4(b)**), and a flowchart of describing the entire process is shown in **Figure 2.5**.

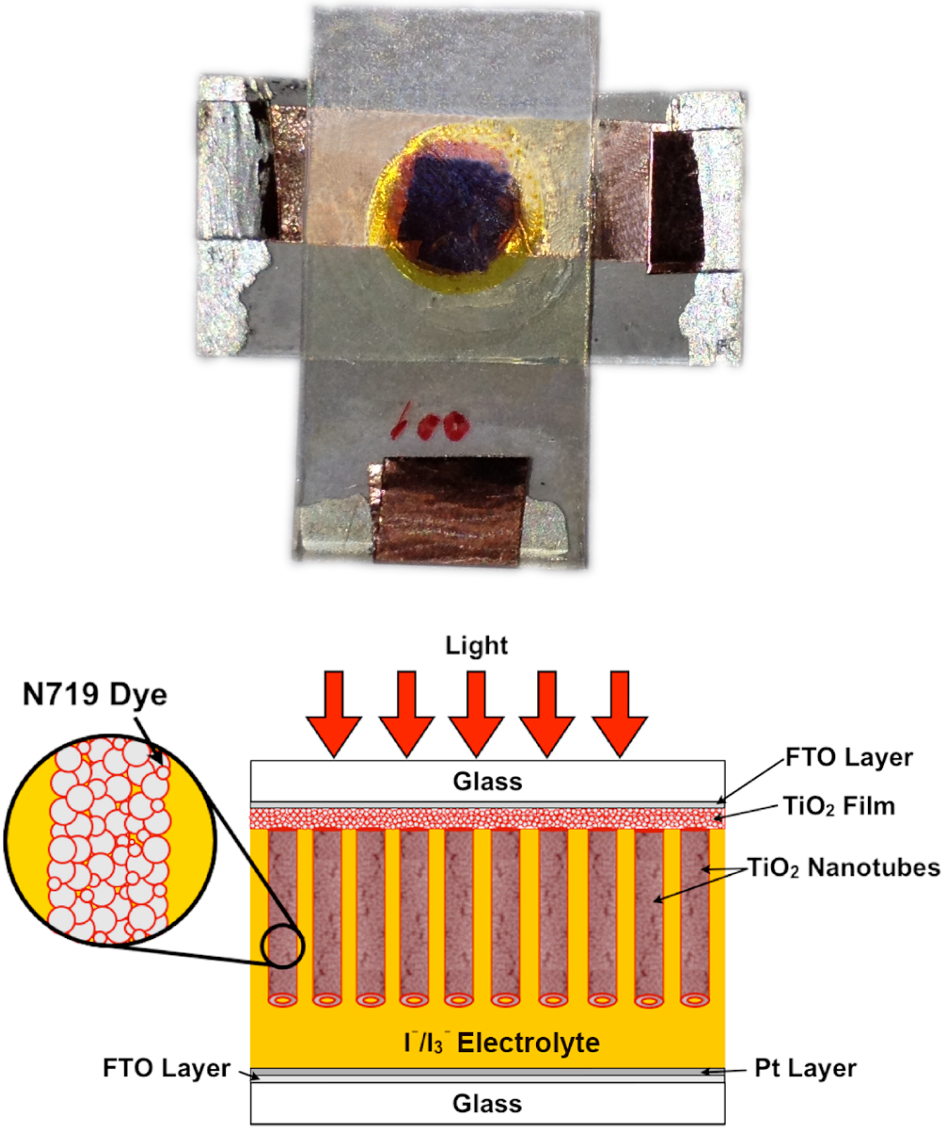

Figure 2.4: A completed titania nanotube-based DSSC with FTO glass that measured 1.3 cm × 2.5 cm (a), and a schematic of the design illustrating to porosity introduced into the walls of the nanotube (b).

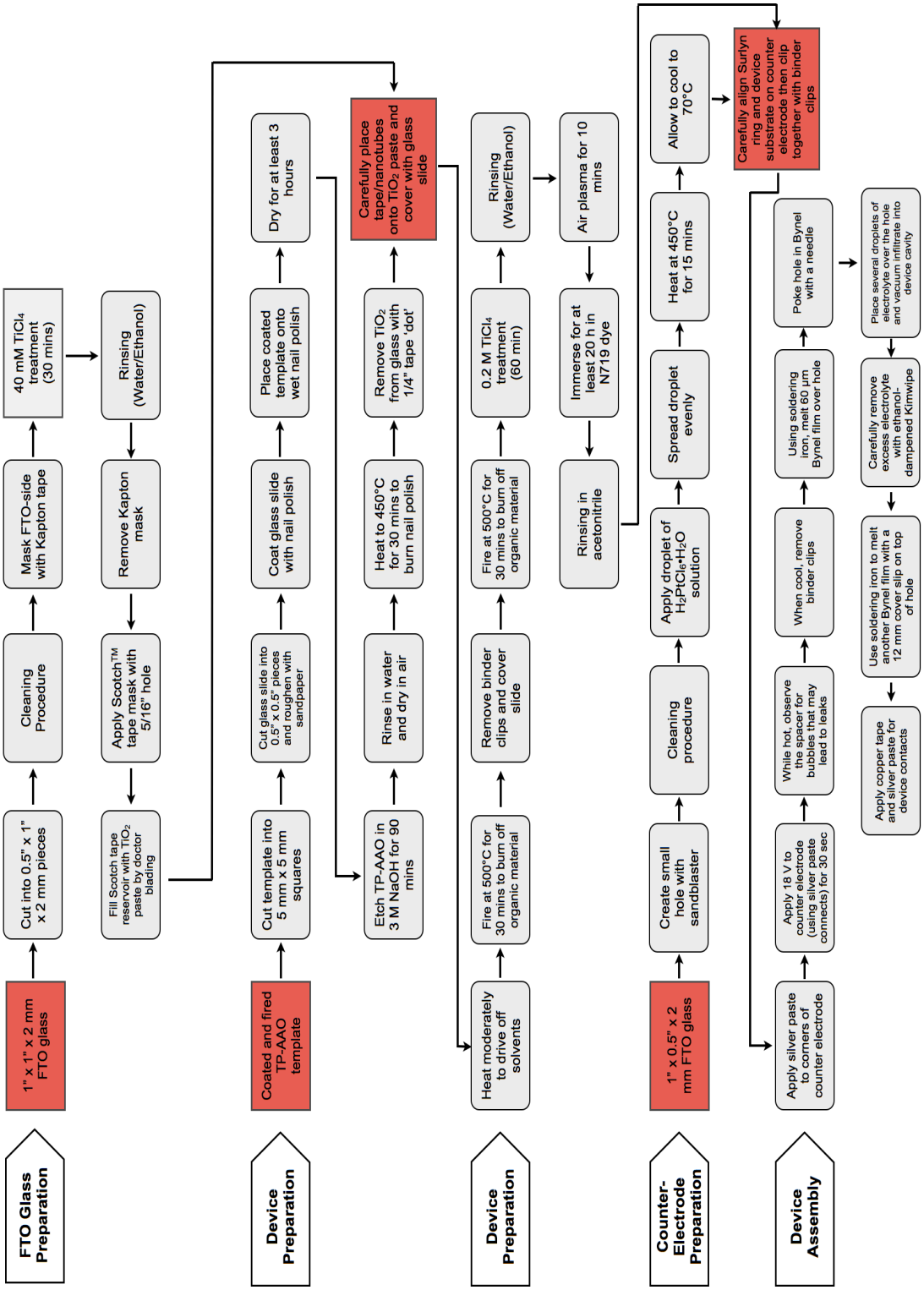

Figure 2.5: A flowchart of the DSSC electrode preparation and assembly process.

2.3.4 Dye Desorption Experiments

After incubation in the N719 dye solution for 24 h, the electrodes were rinsed twice in dry acetonitrile and dried in air. The dye was then removed from the electrodes by immersion in 3 mL of an aqueous solution of 50 vol% ethanol containing 100 mM NaOH for 5 min. The absorbance of this solution at 513 nm was evaluated with a ultraviolet-visible light (UV-vis) spectrometer (Genesys 10S UV-vis, Thermo Fischer Scientific, Inc., Waltham, MA, USA) and compared to a calibration curve prepared from absorbance measurements of five solutions of known N719 dye concentration to obtain the molar concentration of N719 dye. The dye concentration was then normalized to the mass of the fired TiO_2 nanotube array present on the FTO-bearing glass. To allow for comparison with the prior work of Kang, *et al.*,[41] the dye desorption experiments were conducted with nanotube arrays that had not been exposed to the 0.2 M $TiCl_4$/70 ºC/1 h treatment.

2.3.5 Characterization of the Nanotube Arrays and Cells

The micro/nanoscale morphologies of the porous TP-AAO templates and titania nanotube arrays were evaluated with scanning electron microscopy (1530 FEG SEM, LEO/Zeiss Electron Microscopy, Thornwood, NY) and transmission electron microscopy (JEOL 4000 EX, Japan Electron Optics Laboratory, Tachikawa, Tokyo). Transmission electron microscopy was conducted by Dr. Ye Cai (Georgia Institute of Technology, Atlanta, GA, USA). Dimensional analysis was derived from 10 measurements on 5 different areas for 50 total measurements. The error quoted for such measurements correlated to the range of values measured.

The crystal structures of the nanotube arrays were evaluated at room temperature via X-ray diffraction (XRD) analyses (Alpha-1, PANalytical Corp., Almelo, the Netherlands) and selected area electron diffraction analyses (JEOL 4000 EX). XRD analyses were conducted using monochromatic $Cu_{K\alpha 1}$(1.541 Å) radiation emanating from a 1.8 kW ceramic diffraction X-ray tube with a copper anode (45 kV, 40 mA) through a symmetrical Johannson monochromator. The incident beam optics were outfitted with 0.04 rad soller slits, a 1º fixed anti-scatter slit, a ½º programmable divergence slit, and a 10 mm mask. The diffracted beam optics were outfitted with a 5.5 mm anti-scatter slit and 0.04 rad soller slits placed before the X'Celerator detector. Each pattern was produced with a summation of 12 identical 20 min scans conducted with Bragg-Brentano geometry and a step size of 0.067º 2θ ranging from 20º to 70º 2θ.

X-ray photoelectron spectroscopy (XPS) was conducted (Thermo K-alpha, Thermo Fischer Scientific, Inc., Waltham, MA, USA) at a base pressure of $3x10^{-8}$ Pa using a monochromatic Al K_α source (1486.6 eV) with a spot size of 300 μm and a pass energy of 50 eV. Step sizes of 0.01 eV (high-resolution) and 1 eV (low-resolution) were used with dwell times of 50 ms at each energy value. Thermogravimetric analysis (TGA) (Netzsch STA 449 C, Wolverhampton, UK) of the as-coated TP-AAO template was performed at a heating rate of 5 ºC min^{-1} up to 650 ºC in flowing synthetic air gas mixture. Zeta potential measurements were conducted on crushed TP-AAO membranes that were then exposed to various stages of the protamine/TiBALDH process (as described above) using a dip cell on a Zetasizer NS instrument (Malvern Instruments, Malvern, Worcestershire, UK). At each stage of the protamine/TiBALDH process

examined (for each data point in **Figure 2.7(a)**), three zeta potential measurements were obtained from each of three independent crushed samples (i.e., 9 measurements for a given stage of exposure). Current-voltage (*J-V*) measurements were conducted under airmass 1.5 global (AM 1.5G) conditions (Oriel 300 Watt solar simulator, 100 mW cm^{-2}) using an aperture with a measured area of 7.05 mm^2.

2.4 Results and Discussion

2.4.1 Peptide-Enabled Titania Coatings on Porous Anodic Alumina

A peptide-enabled LbL deposition process was used to convert through-pore anodic aluminum oxide (TP-AAO) membranes into aligned, porous-wall nanotube arrays comprised of interconnected nanocrystalline anatase titania. The TP-AAO membranes were prepared by a two-step galvanostatic anodization process described by Kang, *et al*.[41] The aluminum backing was then removed by dissolution in an HCl-$CuCl_2$ solution.[72] Subsequent immersion in a 3 M NaOH solution was used to remove the alumina barrier layer formed during anodization. Secondary electron images revealing the aligned pore channels in such a TP-AAO membrane are shown in **Figures 2.6(a)** and **2.6(b)**. The pore channels possessed an average diameter of 284 ± 80 nm and an average length of 9.9 ± 0.4 μm. However, these dimensions may be tuned by varying anodization and etching conditions.

The TP-AAO membranes were exposed in an alternating fashion to buffered (pH 8.5) aqueous solutions of protamine and titania precursor (TiBALDH) to deposit a protamine/TiO-bearing composite coating. The ability of polycationic protamine molecules to bind to both alumina and titania, and to induce the formation of titania from

the TiBALDH precursor while bound to alumina or titania surfaces, enabled the LbL buildup of a conformal protamine/TiO-bearing composite coating on the TP-AAO membranes shown in **Figures 2.6(c)** and **2.6(d)**. The template was heated to 650 ºC in air for 3 h to crystallize the coating to anatase TiO_2 and pyrolyze organics. Secondary

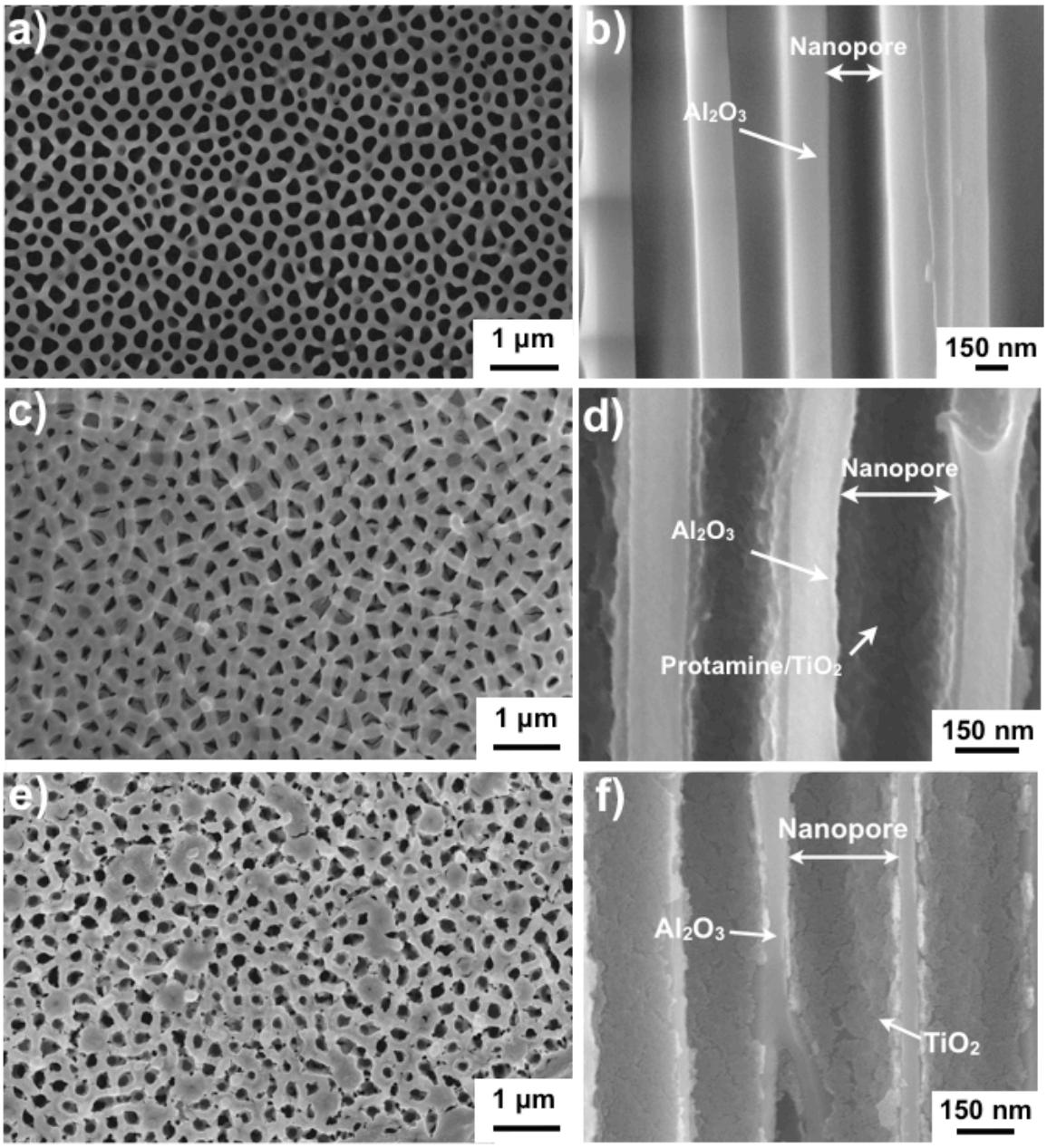

Figure 2.6: Secondary electron images of the top (a) and cross-section (b) of an uncoated TP-AAO template, top (c) and cross-section (d) after coating with 8 protamine/TiBALDH layers, and top (e) and cross-section (f) after heat treatment at 650 ºC for 3 h.

electron images of the heat treated template are shown in **Figures 2.6(e)** and **2.6(f)**. It was apparent from the cross-sectional image that the coating thickness decreased and voids were created due to the pyrolysis of protamine.

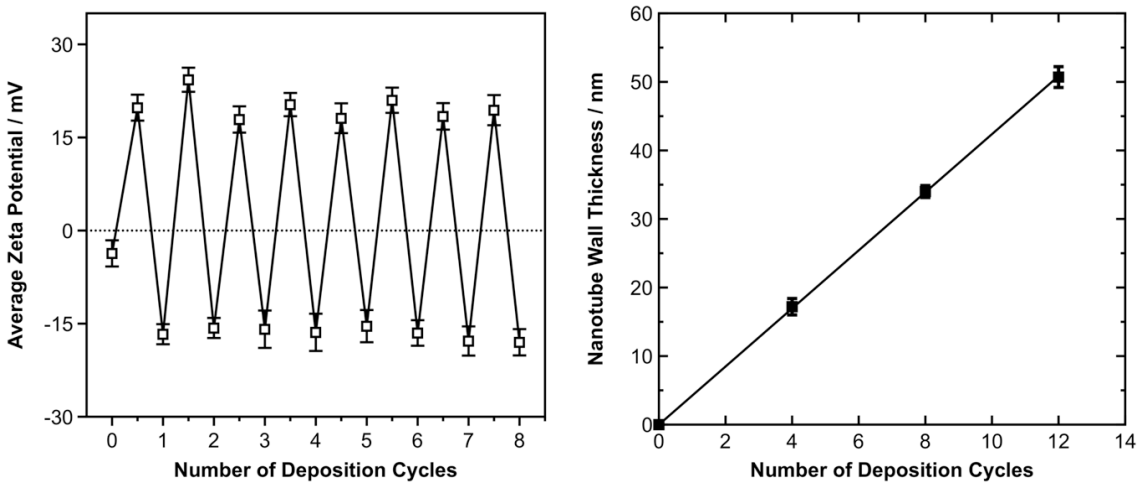

Figure 2.7: Zeta potential measurements obtained from crushed TP-AAO templates after various stages of alternating exposure to protamine-bearing (steps 0.5, 1.5, 2.5, 3.5, 4.5, 5.5, 6.5, and 7.5) and TiBALDH-bearing (steps 1, 2, 3, 4, 5, 6, 7, 8) solutions (a). The first measurement (0 cycles) was obtained from the starting TP-AAO template. Average wall thickness of titania nanotubes (after firing at 650 ºC for 3 h) as a function of the number of deposition cycles (b). The error bars in both plots correspond to the complete range of measured values.

Zeta potential measurements obtained after alternating exposure of crushed TP-AAO membranes to protamine-bearing or TiBALDH-bearing solutions are shown in **Figure 2.7(a)**. After incubation of the crushed TP-AAO in buffer solution at pH 8.5, the TP-AAO displayed a net negative zeta potential, which is consistent with literature. The isoelectric point of Al_2O_3 is reported to be between pH 7.4 and 9.4.[73] Once exposed to a protamine solution at pH 8.5, electrostatic forces drive the polycationic protamine to the alumina surface, which caused a net positive zeta potential. A regular oscillation in the

measured zeta potential was observed after each alternating exposure to the buffered (pH 8.5) protamine and TiBALDH solutions, which was consistent with the presence of an external layer of positively-charged protamine molecules or of negatively-charged TiO-bearing layers, respectively.

The influence of the number of protamine/TiBALDH exposure cycles on the average wall thickness of the nanotubes (determined from measurements obtained from secondary electron images of fired specimen cross-sections) is plotted in **Figure 2.7(b)**. A linear increase in the average wall thickness, from 17 to 51 nm, occurred as the number of exposure cycles was increased from 4 to 12, which corresponded to 4 nm of fired coating thickness for each protamine/TiBALDH deposition cycle. These results demonstrate the ability of peptide-enabled processing to deposit thin, conformal coatings, LbL without specialized equipment or surface functionalization steps.

X-ray photoelectron spectroscopic (XPS) analyses of coated TP-AAO surfaces are shown in **Figures 2.8(a)** and **2.8(b)**. The low- and high-resolution XPS spectra revealed peaks for Ti and O (consistent with a TiBALDH/titania), N and C (consistent with protamine), but not for Al, which indicated that a protamine/TiO-bearing composite coating completely covered the TP-AAO template to a thickness of at least 10 nm (i.e., greater than the information depth). Both SEM and XPS analyses demonstrated that the conformal, LbL nature of the peptide-enabled process allowed the internal nanochannel surfaces of the TP-AAO template to be continuously coated without plugging of the nanopores at the external top and bottom faces of the alumina template.

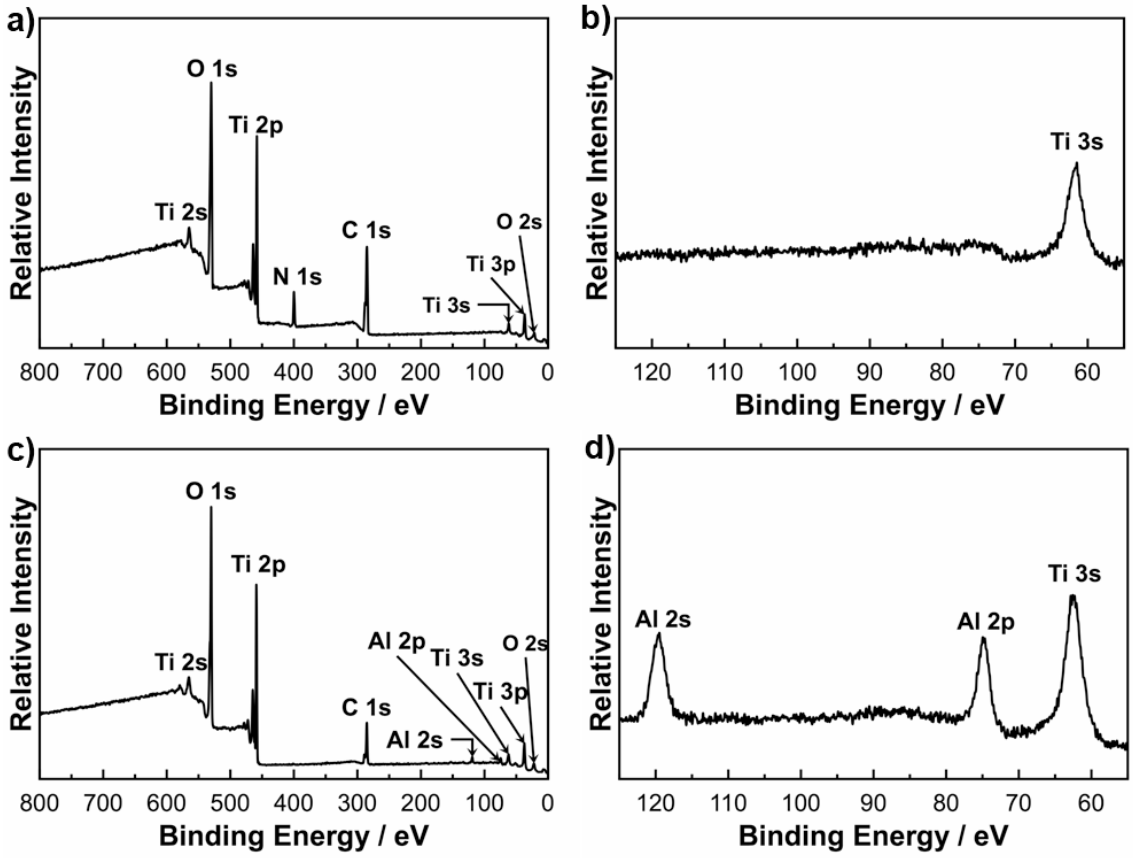

Figure 2.8: X-ray photoelectron spectroscopic analyses of: TP-AAO templates after exposure to 8 protamine/TiBALDH cycles (a, b), and after subsequent heat treatment at 650 ºC for 3 h in air (c, d).

XPS analyses of a coated TP-AAO membrane after heat treatment at 650 ºC for 3 h in air are shown in **Figures 2.8(c)** and **2.8(d)**. The presence of Ti, O, and Al peaks and the absence of N peaks were consistent with protamine pyrolysis and the generation of pores in the titania coating with some of the pores extending through the coating to the underlying alumina. The appreciable interconnected porosity generated throughout the titania coating upon protamine pyrolysis at 650 ºC allowed for subsequent penetration of a sodium hydroxide solution for selective dissolution of the underlying alumina template.

The protamine/Ti-O-coated TP-AAO membranes were heated at 5 ºC min^{-1} to 650 ºC in air and held at this temperature for 3 h to allow for water removal, organic pyrolysis, and titania crystallization. Note, while TiO_2 and Al_2O_3 can react to form Al_2TiO_5, this binary oxide compound is reported to become stable only at temperatures above 1000 ºC.[74, 75] Thermogravimetric analysis (TGA), shown in **Figure 2.9**, revealed an initial reduction (13 wt%) in weight upon heating through 100 ºC, which was consistent with the loss of water, followed by a second larger weight reduction (44 wt%) from about 200 ºC to 475 ºC, which was attributed to protamine pyrolysis. The latter weight loss indicated that appreciable protamine was entrained along with titania in the deposited coating.

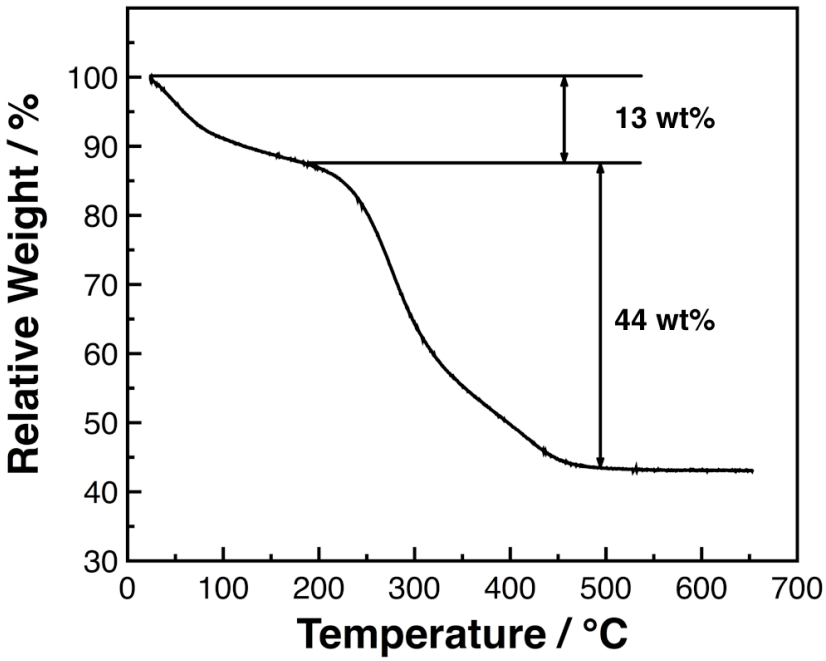

Figure 2.9: Thermogravimetric analysis of a protamine/Ti-O-coated TP-AAO template (via exposure to 8 protamine/TiBALDH cycles) upon heating at 5 ºC min^{-1} to 650 ºC in air.

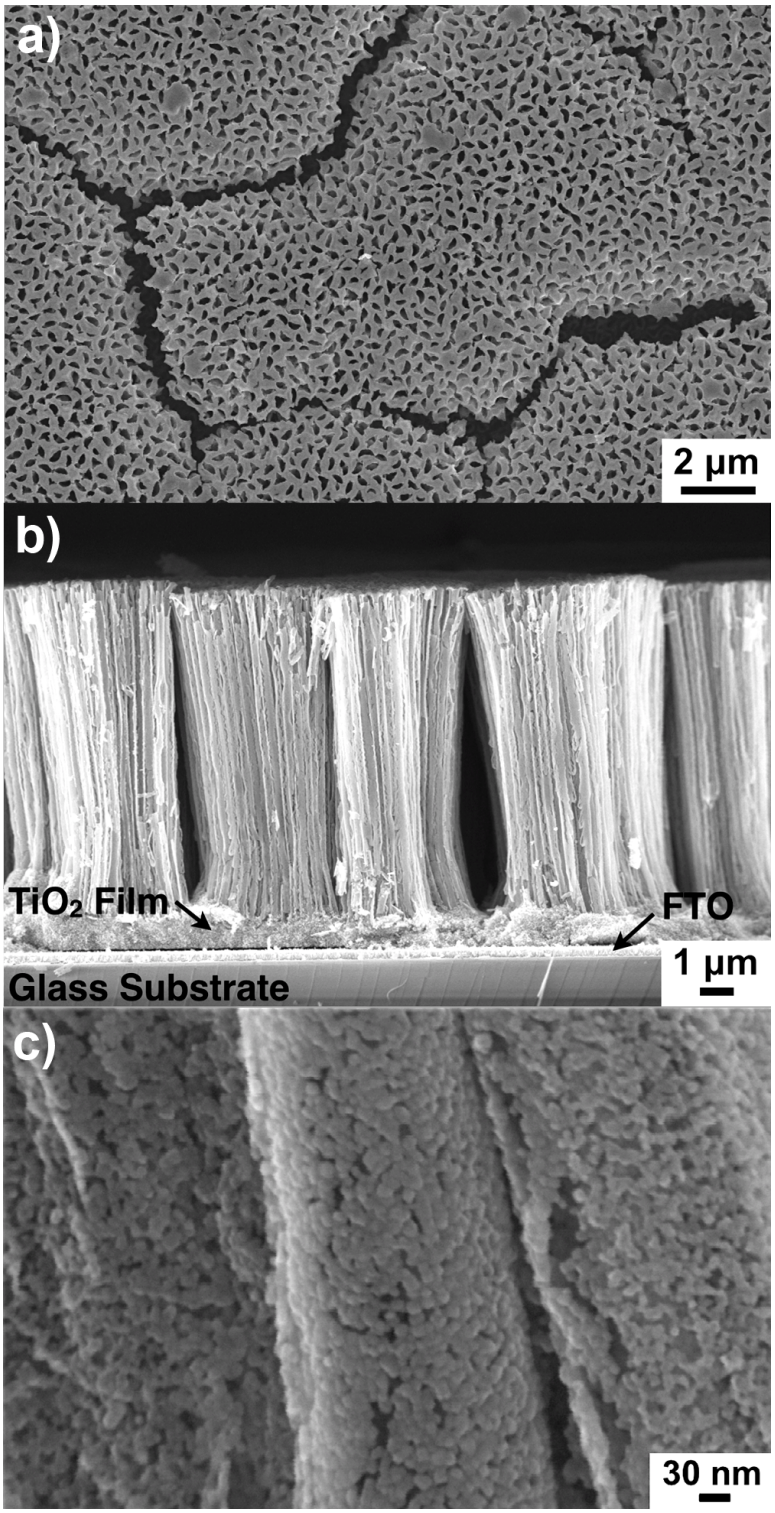

Figure 2.10: Secondary electron images of a plan-view (a) and cross-sectional view (b, c) of freestanding TiO_2 nanotube arrays synthesized via exposure of a TP-AAO template to 8 protamine/TiBALDH cycles, firing at 650 ºC for 3 h in air, selective dissolution of the TP-AAO template in a NaOH solution, transfer of the TiO_2 nanotube array to a TiO_2-coated FTO substrate, and then firing at 500 ºC for 1 h in air.

The structural interconnectivity of the titania nanoparticle network in the fired coatings resulted in freestanding, high-aspect-ratio titania nanotube (9.9 μm length : 35 nm nanotube wall thickness yields a 291:1 aspect ratio) arrays upon removal of the alumina template. The titania nanotube arrays were transferred to transparent, fluorine-doped tin oxide (FTO) coated glass substrates using a thin layer of titania nanoparticle-bearing paste to promote adhesion. After mating the nanotube array to the titania-coated FTO/glass substrate, the assembly was heated in air to 500 ºC for 1 h to pyrolyze the organic material in the paste and to sinter-bond the titania nanotube array to the titania nanoparticle-coated FTO/glass substrate.

Plan- and cross-sectional-view secondary electron images of a titania nanotube array attached to a FTO/glass substrate are shown in **Figures 2.10(a)** and **2.10(b)**, respectively. Because the external top and bottom surfaces of the TP-AAO membrane, along with the internal nanochannel surfaces, had been coated with titania during the protamine/TiBALDH deposition process, appreciable lateral interconnectivity was retained between the titania nanotubes at the top and bottom surfaces of the fired nanotube array after selective alumina dissolution. Such lateral connectivity along the top and bottom ends of the individual nanotubes provided a means of keeping the nanotubes aligned after removal of the TP-AAO template. Note: unlike other conformal coating approaches, the porous nature of the fired coating precluded the need to remove the coated top or bottom titania layers to expose the underlying alumina template for dissolution. Some mud cracking of the interconnected layer and clustering of the nanotubes midway through the thickness of the nanotube array was observed in **Figures**

2.10(a,b), which resulted from the capillary forces present during drying of the freestanding nanotubes (after alumina dissolution) and van der Waals interactions between the tubes.[41] Because the lateral connections between the nanotubes at the top and bottom of the array inhibited such clustering, the nanotube clusters observed in **Figure 2.10(b)** exhibited a slight hourglass shape. A high-magnification secondary electron image in **Figure 2.10(c)** indicated that the freestanding titania tubes were comprised of a porous, yet interconnected, network of nanoparticles with diameters of approximately 15-20 nm.

X-ray diffraction (XRD) analysis of the freestanding tubes (**Figure 2.11(a)**) yielded peaks for anatase titania (Powder Diffraction File No. 21-1272). Scherrer analysis of the anatase diffraction peaks (using a correction factor of 0.9) showed an average crystallite size of 15 ± 3 nm, which indicated that the titania crystals and titania particles seen in **Figure 2.10(c)** were comparable in size (i.e., for the bulk of the titania, many individual particles were comprised of a single anatase crystal). Transmission electron micrographs (TEM) (**Figures 2.11(b)** and **(c)**) indicated that the freestanding titania nanotubes were comprised of a porous network of nanoparticles with sizes on the order of 10 to 20 nm. In dark-field TEM, the crystallites aligned with the zone axis displayed bright contrast, and a comparison between bight-field and dark-field images showed the nanotubes were comprised of randomly oriented polycrystalline titania with crystallite sizes that were largely in agreement with Scherrer analysis. High-resolution transmission electron microscopy (**Figure 2.11(d)**) images displayed lattice fringes spaced 0.24 nm and 0.35 nm apart, which are consistent with the (004) and (101)

interplanar spacings of anatase titania, respectively. Selected area electron diffraction analyses (**Figure 2.11(e)**) also yielded ring patterns consistent with polycrystalline anatase titania.

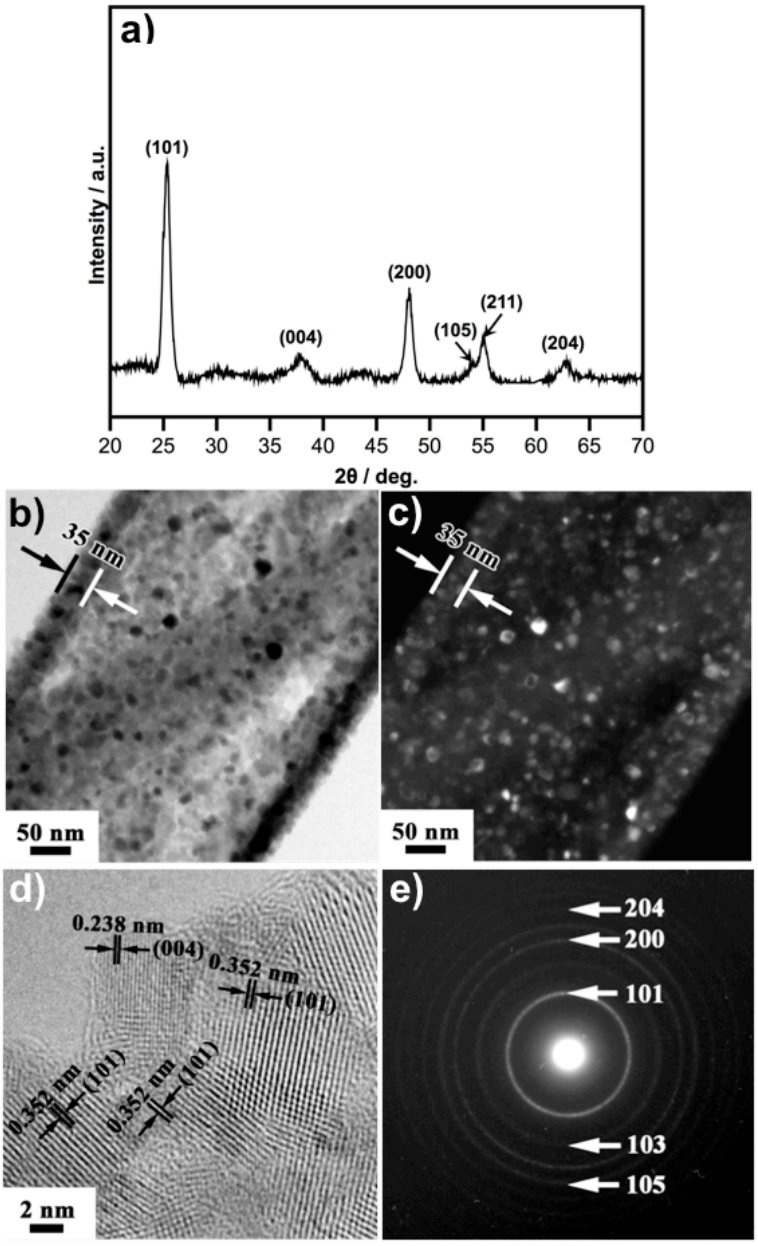

Figure 2.11: X-ray diffraction pattern obtained from a titania nanotube array synthesized via exposure to 8 protamine/TiBALDH cycles and then firing at 650 ºC for 3 h in air (hkl values are shown corresponding to diffraction peaks associated with anatase titania) (a). Bright-field (b) and dark-field (c) transmission electron images of the cross-section of a titania nanotube in such an array. High-resolution transmission electron image (d) and selected area electron diffraction analysis (e) of the titania nanotube shown in (b) and (c).

2.4.2 Utility of the Porous-Wall Titania Nanotube Arrays

The conformal deposition of appreciable protamine and titania in the LbL coating resulted in the generation of a porous, yet interconnected, titania coating upon protamine pyrolysis. Subsequent selective dissolution of the TP-AAO template then yielded aligned, high-aspect-ratio, porous-wall titania nanotube arrays. The porous walls of the nanotubes provided enhanced surface area for the adsorption of functional molecules, whereas the continuity of the titania allowed for use of the nanotubes as aligned electronic semiconductors (i.e., for a potentially more direct electron conduction pathway to an external electrode relative to an unaligned network of titania particles in a thick porous film).

Experiments were conducted to evaluate the extent of adsorption of a ruthenium-based dye onto the porous nanotube arrays. After rigidly attaching the nanotube arrays to an FTO-coated glass substrate as discussed above, N719 dye was adsorbed onto the porous titania nanotubes for 24 h at room temperature. After dye absorption, the nanotube assembly was rinsed in dry acetonitrile and dried in air. The dye was then desorbed from the nanotubes by immersion in 0.1 M NaOH solution. The concentration of the dye in this solution was evaluated by measurement of the absorbance at 513 nm and compared to calibration solutions of known N719 concentration. The average specific N719 dye loading was found to be $1.63 \cdot 10^{-4} \pm 0.70 \cdot 10^{-4}$ mol g^{-1} (normalized to the weight of titania in the nanotube assembly), which was more than twice the amount of such N719 ruthenium dye adsorbed onto less porous titania nanotube arrays prepared via sol-gel infiltration process ($7.42 \cdot 10^{-5}$ mol g^{-1}).[41]

To demonstrate the feasibility of using such aligned, porous-wall, high-aspect-ratio nanotube arrays as working electrodes, the titania nanotube arrays were incorporated into DSSCs. After adsorption of the N719 dye onto the nanotubes and attachment of a platinized FTO-bearing electrode, a redox electrolyte solution (0.6 M 1-butyl-3-methyl imidazolium iodide, 0.1 M guanidinium thiocyanate, 0.03 M I_2, and 0.5 M tert-butylpyridine in acetonitrile and valeronitrile) was vacuum infiltrated into the nanotube arrays. An optical image of an assembled DSSC and a schematic illustration were previously shown in **Figure 2.4**. Eight DSSCs were constructed from anatase TiO_2 nanotube arrays synthesized via the LbL peptide-enabled deposition process using 8 protamine/TiBALDH deposition cycles. The *J-V* behavior of such DSSCs in the dark and under AM 1.5G illumination is shown in **Figure 2.12**. These eight devices exhibited an average open-circuit voltage (V_{oc}) of 757 ± 22 mV, an average short-circuit current density (J_{sc}) of 9.4 ± 0.6 mA cm^{-2}, and an average fill factor (*FF*) of 0.73 ± 0.02, yielding an average power conversion efficiency (η_{eff}) of 5.2 ± 0.4% from **Equation 2.1**

$$\eta_{eff} = \frac{J_{sc} V_{oc} FF}{I_s} \tag{2.1}$$

where I_s is the irradiance of the simulated solar source (100 mW cm^{-2}).

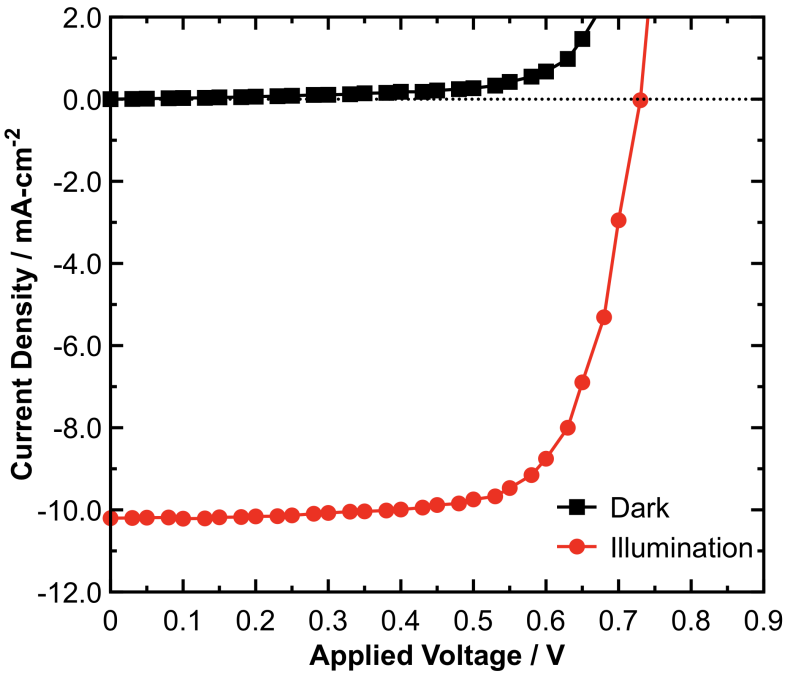

Figure 2.12: The *J-V* characteristics of a porous-wall TiO_2 nanotube dye-sensitized solar cell in the dark (■) and under illumination (●).

These fill factor and open-circuit voltage values were comparable to those reported for DSSCs synthesized with mesoporous titania thick film electrodes (FF = 0.70-0.74, V_{oc} = 778-791 mV).[59] However, the values of short-circuit current density and power conversion efficiency were lower than values reported for DSSCs based upon mesoporous titania films (J_{sc} = 15.6-18.2 mA cm^{-2}, η_{eff} = 9.1-10.1%),[59] which can be explained by comparing roughness factors. Roughness factor is a measure of the internal surface area of a structure relative to its projected surface area. For commercially available TiO_2 nanoparticles, the roughness factor is generally on the order of 1000.[59] The roughness factor of the peptide-enabled nanotube arrays can be estimated by calculating both their geometric surface area and areal density. For nanotubes with an

outer diameter of 284 nm, wall thickness of 35 nm and length of 9.9 μm, the total surface area per tube is approximately 16.6 μm^2. After removing the template, the nanotubes were organized in a roughly hexagonal arrangement with a tube-to-tube spacing of approximately 340 nm leading to an area density of 9.99 nanotubes per μm^2 (or 0.10 μm^2 of projected area per tube) given three nanotubes per hexagonal area. The ratio of these two numbers (16.6:0.1) led to an estimated roughness factor of 166 ± 50. The full calculation with schematics is shown in **Appendix A**. The reduced surface area compared to mesoporous TiO_2 negatively affects the molar quantity of dye adsorbed, which in turn led to a reduction in photocurrent density and device efficiency. The present short-circuit current values are relatively high given the modest percentage (24%) of the cross-sectional area (**Figure 2.13**) occupied by the porous titania walls (i.e., the surfaces available for dye loading) of the nanotube arrays. Further research to optimize the nanotube wall thickness and length for enhanced dye loading and short-circuit current density, along with modifications of DSSC construction (e.g., reduction of nanotube bundling, introduction of a light-scattering layer, use of an anti-reflecting film), may be pursued to achieve higher power conversion efficiencies.[59]

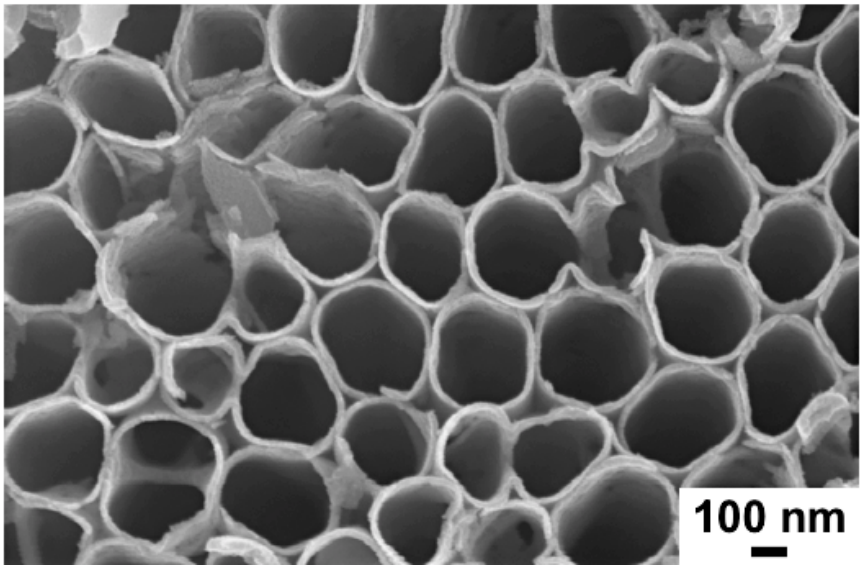

Figure 2.13: Plan-view secondary electron image of bundled titania nanotubes where the interconnected titania layer is missing upon template dissolution illustrating void space due to the nanotube geometry.

2.5 Summary and Outlook

An aqueous peptide-enabled LbL deposition protocol was developed to convert anodic alumina templates with aligned nanopore channels into aligned, high-aspect-ratio, porous-wall nanotube arrays composed of electrically-interconnected titania nanoparticles. These nanotube arrays exhibited: (1) enhanced loading of functional molecules due to the interconnected pores in the nanotube walls, (2) highly-aligned pore channels due to the lateral connectivity of the conformal titania coating deposited at the top and bottom faces of the aligned pore template, and (3) potentially anisotropic electrical conductivity that may be enabled by the interconnected titania nanoparticles within the freestanding, thin-walled, high-aspect-ratio nanotubes. These inherent characteristics of peptide-enabled nanotube arrays make them attractive for use as

electrodes (solar cells, batteries), sensors, adsorbants, (photo)catalysts, and other electrochemical, photochemical, or biochemical devices. When the arrays were incorporated into DSSC devices demonstrating reproducible light-harvesting efficiencies of 5.2 ± 0.4% with fill factors and open-circuit voltages comparable to the state-of-the-art mesoporous TiO_2 films.

This simple aqueous, peptide-based process for fabricating porous-wall, high-aspect-ratio nanotube arrays offered excellent control of the nanotube wall thickness (4 nm of TiO_2 per deposition cycle). This process did not require vapor precursors and specialized/expensive vapor deposition equipment (as are needed for gas-phase methods, such as atomic layer deposition), air/moisture-sensitive liquid precursors, and hydroxyl-rich templates or multistep surface functionalization treatments (as are needed for liquid-phase surface-sol-gel-based LbL deposition). With proper selection of template-binding/mineral-forming proteins, this facile conformal coating approach may be extended to the fabrication of assemblies with a variety of template-directed shapes comprised of peptide-directed networks of nanoscale pores and desired functional inorganic materials.

Future work should investigate of the properties of bioorganic/inorganic films deposited in this fashion (e.g., growth rate, surface area, pore-size distribution) and development of a molecular model for film growth. Such characterization of peptide-enabled deposition will provide guidance for further experimental design and yield insight into both the advantages and limitations of this particular LbL method. Furthermore, the peptide-enabled deposition method thus far has been limited to strictly TiO_2 or SiO_2 film growth. Future work should also attempt to expand peptide-enabled layer-by-layer deposition to new metal and metal oxide precursors to form thin,

conformal coatings of various technologically useful porous materials upon heat treatment.

Regarding nanostructured DSSC working electrode design, this work illustrates the geometric limitations of nanotubular architectures. That is, the roughness factor of the electrodes synthesized are estimated to be an order of magnitude smaller than traditional mesoporous titania, which resulted in a nearly twofold reduction of current density. Therefore, the next challenge is to maintain the aligned nanotube architecture while increasing the areal density of titania nanotubes. This can be done by increasing the areal nanotube density and/or increasing the length of the nanotube. Both of these modifications can be accomplished by simply modifying the porous anodic alumina template fabrication procedures (e.g., adjusting anodization current density, temperature, time, and/or solution). However, smaller nanochannels inhibit wet chemical infiltration and longer nanotubes increase the electron diffusion distance, which enhances the probability of electron-hole recombination. Novel methods for synthesizing aligned multi-wall titania nanotube arrays are investigated in Chapter 3, which can reduce the void space observed in single-wall nanotube arrays.

2.6 References

1. S. Mann, *Biomineralization: Principles and Concepts in Bioinorganic Materials Chemistry*, Oxford University Press, Oxford, NY, 2001.

2. E. Bäuerlein, *Biomineralization: Progress in Biology, Molecular Biology, and Application*, Wiley-VCH, Weinheim, Germany, 2004.

3. M. Sarikaya, C. Tamerler, A. K. Y. Jen, K. Schulten and F. Baneyx, *Nature Materials*, 2003, **2**, 577-585.

4. C. E. Flynn, S. Lee, B. R. Peelle and A. M. Belcher, *Acta Materiala*, 2003, **51**, 5867-5880.

5. R. R. Naik and M. O. Stone, *Materials Today*, 2005, **8**, 18-25.

6. A.-W. Xu, Y. Ma and C. Helmut, *Journal of Materials Chemistry*, 2007, **17**, 415-449.

7. M. B. Dickerson, K. H. Sandhage and R. R. Naik, *Chemical Reviews*, 2008, **108**, 4935-4978.

8. N. Kröger, R. Deutzmann and M. Sumper, *Science*, 1999, **286**, 1129-1132.

9. N. Cha, K. Shimizu, Y. Zhou, S. C. Christiansen, B. F. Chmelka, G. D. Stucky and D. E. Morse, *Proceeding of the National Academy of Science USA*, 1999, **96**, 361-365.

10. J. L. Sumerel, W. Yang, D. Kisailus, J. C. Weaver, J. H. Choi and D. E. Morse, *Chemistry of Materials*, 2003, **15**, 4804-4809.

11. S. V. Patwardhan and S. J. Clarson, *Polymer*, 2005, **46**, 4474-4479.

12. M. B. Dickerson, R. R. Naik, M. O. Stone, Y. Cai and K. H. Sandhage, *Chemical Communications*, 2004, 1776-1777.

13. M. T. Klem, M. Young and T. Douglas, *Materials Today*, 2005, **8**, 28-37.

14. M. Uchida, M. T. Klem, M. Allen, P. Suci, M. Flenniken, E. Gillitzer, Z. Varpness, L. O. Liepold, M. Young and T. Douglas, *Advanced Materials*, 2007, **19**, 1025-1042.

15. M. Okuda, Y. Suzumoto, K. Iwahori, S. Kang, M. Uchida, T. Douglas and I. Yamashita, *Chemical Communications*, 2010, **46**, 8797-8799.

16. G. Ahmad, M. B. Dickerson, Y. Cai, S. E. Jones, E. M. Ernst, J. P. Vernon, M. S. Haluska, Y. Fang, J. Wang, G. Subramanyam, R. R. Naik and K. H. Sandhage, *Journal of the American Chemical Society*, 2008, **130**, 4-5.

17. M. B. Dickerson, S. E. Jones, Y. Cai, G. Ahmad, R. R. Naik, N. Kröger and K. H. Sandhage, *Chemistry of Materials*, 2006, **20**, 1578-1584.

18. R. Balhorn, *Genome Biology*, 2007, **8**, 227.

19. P. Sautière, G. Briand, M. Gusse and P. Chevaillier, *European Journal of Biochemistry*, 1981, **119**, 251-255.

20. J. A. Carr and N. Silverman, *J Cardiovascular Surgery (Torino)*, 1999, **40**, 659-666.

21. H. He, A. E. David, J. Zhang, Y. S. Park, J. Wang, Y. Huang, J. Wang and V. C. Yang, *Macromolecular Research*, 2011, **19**, 1224-1226.

22. L. B. Jaques, *Journal of the Canadian Medical Association*, 1973, **108**, 1291.

23. Y. Zhang, H. Wu, J. Li, L. Li, Y. Jiang, Y. Jiang and Z. Jiang, *Chemistry of Materials*, 2008, **20**, 1041-1048.

24. M. B. Dickerson, C. L. Knight, M. K. Gupta, H. R. Luckarift, L. F. Drummy, M. L. Jespersen, G. R. Johnson and R. R. Naik, *Materials Science and Engineering: C*, 2011, **31**, 1748-1758.

25. Y. Jiang, D. Yang, L. Zhang, Q. Sun, X. Sun, J. Li and Z. Jiang, *Advanced Functional Materials*, 2009, **19**, 150-156.

26. Y. Fang, Q. Wu, M. B. Dickerson, Y. Cai, S. Shian, J. D. Berrigan, N. Poulsen, N. KroÃàger and K. H. Sandhage, *Chemistry of Materials*, 2009, **21**, 5704-5710.

27. N. I. Kovtyukhova, T. E. Mallouk and T. S. Mayer, *Advanced Materials*, 2003, **15**, 780-785.

28. J. Huang and T. Kunitake, *Chemical Communications*, 2005, **21**, 2680-2682.

29. M. R. Weatherspoon, M. B. Dickerson, G. Wang, Y. Cai, S. Shian, S. C. Jones, S. R. Marder and K. H. Sandhage, *Angewandte Chemie International Edition*, 2007, **46**, 5724-5727.

30. G. Wang, Y. Fang, P. Kim, A. Hayek, M. R. Weatherspoon, J. W. Perry, K. H. Sandhage, S. R. Marder and S. C. Jones, *Advanced Functional Materials*, 2009, **19**, 2768-2776.

31. J.-H. Park, S. Kim and A. J. Bard, *Nano Letters*, 2006, **6**, 24-28.

32. G. K. Mor, K. Shankar, M. Paulose, O. K. Varghese and C. A. Grimes, *Nano Letters,* 2006, **6**, 215-218.

33. O. K. Varghese, M. Paulose, T. J. LaTempa and C. A. Grimes, *Nano Letters*, 2009, **9**, 731-737.

34. Y.-Y. Song, F. Schmidt-Stein, S. Bauer and P. Schmuki, *Journal of the American Chemical Society*, 2009, **131**, 4230-4232.

35. M. Paulose, H. E. Prakasam, O. K. Varghese, L. Peng, K. C. Popat, G. K. Mor, T. A. Desai and C. A. Grimes, *The Journal of Physical Chemistry C*, 2007, **111**, 14992-14997.

36. S. P. Albu, A. Ghicov, J. M. Macak, R. Hahn and P. Schmuki, *Nano Letters*, 2007, **7**, 1286-1289.

37. S. Z. Chu, S. Inoue, K. Wada, S. Hishita and K. Kurashima, *Journal of the Electrochemical Society*, 2005, **152**, B116-B124.

38. H. Masuda, K. Kanezawa, M. Nakao, A. Yokoo, T. Tamamura, T. Sugiura, H. Minoura and K. Nishio, *Advanced Materials*, 2003, **15**, 159-161.

39. J. E. Wijnhoven and V. W., *Science*, 1998, **281**, 802-804.

40. D. V. Bavykin, V. N. Parmon, A. A. Lapkin and F. C. Walsh, *Journal of Materials Chemistry*, 2004, **14**, 3370-3377.

41. T.-S. Kang, A. P. Smith, B. E. Taylor and M. F. Durstock, *Nano Letters*, 2009, **9**, 601-606.

42. R. C. Furneaux, W. R. Rigby and A. P. Davidson, *Nature*, 1989, **337**, 147-149.

43. R. Spohr, *Ion Tracks and Microtechnology: Basic Principles and Applications*, Vieweg, Wiesbaden, Germany, 1990.

44. C. R. Martin, *Science*, 1994, **266**, 1961-1966.

45. J. C. Hulteen and C. R. Martin, *Journal of Materials Chemistry*, 1997, **7**, 1075-1087.

46. X. Zhu, Z. Liu and N. Ming, *Journal of Materials Chemistry*, 2010, **20**, 4015-4030.

47. M. S. Sander, M. J. Côté, W. Gu, B. M. Kile and C. P. Tripp, *Advanced Materials*, 2004, **16**, 2052-2057.

48. H. Shin, D. K. Jeong, J. Lee, M. M. Sung and J. Kim, *Advanced Materials*, 2004, **16**, 1197-1200.

49. M. Kemell, V. Pore, J. Tupala, M. Ritala and M. Leskelä, *Chemistry of Materials*, 2007, **19**, 1816-1820.

50. P. Hoyer, *Adv. Mater.*, 1996, **8**, 857-859.

51. B. B. Lakshmi, C. J. Patrissi and C. R. Martin, *Chemistry of Materials*, 1997, **9**, 2544-2550.

52. B. O'Regan and M. Gratzel, *Nature*, 1991, **353**, 737–740.

53. M. D. Archer and A. J. Nozik, *Nanostructured and photoelectrochemical systems for solar photon conversion*, Imperial College Press, London, 2008.

54. A. Listorti, B. O'Regan and J. R. Durrant, *Chemistry of Materials*, 2011, **23**, 3381-3399.

55. S. Nakade, Y. Saito, W. Kubo, T. Kitamura, Y. Wada and S. Yanagida, *Journal of Physical Chemistry B*, 2003, **107**, 8607-8611.

56. A. N. M. Green, E. Palomares, S. A. Haque, J. M. Kroon and J. R. Durrant, *Journal of Physical Chemistry B*, 2005, **109**, 12525–12533.

57. M. K. Nazeeruddin, F. D. Angelis, S. Fantacci, A. Selloni, G. Viscardi, P. Liska, S. Ito, B. Takeru and M. Grätzel, *Journal of the American Chemical Society*, 2005, **127**, 16835-16847.

58. A. Yella, H.-W. Lee, H. N. Tsao, C. Yi, A. K. Chandiran, M. K. Nazeeruddin, E. W.-G. Diau, C.-Y. Yeh, S. M. Zakeeruddin and M. Grätzel, *Science*, 2011, **334**, 629-634.

59. S. Ito, T. N. Murakami, P. Comte, P. Liska, C. Grätzel, M. K. Nazeeruddin and M. Grätzel, *Thin Solid Films*, 2008, **516**, 4613-4619.

60. L. M. Peter, N. W. Duffy, R. L. Wang and K. G. U. Wijayantha, *Journal of Electroanalytical Cemistry*, 2002, **524-525**, 127-136.

61. J. Krüger, R. Plass, M. Grätzel, P. J. Cameron and L. M. Peter, *Journal of Physical Chemistry B*, 2003, **107**, 7536-7539.

62. N. Kopidakis, K. D. Benkstein, J. v. d. Lagemaat and A. J. Frank, *Journal of Physical Chemistry B*, 2003, **107**, 11307-11315.

63. N. Kopidakis, E. A. Schiff, N. G. Park, J. van de Lagemaat and A. J. Frank, *The Journal of Physical Chemistry B*, 2000, **104**, 3930-3936.

64. A. J. Frank, N. Kopidakis and J. v. d. Lagemaat, *Coordination Chemistry Reviews*, 2004, **248**, 1165-1179.

65. N. F. Mott, *Philosophical Magazine*, 1976, **34**, 643-645.

66. J. Nelson and R. E. Chandler, *Coordination Chemistry Reviews*, 2004, **248**, 1181-1194.

67. H. Scher and M. Lax, *Physical Review B*, 1973, **7**, 4491-4502.

68. H. Scher and E. W. Montroll, *Physical Review B*, 1975, **12**, 2455-2477.

69. K. Zhu, N. R. Neale, A. Miedaner and A. J. Frank, *Nano Letters*, 2006, **7**, 69-74.

70. D. Kim, A. Ghicov, S. P. Albu and P. Schmuki, *Journal of the American Chemical Society*, 2008, **130**, 16454-16455.

71. O. K. Varghese, M. Paulose and C. A. Grimes, *Nature Nanotechnology*, 2009, **4**, 592-597.

72. Y. Zhao, M. Chen, Y. Zhang, T. Xu and W. Liu, *Materials Letters*, 2005, **59**, 40-43.

73. M. Tschapek, C. Wasowski and R. M. Torres-Sanchez, *Journal of Electroanalytical Cemistry*, 1976, **74**, 167-176.

74. P. Pena and S. DeAza, *Ceramica (Florence)*, 1980, **33**, 23-30.

75. A. Rahmel and P. J. Spencer, *Oxidation of Metals*, 1991, **35**, 53-68.

CHAPTER 3: SOL-GEL/GAS-SOLID DISPLACEMENT METHOD FOR HIGH-ASPECT-RATIO ALIGNED MULTI-WALLED TITANIA NANOTUBE ARRAYS

3.1 Summary

A non-trivial challenge in aligned nanotube array synthesis is to improve the areal density of TiO_2 nanotubes while maintaining the aligned nanotube structure. This work reveals, for the first time, how an anodic alumina template can be converted into a freestanding, aligned titania nanotube array with a multi-walled geometry via a hybrid processing methodology that combines sol-gel coating of porous anodic aluminum oxide with a gas/solid metathetic displacement reaction. The resulting aligned multi-walled, anatase titania nanotube arrays possessed an increased areal density of nanotubes, which led to an increase in roughness factor, in N719 dye adsorption, and in dye-sensitized solar cell light-to-power conversion efficiency compared to electrodes fabricated using sol-gel-derived single-wall titania nanotube (SWTNT) arrays. The multi-wall titania nanotube (MWTNT) arrays possessed estimated roughness factors of approximately 282 ± 99 and dye loading values of 195 ± 31 nanomoles N719 per cm^2 compared to the values of 75 ± 37 and 87 ± 28 nanomoles N719 per cm^2, respectively for SWTNT arrays prepared by sol-gel infiltration of an AAO template. Dye-sensitized solar cells (DSSCs) utilizing the MWTNT electrodes exhibited light-to-power conversion efficiencies of 5.5 ± 0.8% compared to 3.0 ± 1.0% for SWTNT electrodes. Furthermore, the aligned nanotube structures shown in this work did not display the appreciable nanotube bundling or microcracking typically observed in SWTNT arrays.

3.2. Introduction

In this chapter, a template-assisted method combining sol-gel vacuum infiltration and gas-solid reactive conversion procedures, was developed to synthesize aligned multi-wall titania nanotube arrays. The utility of such nanotube arrays was demonstrated in dye-sensitized cells (DSSCs) with enhanced functional dye loading and light harvesting efficiency compared to single-wall titania nanotube array electrodes.

3.2.1 Motivation for Developing Multi-Wall Titania Nanotube Arrays

As mentioned previously, aligned metal oxide nanotube or nanorod arrays have shown utility in a number of chemical, electrical, electrochemical, optical, photochemical, and biochemical devices.[1-6] Such arrays have been synthesized using anodic oxidation,[5] electrochemical lithography,[7] photoelectrochemical etching,[8] sol-gel processing,[9] hydrothermal synthesis,[10] template synthesis,[11] and peptide-enabled deposition. Unfortunately, the structures synthesized following these methods generally suffer from nanotube agglomeration and/or roughness factors of an order of magnitude less than for mesoporous TiO_2 films.[11-15] For many of the aforementioned applications, such disorder and low areal density of functional oxide material is undesirable.

Mesoporous TiO_2 films for DSSCs are typically comprised of three-dimensional random networks of nanoparticles. While such networks provide ample surface area for dye adsorption and light harvesting, the inherent disorder of the network can significantly lengthen the effective electron transport distance.[16, 17] Because electron transport within the nanocrystalline TiO_2 network is governed by diffusion, high charge-collection efficiencies require that electron transport kinetics be significantly faster than electron-

hole recombination kinetics.[18] Reducing disorder within the electrode material is expected to have an affect on this electron transport dynamic, and a common strategy to improve electron transport is to fabricate aligned nanotube arrays of TiO_2 that reduce the distance along which electrons are required to diffuse.[2, 19, 20]

The ordered nature of aligned TiO_2 nanotube arrays may also be beneficial in the fabrication of solid-state DSSCs where effective organic infiltration of thicker films (>2.5 μm) is still a challenge.[21, 22] However, nanotube agglomeration and the reduced roughness factor of single-wall TiO_2 nanotube arrays (e.g., 150 versus 1000 for mesoporous films[11-15]) diminish the effectiveness of such architectures as photoanodes.[23-25] Nanotube agglomeration and microcracking is caused by capillary forces that act on the nanotubes upon evaporative drying of wet films, with the magnitude of agglomeration being related to factors such as the surface tension of the evaporating liquid, nanotube stiffness, aspect ratio, density, and wall thickness. Overall, nanotube agglomeration may reduce the photogenerated current density by decreasing the surface area available for dye adsorption, causing solid-state electrolyte infiltration to be more difficult, and allowing for lateral diffusion of electrons which serves to increase the diffusion path length.[23-25] Additionally, the reduced roughness factor (illustrated in Chapter 1) limits the amount of surface area available for dye adsorption. A critical challenge in DSSC electrode fabrication is to develop a process that increases the areal density of TiO_2 while maintaining the highly-ordered structure of a nanotube array.

Microcracking and agglomeration have been significantly reduced using supercritical CO_2 drying, but this method does not address the issue to areal TiO_2 density.

[23, 24] The present work seeks to improve the areal density of TiO_2 nanotubes by demonstrating, for the first time, a hybrid coating and reaction method to synthesize aligned, multi-wall TiO_2 nanotube (MWTNT) arrays. Indeed, MWTNTs have previously been synthesized by either atomic layer deposition (ALD) of alternating TiO_2 and sacrificial Al_2O_3 layers or liquid phase infiltration of $TiCl_4$.[26, 27] Using ALD, as many as three concentric TiO_2 nanotubes were synthesized.[26] However, no report developing a method to synthesize aligned, high-aspect-ratio MWTNT arrays has compared the sturtures and performance of SWTNT to MWTNT in DSSCs. As DSSC electrodes, these MWTNT arrays demonstrated improved roughness factor, N719 dye loading capacity, and reduced nanotube agglomeration.

3.2.2 Overview of Multi-Wall Titania Nanotube Array Synthesis

The syntheses of aligned MWTNT arrays consisted of the following steps: (1) vacuum infiltration of a highly-ordered porous anodic aluminum oxide (AAO) template with titanium(IV) isopropoxide (to coat the nanochannel walls of the AAO following methods similar those employed by Kang, *et al.*[11]); (2) removal of the underlying aluminium substrate and Al_2O_3 barrier layer of the AAO (to create a TP-AAO template with widened nanopore channels); (3) gas/solid reaction of the partially etched TiO_2-coated TP-AAO with TiF_4 (to selectively convert Al_2O_3 to AlF_3 and $TiOF_2$) and heat treatment under flow of water vapor (to convert $TiOF_2$ to TiO_2); and (4) selective dissolution of any residual AlF_3 and Al_2O_3. A schematic of this process is shown in **Figure 3.1**.

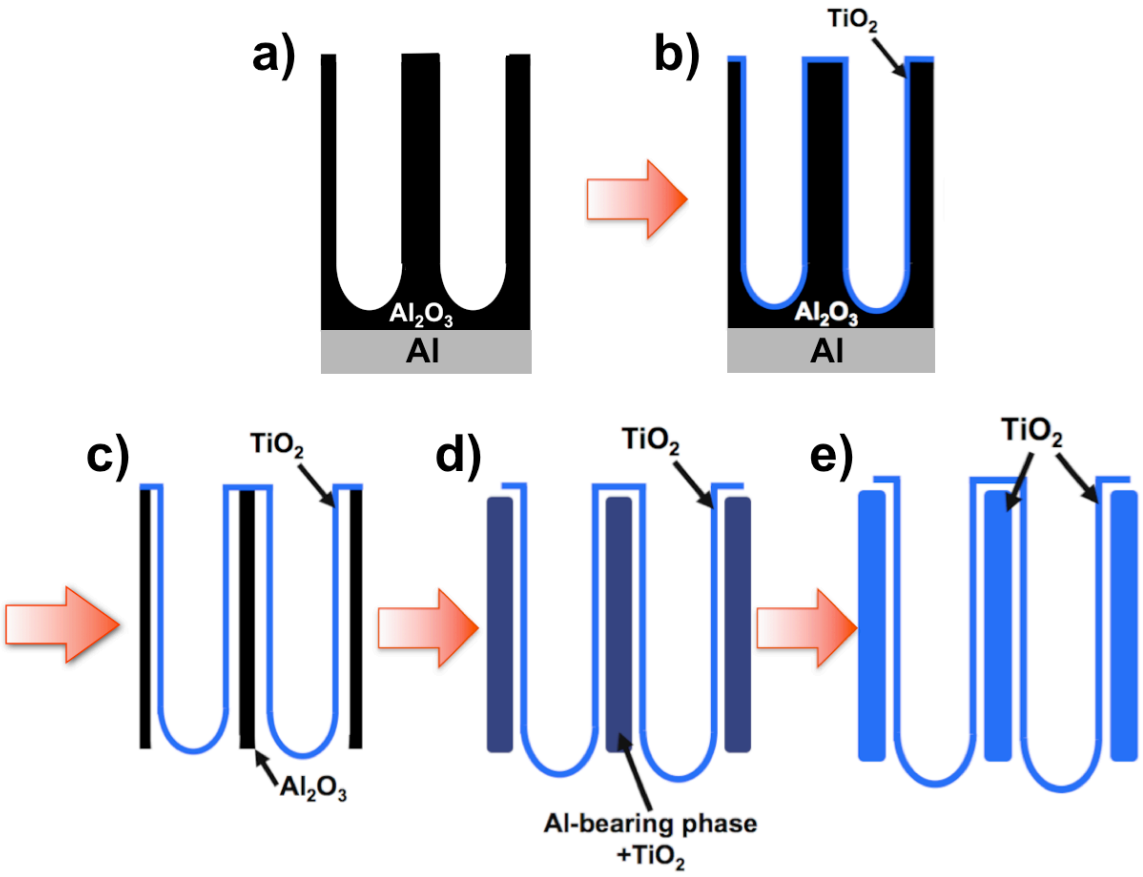

Figure 3.1: A schematic of the hybrid sol-gel coating/gas-solid reaction procedure for the syntheses of MWTNT arrays, which began with an AAO template (a). A TiO_2 coating was deposited within the nanochannels using titanium(IV) isopropoxide (b), then the underlying aluminium substrate and Al_2O_3 barrier layer of the AAO were removed (c). The partially etched TiO_2-coated TP-AAO was reacted with TiF_4 vapor, heat treated under water vapor flow (d), and selective dissolution of any residual AlF_3 and Al_2O_3 was conducted (e).

While sol-gel infiltration is a commonly used approach for coating AAO templates,[11, 28-31] the shape-preserving gas-solid displacement reaction of Al_2O_3 into TiO_2 is a novel method that deserves discussion. Inorganic gas-solid displacement reactions have previously been used to convert SiO_2-based diatomaceous earth or inverse opals into crack-free TiO_2 replicas.[32, 33] Structural replication was achieved by heating the SiO_2

template material in a sealed vessel in the presence of a halide precursor (TiF_4). The net metathetic reaction in the transformation of SiO_2 into TiO_2 is given by **Reaction 3.1**, and the similar net metathetic reaction for the conversion of Al_2O_3 into TiO_2 is given by **Reaction 3.2**. A detailed discussion of the mechanism and thermodynamics governing the shape-preserving metathetic reaction of porous anodic Al_2O_3 into TiO_2 a subject of the doctoral dissertation of Taylor McLachlan, and was beyond the scope of this work.

$$TiF_4(g) + SiO_2(s) \rightarrow TiO_2(s) + SiF_4(g) \quad (3.1)$$

$$3TiF_4(g) + 2Al_2O_3(s) \rightarrow 3TiO_2(s) + 4AlF_3(s) \quad (3.2)$$

Instead, the purpose of this work is to demonstrate a unique method that combines sol-gel infiltration with a metathetic reaction of Al_2O_3 to TiO_2 to generate, for the first time, multi-walled TiO_2 nanotubes in an aligned array. In this work, the utility of aligned MWTNT arrays has been demonstrated in DSSCs and compared to sol-gel derived single wall titania nanotube (SWTNT) based devices. DSSCs utilizing MWTNTs displayed an 83% increase of average efficiency, largely due to the almost two-fold increase in average short-circuit current density, and achieved a maximum efficiency of 6.5%. Note: the devices tested did not incorporate anti-reflective coatings or light-scattering layers known to further increase light-to-power efficiencies.[34] The increase in current density is attributed to the increase in areal density of TiO_2 (i.e., roughness factor) and the lack of large-scale nanotube agglomeration in MWTNT-based devices, which resulted in more adsorbed N719 dye relative to SWTNT-based devices.

3.3 Experimental Procedure

3.3.1 Sol-Gel-Derived Titania Nanotube Synthesis

High-purity aluminum sheets (99.999%, 1 mm thick, Goodfellow, Co., Oakdale, PA) were converted into AAO templates with aligned, one-end-closed nanochannels on top of an Al backing following the anodization procedure reported in Section 1.2.1. In this work, the second anodization step (in 10 vol% phosphoric acid at 4 ºC and 150 V) to grow the AAO template lasted 2.5 h. Templates were pore widened in 3 M NaOH for 1 min, then rinsed with DI water (18.2 MΩ·cm). This pretreatment prior to sol-gel infiltration was found to improve the conformality of the subsequent sol-gel coating by removing surface defects that block access to the nanochannels.

The template was vacuum infiltrated with a titanium(IV) isopropoxide-bearing solution (97+%, Alfa Aesar, Ward Hill, MA USA, 3:1 wt. ratio in anhydrous isopropanol). The AAO template was placed in a vacuum desiccator (10.5 L Pyrex® desiccator, Corning Inc., Corning, NY, USA) and approximately 0.5 mL of precursor was evenly deposited on top of the Al_2O_3 surface of the AAO. The atmosphere within the desiccator was evacuated (approximately 9.9 kPa) for 5 min, during which small air bubbles formed within the precursor due to trapped gas within the AAO. Note: the pressure within the chamber was not low enough to cause boiling of the solvent (i.e., the vapor pressure of isopropanol is 5.3 kPa at 23.8 °C[35]). Air was then introduced into the desiccator, which forced the precursor solution into the nanochannels. The air pressure cycling process was repeated at least five times, or until no small bubbles were noticeable during the evacuation steps.

After vacuum infiltration of the precursor into the AAO nanochannels, the precursor solution was allowed to hydrolyze for at least 16 h in ambient air (20-40% relative humidity, during the months of May-July). Excess TiO_2 formed on the external surface of the AAO was removed using several pieces of adhesive tape until no more TiO_2 was visible on the tape. The removal of residual glue from the tape was critical for the generation of uniform coatings. However, heat treatment to remove the organic residue at this stage would cause cracking of the AAO template due to the coefficient of thermal expansion mismatch between Al_2O_3 and Al metal. Therefore, the adhesive tape residue was subsequently removed by 30 min incubation in dichloromethane (99.9%, VWR, Radnor, PA, USA) with vigorous stirring. Afterwards, the sol-gel vacuum infiltration procedure was repeated a second time to ensure a complete, conformal coating of TiO_2 within the nanochannels, with excess TiO_2 removed again by repeated application of adhesive tape.

3.3.2 Aluminum Substrate Removal and Nanochannel Widening

The AAO-side of TiO_2-infiltrated templates were coated in two layers of clear nailpolish (Double Duty nail polish, Sally Hansen®, Coty, Inc., New York, NY, USA) and allowed to dry for at least 2 h. The nail polish layer served as a mask that allowed the underlying Al substrate to be selectively dissolved in an aqueous solution of 0.25 M copper(II) chloride dihydrate (Sigma Aldrich, St. Louis, MO, USA) in 6 M HCl at room temperature for 20 min under constant agitation. Uneven etching of the Al substrate at this stage will cause uneven etching of the Al_2O_3 barrier layer in subsequent processing steps. Uniform etching was achieved by agitation and rotation of the specimen along

with constant removal of the Cu precipitate that formed on the surface using a Teflon® spatula. The exposed Al_2O_3 barrier layer was removed by immersion in 3 M NaOH for ~25 min at room temperature, which widened the nanochannels and generated gaps between the TiO_2 nanotubes and the remaining AAO template. The nail polish mask that coated and protected the Al_2O_3 membrane was then removed by incubation in acetone for 10 mins. The pore-widened, TiO_2-infiltrated AAO template was heated to 500 ºC for 1 h at a 5 ºC min^{-1} ramp rate to crystallize the TiO_2 coating and pyrolyze organics.

The sol-gel TiO_2-infiltrated templates created at this stage of processing were integrated into DSSC devices following the procedures described in Section 2.3.3.

3.3.3 Gas/Solid Displacement of Residual Anodic Alumina Template

Templates for MWTNT conversion were then wrapped in nickel foil (25.4 μm thick, McMaster-Carr, Cleveland, OH, USA), and loaded into a titanium tube (2.5 cm diameter, 20 cm length; McMaster-Carr, Cleveland, OH, USA) containing a 3.6:1 molar ratio of TiF_4 (Advance Research Chemicals, Catoosa, OK, USA) to AAO and sealed in a dry glovebox under ultra-high purity Ar atmosphere (99.999%, Airgas, Atlanta, GA, USA). The ampoule was heated to 335 ºC for 8 h at a rate of 5 ºC min^{-1} to react the TiO_2-infiltrated AAO template with TiF_4(g). After cooling, the as-reacted template was oxygenated under a humid flowing oxygen atmosphere at 250 ºC for 8 h to convert $TiOF_2$ into TiO_2, and then heated to 500 ºC for 1.5 h in air to further crystallize the reaction product. This reaction procedure was developed and conducted by Taylor McLachlan and Prof. Kenneth H. Sandhage at the Georgia Institute of Technology.

3.3.4 Dye-Sensitized Solar Cell Fabrication

The procedure used for etching, transferring the TiO_2 nanotube arrays to FTO glass, and integration into DSSCs is described in detail in Section 1.3.3 with a modified redox electrolyte solution. The electrolyte solution used was comprised of 0.6 M 1-methyl-3-propyl imidazolium iodide (98+%, Sigma Aldrich, St. Louis, MO, USA), 0.1 M guanidinium thiocyanate (99%, Alfa Aesar, Ward Hill, MA, USA), 0.03 M I_2 (99.99+%, Alfa Aesar, Ward Hill, MA, USA), and 0.5 M tert-butylpyridine (96%, Sigma Aldrich, St. Louis, MO, USA) dissolved in a mixture of 85 vol% acetonitrile (99.9%, VWR, Radnor, PA, USA) and 15 vol% valeronitrile (99%, Alfa Aesar, Ward Hill, MA, USA).

3.3.5 Materials and Dye-Sensitized Solar Cell Characterization

The micro/nanoscale morphology of the AAO and MWTNTs were evaluated with scanning electron microscopy (1530 FEG SEM, LEO/Zeiss Electron Microscopy, Thornwood, NY) and transmission electron microscopy (JEOL 4000 EX, Japan Electron Optics Laboratory, Tachikawa, Tokyo). Transmission electron microscopy (TEM) and selected area electron diffraction were conducted by Dr. Ye Cai, Georgia Institute of Technology. Dimensional analyses of the AAO template, SWTNTs, and MWTNTs were obtained from 10 measurements on 5 different areas for 50 total measurements of each specimen. The error quoted for such measurements corresponded to the full-range of measured values.

The crystal structures of the nanotube arrays were evaluated at room temperature via X-ray diffraction (XRD) analyses (Alpha-1, PANalytical Corp., Almelo, The Netherlands). XRD analyses were conducted on an X'Pert Pro Alpha-1 diffractometer

(PANalytical B.V., ALMELO, Netherlands) with monochromatic $Cu_{K\alpha 1}$ (1.5405980 Å) radiation emanating from a 1.8 kW ceramic diffraction X-ray tube with a copper anode (45 kV, 40 mA) through a symmetrical Johannson monochromator. The incident beam optics were outfitted with 0.04 rad soller slits, a 1º fixed anti-scatter slit, a ½º programmable divergence slit, and a 10 mm mask. The diffracted beam optics were outfitted with a 5.5 mm anti-scatter slit and 0.04 rad soller slits placed before the X'Celerator detector. Each pattern was produced with a summation of 20 identical 40 minute scans conducted with Bragg-Brentano geometry and a step size of 0.067º 2θ ranging from 20º to 70º 2θ. Current-voltage (*J–V*) measurements were conducted under AM 1.5G conditions (Oriel 300 Watt solar simulator, 100 mW cm^{-2}) using an aperture with a measured area of 7.05 mm^2.

Analysis of the areal coverage of TiO_2 nanotubes on the electrode surface was completed using image analysis (Image-J v1.440, National Institute of Health, USA). Five bright-field optical images were taken of SWTNT and MWTNT electrodes at 2000x magnification using a Keyence VHX-600 Digital Microscope (Osaka, Japan). The color images were reduced to a greyscale image, and the "void space" (dark grey/black) could be separated from the nanotubes (light grey/white) through image thresholding. In total, 5 greyscale threshold values were used for each image. The minimum and maximum greyscale threshold values appeared to slightly underestimate the void space and the slightly overestimate the void space, respectively. Three intermediate values were then chosen for the remaining measurements. The same threshold values could be used for the remaining images of a particular electrode. Knowing the total number of pixels in the

image and the number of pixels highlighted by greyscale thresholding, the percent electrode area covered by the nanotubes could be calculated.

3.3.6 Dye Desorption Measurements

Dye desorption measurements were conducted using five electrodes of each structure after 1 h/70 ºC/0.2 M $TiCl_4$ treatment. Electrodes were then incubated in 0.3 mM N719 dye (cis-di(thiocyanato-bis(2,2'-bipyridyl-4,4'-dicarboxylato) ruthenium (II) bis(tetrabutylammonium)) in acetonitrile/t-butanol, 1:1 vol. ratio for 24 hours. After rinsing twice in dry acetonitrile, the dye was desorbed from the surfaces of the electrode by incubating in 2 mL of 0.1 M NaOH in water/ethanol, 1:1 vol. ratio for 5 mins. The absorbance of the dye in solution between 300 and 600 nm was measured by UV-Vis spectroscopy. The peak absorbance of each solution at 513 nm was compared to five standard solutions of known N719 concentration (5, 10, 15, 20, 30 μM N719) that were prepared daily. The amount of N719 adsorbed to the electrodes was normalized to the measured lateral electrode area. The lateral area of each electrode was measured by image analysis (Image-J v1.440, National Institute of Health, USA) of bright-field optical micrographs (Keyence VHX-600 Digital Microscope, Osaka, Japan). The program used for image analysis was developed by James Deneault (Materials and Manufacturing Directorate, Air Force Research Laboratory, Wright-Patterson Air Force Base, OH, USA).

3.4 Results and Discussion

3.4.1 Multi-Wall Titania Nanotube Array Synthesis

AAO templates are readily-available substrates for which both the pore diameter and aspect ratio can be tailored by adjusting anodization conditions.[36] In this study, AAO templates were produced following a modified two-step anodization process described in Chapter 1 to create a highly-ordered porous alumina film with nanopore diameters of 207 ± 29 nm and thicknesses of 13 ± 0.4 μm. Plan view and cross-sectional secondary electron (SE) images of such templates are shown in **Figures 3.2(a)** and **3.2(b).** The AAO template was then vacuum-infiltrated with titanium (IV) isopropoxide in anhydrous isopropanol (3:1 weight ratio) and allowed to hydrolyze in air (~40% relative humidity). This coating process was repeated to increase the nanotube wall thickness and ensure complete conformal coating of the AAO nanochannels. SE images of the coated template in plan view and cross-section after heat treatment (500 °C for 3 h) to crystallize the oxide coating and pyrolyze any residual organics are shown in **Figures 3.2(c)** and **3.2(d)**. From fracture cross-section images, the thickness of the sol-gel coating was measured as 34 ± 15 nm.

Before gas/solid displacement reaction of the AAO template, both the aluminum substrate and the closed-end of the template were removed by wet chemical etching. This selective etching step accomplished several objectives: (1) to remove aluminum so as to improve access of TiF_4(g) to the AAO template for reactive conversion into $TiOF_2$; (2) to create space between the AAO template and the TiO_2 coating such that reactive conversion can occur throughout the nanochannel length, and (3) to enhance the surface

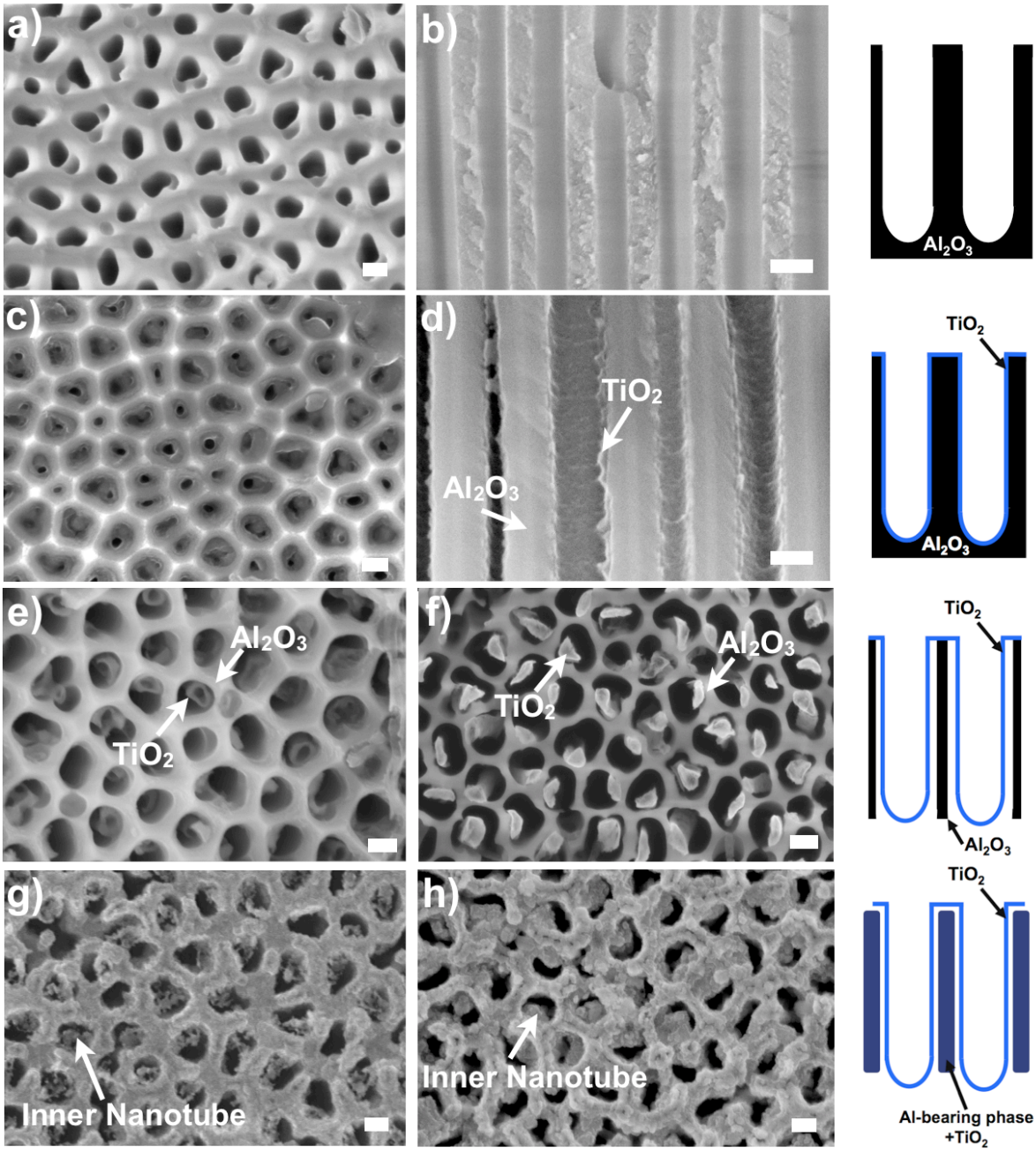

Figure 3.2: Plan view (a) and cross-sectional (b) secondary electron (SE) images of an anodic alumina (AAO) template. SE images of the same template, plan view (c) and in cross-section (d) after two sol-gel vacuum infiltrations of titanium(IV) isopropoxide and heat treatment at 500 ºC for 3 h. SE images of the top (e) and bottom (f) of a sol-gel infiltrated AAO template after aluminum substrate removal and nanochannel widening in NaOH. SE images of the top (g) and bottom (h) of the sol-gel infiltrated template after gas/solid reactive conversion of the AAO into TiO_2 at 335 ºC for 8 h and subsequent hydrolysis at 250 ºC for 8 h. A schematic (right) illustrates each step in the process. All scale bars are 200 nm.

area available for dye adsorption and electrolyte infiltration. SEM images of the top and bottom of the partially etched, TiO_2-coated template are shown in **Figures 3.2(e)** and **3.2(f)**. The sol-gel derived nanotubes were clearly visible and observed to adhere to one side of the widened nanochannels.

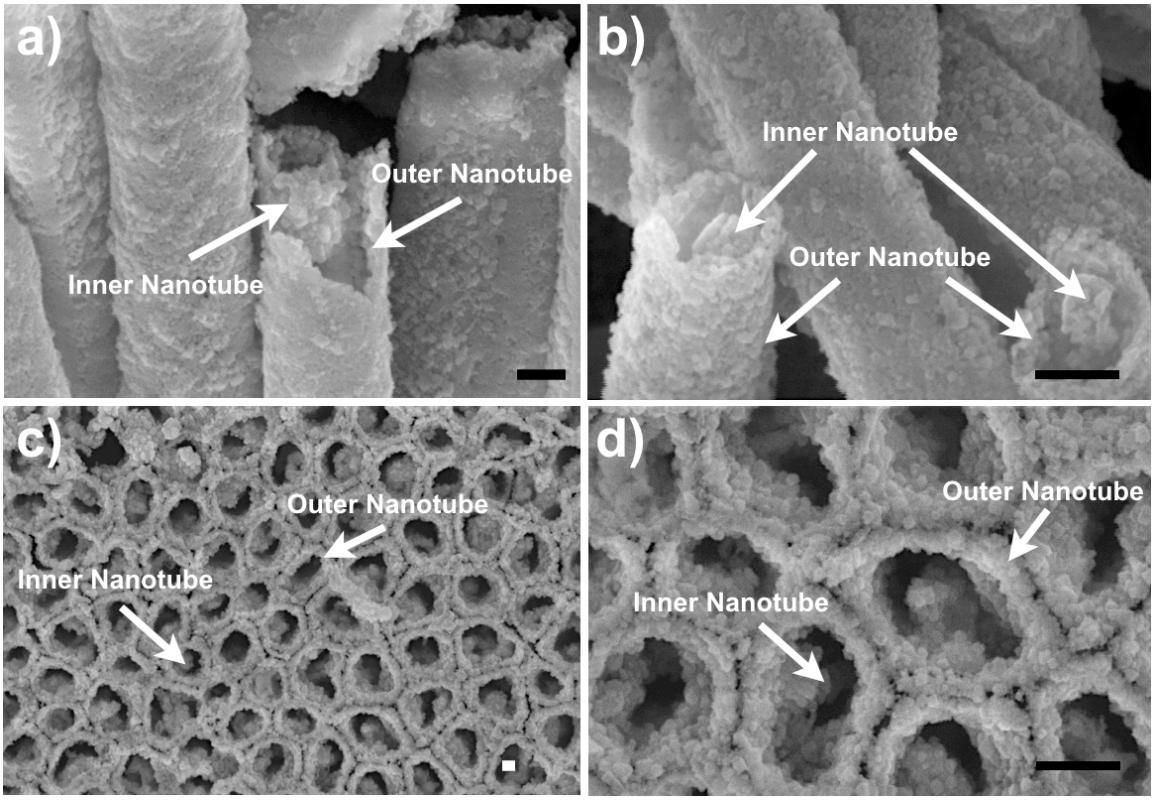

Figure 3.3: SEM images of broken MWTNTs (a, b) and low (c) and high-magnification (d) plan-view images synthesized by sol-gel vacuum infiltration followed by TiF_4 gas/ solid reaction of AAO and selective dissolution of Al-bearing compounds. All scale bars are 200 nm.

The partially-etched, TiO_2-infiltrated AAO was then converted into TiO_2 following the net **Reaction 3.2** using the two-step metathetic gas/solid displacement reaction procedure (see Section 3.3.3) developed by Taylor McLachlan. **Figures 3.2(g)** and **3.2(h)** show SE images of the top and bottom of TiO_2-coated, partially etched AAO

templates after such gas/solid reactive conversion of the AAO with TiF_4 vapor. After halide reaction, the residual AAO template appeared to increase in thickness, which was expected given the calculated increase in volume (235%) associated with the reaction of Al_2O_3 to TiO_2 and AlF_3 according to **Reaction 3.2**. More importantly, the aligned structure of the TiO_2 nanotube and AAO template was preserved after reaction of the remaining AAO with TiF_4 vapor.

After reactive conversion and oxygenation, the templates were mounted on glass slides and incubated in NaOH to selectively dissolve residual Al-bearing species (e.g., AlF_3 or unreacted Al_2O_3). Note: Al_2O_3 and AlF_3 are both soluble in aqueous NaOH solution at room temperature. SEM images shown in **Figure 3.3** illustrate the successful synthesis of MWTNTs using this hybrid method of sol-gel deposition and gas/solid displacement reaction. **Figure 3.3(a, b)** show fractured MWTNTs with a sol-gel derived inner nanotube surrounded by an outer gas/solid reaction derived nanotube. From plan-view SEM images (**Figure 3.3(c, d)**) the sol-gel derived nanotube core can be observed consistently within the outer reactively converted nanotube. Interestingly, the end of the inner nanotube was closed due to the structure of the AAO template during sol-gel infiltration and was retained after gas/solid reaction.

A schematic illustration of a MWTNT is shown in **Figure 3.4**, to clarify that all diameters measurements were of the outer diameter of the nanotubes. The average dimensions determined from 20 measurements in five different areas are given in **Table 3.1**. The initial wall thickness of sol-gel-derived TiO_2 nanotubes was 30 ± 10 nm. The average diameters of the inner sol-gel derived nanotubes and the gas-solid reaction-

derived nanotubes were 154 ± 40 nm and 426 ± 75 nm, respectively. Measurements taken of the widened AAO nanochannel yielded an average diameter of 363 ± 30 nm, and after reactive conversion, the nanotube wall thicknesses were measured to be 34 ± 7 nm and 80 ± 13 nm for the inner and outer nanotubes, respectively. These values were used to calculate the difference in roughness factor between SWTNT and MWTNT arrays.

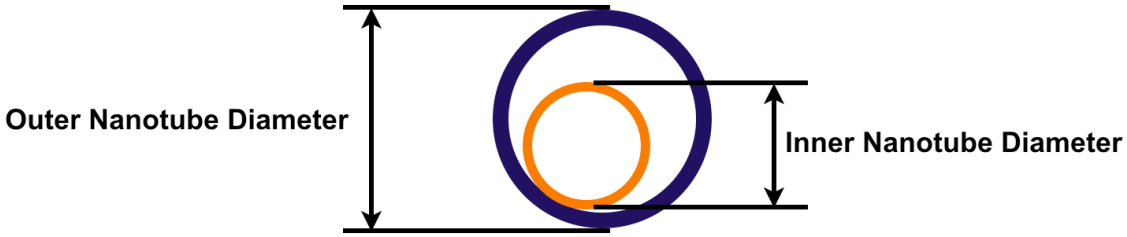

Figure 3.4: A two-dimensional schematic of an inner sol-gel-derived nanotube (orange) within an outer reactively converted nanotube (blue) illustrating the diameters measured in MWTNT arrays.

Table 3.1. Average dimensions of inner and outer nanotubes after gas/solid conversion.[a]

Inner Nanotube Wall Thickness (nm)	Outer Nanotube Wall Thickness (nm)	Inner Nanotube Diameter (nm)	Outer Nanotube Diameter (nm)	Nanotube Length (μm)
34 ± 7	80 ± 13	154 ± 40	426 ± 75	13.2 ± 0.4

[a] Averaged from 10 measurements taken on 5 different SEM images. The error corresponds to the absolute range measured.

The roughness factor (rugosity) is a ratio between the real surface area and the projected surface area.[37] Roughness factors for MWTNT arrays were calculated using the measured dimensions of the MWTNTs after dissolution of residual AlF_3 and Al_2O_3.

The average (real) surface area of a single inner and outer nanotube were estimated as 10.0 ± 2.4 μm^2 and 28.7 ± 5.8 μm^2, respectively using the average values for the nanotube dimensions listed in **Table 3.1**. The sum of these two areas yielded an average total nanotube surface area of 38.7 ± 8.2 μm^2. Assuming a hexagonal arrangement of nanotubes, three pairs of nanotubes per hexagonal area, and an average channel center-to-channel center spacing of 398 ± 70 nm, the areal density was 7.3 nanotubes per μm^2 or 0.137 μm^2 per nanotube (projected surface area). The ratio of these two numbers (38.7:0.137) which yielded a roughness factor of approximately 282 ± 99, which was 3.8 and 2.6 times larger than SWTNT arrays synthesized by sol-gel infiltration (75 ± 37) and peptide-enabled deposition (107 ± 50), respectively.[11, 28] The error reported in the estimates of roughness factor corresponded to the absolute range of roughness factors calculated using the absolute range of geometric parameters measured. A more detailed discussion of the roughness factor calculation is presented in **Appendix A**. The combination sol-gel/reactive conversion method presented here is a first demonstration of the syntheses of aligned MWTNT arrays with two concentric TiO_2 nanotubes. In principle, an increase in the number of concentric TiO_2 nanotubes and/or longer nanotubes (controlled by template processing) can further improve the roughness factor beyond what is typical for standard mesoporous TiO_2 films (~1000).[34]

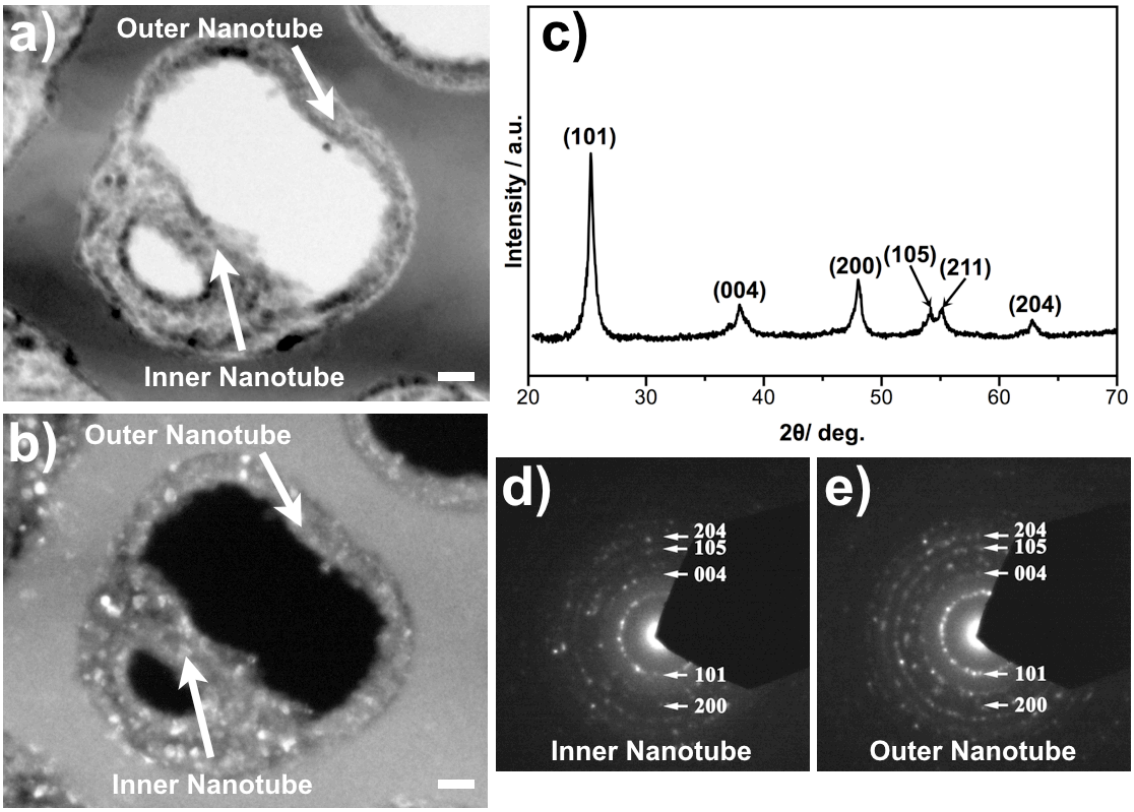

Figure 3.5: TEM cross-sectional images of an AAO template after TiO_2 sol-gel infiltration, pore widening and gas/solid displacement reaction in the bright field (a) and dark field (b). X-ray diffraction pattern (c) obtained from MWTNTs after complete dissolution of the AAO template (hkl values are shown corresponding to diffraction peaks associated with anatase TiO_2). Selected area electron diffraction patterns obtained from the inner sol-gel derived nanotube (d) and outer gas/solid reaction derived nanotube (e). All scale bars are 50 nm.

Bright-field and dark-field transmission electron images of a single nanochannel before selective dissolution of the Al-bearing species (**Figure 3.5(a, d)**) show the multi-wall nanotube in cross-section which allowed for characterization of the crystallinity of both the reactively converted and sol-gel derived TiO_2. Note: the reacted zone did not comprise the entire AAO template. From the dark-field TEM image, the TiO_2 crystallite size appeared to be similar (9 ± 3 nm) in both the sol-gel derived (inner) and reactively converted (outer) nanotubes. Scherrer analysis of the (101), (200), and (204) XRD peaks

showed an average crystallite size of 14 ± 5 nm, which was consistent with crystallite sizes observed in TEM images. The etched MWTNTs were determined to be comprised of polycrystalline anatase TiO_2 from the X-ray diffraction pattern shown in **Figure 3.5(c)** (Powder Diffraction File No. 21-1272). Selected area electron diffraction of the inner and outer nanotube (**Figures 3.5(d, e)**) supported the XRD data, and revealed both the sol-gel derived and reactively converted nanotubes were comprised of only the anatase polymorph of TiO_2.

3.4.2 Utility of Multi-Walled Titania Nanotube Arrays

To determine the relative advantages of MWTNT arrays when integrated into DSSC devices, SWTNT arrays were synthesized following the same sol-gel precursor vacuum infiltration procedure used for MWTNT syntheses. Both arrays were attached to FTO glass with the aid of TiO_2 nanoparticle paste (1.8 ± 0.2 μm thick), and fracture cross-sections of each electrode are shown in **Figure 3.6**. Both nanotube arrays were fabricated from the same AAO template to reduce variance. That is, half of a given AAO template was used for SWTNT synthesis, and the other half was used for MWTNT synthesis. Due to the significant bundling and bending of the SWTNT arrays (**Figure 3.6(a)**), it was difficult to accurately determine the length of the SWTNTs after template dissolution. The SWTNT clusters, which were about 20-30 μm in size, were attributed to capillary forces that acted upon the nanotubes after dissolution of the template and drying in air. In contrast, MWTNT arrays maintained the vertically aligned structure imparted by the AAO template (**Figure 3.6(b)**) with minimal bundling or "hourglass" affects.

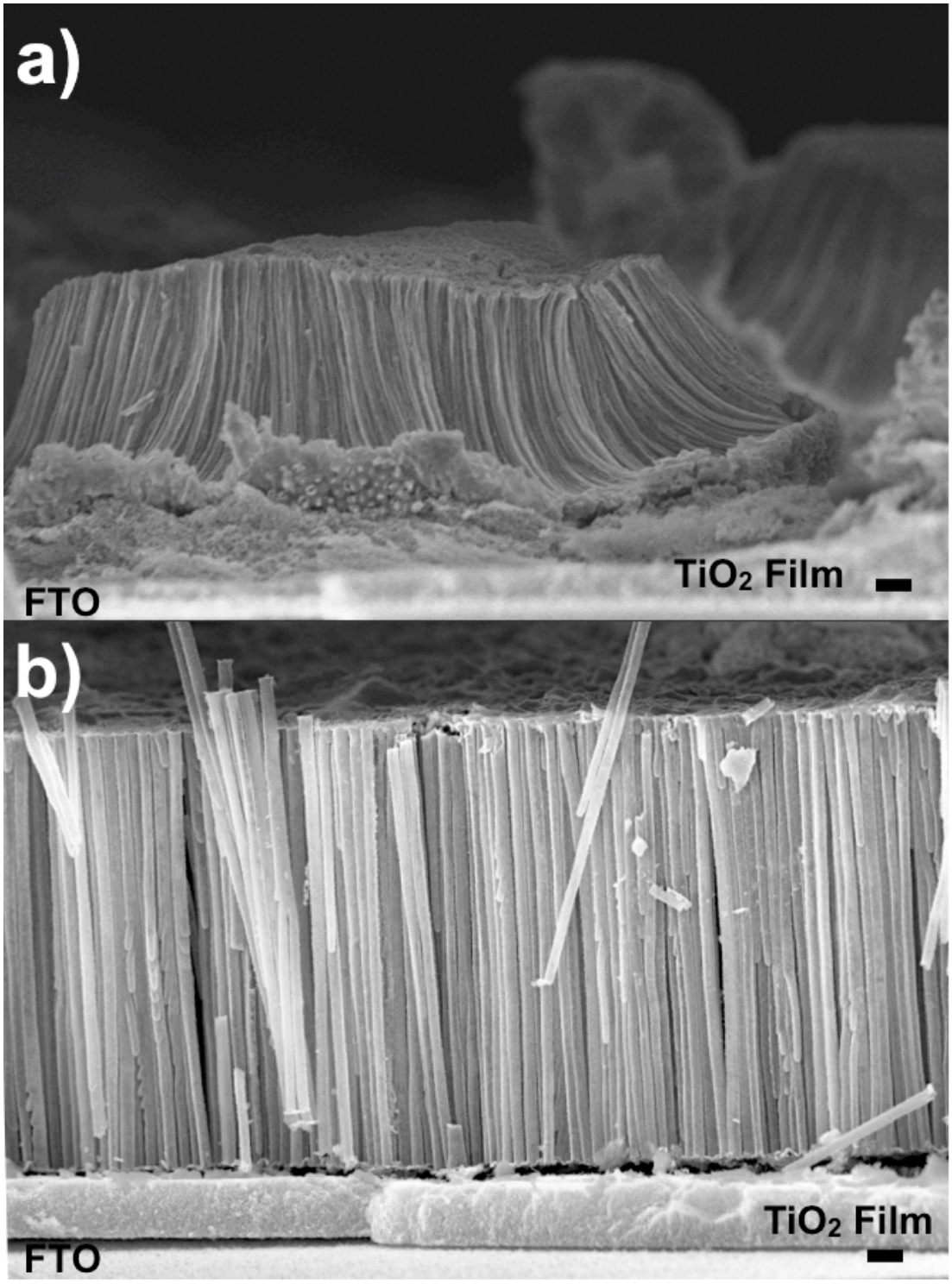

Figure 3.6: SEM images of fracture cross-sections of SWTNT arrays (a) and MWTNT arrays (b) adhered to fluorine-doped tin oxide (FTO) glass with the aid of a TiO_2 film. All scale bars are 1 μm.

The ability to rigidly maintain the ordered structure of the AAO template after dissolution can be attributed to the thicker outer nanotube walls (80 nm) of the MWTNT arrays which apparently increased the resistance of the nanotubes to bending. Nanotube bundling has been observed in other TiO_2 nanotube synthesis approaches (i.e., electrochemical anodization and template-assisted methods[11, 23, 24, 28]), and this clustering effect has been shown to negatively affect electron transport efficiency and light scattering.[23] In the electrode pictured in **Figure 3.6(a)** nanotube bundling may also affect electrical contact between the SWTNT nanotube array and nanoparticle paste. Bundling of the SWTNTs caused the nanotubes to curl at the bottom-half of the SWTNT array, which partially detached the nanotubes from the TiO_2 nanoparticle paste. The detachment of SWTNTs from the nanoparticle paste meant less surface area was in contact with the conducting oxide, and electrons injected into the nanotube array might have experienced a longer diffusion path length prior to being collected as a result.

The effect of nanotube clustering on electrode morphology was seen in plan view optical and SEM images shown in **Figures 3.7(a, b)** where a significant amount of microcracking and void space was observed between SWTNT bundles. Conversely, MWTNT arrays showed less void space and microcracking due to the improvement structural retainment after the AAO template had been completely dissolved (**Figures 3.7(c, d)**). From image analyses, 64 ± 9.6% of the electrode area was covered by SWTNTs, while 80 ± 3.2% of the electrode area was coated by the MWTNTs. The improvement in surface coverage was assumed to have a positive influence on both functional dye loading and DSSC performance.

The reduction in nanotube bundling and corresponding decrease in void space influenced the amount of N719 dye (cis-di(thiocyanato-bis(2,2'-bipyridyl-4,4'-dicarboxylato) ruthenium(II) bis(tetrabutylammonium)) adsorbed by the electrodes, as discussed in the following section. Optical micrographs were taken after 24 h incubation in a 0.3 mM N719 solution (in acetonitrile/t-butanol 1:1 vol. ratio) and subsequent integration into DSSCs (**Figures 3.7(b, inset)** and **3.7(d, inset)**). The images showed that the MWTNT devices possessed a deep, opaque red color, whereas SWTNT devices possessed a lighter red color, and were more translucent. The deep red color observed in MWTNT devices could have been the result of improved dye loading and/or light scattering, which is the subject of the following section.

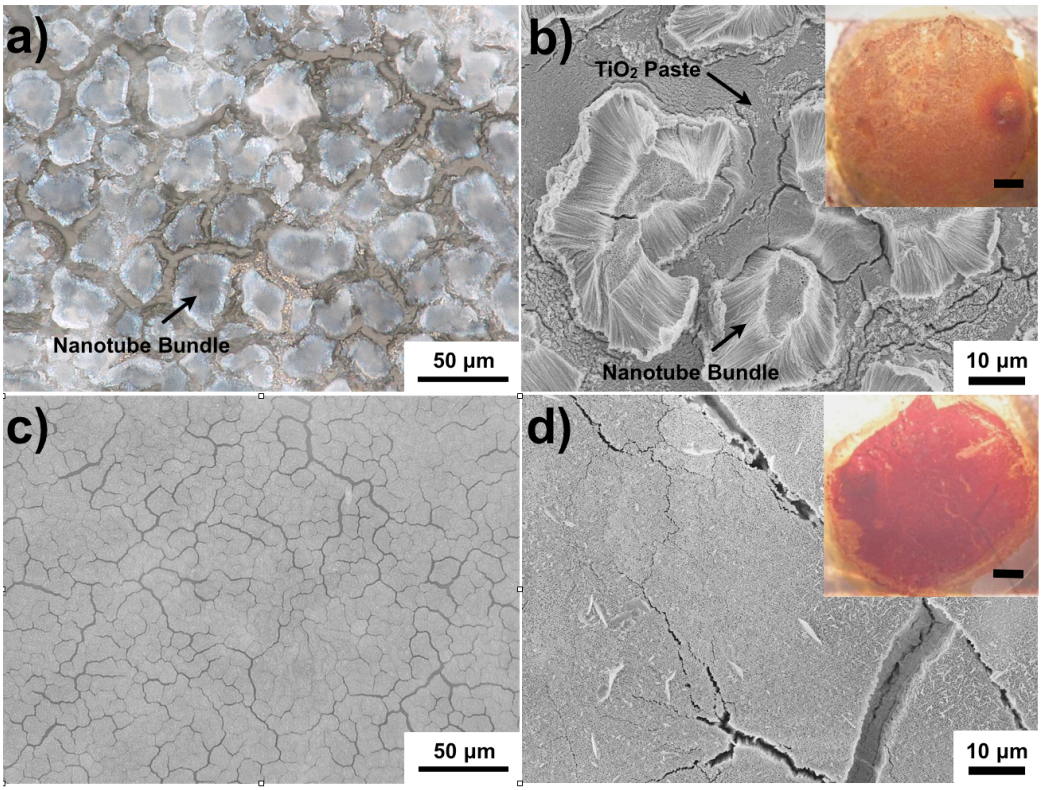

Figure 3.7: Representative SWTNT and MWTNT electrodes viewed by optical microscopy (a, c) and SEM (b, d), respectively. Optical images of representative SWTNT (b, inset) and MWTNT (d, inset) after integration into DSSC devices (1 mm scale bars).

3.4.3 Dye Desorption Measurements Comparing SWTNT and MWTNT Electrodes

Experiments were conducted to determine if the MWTNT architecture had an affect on the amount of N719 dye adsorbed when compared to SWTNT arrays. Five electrodes of each type were incubated for 24 h in 0.3 mM N719 dye solution (in acetonitrile/t-butanol, 1:1 vol. ratio) at room temperature. The dye was subsequently desorbed from the surfaces of the electrode by incubating in 2 mL of 0.1 M NaOH in water/ethanol, 1:1 vol. ratio for 5 mins. The absorbance of desorbed dye in solution was measured by UV-Vis spectroscopy and the N719 dye concentration was obtained by comparison to a calibration curve. The dye concentration was normalized to the active lateral area of the electrode using image analysis software to take into account gaps as small as 6 μm in the nanotube arrays.

The absorbance of the dye in aqueous solution (0.1 M NaOH) was measured by UV-Vis spectroscopy and compared to five solutions of known N719 concentration (5 μM, 10 μM, 15 μM, 20 μM, and 30 μM). The instrument was calibrated on a daily basis with fresh solutions, because N719 degraded over time in aqueous solution. The UV-vis spectra and corresponding calibration curves using the peak absorbance of N719 at 513 nm are shown in **Figures 3.8(a, b)** and **3.9(a, b)**. A calibration curve relating absorbance to the molar concentration of N719 dye was determined by linear regression ($R^2 > 0.99$ in both cases), and used to determine the concentration of N719 dye present in solutions used to desorb N719 dye from SWTNT and MWTNT electrodes (**Figure 3.8(c, d)** and **3.9(c, d)**).

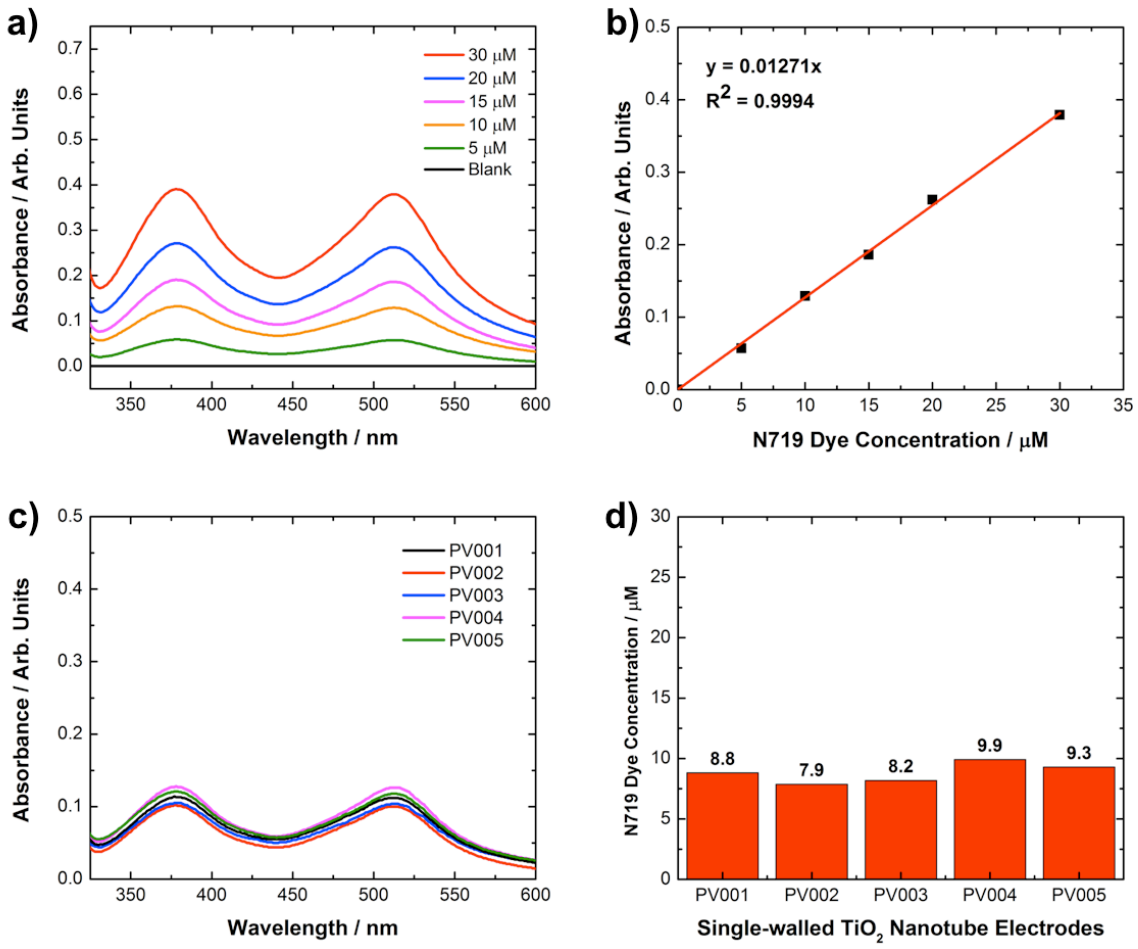

Figure 3.8: UV-vis absorbance spectra of N719 at various known concentrations (a). The absorbance at 513 nm was used to generate a calibration curve (b). UV-Vis absorbance spectra from five SWTNT electrodes (c), and the corresponding N719 dye concentration measured using the calibration curve (d).

Given that 2 mL of solution was used to desorb the N719 dye, the moles of N719 dye desorbed from the electrodes was calculated. Typically, dye desorption is normalized to the mass of TiO_2 on the electrode. In this study, the areal density of TiO_2 is enhanced and surface area is improved by increasing the amount of TiO_2 present. Therefore normalizing on a per unit mass basis could not provide adequate insight into dye loading,

and stronger comparison can be made by normalizing SWTNT and MWTNT electrode dye loading by area.

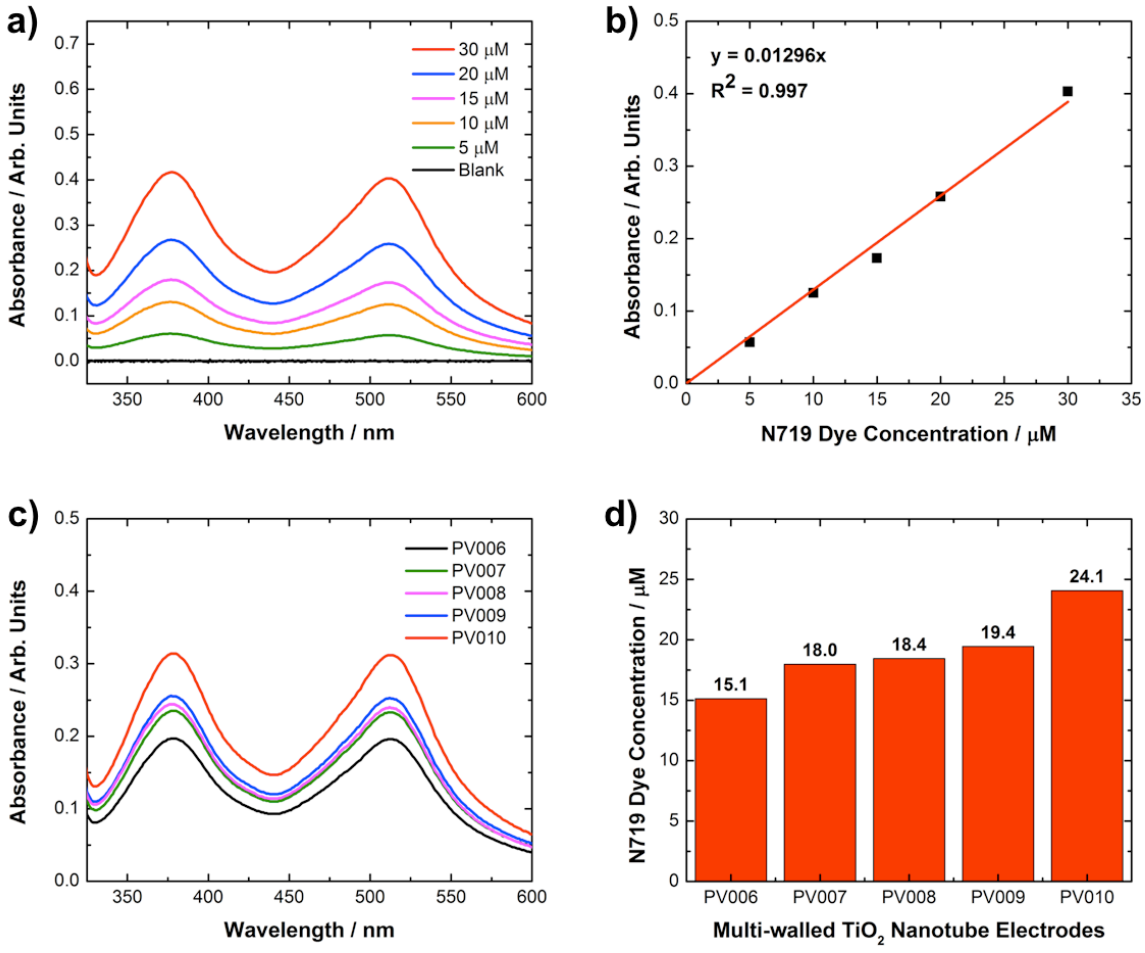

Figure 3.9: UV-vis absorbance spectra of N719 at various known concentrations (a). The absorbance at 513 nm was used to generate a calibration curve (b). UV-Vis absorbance spectra from five MWTNT electrodes (c), and the corresponding N719 dye concentration measured using the calibration curve (d).

Optical image analysis (Image-J) was used to accurately measure electrode area. More specifically, the optical micrographs taken of each electrode were passed through an image analysis macro that filtered the image based on whiteness using four grayscale thresholds. The area determined at each threshold was averaged to give the electrode

area. This program attempted to compensate for the detrimental effect of void space in the electrode, and only take into account area covered by TiO_2 nanotubes. **Figure 3.10** shows example optical micrographs of a SWTNT (**Figure 3.10(a)**) and MWTNT (**Figure 3.10(b)**).

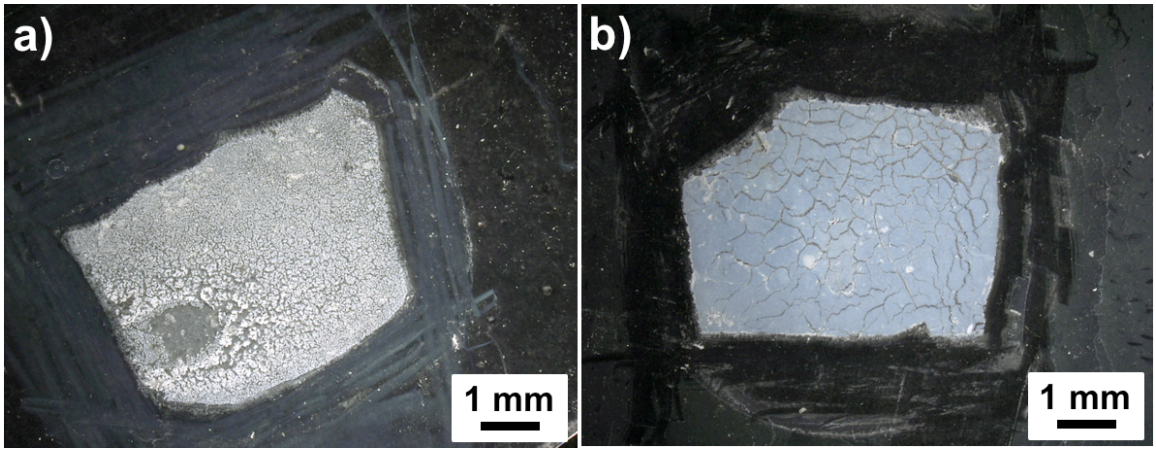

Figure 3.10: Typical optical images of a SWTNT electrode (a) and MWTNT electrode (b) use to measure the electrode area for normalization of dye desorption data.

The average N719 dye loading on five MWTNT electrodes was 195 ± 31 nanomoles N719 per cm^2 which was 2.2 times greater than for SWTNT arrays prepared by sol-gel infiltration alone (87 ± 28 nanomoles N719 per cm^2). This result confirmed that the significant difference in color intensity noted previously was due, in part, to an increase in dye loading. The dye loading ratio (195 : 87) was less than the ratio of estimated roughness factors for MWTNTs and SWTNTs (282 : 73), which may be because of a failure of the roughness factor model to take into account internal porosity within the coating, possible differences in the binding affinity for N719, variability in the nanoparticle paste layer thickness, or inaccessible surface area due to the sol-gel derived nanotube adhering to the wall of the outer nanotube.

3.4.3 Comparison of Dye-Sensitized Solar Cell Performance

To demonstrate the feasibility of aligned MWTNT arrays as working electrodes, and to evaluate the effect of the electrode architecture on DSSC performance, five electrodes of SWTNT and MWTNTs were both fabricated into DSSCs. The current-voltage (*J-V*) behavior of the best-performing MWTNT device (6.5% efficiency) is shown in comparison to the best-performing SWTNT (4.0% efficiency) in **Figure 3.11**, and the overall *J-V* characteristics are shown in **Table 3.2**. It is also important to note that the worst-performing MWTNT device (4.6%) was still better than best-performing SWTNT device. The 83% improvement in average efficiency was primarily due to the increased average short-circuit current density (by a factor of 1.9). The improvement in short-circuit current density exhibited by MWTNT devices was consistent with the improvement in roughness factor and dye loading.

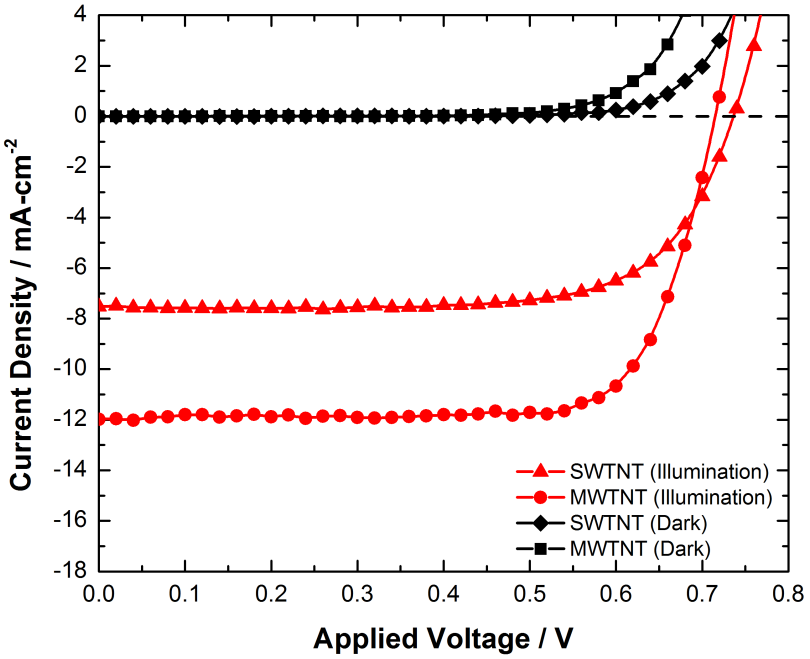

Figure 3.11: Current-voltage behavior of the best performing SWTNT and MWTNT devices in the dark (◆, ■) and under AM 1.5 G illumination (▲,●).

Table 3.2. Dye-sensitized solar cell *J-V* characteristics for SWTNT and MWTNT devices at AM 1.5G illumination.[a]

Parameter	SWTNT Devices	MWTNT Devices
J_{sc} (mA cm^{-2})	5.6 ± 2.0 (3.2-7.6)	10.4 ± 1.2 (9.5-12.0)
V_{oc} (mV)	728 ± 29 (685-763)	710 ± 30 (670-755)
FF	0.714 ± 0.04 (0.66-0.75)	0.714 ± 0.02 (0.71-0.75)
η_{eff} (%)	3.0 ± 1.0 (1.9-4.0)	5.5 ± 0.8 (4.7-6.5)
Dye Adsorption (nmol cm^{-2})	87 ± 28 (63-130)	195 ± 31 (177-250)

[a] Averaged over five devices with the indicated error corresponding to plus-minus one standard deviation, and the values in parentheses correspond to the absolute range.

3.5 Summary and Outlook

A hybrid sol-gel and gas/solid displacement procedure has been developed to generate, for the first time, aligned multi-wall anatase TiO_2 nanotube electrodes. Such electrodes possessed improved roughness factors (282 ± 99) and dye adsorption (195 ± 31 nanomoles N719 per cm^2) when compared to SWTNT electrodes (73 ± 37 and 87 ± 28 nanomoles per cm^2) prepared by sol-gel infiltration of an AAO template. As a result of the improvement in the areal density of TiO_2 and N719 dye loading, MWTNT electrodes showed enhanced average light harvesting efficiencies (5.6%) over SWTNT electrodes (3.0%) when integrated into DSSCs. Furthermore, the aligned nanotube structures shown in this work did not display appreciable bundling, curling, or significant microcracking typically observed in SWTNT arrays.

Further refinement of the MWTNT synthesis procedure may ultimately allow

nanotube electrodes to achieve roughness factors similar to standard mesoporous TiO_2 electrodes. Furthermore, such electrodes would maintain the aligned nanotube architecture, which has been shown to enhance electron transport and improve solid electrolyte infiltration.[19, 38] Future work should include attempts to generate MWTNT arrays of various lengths to improve light-to-power conversion efficiencies.

3.6 References

1. J.-H. Park, S. Kim and A. J. Bard, *Nano Letters*, 2006, **6**, 24-28.

2. G. K. Mor, K. Shankar, M. Paulose, O. K. Varghese and C. A. Grimes, *Nano Letters*, 2006, **6**, 215-218.

3. O. K. Varghese, M. Paulose, T. J. LaTempa and C. A. Grimes, *Nano Letters*, 2009, **9**, 731-737.

4. Y.-Y. Song, F. Schmidt-Stein, S. Bauer and P. Schmuki, *Journal of the American Chemical Society*, 2009, **131**, 4230-4232.

5. M. Paulose, H. E. Prakasam, O. K. Varghese, L. Peng, K. C. Popat, G. K. Mor, T. A. Desai and C. A. Grimes, *The Journal of Physical Chemistry C*, 2007, **111**, 14992-14997.

6. S. P. Albu, A. Ghicov, J. M. Macak, R. Hahn and P. Schmuki, *Nano Letters*, 2007, **7**, 1286-1289.

7. S. Z. Chu, S. Inoue, K. Wada, S. Hishita and K. Kurashima, *Journal of the Electrochemical Society*, 2005, **152**, B116-B124.

8. H. Masuda, K. Kanezawa, M. Nakao, A. Yokoo, T. Tamamura, T. Sugiura, H. Minoura and K. Nishio, *Advanced Materials*, 2003, **15**, 159-161.

9. J. E. Wijnhoven and W. Vos, *Science*, 1998, **281**, 802-804.

10. D. V. Bavykin, V. N. Parmon, A. A. Lapkin and F. C. Walsh, *Journal of Materials Chemistry*, 2004, **14**, 3370-3377.

11. T.-S. Kang, A. P. Smith, B. E. Taylor and M. F. Durstock, *Nano Letters*, 2009, **9**, 601-606.

12. C. Ruan, M. Paulose, O. K. Varghese, G. K. Mor and C. A. Grimes, *The Journal of Physical Chemistry B*, 2012, **109**, 15754-15759.

13. N. K. Allam and C. A. Grimes, *The Journal of Physical Chemistry C*, 2007, **111**, 13028-13032.

14. K. Shankar, G. K. Mor, A. Fitzgerald and C. A. Grimes, *The Journal of Physical Chemistry C*, 2007, **111**, 21-26.

15. X. Feng, K. Shankar, O. K. Varghese, M. Paulose, T. J. Latempa and C. A. Grimes, *Nano Letters*, 2008, **8**, 3781-3786.

16. B. O'Regan and M. Gratzel, *Nature*, 1991, **353**, 737–740.

17. M. K. Nazeeruddin, F. D. Angelis, S. Fantacci, A. Selloni, G. Viscardi, P. Liska, S. Ito, B. Takeru and M. Grätzel, *Journal of the American Chemical Society*, 2005, **127**, 16835-16847.

18. S. Nakade, Y. Saito, W. Kubo, T. Kitamura, Y. Wada and S. Yanagida, *Journal of Physical Chemistry B*, 2003, **107**, 8607-8611.

19. K. Zhu, N. R. Neale, A. Miedaner and A. J. Frank, *Nano Letters*, 2006, **7**, 69-74.

20. H. Wang, C. T. Yip, K. Y. Cheung, A. B. Djurisic, M. H. Xie, Y. H. Leung and W. K. Chan, *Applied Physics Letters*, 2006, **89**, 023508.

21. I. K. Ding, N. Tétreault, J. r. m. Brillet, B. E. Hardin, E. H. Smith, S. J. Rosenthal, F. Sauvage, M. Grätzel and M. D. McGehee, *Advanced Functional Materials*, 2009, **19**, 2431-2436.

22. H. J. Snaith, R. Humphry-Baker, P. Chen, I. Cesar, S. M. Zakeeruddin and M. Grätzel, *Nanotechnology*, 2008, **19**, 424003-424015.

23. K. Zhu, T. B. Vinzant, N. R. Neale and A. J. Frank, *Nano Letters*, 2007, **7**, 3739-3746.

24. J. R. Deneault, X. Xiao, T.-S. Kang, J. S. Wang, C. M. Wai, G. J. Brown and M. F. Durstock, *ChemPhysChem*, 2012, **13**, 256-260.

25. K. Soon Hyung, K. Hyun Sik, K. Jae-Yup and S. Yung-Eun, *Nanotechnology*, 2009, **20**, 355307.

26. C. Bae, Y. Yoon, H. Yoo, D. Han, J. Cho, B. H. Lee, M. M. Sung, M. Lee, J. Kim and H. Shin, *Chemistry of Materials*, 2009, **21**, 2574-2576.

27. I.-S. Park, S.-R. Jang, J. S. Hong, R. Vittal and K.-J. Kim, *Chemistry of Materials*, 2003, **15**, 4633-4636.

28. J. D. Berrigan, T. S. Kang, Y. Cai, J. R. Deneault, M. F. Durstock and K. H. Sandhage, *Advanced Functional Materials*, 2011, **21**, 1693-1700.

29. Y. Lin, G. S. Wu, X. Y. Yuan, T. Xie and L. D. Zhang, *Journal of Physics: Condensed Matter*, 2003, **15**, 2917.

30. Z. Yang, Z. Niu, X. Cao, Z. Yang, Y. Lu, Z. Hu and C. C. Han, *Angewandte Chemie International Edition*, 2003, **42**, 4201-4203.

31. G. Wu, L. Zhang, B. Cheng, T. Xie and X. Yuan, *Journal of the American Chemical Society*, 2004, **126**, 5976-5977.

32. R. R. Unocic, F. M. Zalar, P. M. Sarosi, Y. Cai and K. H. Sandhage, *Chemical Communications*, 2004, 796-797.

33. B. Hatton, L. Mishchenko, S. Davis, K. H. Sandhage and J. Aizenberg, *Proceedings of the National Academy of Sciences*, 2010, **107**, 10354-10359.

34. S. Ito, T. N. Murakami, P. Comte, P. Liska, C. Grätzel, M. K. Nazeeruddin and M. Grätzel, *Thin Solid Films*, 2008, **516**, 4613-4619.

35. *CRC Handbook of Chemistry and Physics*, CRC Press, Boca Raton, FL, 2011.

36. F. Li, L. Zhang and R. M. Metzger, *Chemistry of Materials*, 1998, **10**, 2470-2480.

37. R. N. Wenzel, *The Journal of Physical and Colloid Chemistry*, 1948, **53**, 1466-1467.

38. M. Wang, J. Bai, F. Le Formal, S.-J. Moon, L. Cevey-Ha, R. Humphry-Baker, C. Grätzel, S. M. Zakeeruddin and M. Grätzel, *The Journal of Physical Chemistry C*, 2012, **116**, 3266-3273.

CHAPTER 4: CHARACTERIZATION OF PEPTIDE-ENABLED LAYER-BY-LAYER DEPOSITION OF TITANIA AND COMPARISON TO SYNTHETIC POLYAMINES

4.1 Summary

The alternating exposure of a negatively-charged surface to suitable synthetic or biologically-derived polycations (e.g., protamine or polyethyleneimine) and a reactive metal oxide precursor (e.g., titanium(IV) bis(ammoniumlactato) dihydroxide) has resulted in the deposition of a TiO-bearing coating in a layer-by-layer (LbL) fashion. The relationship between the choice of polyamine (i.e., synthetic or bioorganic) to the TiO-bearing film deposition rate and properties (e.g., film thickness, roughness, surface area) is examined for the first time. Each of these film characteristics are of critical importance for designing future TiO_2 coating methods for various electrical, biochemical, photochemical, and optical applications. In this study, the deposition rate and film characteristics of TiO-bearing films deposited by either synthetic polyethyleneimine (PEI, 600 and 750,000 M_w branched and 2,500 M_w linear) or bioorganic protamine (4.1 kDa) were interrogated to develop relationships between coating characteristics and the polyamine used during deposition. PEI-based films deposited at a linear rate (6 to 10 nm per cycle) consistent with a "surface active" model for electrostatic LbL deposition. Conversely, the thickness of protamine-enabled films increased in a non-linear fashion over 10 deposition cycles, with two distinct regimes. The source of non-linear deposition in protamine-enabled films is shown to be consistent with an "active volume" model, where at least one molecule (presumably protamine) can diffuse "in" and "out" of the film thickness.

4.2 Introduction

In this section, a summary of relevant literature regarding the reactive layer-by-layer (LbL) deposition of metal oxide coatings by synthetic or bioorganic polyamines, and a molecular model for exponential LbL buildup of organic polyelectrolyte multilayers are discussed.

4.2.1 Reactive Layer-by-Layer Deposition of Polyamines and a Precursor of Titania

The alternating exposure of a negatively-charged surface to suitable synthetic or biologically-derived long-chain polyamines (e.g., protamine or polyethyleneimine) and reactive metal oxide precursor (e.g., tetramethoxysilane or titanium(IV) bis(ammoniumlactato) dihydroxide) has been utilized to deposit either SiO- or TiO-bearing coatings in a LbL fashion.[1-4] These reactive LbL methods are based on electrostatic interactions, and the knowledge that long-chain polyamines are capable of inducing the formation of SiO- and TiO-bearing precipitates from aqueous precursor solutions.[5-7] Such reactive deposition has been used to generate three-dimensional replicas comprised of microscale titania structures,[1] high-aspect-ratio aligned titania nanotube arrays,[8] and enzyme functionalized SiO_2 and TiO_2 coatings on SiO_2 microspheres.[9] Additionally, these coating methods have been used to develop components of gas sensors and dye sensitized solar cells, as well as materials for biocatalysis and anti-microbial agents.[1, 8-11] Further investigation into these synthesis methodologies revealed that not only were these methods capable of metal oxide deposition at near-neutral pH, but the as-deposited layers were composed of organic/ inorganic composites which could be converted into porous coatings upon organic

To date, both synthetic polyethyleneimine (PEI) and the arginine-rich peptide, protamine, have been used to enable the buildup of these bioorganic/inorganic composite films.[1, 4, 8, 12] Indeed, several studies have included characterization of reactive protamine- or PEI-based film deposition rate as a function of the number of cycles.[2, 8, 9, 12] However, the conditions used to examine deposition rates (e.g., pH, precursor concentration, drying after each cycle) are not comparable, and a comprehensive micro/nanostructural comparison (i.e., characterization of roughness, specific surface area, pore-size distribution) between metal oxide films deposited by synthetic and bioorganic polyamines does not exist. Each of these film characteristics are of critical importance for designing/selecting future TiO_2 coating methods for desired structure/property relationships for various electrical, biochemical, photochemical, and optical applications.

In this chapter, the film deposition rates and properties of hybrid polyamine/TiO-bearing films based upon either synthetic polyamines of various molecular weights (600 M_w branched PEI, 750,000 M_w branched PEI, and 2,500 M_w linear PEI) or bioorganic protamine (4.1 kDa) were investigated. Branched PEI was chosen for comparison to protamine as a synthetic counterpart due to its availability, solubility, mixed composition of amine moieties (primary, secondary, and tertiary amines), and precedent in literature for LbL TiO_2 deposition.[4, 12] The deposition rate of linear PEI was investigated because of its linear molecular structure (similar to a peptide) and the presence of only secondary amines. Unlike synthetic PEI, protamine is an arginine-rich (64.5%) readily-available biomolecule (see **Figure 4.1** for amino acid sequence) with a mixed composition of functional side chains such as: guanidinium amine groups (from arginine), hydrophobic

groups (from alanine and isoleucine, 9.7%), and polar groups (serine and threonine, 16.1%).[13]

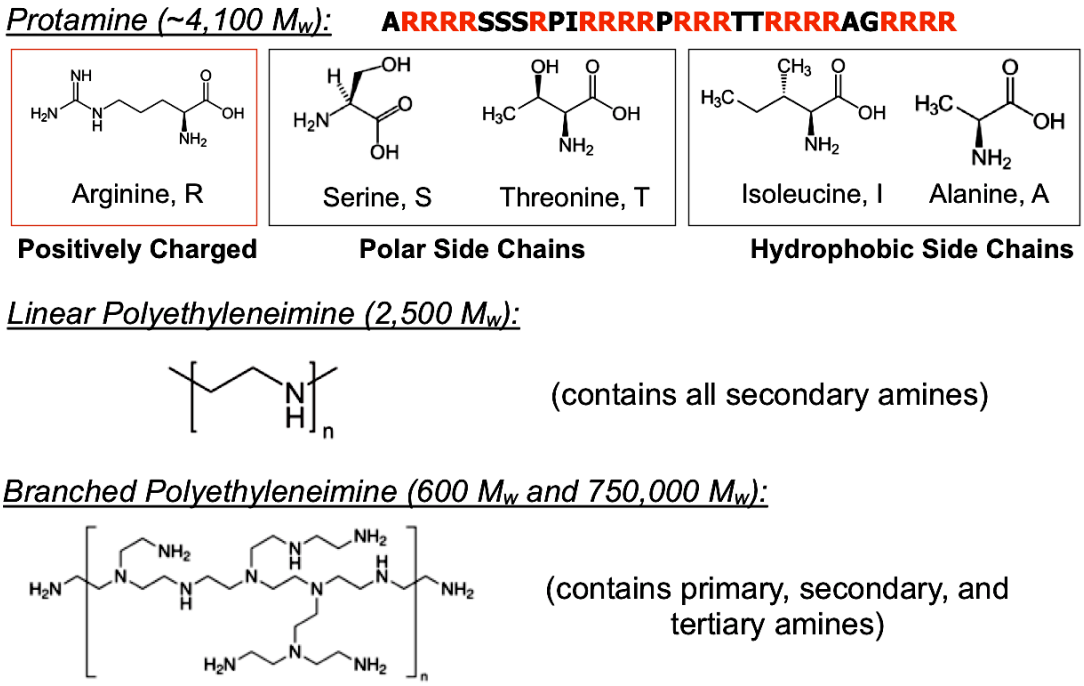

Figure 4.1: The bioorganic and synthetic polyamines examined. The charged, polar, and hydrophobic amino acid side-chains are highlighted from the amino acid sequence of protamine derived from salmon.[13]

The as-deposited films were characterized *in situ* using a quartz crystal microbalance with energy dissipation monitoring (QCM-D) to compare film deposition rates and viscoelastic properties. Ex-situ atomic force microscopy (AFM) was used to compare as-coated film thicknesses and topographies. The films were then heat treated to pyrolyze entrapped organics and characterized by ex-situ AFM (film thickness) and Brunauer-Emmett-Teller (BET) surface area analysis using N_2 adsorption to investigate any differences in specific surface area, pore size distribution and film thickness between the bioorganic-derived and synthetic polyamine-derived TiO_2 coatings.

4.2.2 Models for Linear and Exponential Buildup of Polyelectrolyte Films

In general, two types of electrostatic LbL film buildup processes have been reported: (1) linearly depositing films where thickness increases at a near-constant rate with each deposition cycle and (2) exponentially growing films where coating thickness increases more and more rapidly with each additional deposition cycle (**Figure 4.2**). Typical examples of polyelectrolyte films with a linear deposition rate are poly(allylamine hydrochloride)/poly(styrene sulfonate) (PAH/PSS), poly(diallyldimethylammonium chloride (PDDA)/PSS, and poly(ethyleneimine)/ poly(styrene sulfonate) (PEI/PSS).[14] Polyelectrolyte pairs where film deposition increases exponentially include: poly(L-lysine)/hyaluronic acid (PLL/HA), poly(L-lysine)/poly(L-glutamic acid) (PLL/PGA), and poly(L-glutamic acid)/poly(allylamine hydrochloride) (PLL/PAH).[15, 16]

The linear deposition of polyelectrolyte multilayer films proceeds via surface charge overcompensation upon polyelectrolyte adsorption, which allows for a subsequent layer of oppositely charged polyelectrolytes to be adsorbed to the film surface.[17] The structure of these films can be affected by pH, ionic strength, temperature, and solvent quality.[18-21] By adjusting any one of these parameters, linearly-depositing polyelectrolyte multilayers (e.g., PDDA/PSS, PAH/PSS) can exhibit exponential film deposition.[19, 22, 23]

Two mechanisms used to explain an exponential deposition rate are: (1) active surface area mechanisms or (2) an active volume mechanism.[16] Active surface

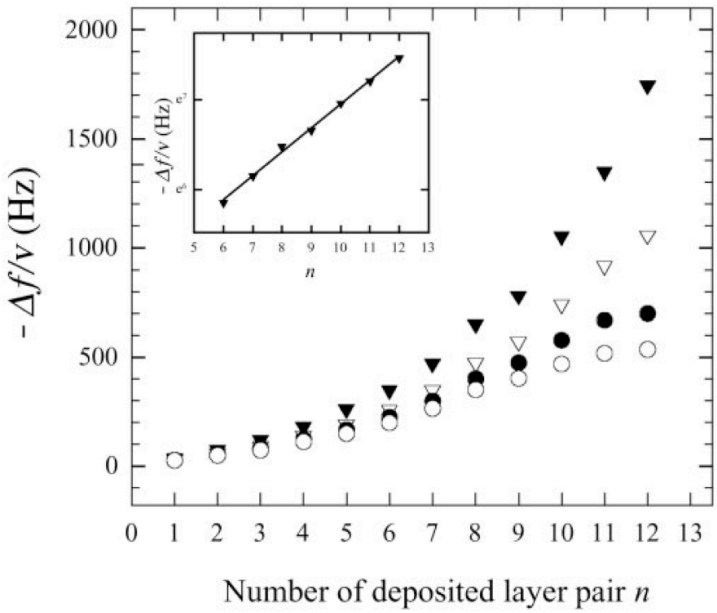

Figure 4.2: Differences in the QCM frequency shifts $-\Delta F/v$ as a function of the number of PLL/HA layer pairs, n deposited on a SiO_2 substrate. Data are given for four harmonics: 5 MHz (▼); 15 MHz (▽); 25 MHz (●); and 35 MHz (○). The evolution of $y = -\Delta F/v - y_o$ as a function of n in a logarithmic scale for the fundamental frequency (5 MHz) for n = 6-12. y_o was obtained by fitting the 5-MHz data by the function $-\Delta F/v = y_o + a \exp(bn)$. The black line corresponds to the linear regression on this logarithmic plot. The linear dependence of ln y with n proves the exponential nature of the deposition process. (Reproduced with permission from ref. 14)

mechanisms for exponential buildup of polyelectrolytes include: buildup due to increasing surface roughness, buildup due to island growth on the surface, or film buildup due to dendritic deposition.[19, 22-24] Increasing surface roughness leads to exponential film buildup because of the escalating amount of surface area available for polyelectrolyte adsorption and has been observed using deposition conditions that reduce the charge density of at least one polyelectrolyte in the multilayer (i.e., strongly acidic/alkaline pH, high salt concentration (> 0.5 M), increased ethanol in the solvent (> 60 vol%)).[19, 22, 23] The precise role of charge density of LbL polyelectrolyte film growth is proported to

depend on the polyelectrolytes used.[18] In the case of PDDA/PSS or PAH/PSS multilayers, solution conditions that reduced the charge density of at least one of the polyelectrolytes may cause the polyelectrolyte chains to fold into a random coil configuration, which increases agglomeration and the surface roughness of the deposited films.[19, 22, 23] Films deposited under these conditions have been shown to exhibit a vermicular surface morphology, and this rough surface morphology provided more active surface area for subsequent polyelectrolyte adsorption with each additional deposition cycle.[19, 22, 23]

The island growth model is a modification of the surface roughness model, which the substrate is presumed to become only partly coated by the first layer of polyelectrolyte.[24, 25] Upon application of the second layer, the substrate is more effectively coated, and the amount of material added with each adsorption step increases because the radius and height of each island increases incrementally.[24] Eventually the islands coalesce and the deposition rate decreases and becomes constant.[24]

The third possible explanation for exponential growth proposed by Haynie, *et al.* is the dendritic model, which is based on the tendency of linear polyelectrolytes to form brush-like structures when bound to an oppositely charged surface.[24, 26] It may be that after the initial polyelectrolyte deposition step, one or more oppositely charged polyelectrolyte molecules can bind to the same surface-adsorbed polyelectrolyte, yielding branch-like structures.[24] Each successive deposition step adds to the number of branches and the amount of material deposited increases.[24] This process can continue until the effects of steric hindrance dominate, and the rate of film buildup levels off because the

number of binding sites becomes limited. The dendritic model for active surface exponential growth has not been investigated experimentally, but appears consistent with films that display a transition from exponential to linear deposition.[24, 27]

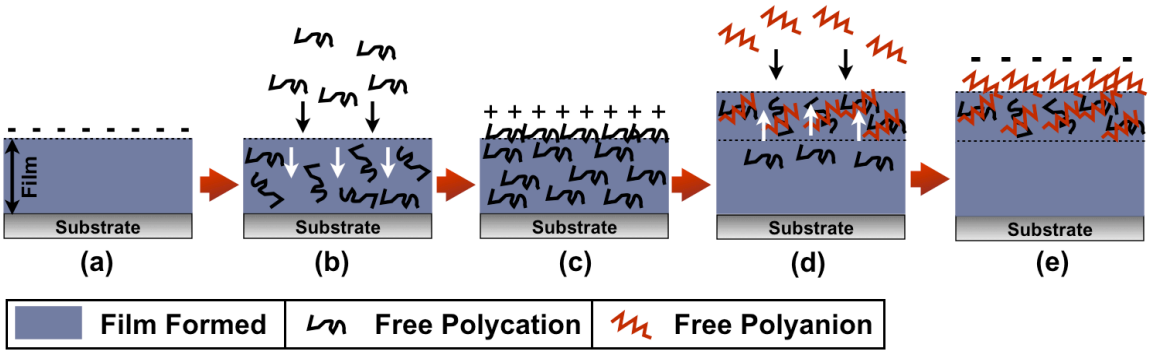

Figure 4.3: A schematic representation of the buildup mechanism for PLL/HA polyelectrolyte multilayers which is based on the diffusion of the polycationic molecule through the film.[18] In the schematic, film growth is assumed to have started with a negatively charged HA-terminated film (a). The film was incubated in PLL which diffuses through the thickness of the as-deposited film and concomitantly creates a positively charged energy barrier (b). After rinsing, some free polycationic molecules remain in the film (c). The film is then placed in contact with HA, and free PLL within the film may diffuse out of the film and undergo complexation with HA at the film/ solution interface (d). Charge overcompensation by HA led to a net negative charge (e), and the film is thicker than it was in step (a). [14,15,23] For simplicity, only surface charge is represented in the schematic.

The active volume mechanism for exponential buildup is a diffusion-based mechanism commonly observed in biological polyelectrolytes where at least one of the polyelectrolytes is capable of inward and outward diffusion within the film thickness.[15] This behavior was first determined for PLL/HA films by examining confocal laser micrographs of vertical cross-sections containing fluorescently-labeled polyelectrolytes (fluorescein isothiocyanate (FITC) labeled PLL and Texas red (TR) labeled HA) at

various stages of the deposition process.[15] From the micrographs, PLL was observed to be mobile and capable of inward and outward diffusion whereas HA-TR remained immobilized in the region in which it was originally deposited.[15]

In this example (illustrated schematically in **Figure 4.3**), film deposition is assumed to have begun with a negatively charged HA layer **Figure 4.3(a)**.[15, 16, 28] The polycationic PLL diffuses through the thickness of the film **Figure 4.3(b)** concomitant with the formation of a positively charged energy barrier at the film surface due to charge overcompensation (**Figure 4.3(c)**).[15, 16, 28] This energy barrier prevents the polycationic molecules from diffusing out of the film during the subsequent rinsing cycles.[15, 16, 28] Once the film is exposed to HA (**Figure 4.3(d)**), the electrostatic energy barrier is neutralized, and free-PLL diffuses out to the film/solution interface (where it undergoes complexation by HA) due to electrostatic force and concentration gradients.[15, 16, 28] Eventually, the reaction slows, and the surface again becomes negatively charged, leading to an increase in film thickness (**Figure 4.3(e)**).

The exponential increase in film thickness can be described mathematically in terms of the number of bilayers, n, the amount of polyelectrolyte that comprises the film, $Q(n)$, and the amount of polyelectrolyte that comprises the new outer layer of the film, $\delta Q(n+1)$.[15, 28] The amount of polyelectrolyte that comprises the new outer layer is the sum of two contributions, which are: (1) polyelectrolyte adsorbed to the outer surface of the film, q_o (assumed to be constant), and (2) the amount of free polyelectrolyte within the film, which is proportional to $Q(n)$.[28] Therefore, the amount of polyelectrolytes that

comprises the new layer can be described mathematically by **Equation 4.1**, where K is a proportionality constant.[15, 28]

$$\delta Q(n+1) = q_o + KQ(n) \tag{4.1}$$

Assuming no precursor layer was deposited, the initial condition is $Q(0) = 0$. From Equation 4.1, a general expression for the exponential growth of $Q(n)$ can be derived (**Equations 4.2-4.11**)

$$\delta Q = K\left(\frac{q_o}{K} + Q(n)\right)\delta n \tag{4.2}$$

$$\frac{\delta Q}{\left(\frac{q_o}{K} + Q(n)\right)} = K\delta n \tag{4.3}$$

$$\int_{Q(0)}^{Q(n)} \frac{\delta Q}{\left(\frac{q_o}{K} + Q(n)\right)} = \int_0^n K\,\delta n \tag{4.4}$$

$$\ln\left(\frac{q_o}{K} + Q(n)\right)_{Q(0)}^{Q(n)} = Kn\Big|_0^n \tag{4.5}$$

$$\ln\left(\frac{q_o}{K} + Q(n)\right) - \ln\left(\frac{q_o}{K}\right) = Kn \tag{4.6}$$

$$\ln\left(\frac{\frac{q_o}{K} + Q(n)}{\frac{q_o}{K}}\right) = Kn \tag{4.7}$$

$$\frac{\frac{q_o}{K} + Q(n)}{\frac{q_o}{K}} = e^{Kn} \tag{4.8}$$

$$\frac{q_o}{K} + Q(n) = \frac{q_o}{K} e^{Kn} \tag{4.9}$$

$$Q(n) = \frac{q_o}{K} e^{Kn} - \frac{q_o}{K} \tag{4.10}$$

$$Q(n) = \frac{q_o}{K}\left(e^{Kn} - 1\right) \tag{4.11}$$

Equation 4.11 can be used to describe both linear and exponential deposition because when $Kn \ll 1$, the equation reduces to $Q(n) \approx q_o n$.[28] When K is large, Equation 4.11 can be approximated as $Q(n) \approx q_o/K \exp(Kn)$, which is representative of exponential deposition.[28] The special case of $K = 0$ occurs when either no polyelectrolyte diffuses into the film thickness, or when polyanion/polycation complexes form away from the film/ solution interface and are not bound to the surface.[28] Because Equation 4.11 can effectively model both linear and exponential deposition rates, it was used for the analysis of protamine-enabled films.

The terminology and representation of "exponential deposition" commonly used in the literature for film buildup (according to the mechanism in **Figure 4.3**) is oversimplified. In fact, the represented scenario may only be maintained for a limited number of deposition steps before transitioning to a linear deposition regime.[29-31] Therefore, the phrase "active volume deposition" will be used herein to describe films with inward and outward diffusion of polyelectrolyte, as this phrase provides a more accurate description of film deposition behavior.

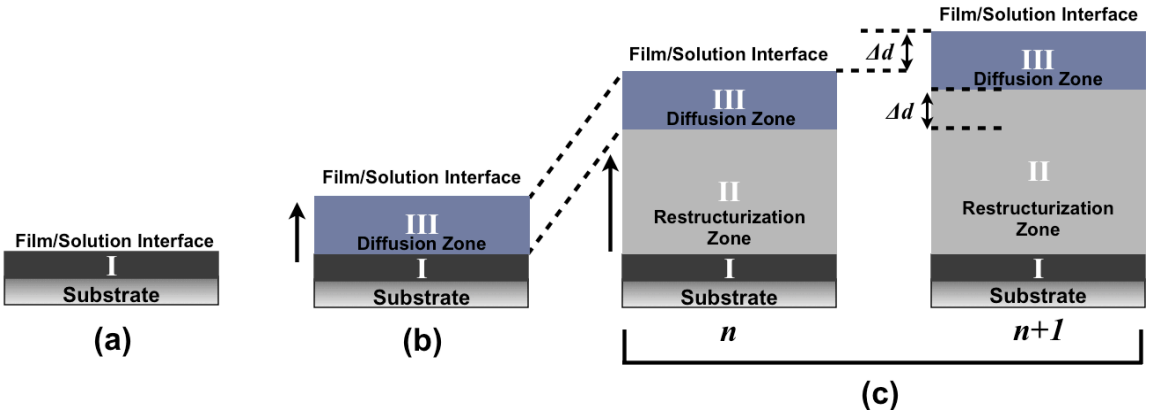

Figure 4.4: Schematic representation of a three-zone buildup mechanism model of an active volume film. The deposition initial layers (Zone I) are highly dependent on the properties of the substrate surface (a). As the number of deposition cycles increases, diffusion of the polyelectrolyte "in" and "out" the film takes place within a diffusion region (Zone III) which leads to exponential buildup of the film (as shown in Figure 4.2) (b). Deposition goes forward and the bottom layers of Zone II restructure and form a Zone II where diffusion is hindered. This causes Zone III to grow at a constant thickness, and the film begins to grow linearly as a function of deposition cycle. Each increase in film thickness is expands zone II (c). The thickness increment per cycle is given by Δd as the number of deposition cycles, n, increases by n+1.[26-29]

Direct physical evidence providing a reason why active volume films undergo an exponential-to-linear transition is still unavailable, but a potential mechanism has been proposed by Porcel, *et al*.[27] A schematic representation of the exponential-to-linear transition in active volume films is presented in **Figure 4.4**.[27, 31-33] As film deposition begins, the initial layer(s) deposited are highly dependent on the substrate surface properties (Zone I).[27, 31-33] As more layers are deposited, the film thickness increases exponentially as one of the polyelectrolytes diffuses "in" and "out" of the film thickness to react at the film/solution interface.[27, 31-33] The region where polyelectrolyte diffusion occurs is defined as Zone III.[27, 31-33] As the film thickness increases, a region below Zone III gradually reorganizes into a relatively dense region and progressively hinders inward

(and outward) diffusion.[27, 31-33] According to this model, the dense reorganized region (Zone II) is inaccessible to polyelectrolyte.[27, 31-33] The thickness of Zone II increases commensurate with Zone III as each layer is deposited.[27, 31-33] No direct evidence of film restructuring in this zone has been observed to date. Determining the mechanism for Zone II formation in protamine-enabled deposition is beyond the scope of this work. It should also be noted that the linear thickness increase with each deposition cycle in active volume films can be much larger than linearly depositing films lacking an initial exponential growth regime (i.e., each cycle can deposit a bilayer hundreds of nanometers thick compared to a few nanometers thick).[30]

This work provides a direct comparison of coatings generated from the reaction of either synthetic polyamines of two different molecular weights or a biological polyamine with the TiO_2 precursor, TiBALDH under identical solution, substrate, and temporal conditions. Differences in deposition rate, coating roughness and properties were noted and discussed. Specifically, the molecular mechanism for protamine LbL growth is investigated and compared to proposed mechanisms for exponentially growing organic polyelectrolyte multilayer films.

4.3 Experimental Procedure

The methods used to deposit and characterize polyamine-enabled TiO_2 coatings on various SiO_2 templates are discussed in this section.

4.3.1 Reactive Polyelectrolyte and Titania Precursor Materials

The reactive polyelectrolytes used were PEI molecular weight (M_w) 600, (99% purity, branched, Alfa Aesar, Ward Hill, MA, USA), PEI (M_w 750,000, M_n 60,000, branched, 50 wt% solution, Sigma-Aldrich, St. Louis, MO, USA), linear PEI (Polyethyleneimine "Max", Mw ~2,500, Polysciencs, Inc., Warrington, PA, USA), and protamine sulfate from salmon (Grade X, Sigma-Aldrich, St. Louis, MO, USA). All solutions were made from Milli-Q ultrapure water (18.2 MΩ·cm) and prepared in Tris-HCl buffer (Tris(hydroxymethyl)aminomethane, 98+%, Alfa Aesar, Ward Hill, MA, USA) at a concentration of 0.1 M and pH 7.5. A polyelectrolyte concentration of 1 mg mL^{-1} was used for all experiments. An aqueous 5 mM solution of titanium (IV) bis(ammoniumlactato) dihydroxide (TiBALDH, 50 wt%, Sigma-Aldrich, St. Louis, MO, USA) in 0.1 M Tris-HCl at pH 7.5 was the precursor for TiO-bearing layers. The primary amines in Tris were capable of precipitating TiBALDH if the solution was left for more than 24 h. As such, all solutions were prepared fresh on the day of use, and no visible precipitation was detected after all experiments.

4.3.2 Quartz Crystal Microbalance Characterization

A quartz crystal microbalance with simultaneous dissipation monitoring (QCM-D, Q-Sense E1 system, Biolin Scientific, Inc., Västra Frölunda, Sweden) was used to interrogate the deposition process. Standard gold-coated quartz sensors were coated with a thin layer (~50 nm) of SiO_2 (Model QSX303, Biolin Scientific, Inc., Västra Frölunda, Sweden) to ensure the results were comparable to coatings on other SiO_2 templates used. The 1^{st}, 3^{rd}, 5^{th}, 7^{th}, 9^{th}, 11^{th}, and 13^{th} harmonics were measured simultaneously during all QCM-D experiments. Of these harmonics, the 5^{th} harmonic was selected for analysis

because smaller harmonics (1st and 3rd) are sensitize to a larger area, and the results can be affected by the O-ring used to hold the sensor. Conversely, higher harmonics can become less sensitive as more material is deposited onto the sensor surface due to the smaller penetration depth of the acoustic waves generated by the quartz crystal. Therefore, the 5th harmonic was judged to have the best balance of areal sensitivity and film penetration depth. Schematic plots illustrating the areal sensitivity and penetration depths associated with various harmonics are shown in **Figure 4.5**.

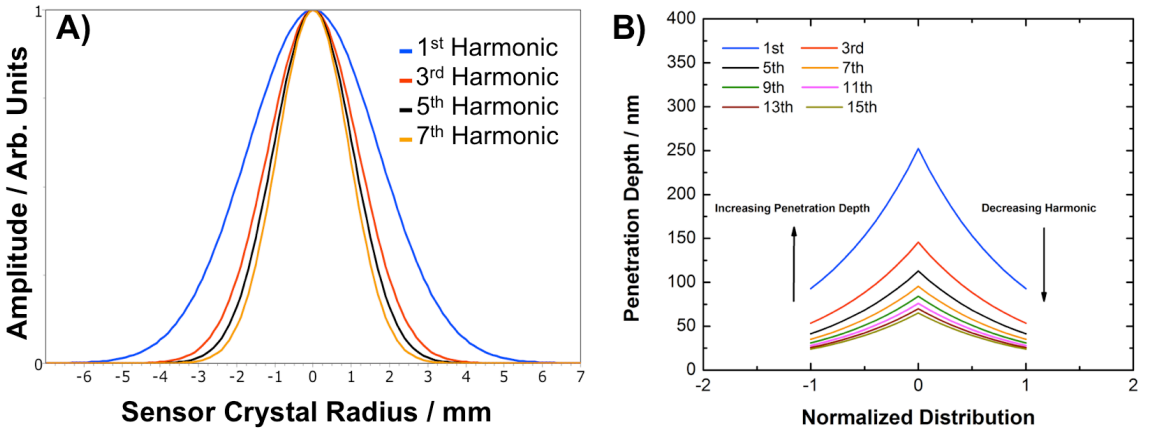

Figure 4.5: The representation of how the sensitivity area (a) and penetration depth (b) of the frequency oscillation of a quartz crystal varies with harmonic frequency. Measurements conducted by Biolin Scientific (Västra Frölunda, Sweden).

All sensors were cleaned by 10 min UV-ozone treatment (UV/Ozone ProCleaner, Bioforce Nanosciences, Inc., Ames, IA, USA) followed by incubation for 30 min in 2% v/v sodium dodecyl sulfate (SDS, 99+% purity, Amresco, Solon, OH, USA) solution. The sensors were rinsed thoroughly with water, dried under nitrogen flow, then cleaned by UV-ozone for 10 min. QCM-D was used to examine ten deposition cycles at a solution flow rate of 0.1 mL min^{-1} and 22 °C. A single cycle consisted of four steps: (1) exposure

to polyelectrolyte (5 min), (2) buffer rinse (5 min), (3) TiBALDH (various times), and (4) buffer rinse (5 min). TiBALDH exposure time varied for each cycle due to changes in reaction kinetics, and TiBALDH flow continued until the resonance frequency change plateaued (i.e., ΔF varied less than 1 Hz per min), which indicated that the sensor surface had effectively completed the reaction of TiBALDH with the deposited polyamine.

4.3.3 Deposition of Reactive Polyamine/TiO-bearing Coatings by Dipping

TiO-bearing films were deposited onto silicon wafer substrates (Wafernet, Inc., San Jose, CA, USA) that were first cleaned by rinsing in ethanol followed by water and dried with nitrogen. Next the wafers were exposed to a 10 min UV-ozone treatment, and incubated in 2% v/v SDS at 70 °C for 30 min. After SDS treatment the Si wafers were rinsed with copious amounts of water, and immersed in 70 °C HCl (1 M, VWR, West Chester, PA, USA) for 10 min. The Si wafers were then rinsed with water and dried with nitrogen. The wafer was then cut into 1.7 cm by 0.7 cm pieces for coating.

Prior to deposition, the Si substrates were incubated in buffer solution for at least 15 min to allow to surface to reach equilibrium. The TiO-bearing films were deposited by dipping the substrate first in polyelectrolyte (3 mL) for 5 min, followed by rinsing three times in buffer. The substrate was then immersed in TiBALDH solution (3 mL) for *x* minutes, where *x* was based upon the time required for saturation according to QCM-D measurements. The Si wafer was then rinsed three times in buffer to remove excess TiBALDH. This four-step process equalled one deposition cycle, and could be repeated to deposit *n* number of bilayers. Note: the Si wafers were never dried between steps unless specifically stated. The wafers were rinsed in deionized water and dried for 5 min

under compressed N_2 after deposition was completed. Each specimen was cut in half lengthwise and heated to 500 °C in a tube furnace (Lindberg / Blue M, NC, USA) at 3 °C min^{-1} for 6 h (AutoFire® Controller, Orton Ceramic Foundation, OH, USA outfitted with a k-type thermocouple, OMEGA Engineering, Inc., CT, USA) in air to allow for organic pyrolysis of the polyamine for inorganic film thickness characterization after heat treatment.

After coating, the coated Si-wafers were evaluated with scanning electron microscopy (1530 FEG SEM, LEO/Zeiss Electron Microscopy, Thornwood, NY), and by X-ray photoelectron spectroscopy conducted (Thermo K-alpha, Thermo Fischer Scientific, Inc., Waltham, MA, USA) at a base pressure of $3x10^{-8}$ Pa using a monochromatic Al K_α source (1486.6 eV) with a spot size of 200 μm and a pass energy of 50 eV. A step size of 0.1 eV was used with dwell times of 50 ms at each energy value. The specimens were examined at three different locations, and representative scans are presented.

4.3.4 Reactive Polyelectrolyte Deposition on Silica Stöber Spheres

Coatings on flat substrates, like Si wafers, were not conducive to specific surface area measurements or zeta (ζ) potential measurements. As such, Stöber SiO_2 spheres (**Figure 4.6**, 1 μm diameter, AngstromSphere Monodispersed silica powder, Fiber Optic Center, Inc., New Bedford, MA, USA) were used as templates for the LbL deposition of TiO-bearing coatings using each of the polyelectrolytes to facilitate characterization by films by N_2 adsorption and ζ potential. The spheres were first dispersed in buffer solution for at least 15 min, separated from solution by centrifugation (5,000 rpm for 5 min). The

supernatant was removed and exchanged for polyelectrolyte solution. The Stöber SiO_2 spheres were suspended in the polyelectrolyte solution via vortexing (Vortex Genie 2, Scientific Industries, Inc., Bohemia, NY, USA) in a 50 mL centrifuge tube and incubated for 5 min on a platform rocker. Afterwards, the spheres were again separated via centrifugation, and the supernatant was exchanged with buffer. The spheres were suspended and washed twice more with buffer following the same centrifugation and suspension process. Once washed, the spheres were exposed to TiBALDH and incubated for a time, *t*, determined by QCM-D experiment. Again the spheres were washed with buffer solution three times, completing one cycle. This process was repeated 7 more times to coat the SiO_2 spheres. N_2 drying of the SiO_2 Stöber spheres was considered, however, compressed N_2 blew chunks of spheres out of the 50 mL tube.

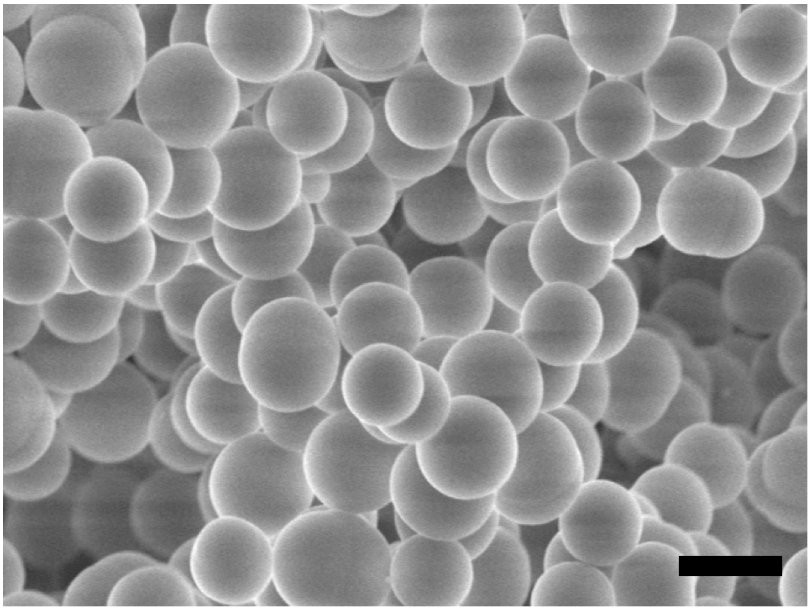

Figure 4.6: An SEM image of the uncoated SiO_2 Stöber spheres used as a template for polyamine-enabled deposition of TiO-bearing coatings. Scale bar: 1 μm.

A portion of the as-coated spheres were heated to 500 °C in a tube furnace (Lindberg / Blue M, NC, USA) at 3 °C min^{-1} for 6 h (AutoFire® Controller, Orton Ceramic Foundation, OH, USA outfitted with a k-type thermocouple, OMEGA Engineering, Inc., CT, USA) in air to allow for organic pyrolysis of the polyamine for specific surface area characterization via BET analysis.

4.3.5 Scanning Probe and Electron Microscopy Characterization

Atomic force microscopy (AFM, Veeco Dimension 3100 Scanning Probe Microscope, Plainview, NY, USA) was performed on polyamine-derived films before and after 500 °C heat treatment for 6 h in air (3 °C min^{-1} ramp rate) on silicon wafers after *n* number of deposition cycles (where *n* = 2, 3, 4, 5, 6, 8, 10 for protamine-enabled films and *n* = 2, 4, 6, 8, 10 for PEI-enabled films). The measurements were carried out in tapping-mode using 10 nm radius of curvature general purpose probes (Mikromasch AFM NSC36, Mikromasch USA, San Jose, CA, USA) with a spring constant of 0.6 N m^{-1} and a resonant frequency of 75 Hz. Half of the Si wafer surface was masked prior to deposition using silicone elastomer (Sylgard 184, Dow Corning, Co., Midland, MI, USA). After deposition was complete, the elastomer mask was peeled off the surface, and 10 thickness measurements were conducted across the coated/uncoated boundary with a scan area of 10 μm by 20 μm defined within Nanoscope Analysis software v1.4r1 (Veeco Instruments, Plainview, NY, USA). An example of one measurement is provided in **Figure 4.7**. The Si portion of each image was plane-leveled and step analysis was performed on 10 different areas of the coating.

Topographical images of the coated area on as-coated and heat treated films were obtained over a 15 μm by 15 μm area. The images were plane-leveled and the root-mean square roughness of the films was measured using Nanoscope Analysis software over five different 5 μm by 5 μm areas.

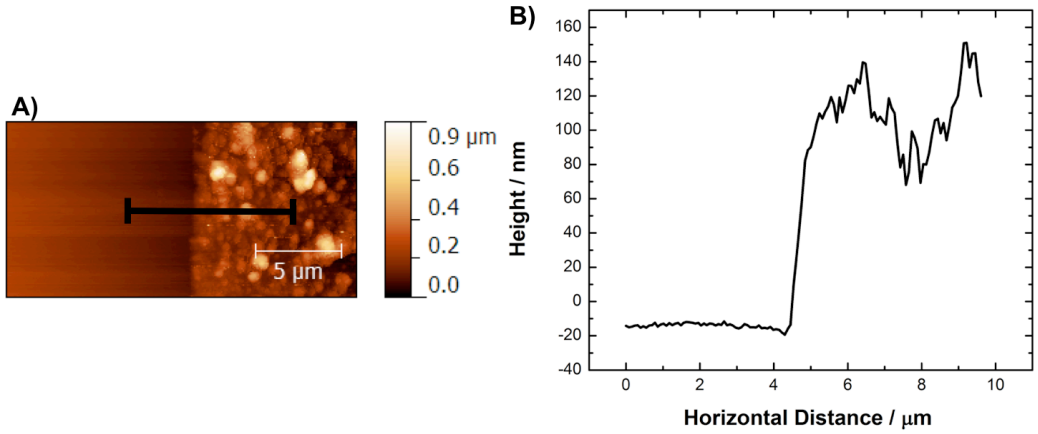

Figure 4.7: A typical ex-situ AFM image (6 cycles of protamine-enabled deposition) taken to measure the thickness of the deposited coating after drying (a). The difference in z-height between uncoated (left) and coated (right) areas in 10 different locations were averaged to determine the thickness of the film (b).

The micro/nanoscale morphology of the polyamine-enabled films were also evaluated with scanning electron microscopy (1530 FEG SEM, LEO/Zeiss Electron Microscopy, Thornwood, NY).

4.3.6 Zeta Potential Characterization

Zeta potential measurements were conducted on 150 nm Stöber SiO_2 spheres (Bangs Laboratories, Fishers, IN, USA) exposed to various stages of polyamine/ TiBALDH processing (see Section 4.3.4). Smaller diameter spheres were used because the spheres were able to remain suspended in solution during analysis. After exposure to either polyamine or TiBALDH and washing in buffer three times, the zeta potential of the

spheres was measured using a dip cell on a Zetasizer NS instrument (Malvern Instruments, Malvern, Worcestershire, UK). Data were averaged over 10 measurement runs, and data evaluation was performed using the Smoluchowski Approximation and General Mode Analysis (Malvern Zetasizer Software v6.20). The mean zeta potential was calculated from three independent experiments.

4.3.7 Specific Surface Area Characterization

Eight cycles of polyamine/TiO-bearing coatings were deposited on Stöber SiO_2 spheres (300 mg, 1 μm diameter) following the procedures described in Section 4.3.4. After coating, the spheres were washed three times in deionized water and dried in air. The specific surface area of cleaned and coated SiO_2 spheres were evaluated using a Quantachrome Autosorb AS-1 (Quantachrome Instruments, Boynton Beach, FL, USA) system before and after heat treatment for 6 h at 500 °C. About 150 mg of each specimen was loaded into a 6 mm elliptical-bottom glass tube and degassed. After degassing, the spheres were weighed, and isothermal gas adsorption/desorption was performed in a liquid nitrogen bath (-196 °C) with nitrogen gas as the adsorbate. A total of 40 adsorption and 40 desorption data points were collected for each sample. BJH analysis was performed on the isothermal desorption data to ascertain the specific pore volume in the mesopore range (2 - 50 nm).[34]

4.3.8 Fluorescent Conjugation of Protamine

Protamine and PEI750K were conjugated with fluorescent fluorescein isothiocyanate (FITC) to determine if the peptide or polymer were capable of outward diffusion from the coating during TiBALDH incubation. FITC contains a succinimidyl

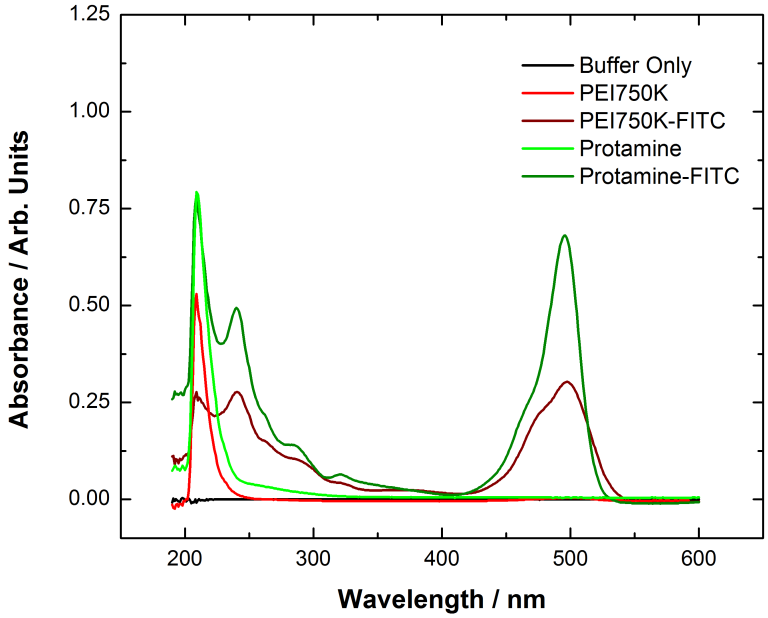

Figure 4.8: UV-vis absorbance spectra of 100 mM Tris-HCl (buffer), PEI750K, and protamine before and after conjugation with FITC and purification. The absorbance peaks centered around 495 nm were indicative of FITC and were not present in native PEI750K and protamine solutions.

ester moiety that reacts specifically with primary amines. Protamine contains a single primary amine at the N-terminus whereas PEI750K contains multiple primary amines per mer unit of the polymer. The polyamine-FITC conjugates were optically active and absorbed light at wavelengths of approximately 495 nm and emitted light at approximately 521 nm, while unmodified protamine and PEI750 were inactive in this region (**Figure 4.8**). Such fluorescent tagging allowed for tracking of the protamine and PEI750K via analyses of fluorescence by the supernatant from the deposition process.

An aqueous 2 mg mL^{-1} protamine solution (488 μM) was prepared in a 50 mL tube, then ultrasonicated for 30 min to completely dissolve the peptide. A 40 mL volume of 0.1 mg mL^{-1} FITC solution was added to 10 mL of the protamine solution. The solution was covered in foil and placed on a rotator for 16 h. For FITC conjugation to

PEI750K, a 2 mg mL^{-1} solution (2.7 μM) was titrated using 6 M HCl (pH 7.5). A 40 mL volume of 0.1 mg mL^{-1} FITC solution in 0.05 M sodium phosphate buffer (pH 7.5) was added to 10 mL of the protamine solution. The solutions were incubated in the dark for 16 h at room temperature. The protamine-FITC and PEI750K-FITC solutions were concentrated by centrifugal filtration (3,000 M_w cutoff, Millipore, Inc., Centriplus YM-3, Bedford, MA, USA) to a volume of approximately 10 mL. The remaining solutions were dialyzed using 1000 M_w cutoff tubing in 5 L DI water under stirring in the dark at 14 °C. The DI water bath was changed every 24 h until unbound FITC was no longer observed in the bath solution (i.e., no detectable fluorescence at 521 nm). The protamine-FITC and PEI750K-FITC conjugate solutions were then transferred from the dialysis tubing by pipette into a 15 mL tube, flash-frozen in liquid nitrogen (-196 °C), and lyophilized to obtain a powder. The protamine-FITC and PEI750K-FITC powders were stored at -20 °C in the dark and were diluted to 1 mg mL^{-1} in 0.1 M Tris-HCl to match the peptide concentration used for LbL deposition. After conjugation, both polyamines were still capable of precipitating TiBALDH from solution.

Following 9 layers of protamine/TiBALDH deposition (or 9 layers of PEI750K/ TiBALDH deposition) on three Si wafers, two of the wafers were exposed to a 1 mg mL^{-1} solution of protamine-FITC (or PEI750K-FITC) for 5 min. The third wafer was coated using unmodified protamine (or PEI750K) as a negative control. All wafers were then rinsed in buffer three times for 1 min each. At this point, one of the two wafers exposed to protamine-FITC (or PEI750K-FITC) was immersed in fresh buffer solution for 30 min as a control while the other two were immersed in separate TiBALDH solutions for 30

min. Afterwards, the wafers were rinsed three times in buffer for 1 min each and set aside. Aliquots (1 mL) of each solution (i.e., the solution in which the wafers were incubated) were collected for analysis in a fluorescent plate reader (Synergy 2, BioTek Instruments, Inc., Winooski, VT, USA). From the collected solutions, 0.2 mL was deposited in a 96-well plate and excited by a white light source bandpass filtered to allow only narrow range of wavelengths (485 ± 20 nm). The detector was set to measure fluorescence at 516 ± 20 nm. The fluorescence was analyzed using the provided Gen5 software (v2.00.18, BioTek Instruments, Inc., Winooski, VT, USA) and used to determine if protamine or PEI750K was capable of desorption from the film during TiBALDH incubation.

4.4 Results and Discussion

4.4.1 Characterization of Polyamine/TiBALDH Layer-by-Layer Deposition

The reaction kinetics of both synthetic PEI-derived and bioorganic protamine-based films during each stage of deposition were examined using QCM-D. Ten deposition cycles were completed on SiO_2-coated sensors at pH 7.5, a flow rate of 100 μL min^{-1} and 22 °C. The results for each polyamine tested at all harmonics are compiled in **Figure 4.9**. Of these harmonics, the 5th harmonic was selected for analysis because smaller harmonics (1st and 3rd) are sensitive to a larger area, and the results can be affected by the O-ring used to hold the sensor (see **Figure 4.9(a)**). Conversely, higher harmonics (11th and 13th) have a smaller penetration depth and can become less sensitive as more materials is deposited onto the sensor surface. These limitations were not readily

apparent from the results, but the 5th harmonic was judged to have the best overall balance of areal sensitivity and film penetration depth. So for simplicity, the 5th harmonic was selected for analysis of film deposition.

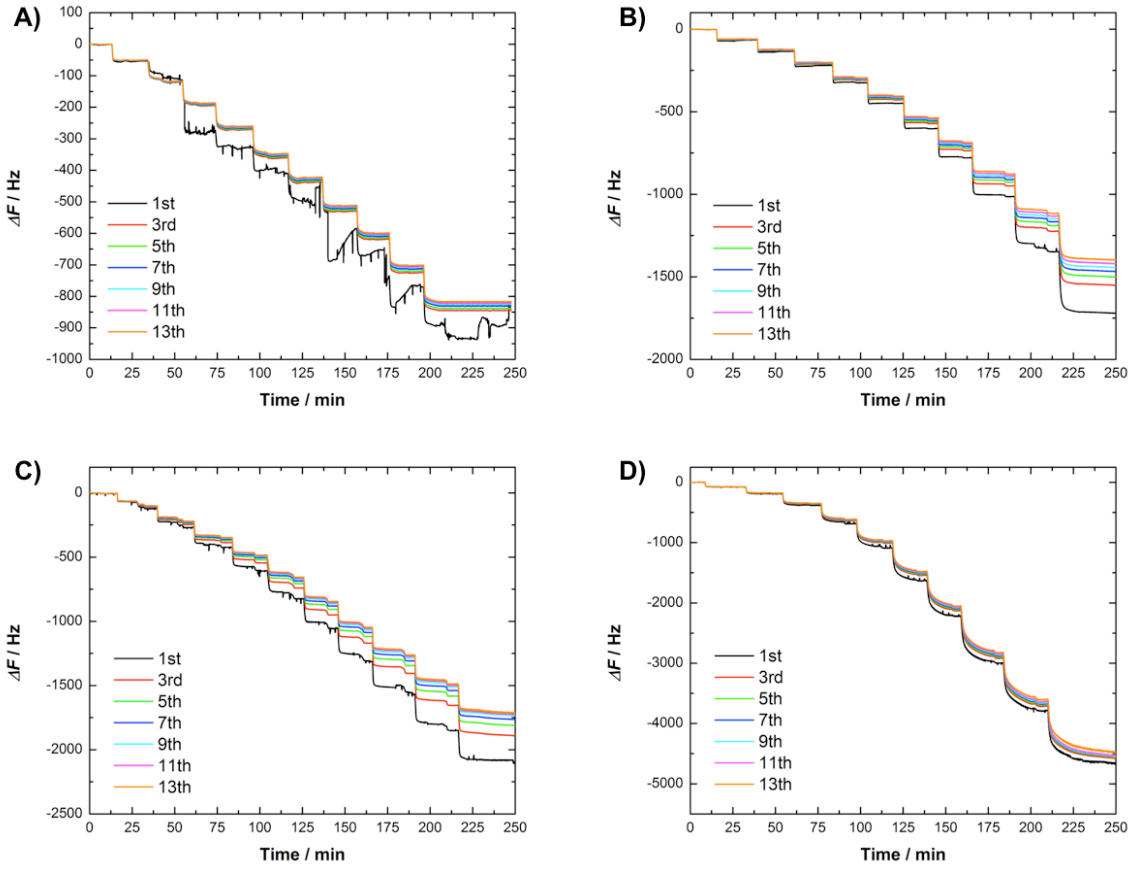

Figure 4.9: Quartz crystal microbalance data showing frequency change (ΔF) during layer-by-layer buildup of inorganic/(bio)organic composites over 10 deposition cycles for L-PEI2500 (a), PEI600 (b), PEI750K (c), and protamine (d). All measured harmonics are shown, and for simplicity the 5th harmonic was used for all subsequent analysis.

From the frequency change (ΔF) of the 5th harmonic of the quartz crystal, it was clear that each film deposited step-wise onto the sensor, but the deposition rate differed significantly for each type of film. More specifically, protamine-based films deposited rapidly and exhibited larger thicknesses overall in comparison to films deposited with PEI. Comparing only PEI-based films, the film buildup rate per cycle of L-PEI2500-

based deposition was slower than both PEI600 and PEI750K-based films. For more detail, an example of the frequency change at each step in the deposition process is shown for L-PEI2500-, PEI600-, PEI750K-, and protamine-based films during the fourth cycle (**Figure 4.10**).

Table 4.1. TiBALDH incubation times used during protamine-enabled deposition.

Cycle number	TiBALDH Incubation Time (min)
1, 2	5
3, 4	10
5, 6	15
7, 8	20
9, 10	30

For all cycles, PEI-based films effectively completed both electrostatic polyamine adsorption (**Figure 4.10(a-c), inset**) and reaction of PEI with TiBALDH within about 5 min (**Figure 4.10(a-c)**). Protamine adsorption required ≤5 min as well to reach effective completion, but the reaction of TiBALDH with protamine required longer incubation times to reach constant ΔF values (**Figure 4.10(d)**). As a result, the incubation times were held to 5 min for all stages of LbL deposition of PEI-based deposition in all studies. For protamine-based deposition, the time required for protamine adsorption remained the same as PEI-based films (5 min), but TiBALDH incubation times varied following **Table 4.1**. This adjustment in incubation time ensured a constant deposition condition was reached during each incubation step in all cases for fair comparison. Effective reaction

completion was defined as occurring when the frequency change over time was less than 1 Hz min^{-1}.

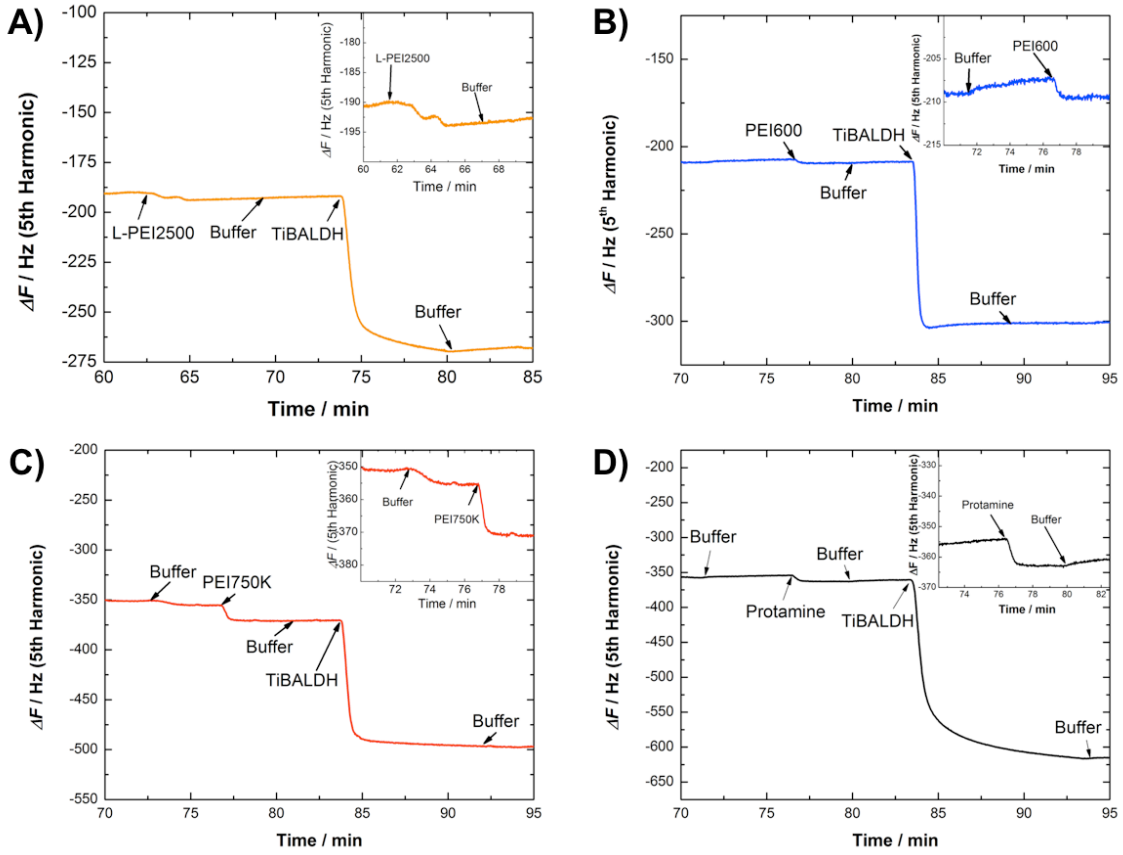

Figure 4.10: QCM-D data showing frequency change (*ΔF*) during the 4th cycle of LbL deposition using L-PEI2500 (a), PEI600 (b), PEI750K (c), and protamine (d).

The evolution of -*ΔF* from QCM-D results versus the number of deposition cycles is presented in **Figure 4.11**. While the Sauerbrey model is typically used to model thickness values from QCM data, the use of this model is limited to rigid films exhibiting a change in dissipation (*ΔD*) of less than 1.[35] After four deposition cycles, *ΔD* was much larger than 1 per 10 Hz, and the measured harmonics (1st, 3rd, 5th, 7th, 9th, 11th, and 13th) all became divergent for all films. The Sauerbrey relation between *ΔF* and adsorbed mass could not be used to accurately relate *ΔF* to film thickness. Therefore, QCM-D data

analysis was completed in terms of ΔF, and later compared to ex-situ AFM thickness measurements of dried films.

From **Figure 4.11**, PEI-based films clearly deposited in a linear fashion on the sensor surface at a rate of 89 ± 2.2 Hz per cycle (R^2 = 0.99), 149 ± 9.0 Hz per cycle (R^2 = 0.97), and 196 ± 5.6 Hz per cycle (R^2 = 0.99) for L-PEI2500-, PEI600- and PEI750K-based films, respectively. The first deposition cycle was ignored due to the potential influence of the substrate. Linear deposition rates were maintained regardless of PEI molecular weight or structure (linear or branched), and the results for PEI750K-based films were consistent with prior work.[12] As expected, PEI750K deposited TiO-bearing layers at a faster rate than PEI600 due to the increased molecular weight. However, a more than 1,000-fold increase in molecular weight resulted in only a nominal 23% increase in the rate of frequency change per deposition cycle.

From QCM-D experiments, protamine-enabled films appeared to exhibit exponential film growth for deposition cycles 2 to 6 before transitioning to a linear growth regime for cycles 6 to 10. Because this behavior has been observed in films shown to deposit according to an active volume mechanism, **Equation 4.11** was used to fit deposition cycles 2 to 6 (**Figure 4.11)**.

$$|\Delta F| = \frac{39.1}{0.53}\left(\exp(0.53n) - 1\right) \qquad (4.12)$$

The values of K and q_o were determined from the linear regression (R^2 = 0.99) of a logarithmic plot of frequency change with respect to protamine-enabled deposition cycle for cycles 2 to 6 (**Figure 4.11(b)**).

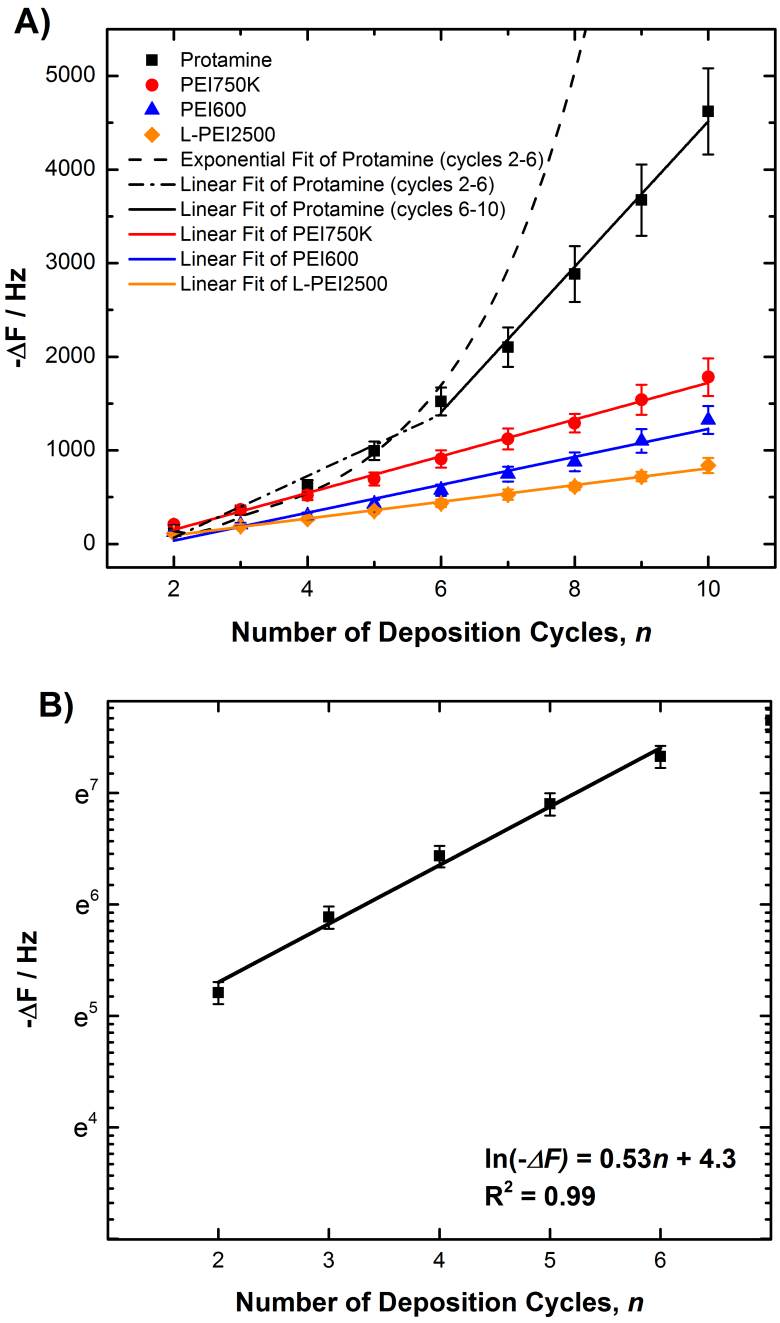

Figure 4.11: The ΔF evaluated using the 5th harmonic from QCM-D measurements. The analysis was conducted over 10 cycles of protamine-, PEI600-, PEI750K, and L-PEI2500-based films (a). Error bars represent the standard deviation recorded from two experiments. Cycles 2 to 6 of the protamine-enabled film were fit using an exponential equation while cycles 6 to 10 were fit with a linear regression. PEI-based films were fit with a linear regression to determine the wet film growth rate. The linear dependence of ln ΔF with n verified the exponential nature of the deposition process (b). The black line corresponds to the linear regression on this logarithmic plot.

From the plot in **Figure 4.11**, it was apparent that the exponential equation failed to fit data points beyond the sixth deposition cycle. After the sixth deposition cycle, the film thickness increased at a linear rate of 777 ± 37 Hz per cycle (R^2 = 0.99), which suggested that an exponential-to-linear transition occurred after the sixth deposition cycle under the conditions used in this work (100 mM Tris-HCl, pH 7.5). The linear growth rate from cycle 6 to 10 was more than four times greater than the linear rate observed in linearly depositing PEI750K-based films under the same conditions (196 Hz per cycle), which has been observed as a characteristic of active volume films.[29-31] Moreover, the appearance of an exponential-to-linear transition further suggests that protamine-enabled film deposition followed the active volume mechanism.

An alternative explanation may be that protamine-enabled deposition instead demonstrated two distinct linear growth regimes, where the initial stages of deposition are non-linear due to the influence of the substrate.[14, 36] A linear fit of cycles 2 through 6 yielded a reasonable R^2 of 0.93 and a slope of 329 ± 44 Hz per cycle (**Figure 4.11(a)**). However, PEI-based films did not appear to display substrate effects beyond the first deposition cycle, and through the first six cycles deposited similar amounts of material relative to protamine-enabled films. Other possible growth mechanisms for protamine/ TiBALDH films include the island growth and dendritic growth models discussed previously.[24] This result is the first published observation that protamine/inorganic composites can also demonstrate such unique behavior, and QCM-D data alone cannot confirm that protamine-enabled TiO-bearing films deposited via the active volume mechanism. However, experiments conducted in this work provided more evidence for

inward and outward diffusion of protamine during bio-enabled deposition in addition to a comparison of the dependence of film properties on the type of polyamine used during deposition.

A plot of ΔD versus ΔF from QCM-D measurements (**Figure 4.11**) eliminated the explicit time parameter and provided insight into differences in adsorption behavior not apparent from **Figures 4.9 and 4.10**. For example, qualitative comparisons can be made between the films regarding viscoelasticity and reorganization during the deposition process.[37] PEI750K-based films showed the largest ΔD to ΔF ratio which suggested that such films possessed the largest viscoelasticity of the four types of (bio)organic-enabled films tested.

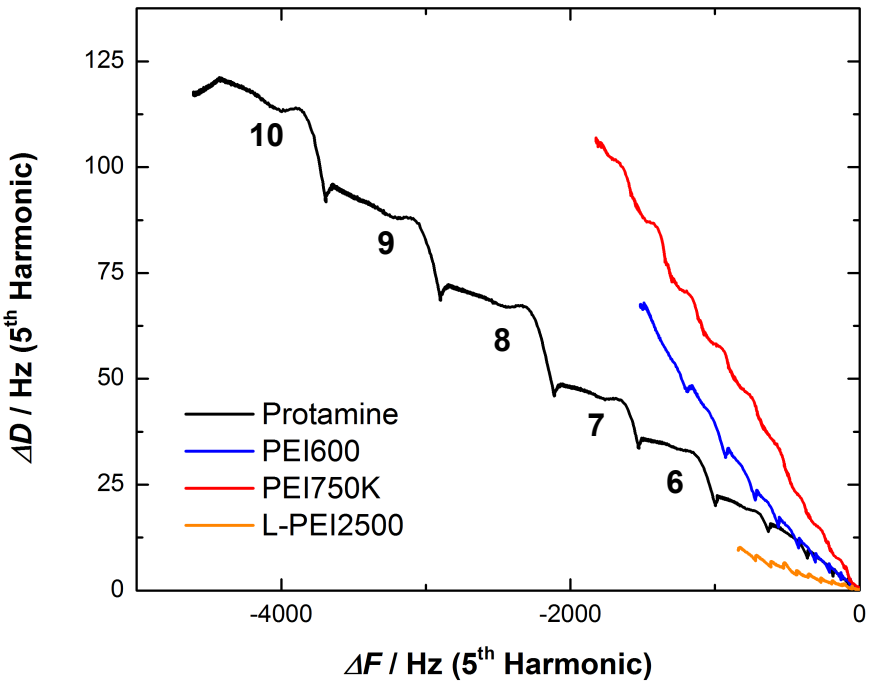

Figure 4.12: Plot of ΔD versus ΔF from QCM-D results used to qualitatively compare the viscoelasticity and restructuring of the protamine-, PEI600-, PEI750K-, and L-PEI2500-based films *in situ*.

Deviations from linearity observed during the deposition of each film suggest different kinetic processes occurred during deposition (e.g., structural reorganization within the film), where the magnitude of the deviation may be correlated to amount of reorganization.[37] All PEI-based films exhibited some non-linearities in **Figure 4.12**, which has also been previously reported in PEI750K-based films.[12] The origins of such non-linearity in PEI/TiBALDH films were unclear from QCM-D measurements, as the technique cannot provide direct observation, and are beyond the scope of this work.

The broad "waves" observed in protamine-based films implied sizable film reorganization compared to PEI-based films, and the "waves" became more pronounced from the sixth deposition cycle onward (**Figure 4.12**). The "waves" also suggested that the reorganization process became more substantial as more material was deposited onto the surface and coincided with the onset of the linear buildup regime. These results were again consistent with the active volume film models presented where one polyelectrolyte (i.e., protamine) was capable of diffusion in and out of the film thickness. A more detailed discussion of the two different electrostatic deposition mechanisms at work in PEI- and protamine-based films can be found in Section 4.4.3. At this point, however, discussion will focus on the comparison of film characteristics and properties. Furthermore, protamine-based films will be compared to only branched PEI (PEI600 and PEI750K-based films) for property measurements because all the PEI-based films examined displayed similar deposition behavior, and the primary aim of this work is to interrogate protamine-enabled TiO-bearing coatings. Branched PEI also allowed for comparison to a broad range of molecular weights, and the polyelectrolyte contained a

mix of functional amines (e.g., primary and secondary), which was similar to protamine (e.g., primary and guanidinium groups).

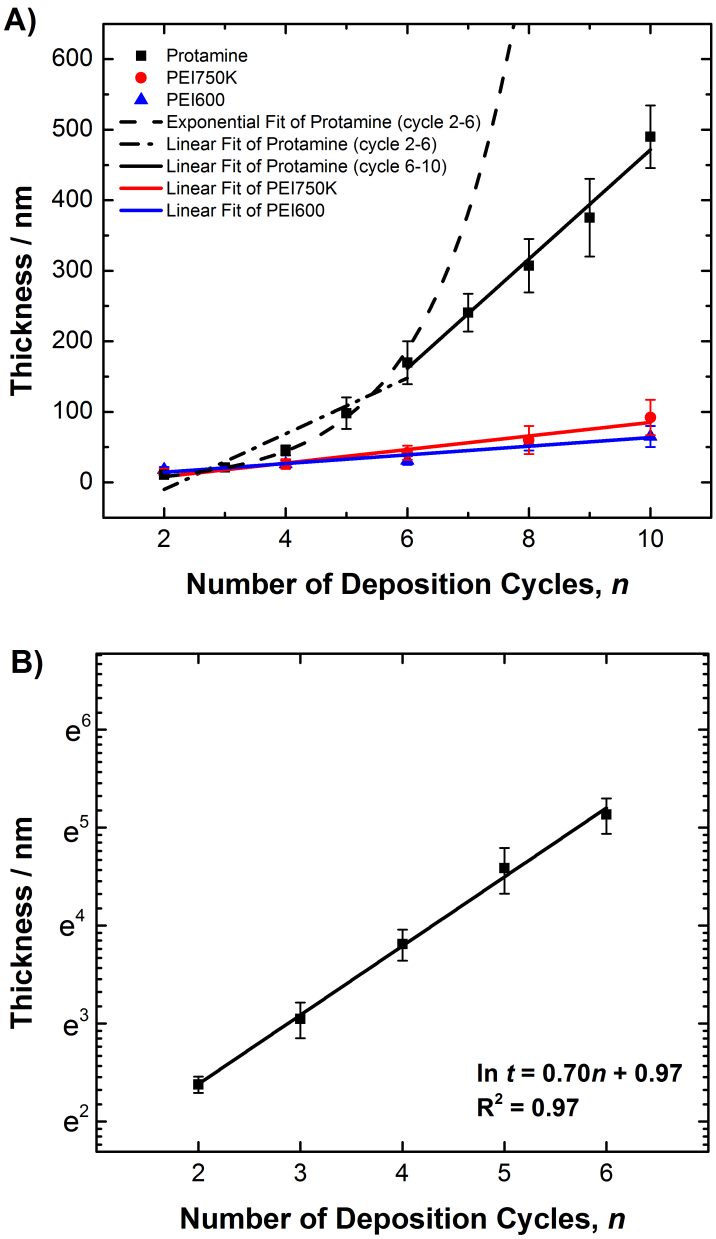

Figure 4.13: Ex-situ AFM characterization of the thickness deposited by protamine-, PEI600-, and PEI750K-based films for comparison to QCM-D measurements. Cycles 2 to 6 of the protamine-enabled film were fit using both exponential and linear equations while cycles 6 to 10 were fit with a linear regression. PEI-based films were fit with a linear regression to determine the wet film growth rate. The linear dependence of ln (*t*) with *n* verified the exponential nature of the deposition process (b). The black line corresponds to the linear regression on this logarithmic plot.

Ex-situ AFM measurements were obtained at the boundary between coated and uncoated regions on Si wafers to determine the dried film thickness as a function of deposition cycles (**Figure 4.13(a)**). Error bars indicate plus-minus one standard deviation calculated from all ten measurements. An example of a typical ex-situ AFM image and the associated analysis technique is shown in **Figure 4.7**. The deposition rate behavior for PEI-based films followed the same linear trend as was observed by QCM-D analysis with rates of 6.2 ± 1.0 nm per cycle ($R^2 = 0.92$) and 9.6 ± 1.0 nm per cycle ($R^2 = 0.95$), respectively. Again, despite the 1,000-fold difference in molecular weight, the deposition rate increased by only 40%.

From ex-situ AFM measurements, protamine-based films again exhibited a rapid film deposition rate similar to what was observed in QCM-D measurements, despite drying. Deposition cycles 2 to 6 were fit using the exponential growth equation, and the measured film thickness, t, as a function of deposition cycles is given by **Equation 4.13.**

$$t = \frac{1.85}{0.70}\left(\exp(0.70n) - 1\right) \tag{4.13}$$

The values of K and q_o were determined from a linear fit of the logarithmic plot of cycles 2 through 6 (**Figure 4.13(b)**, $R^2 = 0.97$). The exponential dependence of film thickness may be indicative of the active volume growth mechanism given that PEI-based films deposited in a linear manner under the same solution conditions. Again, an alternative method to fit cycles 2 through 6 of protamine-enabled deposition may be to use a linear regression. The fit, shown in **Figure 4.13(a)**, yielded a deposition rate of 40 ± 7.4 nm per cycle with an R^2 value of 0.87.

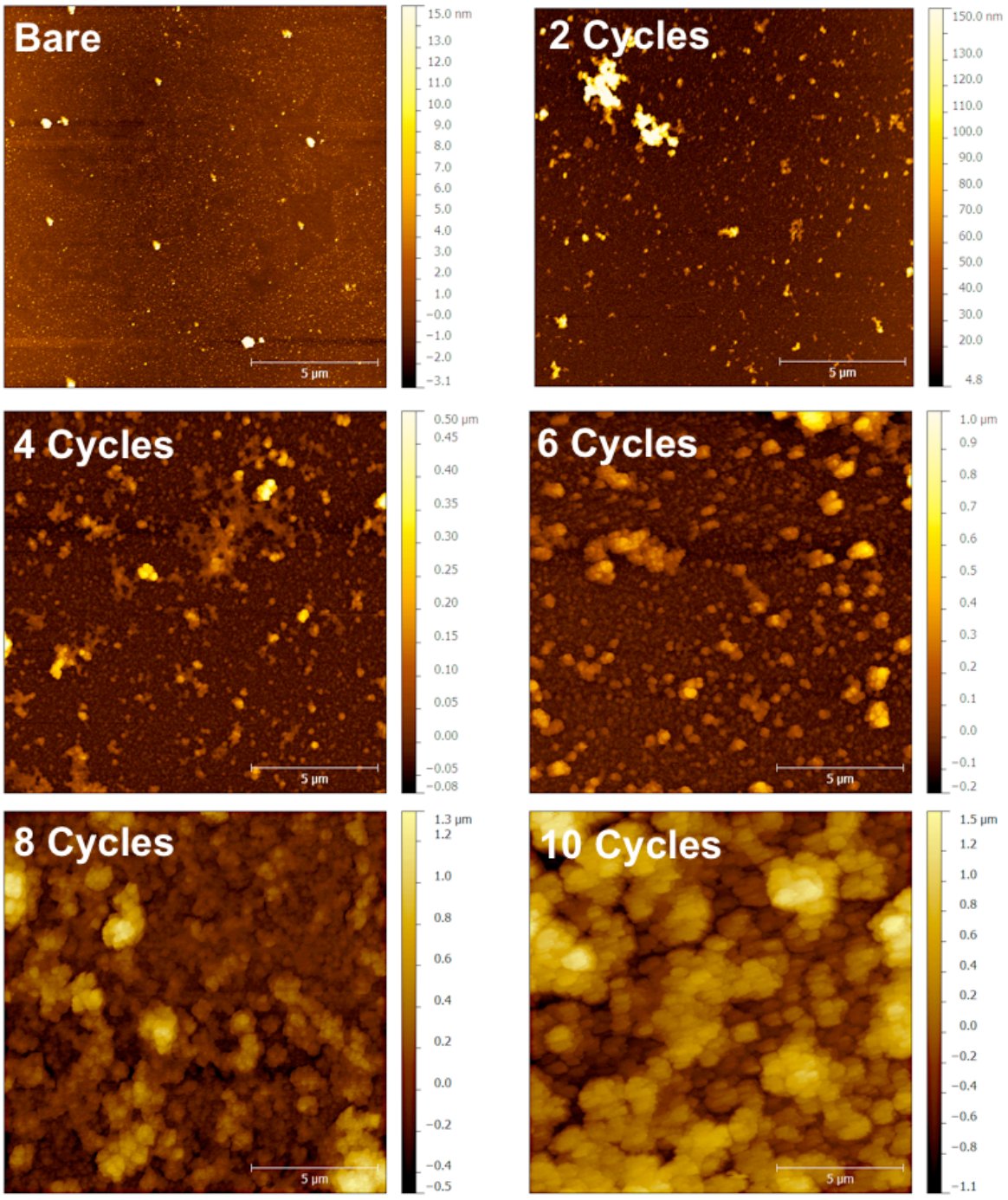

Figure 4.14: Ex-situ AFM images of protamine-based films after the deposition of 0, 2, 4, 6, 8, and 10 cycles, which were then rinsed in water and dried with compressed N_2.

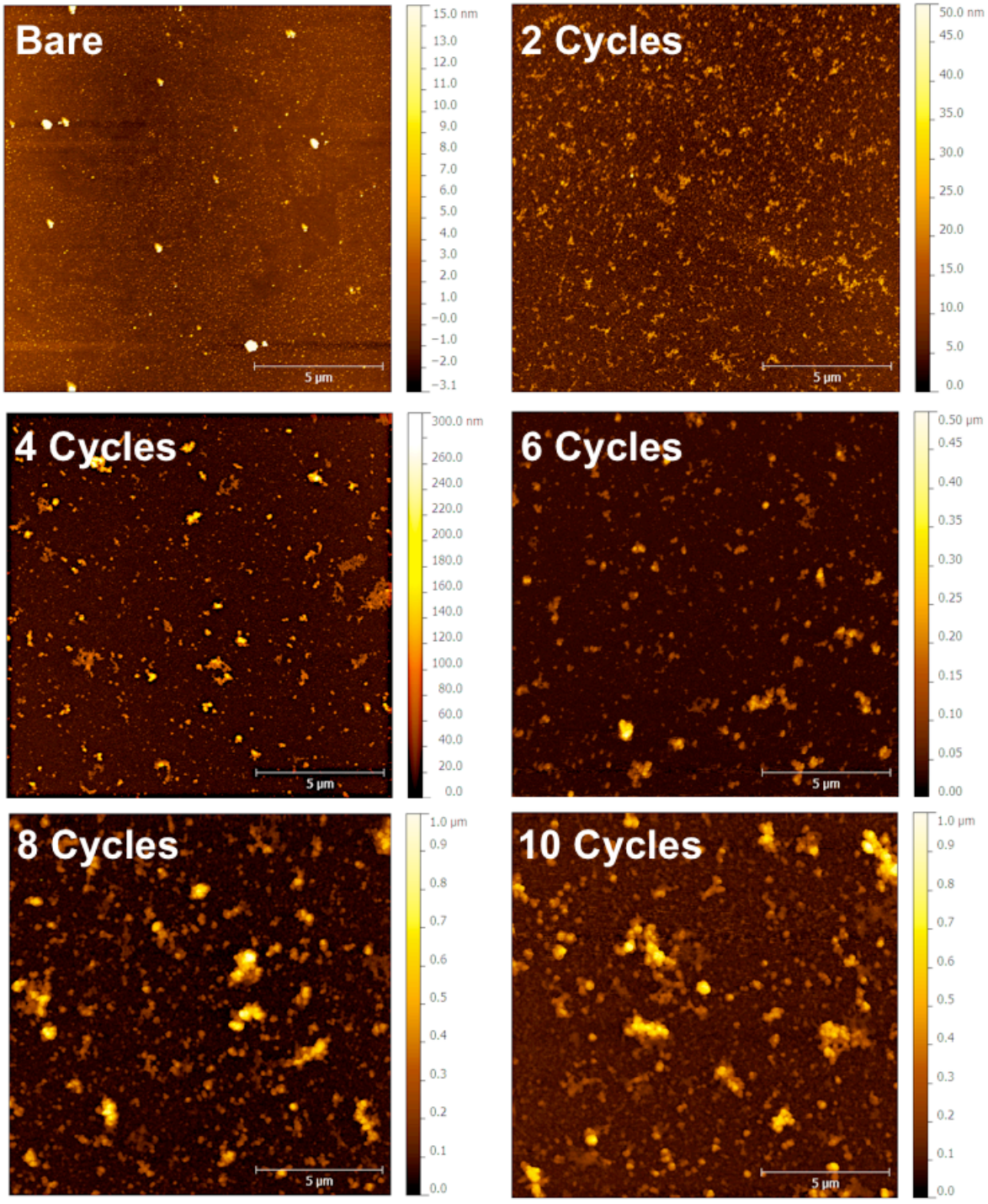

Figure 4.15: Ex-situ AFM images of PEI600-based films after the deposition of 0, 2, 4, 6, 8, and 10 cycles, which were then rinsed in water and dried with compressed N_2.

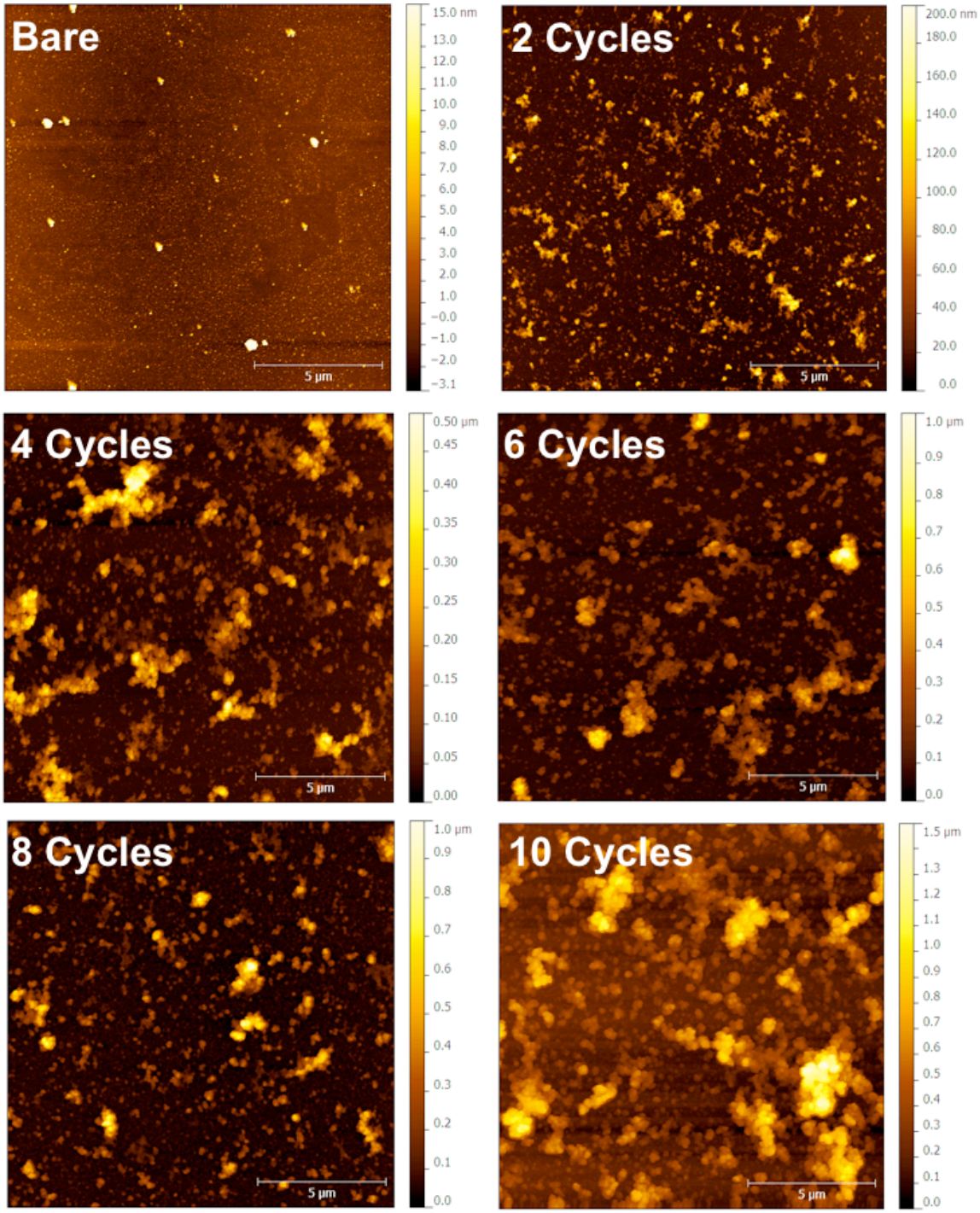

Figure 4.16: Ex-situ AFM images of PEI750K-based films after the deposition of 0, 2, 4, 6, 8, and 10 cycles, which were then rinsed in water and dried with compressed N_2.

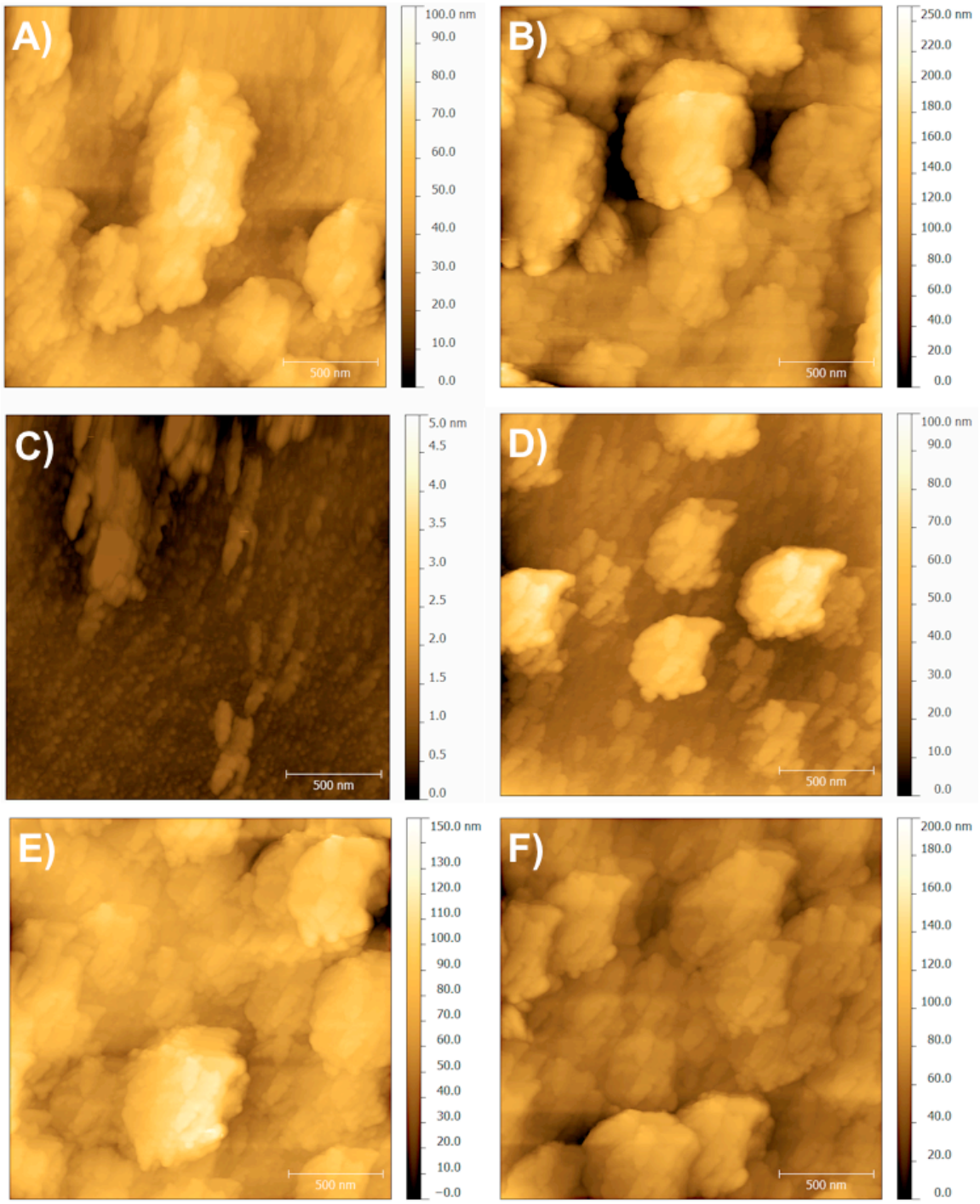

Figure 4.17: Ex-situ AFM images of protamine- (a, b), PEI600- (c, d), and PEI750K-based (e, f) films after 2 and 4 cycles, respectively. Each specimen was rinsed with deionized water and dried using compressed N_2 prior to measurement.

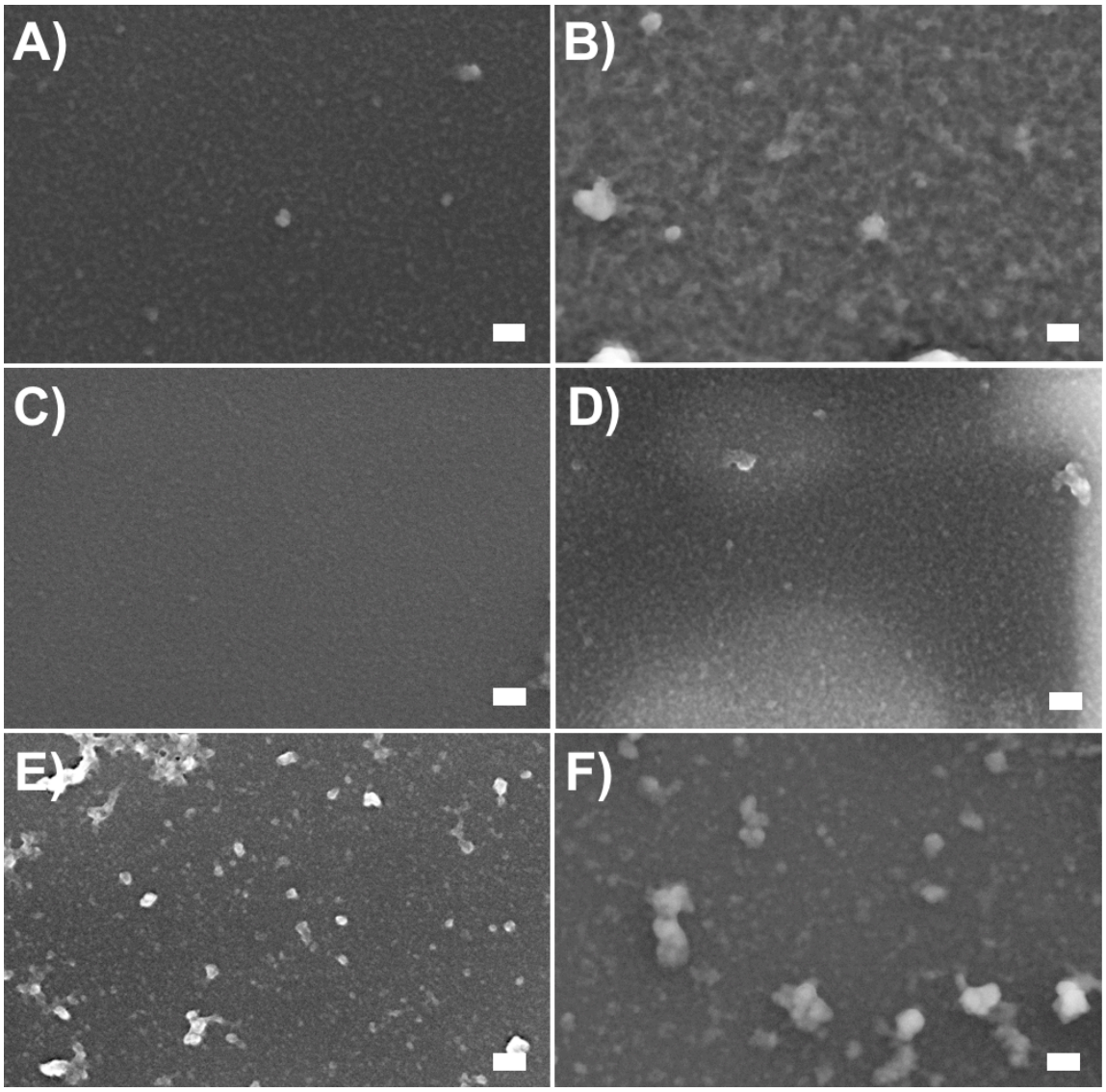

Figure 4.18: SEM images characterization of protamine- (a, b), PEI600- (c, d), and PEI750K-based (e, f) films after 2 and 4 cycles, respectively. Each specimen was rinsed with deionized water and dried using compressed N_2 prior to imaging. All scale bars are 100 nm.

The coating topographies of bioorganic protamine-based films and synthetic PEI-based films was compared using AFM and SEM analyses (**Figures 4.14-4.18**). Representative images of the topography of protamine-, PEI600-, and PEI750K-based films as a function of cycle number are shown in **Figures 4.14-4.16**, respectively.

Protamine-based films showed a similar topography to PEI-based films up to cycle 6, after which the film roughness increased dramatically. From the both the AFM and SEM images, the films did not display evidence of pinholes or islanding. SEM images of the films (**Figure 4.18)** were consistent with the ex-situ AFM images (**Figures 4.14-4.17**), and all polyamine-enabled coatings appeared to completely cover the Si substrate surface. Protamine-enabled films (**Figure 4.17 (a,b)**) did not display evidence of a vermicular topography, which has commonly been observed in active surface films that display exponential deposition rates due pH, ionic strength, temperature, and solvent quality.[19, 22, 23] With respect to PEI-enabled films, it was clear from both AFM and SEM images that PEI750K-enabled films deposited coatings that were more rough compared to PEI600.

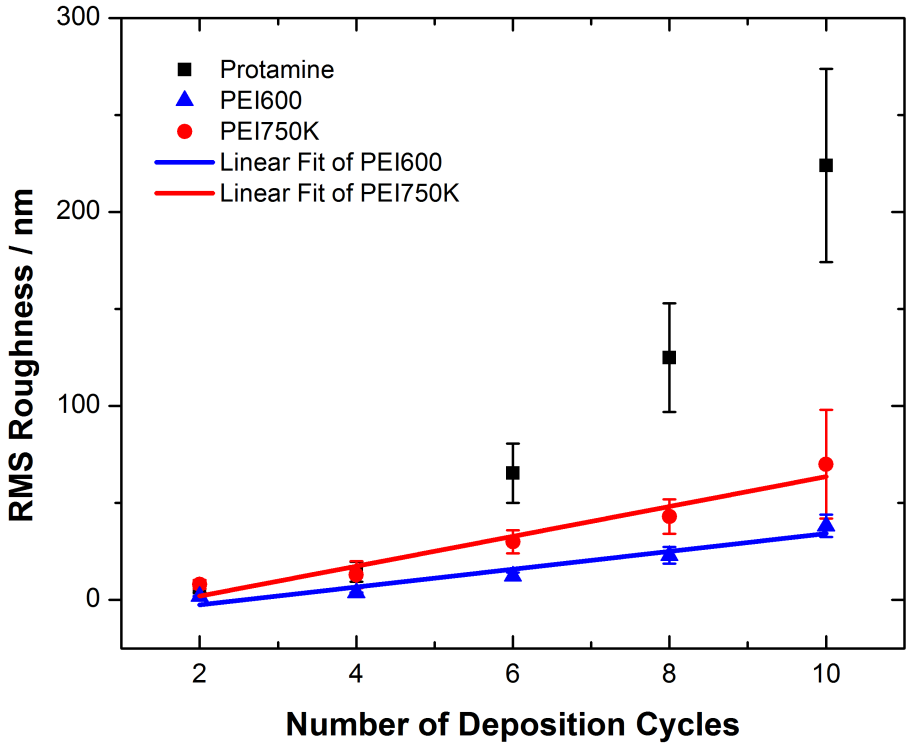

Figure 4.19: Ex-situ AFM characterization of the evolution of root-mean-squared (RMS) roughness for protamine-, PEI600-, and PEI750K-based films dried under N_2 gas for 5 min after 2, 4, 6, 8, and 10 deposition cycles.

Quantitative measurements of root-mean-squared (RMS) surface roughness are presented in **Figure 4.19**. Overall, RMS roughness increased for all films as more polyamine/TiBALDH layers were deposited on the Si surface. PEI600- and PEI750K-based films displayed a linear trend in RMS roughness with increasing cycles that correlated to the linear trend in film growth. The topographies of PEI600-based films remained relatively smooth compared to protamine and PEI750K-based films, and the RMS roughness increased at a rate of 4.6 ± 0.7 nm per cycle. By comparison, PEI750K-based films showed larger RMS roughness values overall, which increased at a rate of 7.7 ± 1.0 nm per cycle. The larger RMS roughness values observed in the PEI750K-based case was likely due to the more than 1000-fold increase in molecular weight, which may have led to the adsorption of larger agglomerates of PEI onto the surface. In contrast, the topographies and RMS roughnesses of protamine-based films changed significantly after cycle 6, which probably coincided with the onset of the exponential-to-linear transition (**Figure 4.19)**. The rapid roughness increase could have provided more surface area for polyamine adsorption in the linear regime and possibly aided film growth in tandem with an active volume mechanism. Note: the measured roughness values were less than the film thickness in all cases, which suggested the coatings were complete over all stages of film deposition.

To determine the thickness at which the polyamine/TiBALDH coatings completely covered the surface of the Si wafer, XPS analyses were conducted as a function of deposition cycle. The coatings were presumed to be complete when the Si 2s (155 eV) and 2p (101 eV) photoelectron peaks from the underlying Si substrate were no

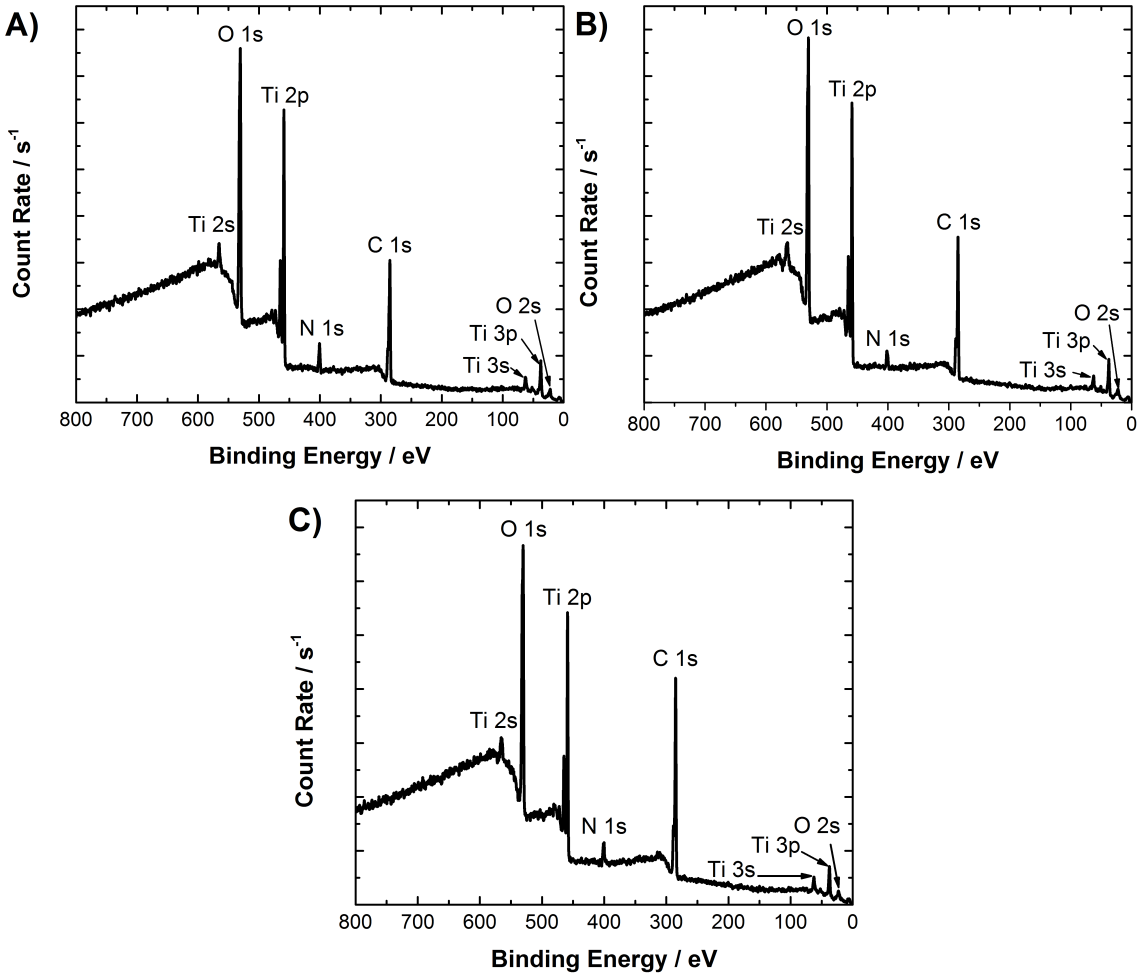

Figure 4.20: XPS spectra of a protamine-enabled film deposited on Si after 3 deposition cycles (a), a PEI600-enabled film deposited on Si after 6 deposition cycles (b), and a PEI750K film deposited on Si after 4 deposition cycles (c).

longer detectable.[39] **Figure 4.20** shows the XPS spectra for protamine- (cycle 3, **Figure 4.20(a)**), PEI600- (cycle 6, **Figure 4.20(b)**), and PEI750K-enabled (cycle 4, **Figure 4.20(c)**) coatings. The Ti and O peaks were attributed to the Ti-O-bearing layer precipitated on the surface, while the N and C peaks were attributed to adventitious carbon and the deposited polyamine. The spectra in **Figure 4.20** were from Si wafers with the fewest number of coating cycles deposited that did not contain photoelectron peaks from the Si wafer. These results showed that protamine-enabled coatings

completely covered the Si surface after 3 cycles; PEI600-enabled coatings were complete after 6 deposition cycles; and PEI750K-enabled coatings were complete after 4 deposition cycles. Assuming the information depth of XPS analyses was less than 10 nm, these results indicated the possibility of pinholes or gaps in the coatings during the early stages of film deposition that were not detected by SEM or AFM analyses. Given that the Si photoelectron peaks were no longer observed once the protamine-, PEI600-, and PEI750K-enabled films reached approximately the same thickness (21 ± 4 nm, 31 ± 6 nm, 26 ± 7 nm, respectively), another possible explanation may be that the photoelectron mean-free-path for these particular films was approximately 25 nm. If true, photoelectron peaks from the Si substrate would be observed for film thicknesses below ~25 nm despite a complete polyamine-enabled coating. However, the inelastic mean-free-path of electrons with a kinetic energy of ~1300 eV has been approximated as 2.0 nm in TiO_2 and 3.8 nm in polyethyleneimine, meaning this explanation is unlikely.[40, 41] The as-deposited films probably have small gaps at deposition cycles below 3 cycles (protamine), 4 cycles (PEI750K), and 6 cycles (PEI600).

As previously observed, these methods for LbL deposition displayed the characteristics of an electrostatically-driven process. Zeta potential measurements on SiO_2 Stöber spheres, shown in **Figure 4.21**, indicated charge overcompensation occurred after each deposition with a regular oscillation between a positive and negative potentials. Both PEI-based films showed relatively little variance as more cycles of polymer were deposited. PEI600-based films oscillated between an average of 11.1 ± 5.1 mV and -6.0 ± 1.7 mV, while PEI750K-based films potentials oscillated between an average of 27.9 ±

2.9 mV and -6.4 ± 1.8 mV. This difference was probably because the increased molecular weight polyelectrolyte provided a larger charge overcompensation upon poly adsorption to the surface. Protamine-enabled LbL showed an overall average oscillation between 14.7 ± 3.3 mV and -4.7 ± 1.1 mV.

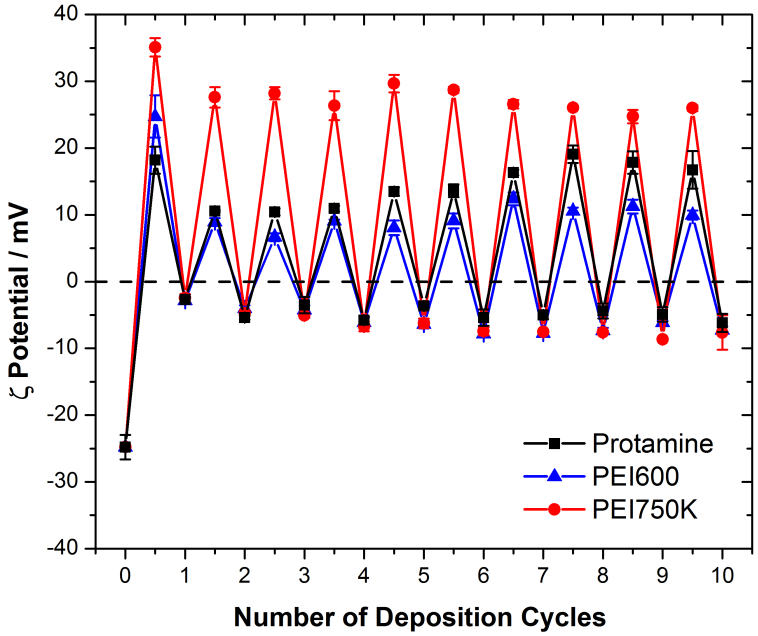

Figure 4.21: Zeta potential measurements conducted on SiO_2 Stöber spheres after alternating deposition of polyamine (half-intervals) and TiBALDH (whole intervals) illustrating the electrostatic nature of film buildup. Each point was obtained from three independent batches of SiO_2 spheres. The horizontal dashed line corresponds to $\zeta = 0$ mV. The solid lines between each point have no physical meaning and are only meant to guide the eye.

4.4.2 Characterization of Heat-Treated Coatings

From experiments conducted in Chapter 1, heat treatment of polyamine/ TiBALDH reactive LbL coatings introduced porosity throughout the coating as a result of organic pyrolysis. In this section, polyamine/TiBALDH coatings were characterized using isothermal N_2 adsorption/desorption, BJH pore size analysis, and AFM. The purpose of these experiments was to quantify specific surface area, pore size, and film

thickness after heat treatment, all of which are important with respect to the incorporation of polyamine-enabled TiO_2 films into engineering applications (e.g., dye-sensitized solar

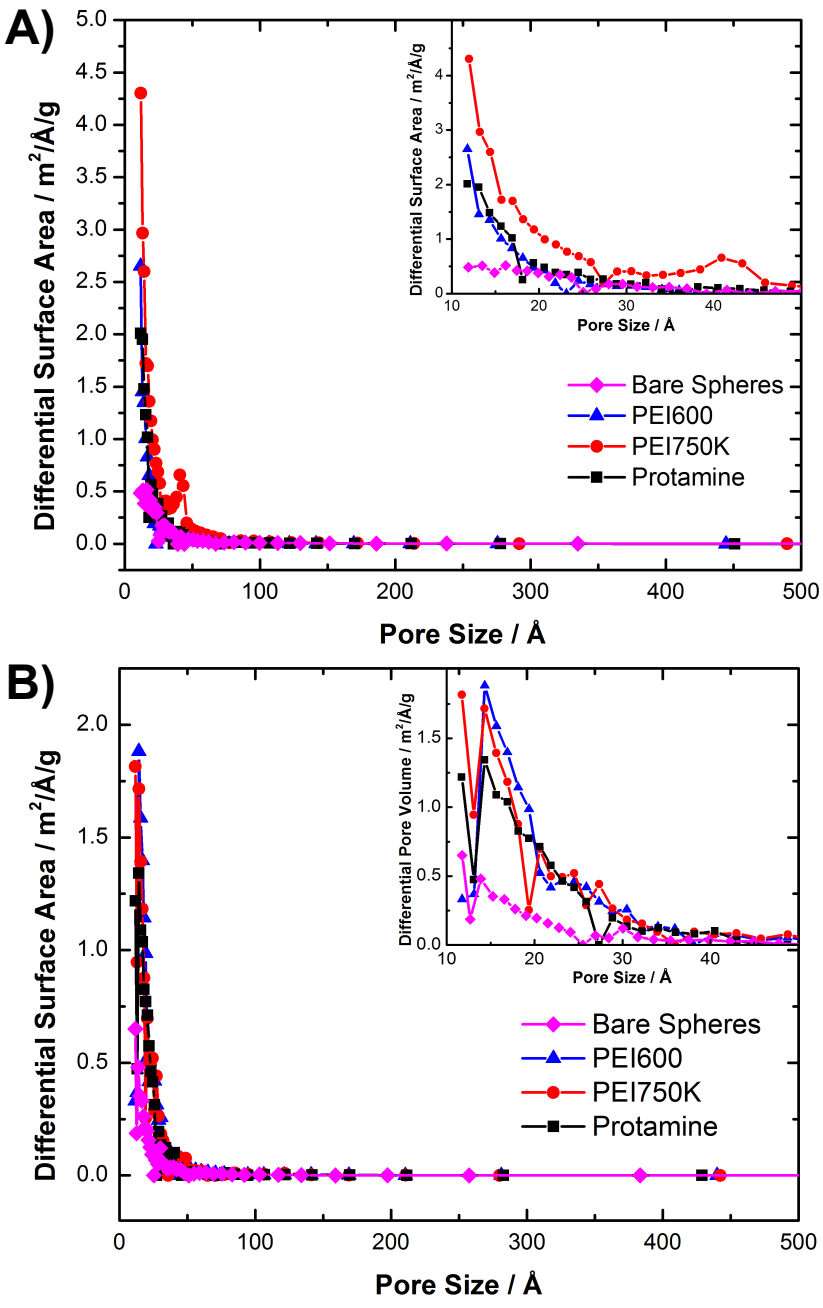

Figure 4.22: The BJH pore-size distribution of 1 μm SiO_2 Stöber spheres before and after 8 cycles of protamine-, PEI600-, or PEI750K-enabled deposition (a) and following 500 °C heat treatment in air for 6 h (b).

cells, gas sensors, catalysis).

Isothermal N_2 adsorption/desorption and Brunauer-Emmett-Teller (BET) analysis was used to determine the specific surface area before and after heat treatment of coatings on 1 μm diameter SiO_2 Stöber spheres after 8 deposition cycles (**Table 4.2**). After 8 deposition cycles, surface area increased in all cases after coatings were deposited onto the SiO_2 surface. In the as-coated state, PEI750K-based coatings showed the largest increase in specific surface area followed by PEI600- and protamine-based coatings. After heat treatment to pyrolyze organic incorporated during deposition, the specific surface area changed for all specimens, and a new trend developed. PEI600-based films exhibited the largest specific surface area (26 ± 3 m^2 g^{-1}), while protamine-enabled films showed the smallest specific surface area (17 ± 2 m^2 g^{-1}). Heat treatment did not change significantly affect the specific surface area of protamine-enabled films, which may be related to the molecular mechanism of deposition (i.e., the active volume deposition).

Table 4.2. Average specific surface area after eight polyamine-enabled coatings on SiO_2 Stöber spheres.[a]

Polyamine	As-Coated (m^2 g^{-1})	Fired (m^2 g^{-1})
Bare Spheres	6.7 ± 1	4.3 ± 1
PEI600	14 ± 2	26 ± 3
PEI750K	30 ± 1	19.8 ± 2
Protamine	14 ± 1	17 ± 2

[a] The error range corresponded to the absolute range of specific surface area values from three measurements of the same specimen.

The differential specific surface area as a function of pore-size using BJH analysis of isothermal desorption was compared for as-coated and heat treated TiO_2 coatings and shown in **Figure 4.22**. The as-coated and fired spheres all displayed similar pore-size distributions where a majority of the specific surface area stemmed from microporosity (< 5 nm diameter) not observed in the bare spheres.

AFM analyses were conducted on the same coated Si wafers after heating to 500 °C for 6 h. These measurements quantified the shrinkage in the films as a result of the heat treatment, and provided useful information for coating process design for specific applications where a particular thickness is necessary (e.g., dye-sensitized solar cells). The results shown in **Figure 4.23** illustrated the same overall trend in growth observed previously between protamine-, PEI600-, and PEI750K-based films (Figures 4.11 and 4.13). The final deposited thickness rate of PEI600- and PEI750K-based films were 1.8 ± 0.4 nm per cycle (R^2 = 0.88) and 4.9 ± 0.7 nm per cycle (R^2 = 0.94) after heat treatment, respectively.

The thicknesses of the fired protamine-enabled films from cycles 3 to 6 were fit using both exponential and linear models, and the exponential expression for film thickness as a function of the number of deposition cycles is given by **Equation 4.14**. A linear regression of cycles 3 through 6 yielded deposition rate after firing of 15 ± 3.5 nm per cycle (R^2 = 0.85). While a linear regression of cycles 6 through 10 yielded a deposition rate after firing of 53 ± 4.7 nm per cycle (R^2 = 0.97).

$$t = \frac{1.38}{0.49}\left(\exp(0.49n) - 1\right) \tag{4.14}$$

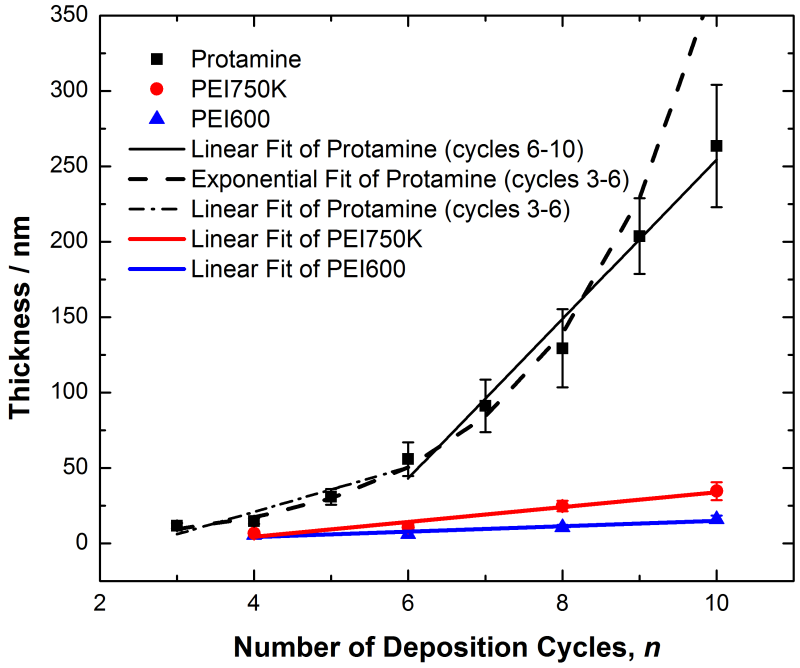

Figure 4.23: Ex-situ AFM analyses of protamine-, PEI600-, and PEI750K-enabled films after depositing 4, 6, 8, and 10 layers, then heat treating the films at 500 °C for 6 h in air to pyrolyze organics and crystallize the coating. Note: results for the second cycle are not shown because the thickness measured was below the radius of curvature of the AFM tip (10 nm). Error bars were determined from the full-width at half-maximum of the distribution of film thicknesses.

4.4.3 Molecular Origins of Exponential Peptide-Enabled Film Growth

Thus far, protamine-enabled LbL deposition has exhibited behavior common to exponentially growing films where one polyelectrolyte is capable of diffusion both into and out of the film thickness. QCM-D and AFM analyses suggested that substantial film reorganization may have occurred during TiBALDH exposure (**Figures 4.9 - 4.13**). An exponential-to-linear transition in deposition rate was observed after the sixth deposition cycle (**Figures 4.11** and **4.13**), which coincided with a rapid rise in surface roughness

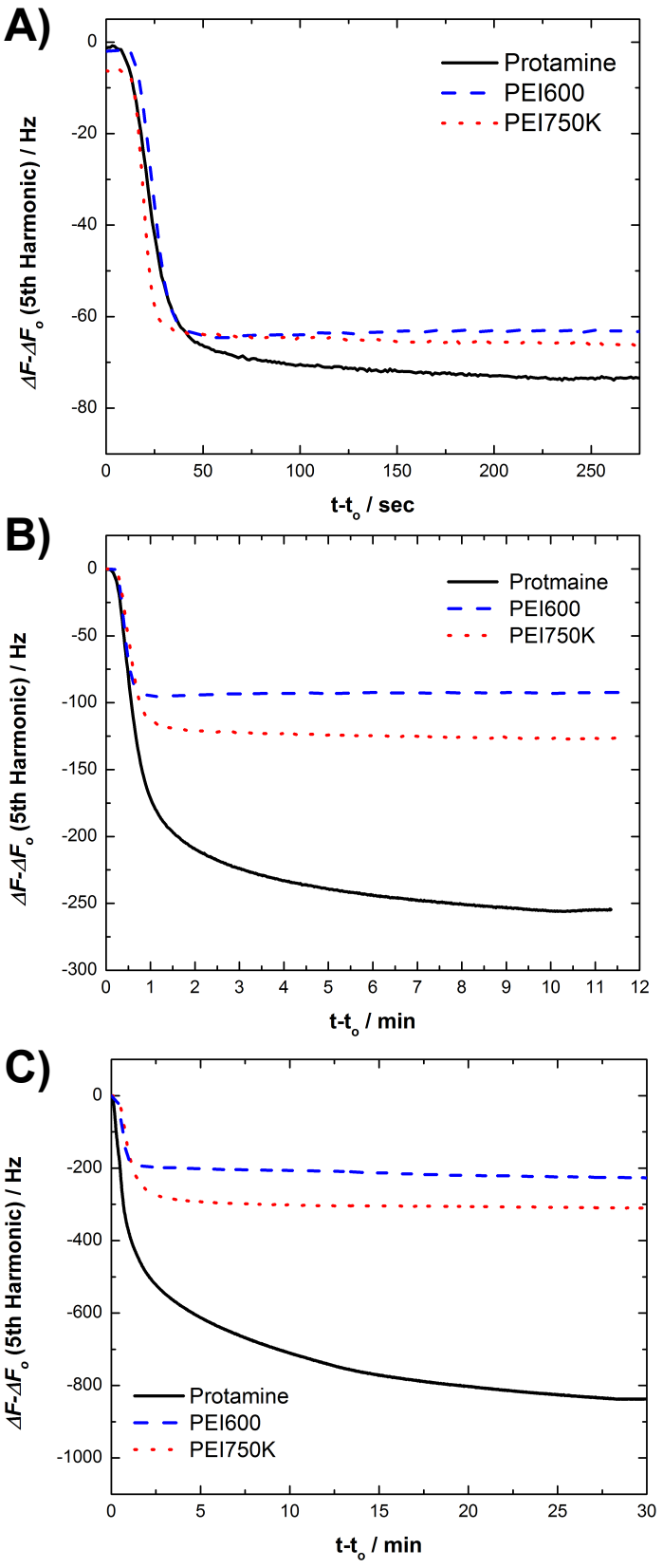

Figure 4.24: Kinetics of TiBALDH reaction measured using QCM-D for each polyamine-based deposition method after 1 cycle (a), 4 cycles (b), and 10 cycles (c).

(**Figures 4.14** and **4.19**). These observations were unique to bioorganic protamine-enabled films and were not observed in synthetically-derived, PEI-enabled films. An exponential-to-linear transition was suggestive of an active volume mechanism for deposition, where at least one polyelectrolyte is capable of diffusion throughout the film thickness. Some of the protamine was assumed to be available as a mobile polyelectrolyte. It was also assumed that TiBALDH formed an immobile phase upon reaction with the polyamine because an exponential-to-linear transition was not observed in PEI-based films.

The kinetics of protamine and PEI reaction with TiBALDH were compared at cycles 1, 4, and 10 to examine the kinetics of individual layer growth in more detail. The results of the QCM-D comparison are shown in **Figure 4.24**. In this experiment, the linearly-depositing films based upon PEI were effectively controls where reaction with TiBALDH apparently occurred solely with PEI deposited at the external surface of the film. The reaction plateaued within about 5 min regardless of the PEI molecular structure, weight, or deposition cycle number. Protamine-enabled films displayed a gradual retardation of deposition kinetics. After the first deposition cycle, the reaction of TiBALDH with polyamine was effectively complete within about 5 min, just like PEI-based films, which was consistent with protamine reaction with TiBALDH strictly on the surface (i.e., there was no pre-existing TiO-bearing film for inward and outward protamine to occur). However, at cycle 4, the protamine/TiBALDH reaction took longer to reach completion (~10 min), and by cycle 10 the protamine/TiBALDH film reaction lasted approximately 30 min. The change in protamine/TiBALDH film reaction kinetics

implied that the deposition rate was influenced by more than simply an active surface mechanism. An active volume mechanism may also be affecting protamine-enabled deposition of TiO-bearing films.

An active volume of protamine within the film that diffused outward to the film/ solution interface for reaction with TiBALDH could explain the differences in kinetic behavior relative to PEI-derived films. The increase of protamine/TiBALDH reaction time with respect to the number of the deposition cycles has not been reported before in exponentially growing organic films, but it was consistent conceptually with the active volume molecular mechanism model proposed by other authors.[27, 31-33] Unfortunately, QCM-D measurements cannot not provide direct observation of the specific molecular dynamics involved in mass gain/loss.

Both protamine and PEI750K (control) were conjugated to fluorescein isothiocyanate (FITC) to spectroscopically determine if protamine was capable of desorption during film incubation with TiBALDH. Following 9 LbL deposition cycles onto a Si wafer, the protamine- and PEI750K-enabled films were exposed to the respective FITC-conjugated polycations (5 min), washed in buffer three times (1 min incubation each), then exposed to TiBALDH for equal periods of 30 min. As a control, one wafer was set aside and incubated in buffer for 30 min. The supernatant from all solutions were extracted and examined for the presence of fluorescent activity, which would indicate if either protamine or PEI750K were mobile and capable of diffusion back into the bulk solution.

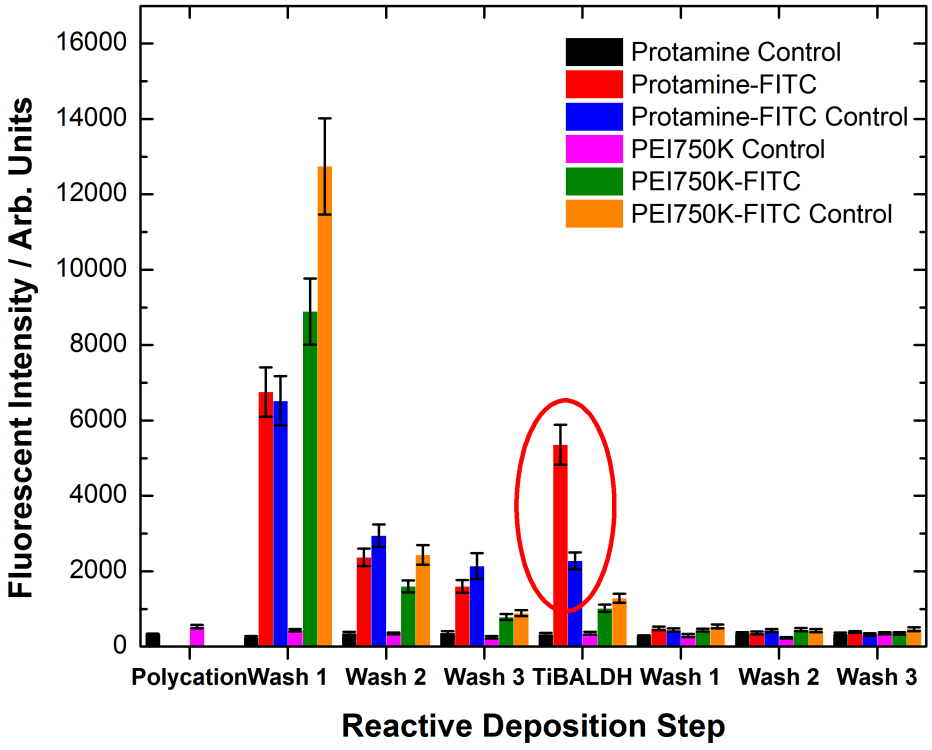

Figure 4.25: Fluorescent intensity of supernatant solutions sampled after each step in the reactive deposition process. Both protamine and PEI750K were tagged with fluorescein isothiocyanate (FITC). The protamine control and PEI750K controls did not contain FITC functionalization and the polycation-FITC control were incubated in buffer instead of TiBALDH for an equivalent amount of time. Note: both FITC-conjugated polycation solutions saturated the detector at the gain necessary for detect the polycations in TiBALDH and could not be plotted on the same scale.

After incubation in protamine-FITC and PEI750-FITC, the supernatant of the first wash step displayed varying amounts of fluorescence due to excess polyelectrolyte being removed from the film surface (**Figure 4.25**). From the TiBALDH incubation step shown in **Figure 4.25**, only protamine-enabled coatings showed a significant increase in fluorescent activity relative to the controls and PEI-enabled coatings. This indirect measurement demonstrated that protamine was not completely immobilized by

electrostatic interaction upon incubation, which was consistent with prior work that showed protamine adsorbed during organic/inorganic multilayer formation was capable of exchanging with bulk protamine in subsequent protamine incubations.[38]

Next, the effect of film drying after each complete cycle on the protamine-enabled film deposition rate was investigated. The assumption made for this experiment was that drying after each cycle caused the organic/inorganic film to reorganize and densify due in part to a presumed reduction in film volume. The model for active volume deposition relies on the ability of protamine to infiltrate through the thickness of the film. Therefore, the assumed densification of the coating by drying after each cycle should inhibit protamine migration and alter film growth behavior. For linear LbL growth, changing the density of the coating can alter the deposition rate (e.g., due to surface roughness alteration), but because the PEI/TiBALDH adsorption and reaction is limited to the external surface, film growth should still remain linear with respect to the number of deposition cycles. As such, PEI750K/TiBALDH films were used as a controls to ensure that drying did not significantly affect the linear growth rate.

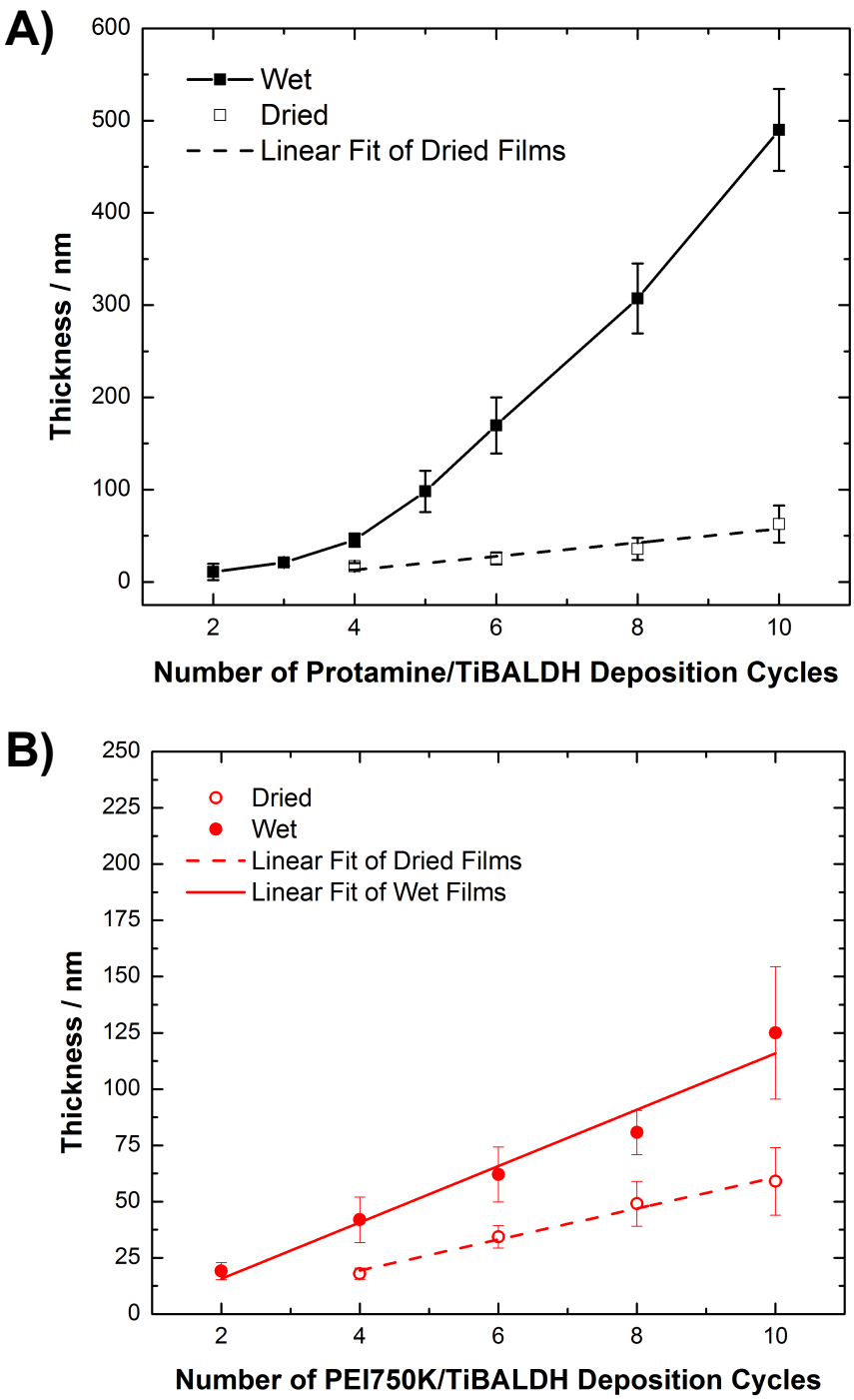

Figure 4.26: Ex-situ AFM thickness measurements of protamine- (a) and PEI750K-based (b) reactive coatings dried by dry, compressed N_2 for 5 min after each complete cycle compared to films that were kept wet during coating. The thickness values after 2 deposition cycles were not shown because the values were less than the tip radius. The black line in (a) is only to guide the eye.

AFM analyses of the thickness of protamine/TiBALDH and PEI750K/TiBALDH films are shown in **Figure 4.26**. Drying for 5 min with dry, compressed N_2 after each complete cycle affected the deposition rate of protamine-enabled films relative to protamine-enabled films that remained wet during the deposition process. Protamine-enabled films switched from an active volume film deposition behavior to linear film deposition when the coating was dried after each complete deposition cycle (**Figure 4.26(a)**). A linear fit of the repeatedly dried protamine-enabled films showed a deposition rate of 7 ± 1.5 nm per cycle ($R^2 = 0.88$).

Conversely, PEI750K-based films continued to buildup in a linear fashion even after drying after each complete cycle, albeit at a reduced rate (7 ± 0.5 nm per deposition cycle ($R^2 = 0.98$) instead of 10 ± 1 nm per cycle, **Figure 4.26(b)**). These results indicated that film density affects deposition rate, especially in protamine-enabled films that display exponential growth when left wet. From this conclusion, it can be inferred that the increased film density inhibited protamine diffusion through the film during the protamine adsorption step in LbL deposition, so that the active volume model of exponential growth was inhibited. Instead, protamine was presumably deposited largely onto the external surfaces of the dried films, which resulted in linear growth. While not direct evidence, this result was consistent with models presented in the literature.[31, 32] In the context of other QCM, AFM, and fluorescence tagging evidence collected in this work, protamine-enabled deposition likely follows the active volume model of growth, for which some free protamine was capable of diffusion "in" and "out" of the thickness of the film.

4.5 Summary and Outlook

In this work, the deposition behavior of electrostatically deposited TiO-bearing films based on synthetic and biologically-derived polycations (polyethyleneimine or protamine) and the reactive metal oxide precursor titanium(IV) bis(ammoniumlactato) dihydroxide were interrogated. Both branched 600 M_w and 750,000 M_w PEI were shown to deposit TiO-bearing coatings on SiO_2 surfaces at a linear rate (6 ± 0.9 nm per cycle and 10 ± 1 nm per cycle, respectively) with slight increase in RMS roughness over the course of 10 deposition cycles (4.6 ± 0.7 nm per cycle and 14 ± 1.2 nm per cycle, respectively). Protamine-enabled films displayed exponential film buildup for the first six cycles according to both QCM-D and ex-situ AFM thickness analyses before transitioning to a linear deposition regime with a large deposition rate (174 ± 5 nm per cycle).

The incorporation of protamine and PEI750K conjugated with fluorescent FITC implied that protamine was appreciably more mobile upon incubation in TiBALDH. When protamine-enabled films were dried after each cycle, the deposition rate became linear and similar in magnitude to PEI600-based films. The results of these experiments were consistent with the molecular model for active volume deposition where free protamine can diffuse both “in” and “out” of the film thickness. From the data gathered in this work (i.e., deposition rates, roughnesses, specific surface areas, and pore size distribution), a particular polyamine can be chosen to deposit TiO-bearing coatings in a manner that satisfies specific engineering requirements. For example, a thin film with minimal roughness can be deposited using PEI600-based films and thick rough films can be generated through protamine-based deposition. The selection of either synthetic or

bioorganic molecules, and the size of such molecules may also be used to tune the porosity of such composite coatings after organic pyrolysis of organic component. The LbL assembly methods discussed could allow for the integration of various particles, biomolecules, DNA or proteins into inorganic coatings. The active volume deposition behavior may be useful as part of a release mechanism in colloidal particles, when the as-deposited films are subjected to certain conditions.

Further investigation into the molecular mechanism of peptide-enabled deposition should include conjugation of the peptide with an inert fluorine-rich molecule for analysis by XPS depth-profiling. A Si wafer coated with a predetermined number of deposition cycles, could be exposed to the fluorine-conjugated peptide. If inward-diffusion of the peptide occurs, fluorine should be present throughout the thickness in the depth profile. A depth-profile of the sample after exposure to TiBALDH should reveal that the fluorine-conjugated peptide migrated to the film/solution interface. Further QCM analyses under varying incubation times, temperatures, pH, and ionic strengths may show that the exponential-to-linear transition can be shifted, thereby providing more evidence that film deposition follows an active volume model.

4.6 References

1. Y. Fang, Q. Wu, M. B. Dickerson, Y. Cai, S. Shian, J. D. Berrigan, N. Poulsen, N. Kröger and K. H. Sandhage, *Chemistry of Materials*, 2009, **21**, 5704-5710.

2. Y. Jiang, D. Yang, L. Zhang, Q. Sun, X. Sun, J. Li and Z. Jiang, *Advanced Functional Materials*, 2009, **19**, 150-156.

3. Y. Zhang, H. Wu, J. Li, L. Li, Y. Jiang, Y. Jiang and Z. Jiang, *Chemistry of Materials*, 2008, **20**, 1041-1048.

4. V. Ball, L. Dahéron, C. Arnoult, V. Toniazzo and D. Ruch, *Langmuir*, 2011, **27**, 1859-1866.

5. A. Bernecker, R. Wieneke, R. Riedel, M. Seibt, A. Geyer and C. Steinem, *Journal of the American Chemical Society*, 2009, **132**, 1023-1031.

6. Y. Jiang, D. Yang, L. Zhang, L. Li, Q. Sun, Y. Zhang, J. Li and Z. Jiang, *Dalton Transactions*, 2008, 4165-4171.

7. M. R. Knecht and D. W. Wright, *Langmuir*, 2004, **20**, 4728-4732.

8. J. D. Berrigan, T. S. Kang, Y. Cai, J. R. Deneault, M. F. Durstock and K. H. Sandhage, *Advanced Functional Materials*, 2011, **21**, 1693-1700.

9. N. R. Haase, S. Shian, K. H. Sandhage and N. Kröger, *Advanced Functional Materials*, 2011, **21**, 4243-4251.

10. M. B. Dickerson, C. L. Knight, M. K. Gupta, H. R. Luckarift, L. F. Drummy, M. L. Jespersen, G. R. Johnson and R. R. Naik, *Materials Science and Engineering: C*, 2011, **31**, 1748-1758.

11. H. R. Luckarift, M. B. Dickerson, K. H. Sandhage and J. C. Spain, *Small*, 2006, **2**, 640-643.

12. N. Ladhari, C. Ringwald, O. Ersen, I. Florea, J. Hemmerlé and V. Ball, *Langmuir*, 2011, **27**, 7934-7943.

13. P. Sautière, G. Briand, M. Gusse and P. Chevaillier, *European Journal of Biochemistry*, 1981, **119**, 251-255.

14. Y. Lvov, K. Ariga, M. Onda, I. Ichinose and T. Kunitake, *Colloids and Surfaces A: Physicochemical and Engineering Aspects*, 1999, **146**, 337-346.

15. C. Picart, J. Mutterer, L. Richert, Y. Luo, G. D. Prestwich, P. Schaaf, J. C. Voegel and P. Lavalle, *Proceedings of the National Academy of Sciences*, 2002, **99**, 12531-12535.

16. P. Lavalle, C. Gergely, F. J. G. Cuisinier, G. Decher, P. Schaaf, J. C. Voegel and C. Picart, *Macromolecules*, 2002, **35**, 4458-4465.

17. P. T. Hammond, *Current Opinion in Colloid & Interface Science*, 1999, **4**, 430-442.

18. B. Schoeler, G. Kumaraswamy and F. Caruso, *Macromolecules*, 2002, **35**, 889-897.

19. E. Poptoshev, B. Schoeler and F. Caruso, *Langmuir*, 2004, **20**, 829-834.

20. S. L. Clark, M. F. Montague and P. T. Hammond, *Macromolecules*, 1997, **30**, 7237-7244.

21. O. J. Rojas, M. Ernstsson, R. D. Neuman and P. M. Claesson, *Langmuir*, 2002, **18**, 1604-1612.

22. B. Schoeler, E. Poptoshev and F. Caruso, *Macromolecules*, 2003, **36**, 5258-5264.

23. R. A. McAloney, M. Sinyor, V. Dudnik and M. C. Goh, *Langmuir*, 2001, **17**, 6655-6663.

24. D. T. Haynie, E. Cho and P. Waduge, *Langmuir*, 2011, **27**, 5700-5704.

25. J. Ruths, F. Essler, G. Decher and H. Riegler, *Langmuir*, 2000, **16**, 8871-8878.

26. W. Senaratne, L. Andruzzi and C. K. Ober, *Biomacromolecules*, 2005, **6**, 2427-2448.

27. C. Porcel, P. Lavalle, V. Ball, G. Decher, B. Senger, J.-C. Voegel and P. Schaaf, *Langmuir*, 2006, **22**, 4376-4383.

28. P. Lavalle, C. Picart, J. Mutterer, C. Gergely, H. Reiss, J.-C. Voegel, B. Senger and P. Schaaf, *The Journal of Physical Chemistry B*, 2004, **108**, 635-648.

29. M. Michel, A. Izquierdo, G. Decher, J. C. Voegel, P. Schaaf and V. Ball, *Langmuir*, 2005, **21**, 7854-7859.

30. C. Porcel, P. Lavalle, G. Decher, B. Senger, J. C. Voegel and P. Schaaf, *Langmuir*, 2007, **23**, 1898-1904.

31. M. Salomäki, I. A. Vinokurov and J. Kankare, *Langmuir*, 2005, **21**, 11232-11240.

32. G. Ladam, P. Schaad, J. C. Voegel, P. Schaaf, G. Decher and F. Cuisinier, *Langmuir*, 1999, **16**, 1249-1255.

33. N. Hoda and R. G. Larson, *The Journal of Physical Chemistry B*, 2009, **113**, 4232-4241.

34. E. P. Barrett, L. G. Joyner and P. P. Halenda, *Journal of the American Chemical Society*, 1951, **73**, 373-380.

35. C. C. White and J. L. Schrag, *The Journal of Chemical Physics*, 1999, **111**, 11192-11206.

36. Y. Lvov, K. Ariga, I. Ichinose and T. Kunitake, *Journal of the American Chemical Society*, 1995, **117**, 6117-6123.

37. F. Höök, M. Rodahl, B. Kasemo and P. Brzezinski, *Proceedings of the National Academy of Sciences*, 1998, **95**, 12271-12276.

38. S. Hiller, S. Leporatti, A. Schnäckel, E. Typlt and E. Donath, *Biomacromolecules*, 2004, **5**, 1580-1587.

39. NIST X-ray Photoelectron Spectroscopy Database, v. 3.5, National Institute of Standards and Technology, Gaithersburg, 2003; http://srdata.nist.gov/xps/.

40. P. J. Cumpson, *Surface and Interface Analysis*, 2001, **31**, 23-34.

41. G. G. Fuentes, E. Elizalde, F. Yubero and J. M. Sanz, *Surface and Interface Analysis*, 2002, **33**, 230-237.

CHAPTER 5: ENHANCED OXYGEN REDUCTION BY PROTAMINE-LACCASE HYBRID ENZYMES TETHERED TO CARBON NANOTUBES

5.1 Summary

Multicopper oxidases, such as laccase, are enzymes known to reduce molecular oxygen at high redox voltages, which makes the enzymes attractive biocatalysts for a variety of applications (e.g., biological fuel cells). In this chapter, a method is developed to immobilize laccase (from *Trametes versicolor*) to the surface of carbon nanotube "buckypaper" (CNT-BP) with the aid of protamine and 1-pyrenebutanoic acid, succinimidyl ester (PBSE). Despite the added protein, PBSE-treated Lac-PA electrodes displayed a 33 mV increase in onset voltage, and a nearly two-fold increase in maximum current density (137 $\mu A\ cm^{-2}$ to 271 $\mu A\ cm^{-2}$), when compared to PBSE-treated laccase electrodes. Biochemical assays of the immobilized enzyme on PBSE-treated CNT-BP showed a 12% increase in loading, and a 48% increase in relative activity for Lac-PA relative to laccase. After 20 galvanostatic loading/unloading cycles lasting 4 h each, Lac-PA on PBSE-treated CNT-BP retained 10% more half-cell voltage compared to laccase. In an attempt to elucidate the basis for the improved current density of the PBSE-treated Lac-PA electrodes, three synthetic peptides were cross-linked to laccase (RRRR, RRRTTR, and RRRTTRRRRAGRRRR). The resulting electrochemical testing strongly supported the hypothesis that protamine accommodated the conformational changes necessary for enzyme immobilization, thereby allowing laccase to remain in a conformation more similar to the free enzyme.

5.2 Introduction

Thus far, the protamine LbL deposition process has been used to apply TiO-bearing coatings onto porous anodic aluminum oxide (AAO) templates that have been converted by pyrolysis and subsequent AAO dissolution into aligned, porous-wall TiO_2 nanotube arrays.[1] Such TiO_2 nanotube arrays displayed improved functional dye-loading when compared to typical sol-gel techniques, due to enhanced porosity generated upon pyrolysis of entrapped protamine within the as-deposited films. In this chapter, protamine was cross-linked to the multicopper oxidase enzyme, laccase (from *Trametes versicolor*) and such cross-linking resulted in improved catalysis of oxygen reduction.

The four-electron electrochemical reduction of oxygen to yield water, given by **Equation 5.1**, is an important reaction for various electrochemical processes and technologies (e.g., corrosion inhibition, sensors, metal-air batteries, and fuel cells).[2-9]

$$O_2 + 4\ e^- + 4H^+ \longrightarrow 2\ H_2O \qquad E^0 = 1.23\ V \qquad (5.1)$$

More specifically, fuel cells commonly utilize the oxygen reduction reduction (ORR) as the cathodic reaction.[10, 11] This is due to both the ubiquity of oxygen as a reactant and the large thermodynamic driving force (E^0 = 1.23 V).[12] Unfortunately, the kinetics of the ORR are slow, and cleaving the strong O=O bond (498 kJ/mol) requires either an electrocatalyst, or a reduction in electrode voltage.[13] This difference between the electrode voltage (E) and the equilibrium voltage (E_{eq}) is called the overvoltage, η, and is described by **Equation 5.2.**[14]

$$\eta = E - E_{eq} \qquad (5.2)$$

Put another way, the overvoltage is the added driving force necessary to drive the

reaction and achieve reasonable current densities. Platinum and platinum alloys are the most widely used catalysts for the ORR, but require large overvoltages of 500-600 mV to obtain a useful current density.[13, 15] While these overvoltages can be reduced by loading the electrodes with more catalyst or by applying a smaller overvoltage (less driving force), neither of these options are ideal.[15] The high-cost and scarcity of platinum has led to extensive international efforts to reduce the amount of platinum loading and to examine alternative electrocatalyst materials, such as enzymes.

Enzymes are large proteins capable of catalyzing complex chemical reactions at rates often more than a million-fold faster than the uncatalyzed reaction with not just selectivity, but specificity, under relatively mild conditions.[16] Multicopper oxidases (e.g., laccase, bilirubin oxidase, and ascorbate oxidase) are capable of catalyzing the oxidation of a wide-range of aromatic compounds (e.g., phenols, benzothiols, substituted polyphenols) concomitantly with the reduction of oxygen to yield water with little overvoltage.[17, 18] Of these multicopper oxidases, laccase-modified electrodes have demonstrated ORR onset voltages that can approach 1.2 V_{RHE} of reversible voltage for the O_2/H_2O half-cell.[19] As a result, laccase has drawn significant attention as a cathode material for biofuel cells.[20-23] Examples of current research in the field include efforts to synthetically replicate the active center,[24, 25] efforts to modify or enhance the active center,[26, 27] and the development of new enzyme immobilization strategies.[28]

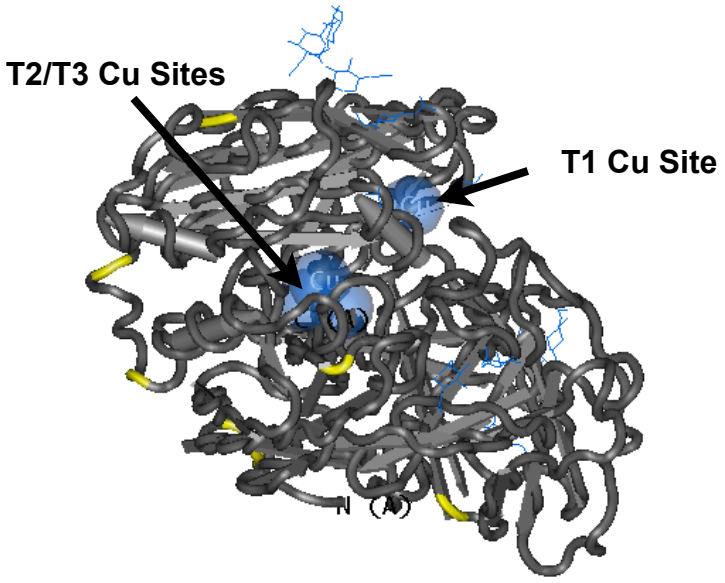

Figure 5.1: The structure of laccase (*Trametes versicolor*) is shown with the T1 and trinuclear copper (T2 and T3) sites highlighted (blue spheres). All eight lysine residues in the protein are highlighted in yellow.[31] (PDB code 1GYC)

The ORR is catalyzed by laccase at the enzyme redox center by four coordinated copper atoms grouped into three types based on their spectroscopic characteristics.[18, 29] These sites are designated as type 1 (T1), type 2 (T2), and type 3 (T3, 2 of these) copper sites.[18] The T1 site is located in a cavity approximately 13 Å away from the trinuclear copper center and facilitates electron transfer from the substrate to the trinuclear copper cluster for oxygen reduction reaction through an electron-transfer pathway (T1-His-Cys-His-T2/T3).[30, 31] The T2 and T3 sites form a trinuclear cluster where oxygen is subsequently reduced to water.[31, 32] A model of laccase from *Trametes versicolor* is shown in **Figure 5.1** (PDB code 1GYC),[33] and a more detailed explanation of the catalytic mechanisms, along with the structure-function relationship of fungal laccases, is discussed by both Giardina, *et al.* and Solomon, *et al*.[34, 35]

The design of enzyme-modified electrode materials must fulfill several requirements, including: (1) stability over time and at various applied voltages, (2) large surface loading per geometric area, and (3) intimate electrical communication between the active redox center and the electrode. Two general strategies have been employed to immobilize enzymes onto electrode surfaces. The first method is to deposit thick layers of enzyme with an electron mediator (typically an osmium complex) that transfers electrons between the electrode and the enzyme.[36-39] Electrodes using mediated electron transfer (MET) can be fabricated with thick enzyme layers which enable large enzyme loading and high current densities.[38-40] However, the addition of an electron mediator adds another level of complexity to electrode design, and performance becomes limited by mediator stability and properties as well as the enzyme.[39]

The second strategy is to achieve direct electron transfer (DET) between the T1 Cu site and the electrode by obtaining intimate electrical communication between a thin layer of enzyme and electrode.[41, 42] DET is difficult to attain due to the insulating effect of the protein surrounding the redox center of the enzyme. However, establishing DET eliminates the limitations and complexity introduced by MET materials (e.g., electrode voltage dictated by the mediator, biocompatability) albeit at the cost of current density.[43, 44] Strategies for achieving electrical connection between the enzyme and the electrode include: physisorption or covalent linkage,[45] entrapment in polymeric films (e.g., polythiophene and polypyrrole),[46] association with metal colloids,[47] and encapsulation in porous matrices that incorporate a conductive nanomaterial.[48, 49]

Enzyme loading on electrodes employing the DET strategy is typically low, due to the thin layer of deposited enzyme required by the large size of the protein (53 kDa) relative to the size of the metal catalyst centers. To circumvent the geometric constraints, loading is generally improved by synthesizing high surface area electrode materials (e.g., three-dimensional gold nanoparticle assemblies, carbon black, and carbon nanotubes).[50-52] Multi-wall carbon nanotubes (CNT) have been used in this chapter as the electrode material because CNTs can be fashioned into a three-dimensional, conductive, porous matrix onto which laccase (or other redox biocatalysts) can be immobilized and achieve DET.[53]

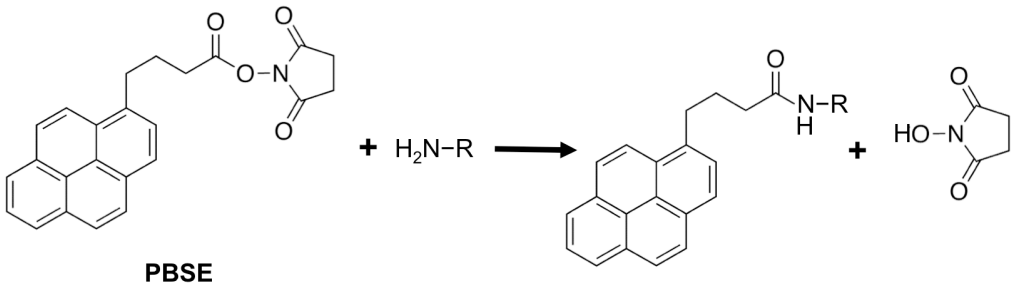

PBSE

Figure 5.2: A schematic representation of the reaction of 1-pyrenebutanoic acid, succinimidyl ester (PBSE) with the primary amines found in laccase (R) to form a covalent bond. PBSE is a heterobifunctional molecule that can strongly adsorb to the surface of a CNT through π-π stacking with the pyrene moiety.

Previous reports have utilized 1-pyrenebutanoic acid, succinimidyl ester (PBSE) to tether laccase to multi-wall CNTs.[52, 54, 55] PBSE is a heterobifunctional molecule that is capable of strong adsorption to the surface of a CNT through a π-π interaction between the CNT and the pyrene group.[56] Upon incubation of PBSE-modified electrodes with the protein, the succinimidyl ester moiety reacts with primary amines in the protein (i.e., lysine residues and the N-terminus) to form covalent amide bonds that link the laccase to

the CNT.[56] A schematic representation of the PBSE reaction with primary amines is shown in **Figure 5.2.** The PBSE-tethering strategy has been shown to significantly improve cathodic performance and facilitate DET from the electrode to the redox center of laccase.[52] These laccase/CNT biocomposites have been demonstrated as biofuel cell cathodes and long-term information relays.[42, 52]

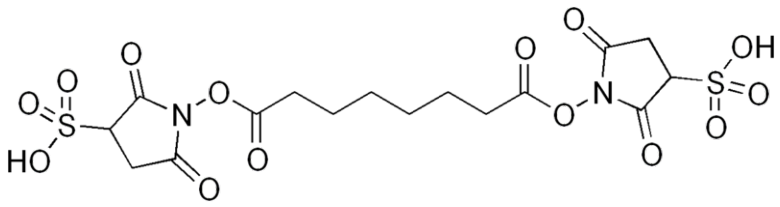

Figure 5.3: Chemical structure of the amine-reactive molecule bis(sulfosuccinimidyl) suberate (BS3) used to cross-link protamine to laccase.

In this work, a procedure is adapted from prior work that used α-amine reactive bis(sulfosuccinimidyl) suberate (BS3) to cross-link protamine to glucose oxidase.[57] The scheme utilized the dual functionality of polycationic protamine to immobilize (via electrostatics) and encapsulate the enzyme (via biomineralization of metal oxide by protamine) to enhance enzyme longevity. However, the protamine-enabled immobilization strategy has not been expanded to new enzymes (e.g., laccase) to investigate the effect of added peptide on biocatalysis of the ORR. BS3, is a homobifunctional cross-linking agent with succinimidyl ester groups on either end (**Figure 5.3**). These groups react predominantly with primary amines present in both protamine and laccase following the chemical reaction shown in **Figure 5.2**.

Highlighted in yellow in **Figure 5.1** are nine primary amines available for BS3 to cross-link protamine (eight lysine residues plus the N-terminus). These protamine/laccase

hybrid molecules were then immobilized onto CNT electrodes via the PBSE tethering reaction. A schematic illustration of the strategy is shown in **Figure 5.4**. This chapter demonstrates, for the first time, that the addition of protamine to the outer protein sphere of laccase enhanced both enzyme loading and electrocatalysis of the ORR. Other peptide sequences (RRRR, RRRTTR, and RRRTTRRRRAGRRRR (half protamine, HPA)) were linked to laccase via reaction with BS3 to provide insight into the mechanism of immobilization and the possible origins of electrocatalytic activity enhancement.

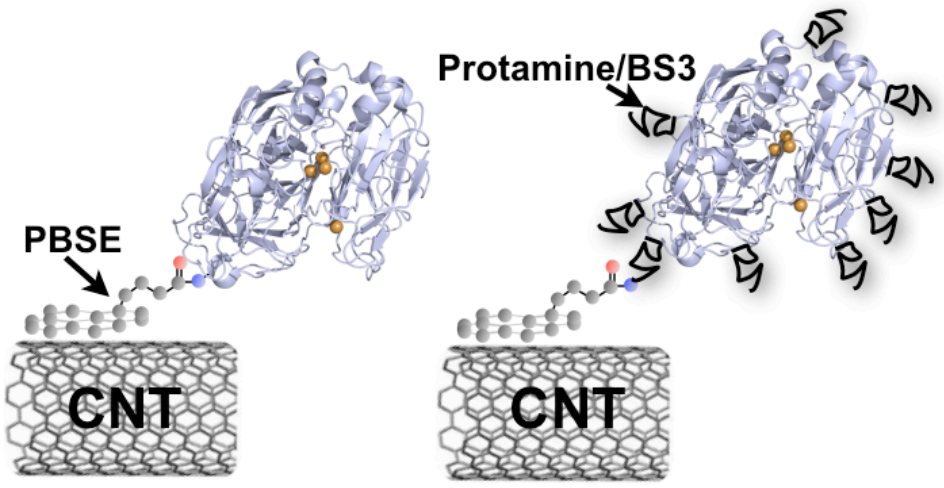

Figure 5.4: Schematic illustration of carbon nanotubes (CNT) functionalized by 1-pyrenebutanoic acid, succinimidyl ester (PBSE) with unmodified laccase (left), and protamine-modified laccase using bis(sulfosuccinimidyl) suberate (BS3) as the cross-linker (right) immobilized on the surface.

5.3 Experimental Procedure

In this section, the methods used to: (1) covalently bond protamine to fungal laccase (*Trametes versicolor*), (2) immobilize the enzymes to carbon nanotubes and (3)electrochemically characterize the resulting electrodes are discussed. All chemicals

electrochemically characterize the resulting electrodes are discussed. All chemicals used in this section were of the highest available purity.

5.3.1 Cross-linking of Laccase from *Trametes versicolor* with Protamine

Laccase derived from *Trametes versicolor* (Sigma Aldrich, St. Louis, MO, USA) and protamine sulfate (PA) (Grade X, Sigma Aldrich, St. Louis, MO, USA) were chemically cross-linked using the homobifunctional amine-reactive molecule bis(sulfosuccinimidyl) suberate (BS3, ThermoFischer, Rockford, IL, USA). To ensure laccase was cross-linked with protamine, and to reduce the formation of cross-linked laccase multimers, the reaction was performed using molar ratios of 20:1 protamine : laccase and 40:1 BS3 : laccase.

A typical cross-linking reaction was conducted as follows: laccase was prepared by dialyzing against 0.02 M potassium phosphate pH 5.8, then flash-frozen in liquid nitrogen, lyophilized for at least 24 h, and stored at -20 °C until used. Prepared laccase (1 mg, in a stock 1 mg mL^{-1} solution in 0.05 M sodium acetate (NaAc) at pH 5.1) and PA (1.5 mg, in a fresh stock 20 mg mL^{-1} solution in water) were mixed in a solution containing (4-(2-hydroxyethyl)-1-piperazineethanesulfonic acid (HEPES, pH 7.5, 0.01 M) and 0.12 M NaCl. BS3 (1 mg, in a 2 mg mL^{-1} solution in water) was added last, and the reaction solution was incubated for 1 hour at room temperature on a rotator mixer, followed by quenching with the addition of Tris-HCl pH 7.5 (1 M) to a final concentration of 0.1 M. The primary amine in Tris serves to passivate any unreacted BS3 still present in solution. The reaction solution was then dialyzed against three changes of NaAc (0.05 M, pH 5.1), flash-frozen in liquid nitrogen, lyophilized for at least 24 h,

diluted to a laccase concentration of 1 mg mL^{-1} in 0.05 M NaAc pH 5.1, and stored beside the native enzyme at 4 °C. The concentration of the cross-linked product, termed Lac-PA, was determined via biochemical activity assay. Note: the procedure described in Section 5.3.1 was developed and performed by Nick Haase (Georgia Institute of Technology, Atlanta, GA,USA).

5.3.2 Biochemical Activity Measurements

Laccase or Lac-PA was diluted to a concentration of 1 µg mL^{-1} in sodium acetate (0.05 M, pH 5.1) and used in aliquots of 1 – 10 µL. 2,2'-azino-bis(3-ethylbenzothiazoline-6-sulphonic acid, ABTS) was used at a concentration of 0.05 M. The assay was performed in a buffer of NaAc (0.05 M, pH 5.1). The assay solution was allowed to incubate for 20 minutes at room temperature, after which time the absorption of each sample at 418 nm was recorded. The procedure described in Section 4.3.2 was developed and performed by Nick Haase (Georgia Institute of Technology, Atlanta, GA, USA).[57]

5.3.3 Enzyme/Carbon Nanotube Composite Electrode Fabrication

Using a hole punch, electrodes were cut into 0.397 cm diameter discs (0.124 cm^2) from pressed sheets (27.6 ± 4 µm thick) of multi-wall carbon nanotubes commonly called "buckypaper" (CNT-BP) (JM-082611-01, Buckeye Composites, Kettering, OH, USA). For bare and physisorbed enzyme controls, the nanotube electrodes were placed in a watch glass and incubated in dimethyl sulfoxide (DMSO) (ThermoFisher, Rockford, IL, USA) for 1 h. Other electrodes were functionalized in a 0.01 M 1-pyrenebutanoic acid, succinimidyl ester (PBSE, Anaspec Inc., Fremont, CA, USA) in DMSO for 1 h. The

molecular structure of PBSE is shown in **Figure 5.4**. After incubation, the electrodes were placed on filter paper (185 mm, Grade 1, Whatman, Piscataway, NJ, USA) and repeatedly blotted until DMSO oil spots were no longer observed on the filter paper. Following the treatments shown in **Table 5.1**, all electrodes were incubated in 1 mL of NaAc (0.05 M, pH 5.1) solution for 1 h at 4°C, then rinsed in buffer and stored at 4 °C in 0.05 M NaAc buffer, pH 5.1. All synthetic peptides (RRRR, RRRTTR, and HPA) were of > 98% purity and supplied by Genscript USA, Inc. (Piscataway, NJ, USA).

Table 5.1. Collection of electrodes and enzyme immobilization solutions prepared.

Blank	0.05 M sodium acetate, pH 5.1
PBSE	0.05 M sodium acetate, pH 5.1
Laccase	0.2 mg/ml laccase in 0.05 M sodium acetate, pH 5.1
Lac-PA	0.2 mg/ml laccase/protamine in 0.05 M sodium acetate, pH 5.1
PBSE + Laccase	0.2 mg/ml laccase in 0.05 M sodium acetate, pH 5.1
PBSE + Lac-PA	0.2 mg/ml laccase/protamine in 0.05 M sodium acetate, pH 5.1
PBSE+Lac-RRRR	0.2 mg/ml laccase/RRRR in 0.05 M sodium acetate, pH 5.1
PBSE+Lac-RRRTTR	0.2 mg/ml laccase/RRRTTR in 0.05 M sodium acetate, pH 5.1
PBSE+Lac-HPA	0.2 mg/ml laccase/HPA in 0.05 M sodium acetate, pH 5.1

5.3.4 Electrochemical Characterization

CNT-BP electrodes were held in a capped glassy carbon shaft working electrode (CH Instruments Inc., Austin, TX, USA) and tested in a voltammetric cell (Ace Glass, Vineland, NJ, USA). To test a CNT-BP electrode, it was first removed from the storage

buffer and gently placed on the end of the glassy carbon electrode. A Teflon™ cap with a 0.5 cm^2 hole was placed over the CNT-BP, and the entire electrode assembly was immersed in 200 mL of 0.05 M NaAc, pH 5.1. A platinum counter electrode (MF-2013, BASi, Inc., West Lafayette, IN, USA) and a Ag/AgCl reference electrode (MF-2052, BASi, Inc., West Lafayette, IN, USA) were both immersed in the electrochemical cell solution. An image of the electrochemical cell used is shown in **Figure 5.5**. The cell was purged by continuous bubbling of either ultra-high purity (99.999%) oxygen or nitrogen (Airgas, Atlanta, GA, USA) for at least 20 mins to ensure the system reached equilibrium.[58]

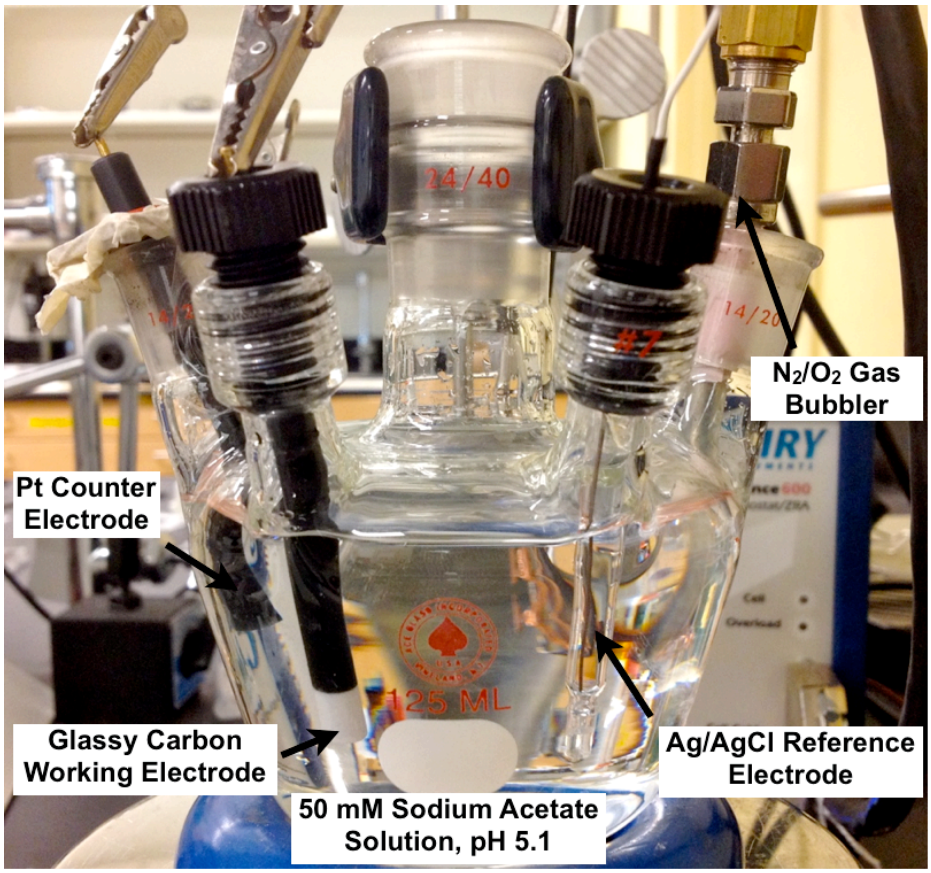

Figure 5.5: Image of the electrochemical cell used for testing in this chapter.

Electrochemical measurements were conducted using a potentiostat (Gamry Instruments Reference 600 Potentiostat/Galvanostat/ZRA, Warminster, PA, USA) and analyzed using the associated software (Gamry EChem Analyst Software, v. 5.65, Warminster, PA, USA). The open-circuit voltage of the electrode was then recorded every second for 20 mins. Cyclic voltammetry (CV) under nitrogen and oxygen bubbling was obtained by scanning a voltage range of 0.7 V to -0.1 V ten times at a rate of 10 mV s^{-1}, with measurements taken every second. Onset potentials were estimated from the first derivative of the CV curve during reduction sweep (from 0.8 V to -0.2 V) using two intersecting linear fits. A linear regression was used to fit the regions before and after the onset of the ORR. The lines were extrapolated, and the voltage at which the lines intersected provided an estimate of the onset voltage. An example of how onset voltage was estimated is shown in **Figure 5.6**.

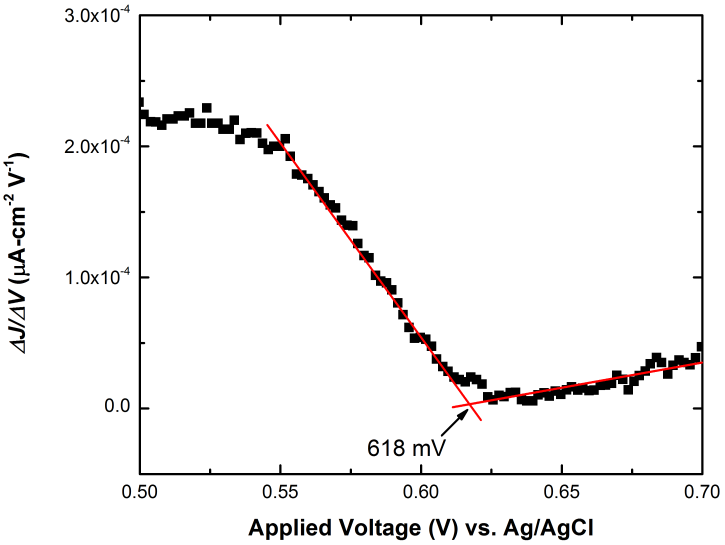

Figure 5.6: The first derivative of a cyclic voltammogram from 0.7 V to 0.5 V of a PBSE-treated Lac-PA electrode. A linear regression was used to fit the region before and after the onset of the ORR. The lines were extrapolated, and the voltage at which the lines intersected provided an estimate of the onset voltage.

Potentiostatic polarization measurements for each electrode were obtained in 0.05 M NaAc, pH 5.1 buffer under oxygen bubbling. An overvoltage was applied within the range of 0 and -0.7 V at intervals of 0.02 V. At each step, the current density was measured for 15 mins to allow enough time for the electrode to reach equilibrium. Tafel slopes were obtained from the plots of working electrode voltage versus current density without convective transport.

5.3.5 Immobilized Enzyme Lifetime Measurement

Using the electrochemistry setup discussed previously, the open-circuit voltage of PBSE-treated electrodes with either laccase or Lac-PA tethered to the surface were measured every 10 sec for 4 h under bubbling oxygen. A current density of 40 $\mu A\text{-}cm^{-2}$ was then applied for 4 h, and the resulting half-cell voltage was recorded every 10 sec. The electrode was cycled between unpolarized and polarized states a total of 20 times. The final 5 measurements of a 4 h measurement cycle were averaged, then normalized to the maximum overall value recorded during the 20 cycle test. Normalization was required to provide fair comparison between the two enzyme systems, given the difference in starting voltages. Note: when current was first applied, the measured voltage did not decrease more than 0.1 V, meaning that the electrodes were kept within the ohmic polarization regime and mass transport limitations did not significantly contribute to the results.

5.3.6 Materials Characterization

The micro/nanoscale morphologies of CNT-BP electrodes before and after enzyme immobilization were evaluated with scanning electron microscopy (1530 FEG

SEM, LEO/Zeiss Electron Microscopy, Thornwood, NY). X-ray photoelectron spectroscopy was conducted (Thermo K-alpha, ThermoFischer Scientific, Inc., Waltham, MA, USA) at a base pressure of $3x10^{-8}$ Pa using a monochromatic Al K_α source (1486.6 eV) with a spot size of 300 μm and pass energy of 50 eV. Step sizes of 0.5 eV were used with dwell times of 50 ms at each energy value. Zeta potential measurements (performed by Nick Haase) were conducted on native laccase and Lac-PA in solution using a dip cell on a Zetasizer NS instrument (Malvern Instruments, Malvern, Worcestershire, UK).

5.4 Results and Discussion

5.4.1 Investigation of the Electrocatalytic Activity of Protamine-Modified Laccase

The primary amine-reactive homobifunctional crosslinker BS3 was employed to link the α-amino group at the N-terminus of protamine to laccase at its N-terminus and the eight lysine residues that exist on each enzyme subunit. The cross-linking procedure was shown to be successful via zeta potential measurements. Native laccase, with an isoelectric point of 5.8, exhibited a zeta potential of -9.54 ± 0.94 mV at pH 7. Upon cross-linking of polycationic protamine to the enzyme, the modified laccase (Lac-PA) exhibited a less negative zeta potential of -3.65 ± 0.16 mV at pH 7, which indicated the influence of attached protamine moieties to the outer surface of the enzyme. Biochemical activity assays using 2,2'-azino-bis(3-ethylbenzothiazoline-6-sulphonic acid (ABTS) showed that Lac-PA retained greater than 90% of its enzymatic activity after cross-linking (**Figure 5.7**), demonstrating that the attached protamine molecules and the cross-linking process had minimal effect on biocatalytic activity.

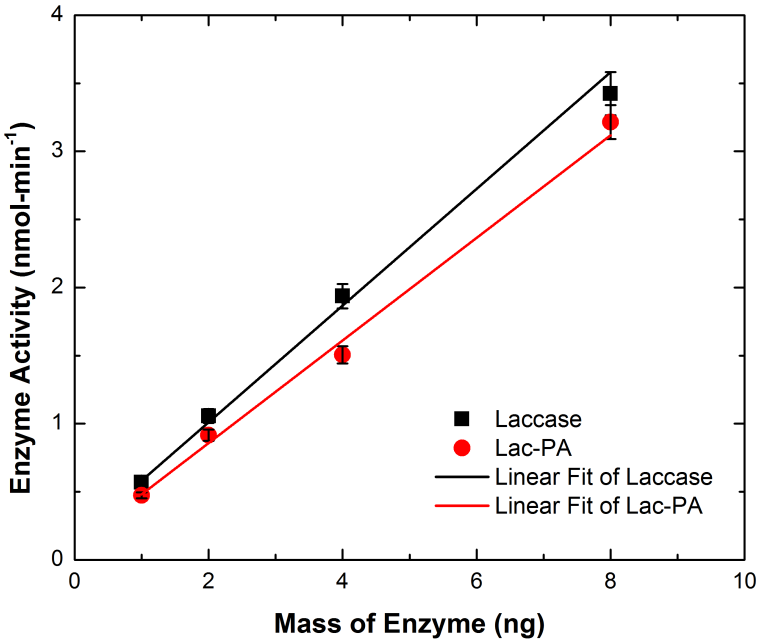

Figure 5.7: Relative activity plot of native laccase (■) compared to protamine-modified laccase (Lac-PA, ●) illustrating a retention of 90% of enzymatic activity after cross-linking. (Analyses conducted by N. Haase).

Both laccase and Lac-PA were subsequently immobilized onto highly-conductive (255 S-cm^{-1}) pressed multi-wall CNT-BP, which had been cut into 0.12 cm^2 discs. Low- and high-magnification secondary electron images of as-received CNT-BP (**Figure 5.8(a**, **b**)) revealed that the electrodes were comprised of a random network of carbon nanotubes with diameters ranging between approximately 20 and 300 nm. XPS was used to evaluate the surface elemental composition of the CNT-BP (**Figure 5.8(c)**), and all electrodes were found to be free of detectable surface contamination from Fe or Co catalysts used in CNT synthesis. The presence of oxygen in the XPS spectra likely stemmed from physisorbed oxygen and/or defect sites created during synthesis.[59]

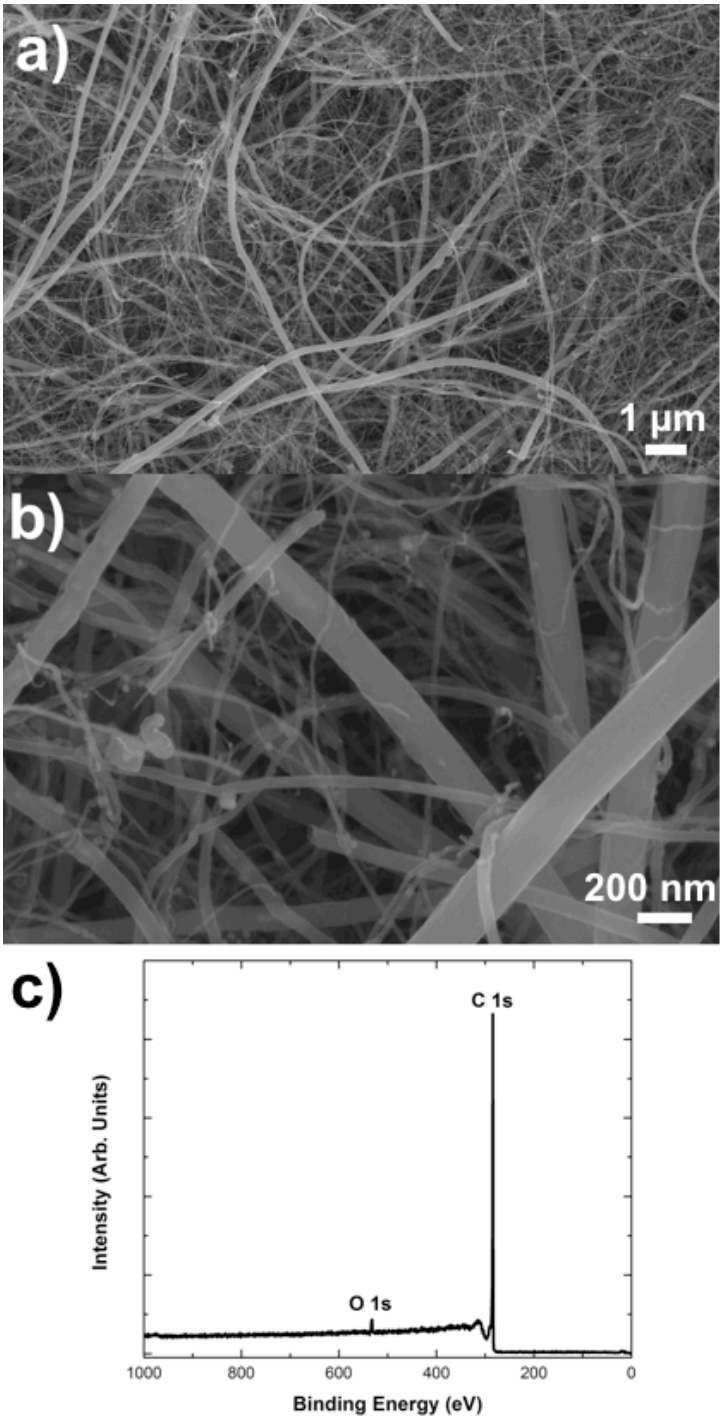

Figure 5.8: Secondary electron images of bare CNT-BP electrodes viewed at (a) low magnification and (b) high magnification indicating that the electrodes were comprised of a random network of carbon nanotubes with diameters ranging from approximately 20 to 300 nm. (c) XPS of CNT-BP electrodes indicating that the material was free of detectable catalyst (Fe or Co) contamination.

Prior to enzyme immobilization, the CNT-BP electrodes were incubated in PBSE, a heterobifunctional molecule with a pyreneyl moiety capable of both irreversibly adsorbing to CNT walls (through π-π stacking) and of immobilizing proteins predominantly by reaction of the N-hydroxysuccinimide (NHS) ester with primary amines. In addition to primary amines found on lysine and the N-termini of proteins, NHS esters have recently been shown to react with the hydroxyl groups of serine, threonine, or tyrosine in the presence of arginine or histidine.[60, 61] The use of PBSE enabled the immobilization redox enzymes, laccase and Lac-PA, onto the CNT-BP such that DET could occur from the CNT-BP to the active center of the enzyme.

After incubation with enzyme, the activity of the bound (electrode) and unbound (supernatant) enzyme was assayed relative to a control solution of either laccase or Lac-PA. The assay results are shown graphically in **Figure 5.9**; the mass of enzyme immobilized on CNT-BP electrodes is tabulated in **Table 5.2**. Covalent tethering of the enzyme via PBSE had no effect on the amount of enzyme immobilized or the relative activity in the case of native laccase. However, PBSE+Lac-PA electrodes showed a 13% increase in the amount of enzyme immobilized compared to PBSE+laccase, along with a 48% increase in biochemical activity compared to the same. Untreated CNT-BP electrodes revealed no significant difference (laccase vs. Lac-PA) in either the amount of physisorbed enzyme or relative activity of the immobilized enzyme. For both laccase and Lac-PA, physisorption onto CNT-BP led to a decrease in biochemical activity of ~60-70% compared to the free enzyme in solution, whereas PBSE+Lac-PA electrodes lost only ~18% of free enzyme activity. These results suggest that protamine is likely

interacting with the PBSE tether on the CNT-BP to yield a larger retention of the immobilized enzyme activity. The possible reasons as to why PBSE+Lac-PA electrodes showed a dramatic increase in relative biochemical activity compared to others will be discussed later, in tandem with the results of electrochemical characterization.

Table 5.2. The amount of enzyme immobilized on each CNT-BP electrode as determined by a biochemical assay of the unbound enzyme in the immobilization solution.(Analyses conducted by N. Haase)

Laccase	175 ± 5 µg
Lac-PA	161 ± 22 µg
PBSE + Laccase	169 ± 4 µg
PBSE + Lac-PA	191 ± 2 µg

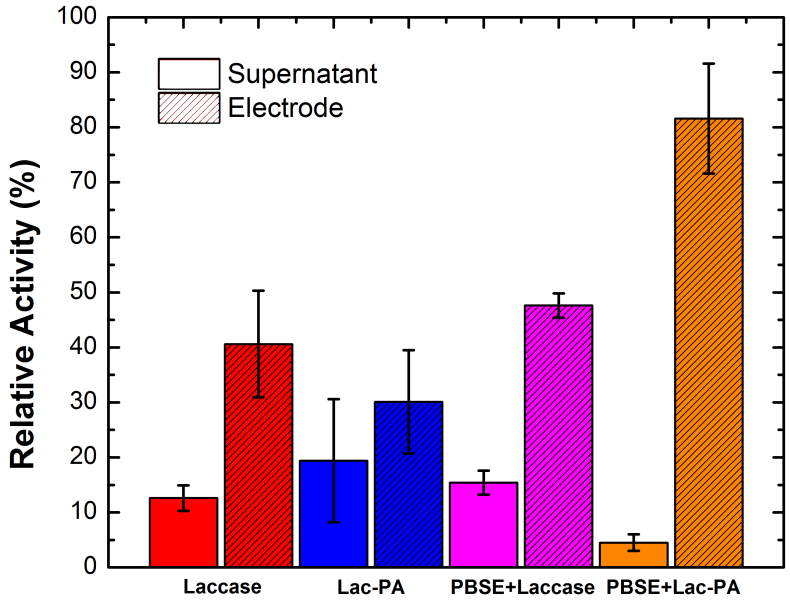

Figure 5.9: Biochemical assay measuring the relative activities of the incubation solution (supernatant) and the enzyme immobilized on CNT-BP (electrode) for PBSE-treated and untreated electrodes. (Analyses conducted by N. Haase)

The overall decrease in relative enzyme activity observed for all electrodes, relative to the free enzyme in solution, may be explained by the reduced accessibility of the substrate to the active site of the enzyme, as there is no apparent orientation specificity to the immobilization process, and/or to conformational rearrangements of laccase due to immobilization. The increase in enzyme loading on PBSE+Lac-PA electrodes is interesting in that protamine modification adds a significant mass to the outer shell of the enzyme (~36 kDa). Given that there are a limited number of available PBSE-sites on the CNT-BP onto which laccase or Lac-PA can covalently bind, the smaller unmodified laccase was expected to exhibit higher loading, which lends credence to the possibility of laccase dimers formed during cross-linking becoming immobilized on the CNT-BP surface (despite efforts taken to limit their formation).

Table 5.3. Open-circuit and estimated onset voltages for oxygen reduction measured for each electrode after saturating the solution with oxygen.[a]

Electrode	Open Circuit Voltage (mV)	Estimated Onset Voltage (mV)
Blank	199 ± 4.4	-
PBSE	211 ± 3.2	-
Laccase	624 ± 4.5	601 ± 5.3
Lac-PA	621 ± 6.3	618 ± 3.6
PBSE + Laccase	641 ± 6.3	607 ± 11
PBSE + Lac-PA	657 ± 3.4	627 ± 5.1

[a]The error reported corresponds to plus-minus one standard deviation from the mean.

Electrochemical testing was conducted to investigate the electrochemical activity, utility, and electrical connection between the enzyme and CNT-BP electrode. Blank and PBSE-treated CNT-BP electrodes in an oxygen atmosphere showed only capacitive currents, no Faradaic currents, and similar open-circuit voltages (OCV) of 199 ± 4.4 mV (n = 4) and 211 ± 3.2 mV (n = 3), respectively. The OCV of all CNT-BP electrodes are tabulated in **Table 5.3**. CNT-BP electrodes with physisorbed laccase and Lac-PA also had similar OCVs (624 ± 4.5, n = 4 and 621 mV ± 6.3 mV, n = 3, respectively), indicating that the protamine and BS3 cross-linker did not significantly impede direct transfer of electrons from the electrode to the active T1 Cu-site of the enzyme.

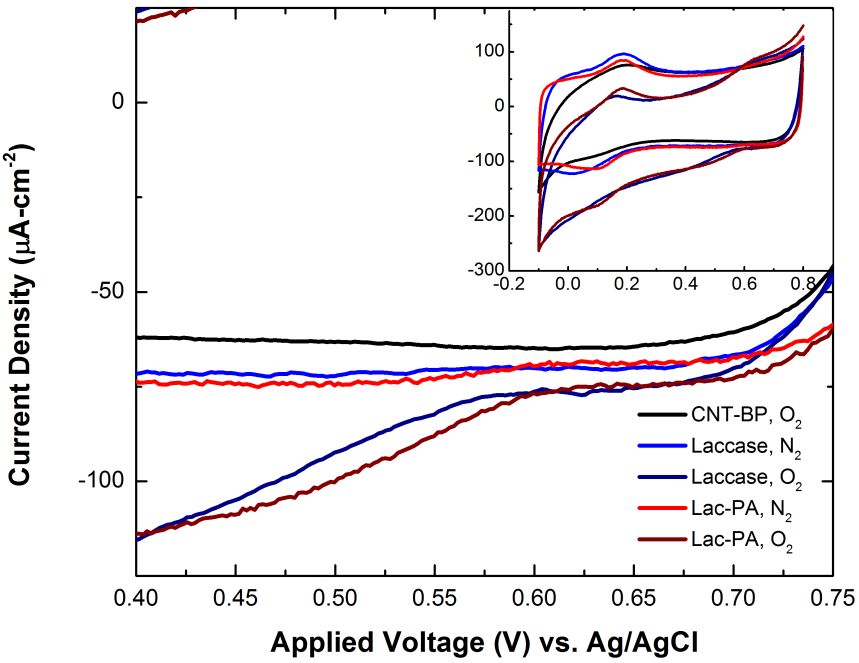

Figure 5.10: Cyclic voltammograms of CNT-BP with physisorbed enzyme (laccase and Lac-PA) in 0.05 M sodium acetate buffer purged with N_2 or O_2, pH 5.1 at a scan rate of 10 mV-s^{-1}. The onset of oxygen reduction is highlighted, and the full scan is shown in the inset.

Cyclic voltammetry (CV) sweeps of the physisorbed laccase and Lac-PA both showed an obvious deflection from the nitrogen-flushed and bare CNT-BP controls below 600 mV (**Figure 5.10**). From the onset voltages, (582 ± 4.2 mV; n = 4 and 606 ± 3.1 mV; n = 3, respectively) protamine reduced the voltage necessary for the ORR, even without the PBSE tether. Note: the reversible peaks observed at approximately 100 mV were present in all electrodes and considered a characteristic of the CNT-BP.

When laccase and Lac-PA were covalently bonded to the CNT-BP by PBSE, the electrocatalytic activity was improved in both electrodes compared to physisorbed enzyme, as evidenced by cyclic voltammograms in **Figure 5.11**. The cathodic sweeps of both electrodes in an oxygen flushed electrolyte show an obvious deflection compared to the blank CNT-BP electrode and enzyme-immobilized electrodes tested in a nitrogen-purged electrolyte. PBSE+laccase electrodes showed an OCP of 637 ± 3.8 mV; n = 5, and reduced oxygen at an onset voltage of 602 ± 9.3 mV; n = 5. The half-peak voltage was 479 ± 22 mV; n = 5 and oxygen reduction became mass transport limited at ~400 mV. These results were in good agreement with previous work using laccase tethered to PBSE-modified CNT-BP electrodes.[52, 54] PBSE+Lac-PA electrodes showed an increase in OCP to 657 mV ± 3.4; n = 5 with an onset voltage of 635 ± 4.8; n = 5, and half-peak voltage of 514 ± 15 mV; n = 5. The improvement in the onset voltage by approximately 20 mV is highlighted in **Figure 5.11 (inset)** and indicated that the addition of protamine to the outer shell of laccase was facilitating the oxygen reduction reaction due to any or all of the reasons mentioned previously. Again, the reversible peaks at approximately 75

mV that appeared in all voltammograms were attributed to the PBSE-treated CNT-BP electrode material.

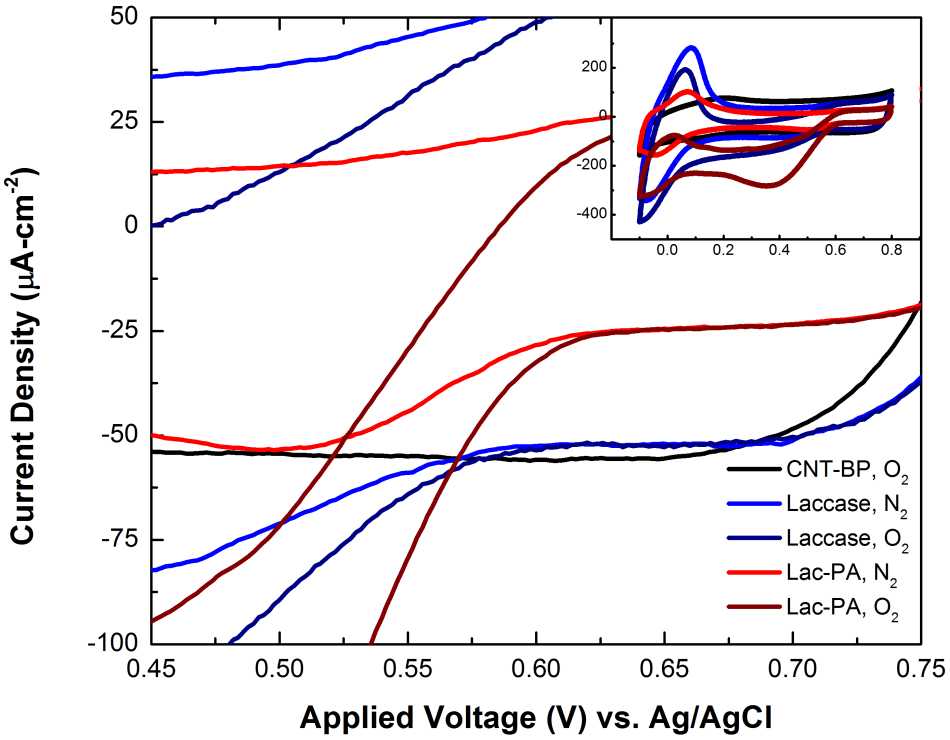

Figure 5.11: Cyclic voltammograms of PBSE-treated CNT electrodes with laccase and Lac-PA immobilized to the surface under N_2 and O_2 flow. The onset of oxygen reduction is highlighted, and the full scan is shown in the inset.

The electrocatalysts have been compared by examining the current density generated by the ORR at a given voltage, and the potentiostatic polarization curves of all electrodes under bubbling O_2 solution are shown in **Figure 5.12**. Bare and PBSE-treated CNT-BP controls showed minimal current densities (20 μA cm^{-2}) as expected. Physisorbed laccase and Lac-PA performed similarly, but also showed minimal current densities (55 μA-cm^{-2}) due to instability from the lack of strong bonding to the CNT-BP

surface. Once the enzyme was tethered to the CNT-BP electrode via PBSE, the performance significantly increased. PBSE+laccase electrodes demonstrated current densities in excess of 137 μA-cm^{-2}, which was similar to previous reports.[42, 54] PBSE +Lac-PA showed an almost two-fold improvement in maximum current density (271 μA-cm^{-2}).

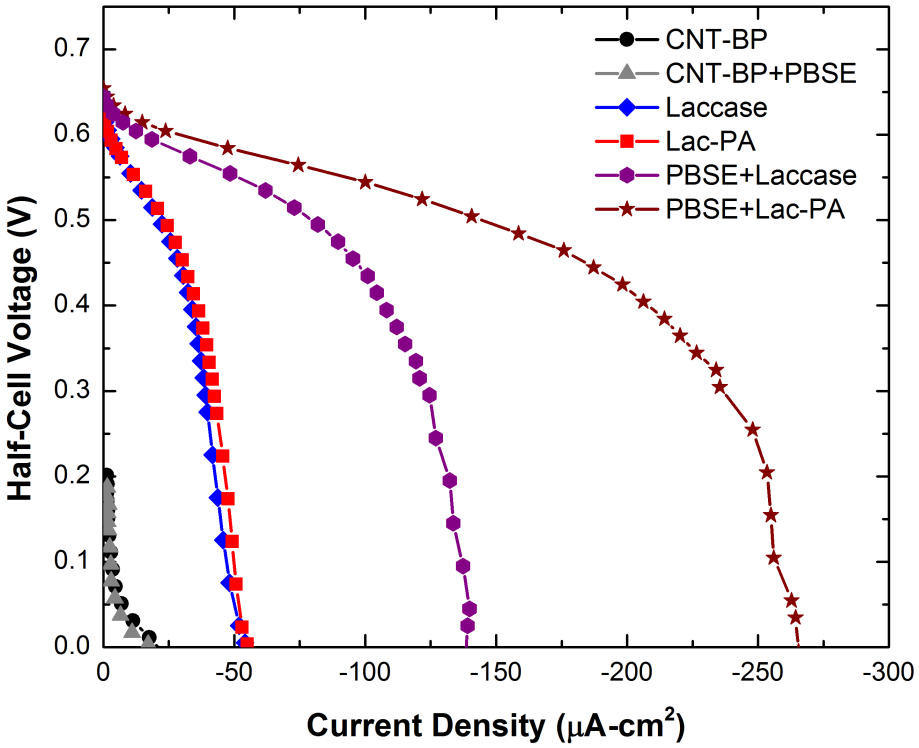

Figure 5.12: Potentiostatic polarization curves of CNT-BP (●), PBSE-treated CNT-BP (▲), physisorbed laccase (◆), physisorbed Lac-PA (■), laccase on PBSE-treated CNT-BP (⬢), and Lac-PA on PBSE-treated CNT-BP (★). Applied voltages less than zero are not shown.

The results of both biochemical and electrochemical characterization indicate that not only does protamine cross-linking improve the amount of laccase immobilized, but

the enzyme remains significantly more active on the electrode surface. With respect to biochemical activity, the increase in relative activity on the electrode surface (**Figure 5.9**) is larger than the difference in molar quantity of Lac-PA versus laccase immobilized on the CNT-BP (**Table 5.2**). This difference is also observed in the current density of PBSE +Lac-PA compared to PBSE+laccase (**Figure 5.12**), indicating the possibility of a secondary benefit to protamine cross-linking.

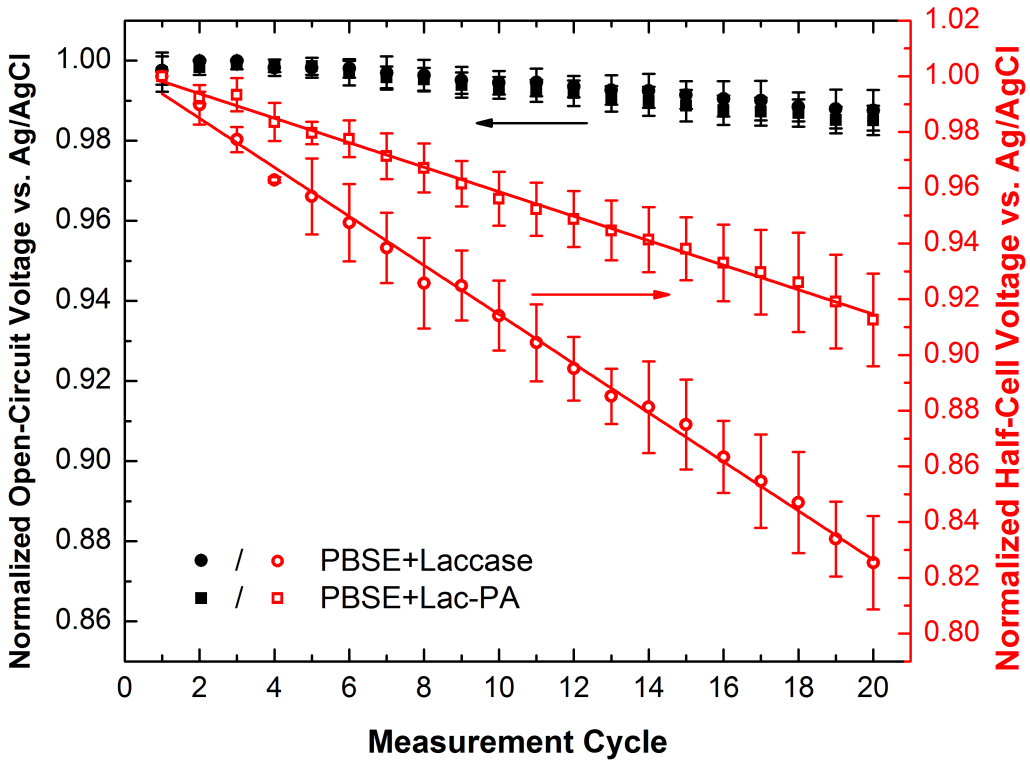

Figure 5.13: The degradation of the open-circuit (● and ■) and half-cell voltages (○ and □) of PBSE+laccase and PBSE+Lac-PA electrodes over the course of 20 unpolarized/ polarized cycles. Each cycle consisted of a 4 h open-circuit voltage measurement followed by a 4 h galvanostatic polarization at 40 μA-cm^{-2} at room temperature and bubbling O_2.

The lifetimes of PBSE+laccase (n = 3) and PBSE+Lac-PA (n = 2) electrodes under repeated galvanostatic polarizations were investigated to determine if protamine modification of laccase provided additional practical benefits when immobilized onto CNT-BP (**Figure 5.13**). After 20 galvanostatic polarizations lasting 4 h each, PBSE +laccase electrodes retained 82.5 ± 1.7% of the maximum half-cell voltage while PBSE +Lac-PA electrodes preserved 90.8 ± 2.0% of the maximum half-cell voltage. The normalized half-cell voltage decreased at rates of 0.88 ± 0.01% per cycle and 0.44 ± 0.01% per cycle for PBSE+laccase and PBSE+Lac-PA, respectively. The open-circuit voltages of the PBSE-treated laccase and Lac-PA electrodes did not decrease by more than 3% during testing indicating that the T1 copper center likely remained intact, and the thermodynamic driving force for the ORR remained essentially the same during testing. However, the decrease in half-cell voltage was indicative either enzyme reorganization, desorption, or denaturation. From the lifetime measurements, protamine modification appeared to cause a reduction in the detrimental effects of repeated galvanostatic polarizations, which is beneficial for practical applications.

The improved catalytic activity observed in PBSE-tethered Lac-PA may be the result of multiple factors. Cross-linking may cause a preferred orientation of the T1-site to the CNT surface upon adsorption. Alternatively, cross-linked protamine may accommodate some of the conformational changes necessary for the enzyme to bind to the electrode surface when tethered by PBSE. As a result, the active site would retain a more natural conformation versus unmodified laccase. This behavior could affect both the substrate access to the enzyme active site, as well as the intra-enzyme electron

transfer between the Cu sites. Laccase multimers randomly synthesized during cross-linking may also be tethered to the CNT-BP surface along with monomer Lac-PA, leading to improved catalysis. Elucidating the mechanisms primarily responsible for the improved electrocatalysis in PBSE-tethered Lac-PA electrodes is the subject of continuing research.

5.4.2 Evaluation of the Effects of the Cross-Linked Peptide Primary Structure

The succinimidyl ester moieties of both PBSE and BS3 are often described as being exclusively reactive to nucleophilic substitution by primary amines to form amide linkages.[62] This formed the chemical foundation for laccase immobilization onto PBSE-modifed CNT-BP. When the CNT-BP electrodes were immersed in a solution containing laccase, the succinimidyl ester reacted with primary amines found at lysine residues and the N-terminus of the protein. Protamine modification utilizes the same succinimdyl ester chemistry and therefore, Lac-PA likely had little or no primary amines available for PBSE tethering. Mädler, *et al.* studied the cross-linking reactions of commercial and model peptides with NHS esters and found that while primary amines were the first reaction site, when those sites were unavailable, other amino acids (such as serine, threonine, and tyrosine showed significant reactivity).[60] The activity was shown to be related to the neighboring amino acids, namely histidine and arginine. It has been hypothesized that when arginine residues neighbor serine, threonine, or tyrosine, transient hydrogen bonds form between the guanidinium group and carbonyl oxygens which serve to catalyze the nucleophilic substitution.[61] Protamine contains two regions where serine and threonine neighbor arginine on either side

(ARRR**RSSSR**PIRRRRPRR**RTTR**RRRAGRRRR). These regions are therefore identified as potential binding moieties with PBSE on the CNT-BP.

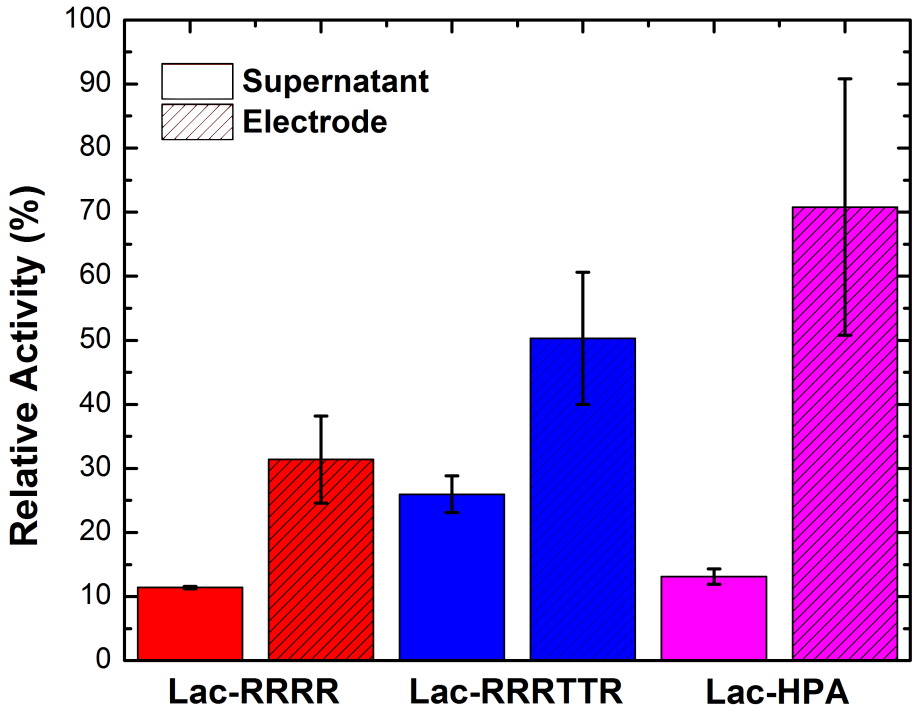

Figure 5.14: Biochemical assay measuring the relative activities of the incubation solution (supernatant) and the enzyme immobilized on CNT-BP (electrode) for PBSE-treated electrodes incubated in Lac-RRRR-, Lac-RRRTTR-, and Lac-HPA-containing solutions. (Analyses conducted by N. Haase)

To provide some insight into the cause of the improved electrocatalysis exhibited by PBSE+Lac-PA, laccase was cross-linked, using the same procedure, to a 4 amino acid peptide of polyarginine (Arg-Arg-Arg-Arg, Lac-RRRR), a 6 amino acid peptide (Arg-Arg-Arg-Thr-Thr-Arg, Lac-RRRTTR, and a 15 amino acid peptide approximately half the size of protamine (RRRTTRRRRAGRRRR, Lac-HPA). The purpose of testing PBSE

+Lac-RRRR was to determine if serine and/or threonine were responsible for Lac-PA immobilization onto PBSE-treated CNT-BP, or if the improvement in electrochemical activity was somehow due to the enzyme cross-linking process itself. By cross-linking a polyarginine peptide to laccase via BS3, all of the primary amine groups in laccase were likely reacted, just as in Lac-PA. However, in this case there are no threonine or serine residues in the peptide to aid in tethering the enzyme to the PBSE-treated CNT-BP, so the tethering of Lac-RRRR to the CNT-BP required binding directly with the enzyme. Specifically, binding could only occur at one of 28 potential sites according to the amino acid sequence of the enzyme (i.e., locations on the enzyme where serine, threonine, or tyrosine neighbor histidine or arginine).[33]

Table 5.4. The amount of enzyme immobilized on each CNT-BP electrode determined by a biochemical assay of the unbound enzyme in the immobilization solution.[a](Analyses conducted by N. Haase)

Electrode	Mass Adsorbed (µg)
PBSE + Lac-RRRR	177 ± 1.4
PBSE+Lac-RRRTTR	148 ± 5.7
PBSE+Lac-HPA	174 ± 2.4

[a]The error reported corresponds to plus-minus one standard deviation from the mean.

Biochemical assays were to determine the amount of enzyme immobilized onto the CNT-BP as well as the relative activity of the enzyme on the electrode surface (**Figure 5.14**). Biochemical assays revealed that Lac-RRRR and Lac-HPA were capable

of binding well to PBSE-modified CNT-BP, while PBSE+Lac-RRRTTR displayed a reduction in adsorbed enzyme. Because both HPA and RRRTTR contain potential catalytic sites (i.e., threonine/arginine) and Lac-RRRR contains no such potential PBSE-binding sites, the reason for improved enzyme loading in Lac-PA is still unclear. However, the relative activity of peptide cross-linked laccase immobilized onto the PBSE-treated CNT-BP showed a slight trend upward as the length of the cross-linked peptide increased (RRRR to HPA), potentially indicating that the increased molecular mass may inhibit activity loss due to the enzyme changing conformation during immobilization.

Table 5.5. Open-circuit and onset voltages for oxygen reduction measured for each electrode after saturating the solution with oxygen.[a]

Electrode	Open Circuit Voltage (mV)	Onset Voltage (mV)
PBSE + Lac-RRRR	630 ± 0.4	598 ± 6.4
PBSE+Lac-RRRTTR	649 ± 5.9	612 ± 7.2
PBSE+Lac-HPA	646 ± 3.7	623 ± 4.8

[a]The error reported corresponded to plus-minus one standard deviation from the mean.

As shown in **Table 5.5**, PBSE+Lac-RRRR electrodes displayed open-circuit voltages (630 ± 0.4 mV, n = 3) slightly greater than physisorbed enzyme on CNT-BP, but less than both PBSE+Laccase and PBSE+Lac-PA, which indicated that PBSE was still capable of tethering the enzyme despite a minimal number of available primary amines.

Binding likely occurs at one of the other 28 potential secondary binding sites on the enzyme. The onset voltage of oxygen reduction (598 ± 6.4 mV, n = 3) was similar to PBSE+laccase and less than PBSE+Lac-PA according to cyclic voltammograms shown in **Figure 5.15**. Note: the reversible peaks observed at approximately 75 mV are characteristic of PBSE-treated CNT-BP and typically observed in blank electrodes.

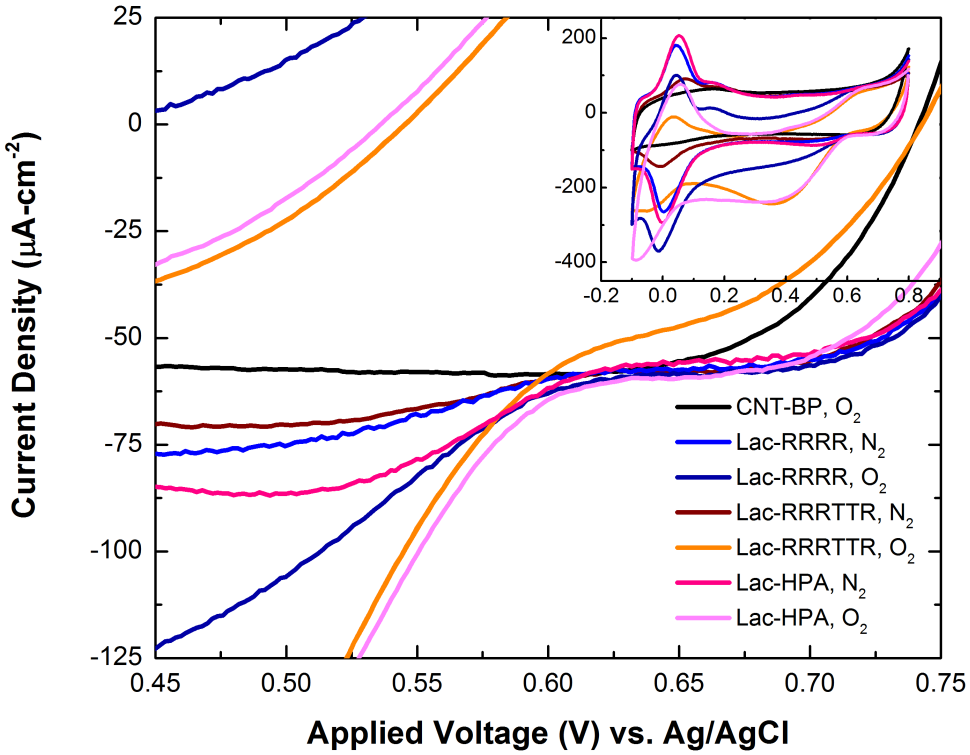

Figure 5.15: Cyclic voltammograms of PBSE-treated CNT-BP electrodes with and without Lac-RRRR, Lac-RRRTTR, or Lac-HPA immobilized to the surface under N_2 and O_2 bubbling. The onset of oxygen reduction is highlighted, and the full scan is shown in the inset.

To demonstrate further the role of both threonine in Lac-PA binding to PBSE-treated CNT-BP as well as peptide chain length, either peptides RRRTTR or

RRRTTRRRRAGRRRR was cross-linked to laccase via BS3 (Lac-RRRTTR and Lac-HPA). RRRTTR is a sub-section of protamine with a similar percentage of arginine content (67% for RRRTTR compared to 65% for protamine) and a molar mass of 845 Da (compared to 4.1 kDa for protamine). RRRTTRRRRAGRRRR is comprised of the final 15 amino acids that constitute protamine (73% arginine and 2.1 kDa). After immobilization onto PBSE-treated CNT-BP, the open-circuit voltages of Lac-RRRTTR and Lac-HPA-based electrodes were 649 ± 5.9 mV (n = 3) and 646 ± 3.7 mV (n = 3), respectively. These values were between Lac-RRRR (630 ± 0.4 mV) and Lac-PA (657 ± 3.4 mV) tethered to PBSE-treated CNT-BP. Cyclic voltammograms of PBSE+Lac-RRRTTR and PBSE+Lac-HPA are shown in **Figure 5.14,** and the estimated onset voltages of the electrodes were 612 ± 7.2 mV (n = 3) and 623 ± 4.8 mV (n = 3), respectively. The estimated onset voltages of PBSE+Lac-RRRTTR and Lac-HPA electrodes were statistically similar and fell between the estimated onset voltages of PBSE+Laccase (602 ± 9.3 mV) and PBSE+Lac-PA (635 ± 4.8 mV). Note: the reversible peaks observed in the CV curves at approximately 75 mV are characteristic of PBSE-treated CNT-BP and typically observed in blank electrodes.

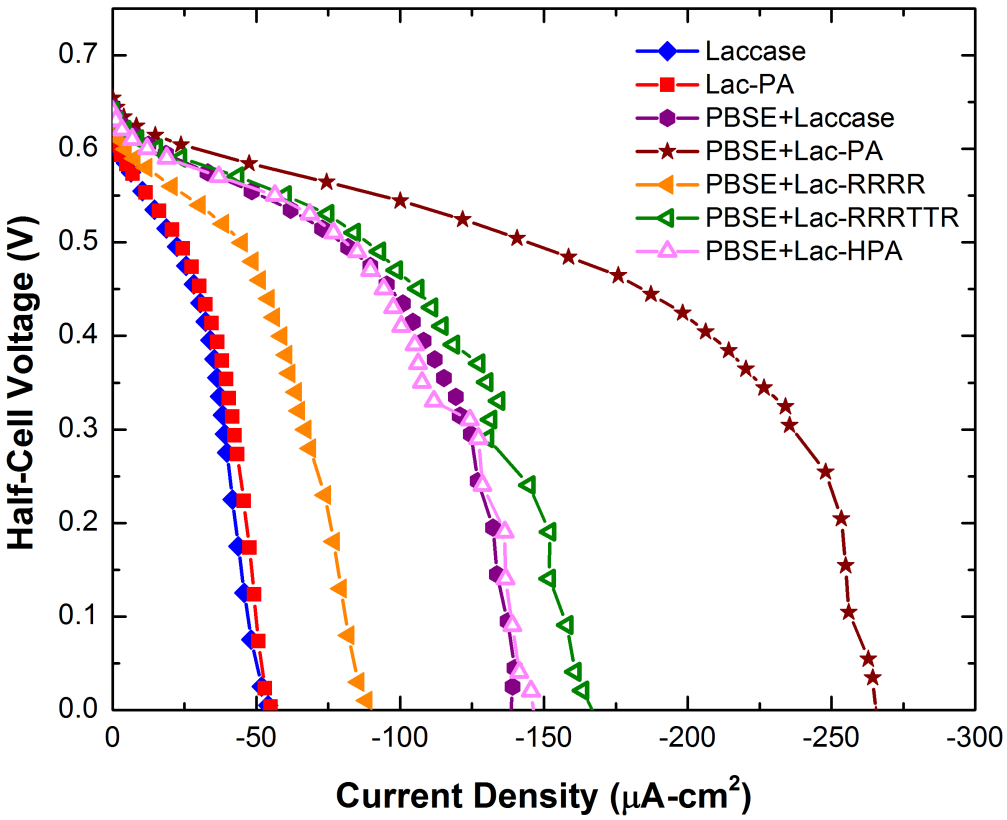

Figure 5.16: Potentiostatic polarization curves of laccase (⬣), Lac-PA (★), Lac-RRRR (◀), Lac-RRRTTR (◁), and Lac-HPA (△) on PBSE-treated CNT-BP. Applied voltages less than zero are not shown.

The aerobic potentiostatic polarization curves of Lac-RRRR, Lac-RRRTTR, and Lac-HPA immobilized on PBSE-treated CNT-BP electrodes are shown in **Figure 5.16**. PBSE+Lac-RRRR electrodes displayed a maximum current density of 88 μA cm^{-2}, which was a 38% decrease compared to PBSE+Laccase electrodes and 38% larger than physisorbed laccase immobilized on CNT-BP (**Figure 5.12**). The improvement PBSE +Lac-RRRR displayed compared to physisorbed laccase electrodes indicated that serine and threonine residues were critical to the effective tethering of laccase to CNT-BP via reaction with PBSE. The potentiostatic polarization curves for PBSE+Lac-RRRTTR and

Lac-HPA electrodes showed maximum current densities of 169 μA cm^{-2} and 147 μA cm^{-2}, respectively, which also supported the need for threonine residues in the cross-linked peptide because the maximum current density was almost twofold greater than the observed values for PBSE+Lac-RRRR electrodes. Furthermore, the smaller peptide chain length in PBSE+Lac-RRRTTR and PBSE+Lac-HPA electrodes reduced the observed maximum current density compared to PBSE+Lac-PA electrodes by ~40% in both cases. The reduced current density exhibited by PBSE+Lac-RRRTTR and Lac-HPA compared to PBSE+Lac-PA electrodes may be due to either less enzyme immobilized on the electrode surface (due to the lack of a second active binding group on the peptide) and/or that the short 6/15 amino acid peptides may not be large enough to accommodate the conformational change induced by immobilization onto the CNT-BP surface. As a whole, these results suggested that the improvement in biocatalysis of the ORR exhibited by PBSE+Lac-PA-bearing electrodes was likely enabled by the fortuitous primary structure and molecular weight of protamine.

5.5 Summary and Outlook

In this work, modification of the outer protein shell of laccase (from *Trametes versicolor*) by cross-linking to protamine was shown to be beneficial to bioelectrocatalysis of the ORR on CNT-BP electrodes. This method expands upon previous work where laccase was tethered directly to CNT-BP via the heterobifunctional molecule PBSE by chemically cross-linking protamine to 9 primary amine sites on the enzyme. PBSE+Lac-PA electrodes displayed an increase in the amount of enzyme

immobilized and retained more activity after immobilization CNT-BP compared to PBSE +laccase-bearing electrodes. Biochemical assays of the immobilized enzyme showed a 12% increase in enzyme loading and a 48% increase in relative activity. Moreover, the added protein (~36 kDa), that at first-glance may be considered to be detrimental to achieving direct transfer of electrons from the electrode to the enzyme, appeared to enhance electrochemical activity. PBSE-treated Lac-PA electrodes exhibited a 33 mV increase in onset voltage and an almost twofold increase in maximum current density (137 $\mu A\ cm^{-2}$ to 271 $\mu A\ cm^{-2}$) when compared to PBSE-treated laccase electrodes.

To further elucidate a cause for the improved current density, three synthetic peptides (Arg-Arg-Arg-Arg, Arg-Arg-Arg-Thr-Thr-Arg, and HPA) were each cross-linked to laccase following the same procedure as for protamine. When the four arginine peptide was cross-linked to laccase (Lac-RRRR), the resulting electrochemical testing showed a sharp decrease in maximum current density that was below even the unmodified enzyme (85 $\mu A\ cm^{-2}$ to 137 $\mu A\ cm^{-2}$). The purpose of testing PBSE+Lac-RRRR was to determine if serine and/or threonine were responsible for Lac-PA immobilization onto PBSE-treated CNT-BP, or if the improvement in electrochemical activity was somehow due to the enzyme cross-linking process itself. The severe reduction in electrochemical performance supported the claim that arginine alone could not effectively tether Lac-PA to the PBSE-modified CNT-BP. When threonine-containing peptides were cross-linked to laccase (Lac-RRRTTR), the maximum current measured by potentiostatic polarization increased by almost twofold compared to Lac-RRRR which lent further support to the hypothesis that threonine residues were critical to Lac-PA

tethering to PBSE-treated CNT-BP. Moreover, RRRTTR is a subsection of the protamine with a similar percentage of arginine content (67% for RRRTTR compared to 65% for protamine) and a molar mass of 845 Da (compared to 4.1 kDa for protamine). The reduced current density exhibited by PBSE+Lac-RRRTTR compared to the PBSE+Lac-PA may be due to either less enzyme immobilized on the electrode surface (due to the lack of a second active binding group on RRRTTR) or the short 6 amino acid peptide may not be large enough to accommodate the conformational change induced by immobilization onto the CNT-BP surface. As a whole, these results illustrate the improvement in ORR uniquely exhibited by PBSE+Lac-PA electrodes was likely enabled by the fortuitous primary structure and molecular weight protamine.

This work outlines a new strategy for enzyme tethering to PBSE-treated CNT-BP electrodes where protamine was added to the protein shell of the enzyme. The protamine-laccase conjugates demonstrated enhanced enzyme loading and electrochemical activity compared to unmodified laccase. Protamine cross-linking could be extended to other redox enzymes useful for biofuel cell anodes that also contain primary amines for BS3 conjugation (e.g., alcohol dehydrogenase, methanol dehydrogenase, or glycerol dehydrogenase). The extension to other enzymes could demonstrate the broad utility of this method and allow for construction of a complete biofuel cell based on this immobilization paradigm.

5.6 References

1. J. D. Berrigan, T. S. Kang, Y. Cai, J. R. Deneault, M. F. Durstock and K. H. Sandhage, *Advanced Functional Materials*, 2011, **21**, 1693-1700.

2. M. Seter, B. Hinton and M. Forsyth, *Journal of the Electrochemical Society*, 2012, **159**, C181-C189.

3. R. Touir, N. Dkhireche, M. Ebn Touhami, M. Sfaira, O. Senhaji, J. J. Robin, B. Boutevin and M. Cherkaoui, *Materials Chemistry and Physics*, 2010, **122**, 1-9.

4. F. H. Garzon, R. Mukundan and E. L. Brosha, *Solid State Ionics*, 2000, **136–137**, 633-638.

5. G. W. McLaughlin, K. Braden, B. Franc and G. T. A. Kovacs, *Sensors and Actuators B*, 2002, **83**, 138-148.

6. Y. Wang and H. Zhou, *Chemical Communications*, 2010, **46**, 6305-6307.

7. A. Débart, J. Bao, G. Armstrong and P. G. Bruce, *Journal of Power Sources*, 2007, **174**, 1177-1182.

8. N. R. Elezović, B. M. Babić, L. Gajić-Krstajić, V. Radmilović, N. V. Krstajić and L. J. Vračar, *Journal of Power Sources*, 2010, **195**, 3961-3968.

9. F. Jaouen, S. Marcotte, J.-P. Dodelet and G. Lindbergh, *The Journal of Physical Chemistry B*, 2003, **107**, 1376-1386.

10. L. Qu, Y. Liu, J.-B. Baek and L. Dai, *ACS Nano*, 2010, **4**, 1321-1326.

11. Y. Bing, H. Liu, L. Zhang, D. Ghosh and J. Zhang, *Chemical Society Reviews*, 2010, **39**, 2184-2202.

12. W. Vielstich, A. Lamm, H. A. Gasteiger and H. Yokokawa, *Handbook of Fuel Cells: Fundamentals, Technology and Applications*, Wiley, Chichester, England, 2003.

13. A. A. Gewirth and M. S. Thorum, *Inorganic Chemistry*, 2010, **49**, 3557-3566.

14. E. Gileadi, *Electrode Kinetics for Chemists, Chemical Engineers, and Materials Scientists*, VCH Publishers, Inc., New York, NY, USA, 1993.

15. H. A. Gasteiger, J. E. Panels and S. G. Yan, *Journal of Power Sources*, 2004, **127**, 162-171.

16. T. D. H. Bugg, *Introduction to Enzyme and Coenzyme Chemistry*, Blackwell Science, Ltd., Malden, MA, USA, 1997.

17. L. Quintanar, C. Stoj, A. B. Taylor, P. J. Hart, D. J. Kosman and E. I. Solomon, *Accounts of Chemical Research*, 2007, **40**, 445-452.

18. E. I. Solomon, U. M. Sundaram and T. E. Machonkin, *Chemical Reviews*, 1996, **96**, 2563-2605.

19. N. Mano, V. Soukharev and A. Heller, *The Journal of Physical Chemistry B*, 2006, **110**, 11180-11187.

20. N. Mano, J. L. Fernandez, Y. Kim, W. Shin, A. J. Bard and A. Heller, *Journal of the American Chemical Society*, 2003, **125**, 15290-15291.

21. G. Gupta, V. Rajendran and P. Atanassov, *Electroanalysis*, 2004, **16**, 1182-1185.

22. W. E. Farneth, B. A. Diner, T. D. Gierke and M. B. D'Amore, *Journal of Electroanalytical Chemistry*, 2005, **581**, 190-196.

23. K. Stolarczyk, E. Nazaruk, J. Rogalski and R. Bilewicz, *Electrochimica Acta*, 2008, **53**, 3983-3990.

24. M. S. Thorum, J. Yadav and A. A. Gewirth, *Angewandte Chemie International Edition*, 2009, **48**, 165-167.

25. M. S. Thorum, C. A. Anderson, J. J. Hatch, A. S. Campbell, N. M. Marshall, S. C. Zimmerman, Y. Lu and A. A. Gewirth, *The Journal of Physical Chemistry Letters*, 2010, **1**, 2251-2254.

26. K. Kataoka, S. Hirota, Y. Maeda, H. Kogi, N. Shinohara, M. Sekimoto and T. Sakurai, *Biochemistry*, 2010, **50**, 558-565.

27. G. Hong, D. M. Ivnitski, G. R. Johnson, P. Atanassov and R. Pachter, *Journal of the American Chemical Society*, 2011, **133**, 4802-4809.

28. H. Qiu, C. Xu, X. Huang, Y. Ding, Y. Qu and P. Gao, *The Journal of Physical Chemistry C*, 2009, **113**, 2521-2525.

29. R. Malkin and B. G. Malmström, *Advances in Enzymology and Related Areas of Molecular Biology*, 1970, **33**, 177-244.

30. H. B. Gray, B. G. Malmström and R. J. P. Williams, *Journal of Biological Inorganic Chemistry*, 2000, **5**, 551-559.

31. E. I. Solomon, A. J. Augustine and J. Yoon, *Dalton Transactions*, 2008, 3921-3932.

32. T. Sakurai and K. Kataoka, *The Chemical Record*, 2007, **7**, 220-229.

33. K. Piontek, M. Antorini and T. Choinowski, *Journal of Biological Chemistry*, 2002, **277**, 37663-37669.

34. P. Giardina, V. Faraco, C. Pezzella, A. Piscitelli, S. Vanhulle and G. Sannia, *Cellular and Molecular Life Sciences*, 2010, **67**, 369-385.

35. E. I. Solomon, J. W. Hare and H. B. Gray, *Proceedings of the National Academy of Sciences*, 1976, **73**, 1389-1393.

36. J. W. Gallaway and S. A. Calabrese Barton, *Journal of the American Chemical Society*, 2008, **130**, 8527-8536.

37. I. R. Wheeldon, J. W. Gallaway, S. C. Barton and S. Banta, *Proceedings of the National Academy of Sciences*, 2008, **105**, 15275-15280.

38. S. C. Barton, H. H. Kim, G. Binyamin, Y. C. Zhang and A. Heller, *Journal of the American Chemical Society*, 2001, **123**, 5802-5803.

39. J. Gallaway, I. Wheeldon, R. Rincon, P. Atanassov, S. Banta and S. C. Barton, *Biosensors and Bioelectronics*, 2008, **23**, 1229-1235.

40. S. C. Barton, *Electrochimica Acta*, 2005, **50**, 2145-2153.

41. C. F. Blanford, C. E. Foster, R. S. Heath and F. A. Armstrong, *Faraday Discussions*, 2009, **140**, 319-335.

42. G. Strack, H. R. Luckarift, R. Nichols, K. Cozart, E. Katz and G. R. Johnson, *Chemical Communications*, 2011, **47**, 7662-7664.

43. F. A. Armstrong, H. A. O. Hill and N. J. Walton, *Quarterly Reviews of Biophysics*, 1985, **18**, 261-322.

44. S. Shleev, J. Tkac, A. Christenson, T. Ruzgas, A. I. Yaropolov, J. W. Whittaker and L. Gorton, *Biosensors and Bioelectronics*, 2005, **20**, 2517-2554.

45. O. Schaetzle, F. Barriere and U. Schroder, *Energy & Environmental Science*, 2009, **2**, 96-99.

46. M. Mazur, A. Krywko-Cendrowska, P. Krysiński and J. Rogalski, *Synthetic Metals*, 2009, **159**, 1731-1738.

47. H. R. Luckarift, D. Ivnitski, R. Rincón, P. Atanassov and G. R. Johnson, *Electroanalysis*, 2010, **22**, 784-792.

48. L. M. Ellerby, C. R. Nishida, F. Nishida, S. A. Yamanaka, B. Dunn, J. S. Valentine and J. I. Zink, *Science*, 1992, **255**, 1113-1115.

49. D. Ivnitski, K. Artyushkova, R. A. Rincón, P. Atanassov, H. R. Luckarift and G. R. Johnson, *Small*, 2008, **4**, 357-364.

50. K. Murata, K. Kajiya, N. Nakamura and H. Ohno, *Energy & Environmental Science*, 2009, **2**, 1280-1285.

51. T. Tamaki, T. Ito and T. Yamaguchi, *The Journal of Physical Chemistry B*, 2007, **111**, 10312-10319.

52. R. P. Ramasamy, H. R. Luckarift, D. M. Ivnitski, P. B. Atanassov and G. R. Johnson, *Chemical Communications*, 2010, **46**, 6045-6047.

53. P. F. Harris, *Carbon Nanotube Science*, Cambridge Publishers, Cambridge, UK, 2009.

54. N. S. Parimi, Y. Umasankar, P. Atanassov and R. P. Ramasamy, *ACS Catalysis*, 2011, **2**, 38-44.

55. C. Lau, E. R. Adkins, R. P. Ramasamy, H. R. Luckarift, G. R. Johnson and P. Atanassov, *Advanced Energy Materials*, 2012, **2**, 162-168.

56. R. J. Chen, Y. Zhang, D. Wang and H. Dai, *Journal of the American Chemical Society*, 2001, **123**, 3838-3839.

57. N. R. Haase, S. Shian, K. H. Sandhage and N. Kröger, *Advanced Functional Materials*, 2011, **21**, 4243-4251.

58. J. Wang, *Analytical Electrochemistry*, John Wiley & Sons, Inc., Hoboken, NJ, USA, 2006.

59. V. Datsyuk, M. Kalyva, K. Papagelis, J. Parthenios, D. Tasis, A. Siokou, I. Kallitsis and C. Galiotis, *Carbon*, 2008, **46**, 833-840.

60. S. Mädler, C. Bich, D. Touboul and R. Zenobi, *Journal of Mass Spectrometry*, 2009, **44**, 694-706.

61. S. Mädler, S. Gschwind and R. Zenobi, *Analytical Biochemistry*, 2010, **398**, 123-125.

62. A. J. Lomant and G. Fairbanks, *Journal of Molecular Biology*, 1976, **104**, 243-261.

CHAPTER 6: OVERALL CONCLUSIONS AND RECOMMENDATIONS FOR FUTURE WORK

6.1 Overall Conclusions and Recommendations for Future Work

The syntheses of functional, ordered, porous nanostructures with tunable three-dimensional morphologies is a significant challenge with potential applications in chemical, electrical, electrochemical, optical, photochemical, and biochemical devices. As a result, several novel bio-enabled and synthetic approaches were developed in this work to synthesize both aligned nanotubes of nanostructured titania and carbon nanotube/ enzyme biocomposites.[1-7] The utility of aligned titania nanotube arrays and carbon bio-nano composite materials produced by these bio-enabled and synthetic methods was demonstrated both in dye-sensitized solar cells (DSSC) and in electrochemical oxygen reduction applications. The development of these novel coating methodologies led to several discoveries including, the unique materials properties imparted by the methods used for production, the molecular mechanism of protamine-enabled deposition, and the advantages each processing method conferred to the particular application.

Peptide-enabled deposition utilizes the ability of certain readily-available arginine-rich peptides (e.g., protamine) to both bind-to and induce the precipitation of TiO_2 from *aqueous solution* under *ambient conditions* and *near-neutral pH*. A method was developed to deposit conformal TiO_2 coatings using peptide-enabled deposition onto ordered porous anodic alumina templates. The coatings deposited in this work were confirmed to be comprised of an inorganic/bioorganic composite that, upon heat treatment, became porous due to organic pyrolysis. Dissolution of the underlying

alumina template yielded high-aspect-ratio, aligned, porous-wall titania nanotube arrays with enhanced loading of functional dye molecules (Ru-based N719 dye) relative to sol-gel approaches. The porous-wall titania nanotube arrays synthesized using this new bio-enabled methodology were integrated into DSSCs that yielded power conversion efficiencies up to 5.2 ± 0.4%.

Prior studies of peptide-enabled deposition failed to investigate the versatility of the technique (i.e., the deposition of conformal coatings on synthetic metal oxide templates) or the utility of internal porosity within peptide-enabled titania films after organic pyrolysis. DSSCs were chosen to interrogate the utility of such porosity because the random nature of the oxide network in typical mesoporous titania films is not ideal for electron transport, and there is a strong desire to create ordered, porous titania electrodes. However, nanostructured TiO_2 architectures have also proven useful for a number of chemical, electrical, electrochemical, optical, photochemical, and biochemical devices.[8-13]

After peptide-enabled titania nanotube arrays were developed, it was thought that device efficiency could be improved by increasing the areal density of titania while maintaining the ordered, aligned nanotube geometry. As such, sol-gel deposition and a shape-preserving gas-solid displacement reaction method were combined, for the first time, to synthesize aligned, high-aspect-ratio, multi-walled TiO_2 nanotube (MWTNT) arrays that increased the roughness factor (73 to 282), loading of functional molecules (N719 dye, 195 ± 31 nmol cm^{-2} to 87 ± 28 nmol cm^{-2}), and the average efficiency in DSSCs relative to similarly prepared sol-gel derived single-wall TiO_2 nanotube arrays

(5.5 ± 0.8% to 3.0 ± 1.0%). MWTNTs had previously been synthesized using gas-phase ALD, liquid-cphase sol-gel, or electrochemical anodization methods.[14-16] However, no report developing a method to synthesize aligned, high-aspect-ratio, anatase MWTNT arrays has compared the performance of SWTNT to MWTNT in DSSCs. [14, 15] Furthermore, by combining the sol-gel infiltration of an anodic aluminum oxide (AAO) template with a shape-preserving gas-solid reaction technique, it was possible to overcome aspect-ratio limitations encountered when MWTNTs were synthesized via electrochemical anodization of Ti foil.[16] Peptide-enabled deposition was attempted, but these attempts failed. Successful syntheses of multilayered structured required a detailed understanding of the peptide-enabled layer-by-layer deposition process.

The alternating exposure of a negatively-charged surface to suitable synthetic or biologically-derived long-chain polyamines (e.g., protamine or polyethyleneimine) and reactive metal oxide precursor (e.g., tetramethoxysilane or titanium(IV) bis(ammoniumlactato) dihydroxide) has been utilized to deposit either SiO- or TiO-bearing coatings in a LbL fashion.[17-20] Such reactive deposition has been used to generate three-dimensional replicas comprised of microscale titania structures,[17] high-aspect-ratio aligned titania nanotube arrays,[21] and enzyme functionalized SiO_2 and TiO_2 coatings on SiO_2 microspheres.[22] Additionally, these coating methods have been used to develop components of gas sensors and DSSCs, as well as materials for biocatalysis and anti-microbial materials.[17, 21-24]

As such, a study was conducted to provide insight into both the effects of polyamine on TiO-bearing coating properties, and develop a basic understanding of the

molecular mechanism for peptide-enabled deposition. The relationship between the choice of polyamine (i.e., synthetic or bioorganic) to the TiO-bearing film deposition rate and properties (e.g., film thickness, roughness, surface area) was examined for the first time. Each of these film characteristics are of critical importance for designing future TiO_2 coating methods for various electrical, biochemical, photochemical, and optical applications. In this study, the deposition rate and film characteristics of TiO-bearing films deposited by either synthetic polyethyleneimine (PEI, 600 and 750,000 M_w branched and 2,500 M_w linear) or bioorganic protamine (~4.1 kDa) were investigated. PEI-based films deposited at a linear rate (6 to 10 nm per cycle) consistent with a "surface active" model for electrostatic LbL deposition. Conversely, the thickness of protamine-enabled films increased in a non-linear fashion over 10 deposition cycles, with two distinct regimes. The source of non-linear deposition in protamine-enabled films was shown to be consistent with an "active volume" model, where at least one molecule (presumably protamine) can diffuse "in" and "out" of the film thickness.

The discovery that peptide-enabled deposition can occur in a non-linear fashion may allow thick (micrometer scale), porous composite metal oxide coatings loaded with proteins, dyes, drugs, multivalent ions, or nanoparticles. The loading may be reversible or irreversible depending on solution conditions and external stimuli, making peptide-enabled deposition advantageous for various electrochemical, optical, photochemical, and biochemical applications.

In an effort to expand peptide-enabled deposition beyond metal oxide coatings, protamine was used to immobilize laccase onto the surfaces of multi-walled carbon

nanotubes by chemically cross-linking protamine with the multicopper oxidase laccase. Laccase is an enzyme known to catalyze the oxygen reduction to water at relatively low overvoltages under mildly acidic (pH 5.1) conditions, making it an attractive, renewable alternative to traditional platinum-based electrodes. Protamine-modified laccase was shown to improve both the amount of enzyme adsorbed onto carbon nanotube electrodes, and the enzyme retained 48% more activity upon immobilization onto the surface. Furthermore, the addition of protamine to the enzyme did not have an appreciable effect on the direct electron transfer of electrons from the carbon nanotube tube to the T1 copper site in the enzyme. In fact, protamine-modified laccase displayed an almost twofold improvement in maximum current density relative to unmodified laccase (271 $\mu A\ cm^{-2}$ to 137 $\mu A\ cm^{-2}$), when employed as an electrode in an electrochemical half-cell. The enzyme lifetime was also extended by a factor of 2.1 relative to laccase over repeated cycling for seven days.

To elucidate a cause for the improved current density, three synthetic peptides (Arg-Arg-Arg-Arg, Arg-Arg-Arg-Thr-Thr-Arg, and half-protamine (HPA)) were each cross-linked to laccase following the same procedure as for protamine. When the four arginine peptide was cross-linked to laccase (Lac-RRRR), the resulting electrochemical testing showed a sharp decrease in maximum current density that was below even the unmodified enzyme (85 $\mu A\ cm^{-2}$ compared to 137 $\mu A\ cm^{-2}$). The reduction in maximum current density and biochemical activity observed in PBSE-Lac-RRRR electrodes highlighted the importance of both the peptide chain length and the amino acid composition. When threonine-containing peptides were cross-linked to laccase (Lac-

RRRTTR), the maximum current measured by potentiostatic polarization increased by almost twofold compared to Lac-RRRR which lent support to the hypothesis that threonine residues were critical to Lac-PA tethering to PBSE-treated CNT-BP. However, when the peptide was modified further to 15 amino acids (Lac-HPA) the maximum current density remained similar to Lac-RRRTTR, which indicated that the improvement in ORR exhibited by PBSE+Lac-PA electrodes was due to the combination of primary structure and molecular weight protamine. Modification of enzymes with protamine was a new strategy for enzyme immobilization and can be extended to other redox enzymes (e.g., alcohol dehydrogenase, methanol dehydrogenase, or glycerol dehydrogenase) for bioelectrochemical applications (e.g., enzymatic biofuel cells, sensors) with improved performance and enzyme lifetime. The extension to other enzymes could demonstrate the broad utility of this method and allow for construction of a complete biofuel cell based on this immobilization paradigm.

Overall, several techniques were developed for the syntheses of functional, ordered, porous nanostructures using several novel bio-enabled and synthetic approaches. These approaches yielded aligned nanotubes of nanostructured titania and carbon nanotube/enzyme biocomposites that imparted beneficial properties to the electrodes. In the future, these methods can find broad applicability for functional, inorganic/(bio)organic coatings that can be deposited on various 3-D template materials.

6.2 References

1. S. Mann, *Biomineralization: Principles and Concepts in Bioinorganic Materials Chemistry*, Oxford University Press, Oxford, NY, 2001.

2. E. Bäuerlein, *Biomineralization: Progress in Biology, Molecular Biology, and Application*, Wiley-VCH, Weinheim, Germany, 2004.

3. M. Sarikaya, C. Tamerler, A. K. Y. Jen, K. Schulten and F. Baneyx, *Nature Materials*, 2003, **2**, 577-585.

4. C. E. Flynn, S. Lee, B. R. Peelle and A. M. Belcher, *Acta Materiala*, 2003, **51**, 5867-5880.

5. R. R. Naik and M. O. Stone, *Materials Today*, 2005, **8**, 18-25.

6. A.-W. Xu, Y. Ma and C. Helmut, *Journal of Materials Chemistry*, 2007, **17**, 415-449.

7. M. B. Dickerson, K. H. Sandhage and R. R. Naik, *Chemical Reviews*, 2008, **108**, 4935-4978.

8. J.-H. Park, S. Kim and A. J. Bard, *Nano Letters*, 2006, **6**, 24-28.

9. G. K. Mor, K. Shankar, M. Paulose, O. K. Varghese and C. A. Grimes, *Nano Letters*, 2006, **6**, 215-218.

10. O. K. Varghese, M. Paulose, T. J. LaTempa and C. A. Grimes, *Nano Letters*, 2009, **9**, 731-737.

11. Y.-Y. Song, F. Schmidt-Stein, S. Bauer and P. Schmuki, *Journal of the American Chemical Society*, 2009, **131**, 4230-4232.

12. M. Paulose, H. E. Prakasam, O. K. Varghese, L. Peng, K. C. Popat, G. K. Mor, T. A. Desai and C. A. Grimes, *The Journal of Physical Chemistry C*, 2007, **111**, 14992-14997.

13. S. P. Albu, A. Ghicov, J. M. Macak, R. Hahn and P. Schmuki, *Nano Letters*, 2007, **7**, 1286-1289.

14. C. Bae, Y. Yoon, H. Yoo, D. Han, J. Cho, B. H. Lee, M. M. Sung, M. Lee, J. Kim and H. Shin, *Chemistry of Materials*, 2009, **21**, 2574-2576.

15. I.-S. Park, S.-R. Jang, J. S. Hong, R. Vittal and K.-J. Kim, *Chemistry of Materials*, 2003, **15**, 4633-4636.

16. S. E. John, S. K. Mohapatra and M. Misra, *Langmuir*, 2009, **25**, 8240-8247.

17. Y. Fang, Q. Wu, M. B. Dickerson, Y. Cai, S. Shian, J. D. Berrigan, N. Poulsen, N. Kröger and K. H. Sandhage, *Chemistry of Materials*, 2009, **21**, 5704-5710.

18. Y. Jiang, D. Yang, L. Zhang, Q. Sun, X. Sun, J. Li and Z. Jiang, *Advanced Functional Materials*, 2009, **19**, 150-156.

19. Y. Zhang, H. Wu, J. Li, L. Li, Y. Jiang, Y. Jiang and Z. Jiang, *Chemistry of Materials*, 2008, **20**, 1041-1048.

20. V. Ball, L. Dahéron, C. Arnoult, V. Toniazzo and D. Ruch, *Langmuir*, 2011, **27**, 1859-1866.

21. J. D. Berrigan, T. S. Kang, Y. Cai, J. R. Deneault, M. F. Durstock and K. H. Sandhage, *Advanced Functional Materials*, 2011, **21**, 1693-1700.

22. N. R. Haase, S. Shian, K. H. Sandhage and N. Kröger, *Advanced Functional Materials*, 2011, **21**, 4243-4251.

23. M. B. Dickerson, C. L. Knight, M. K. Gupta, H. R. Luckarift, L. F. Drummy, M. L. Jespersen, G. R. Johnson and R. R. Naik, *Materials Science and Engineering: C*, 2011, **31**, 1748-1758.

24. H. R. Luckarift, M. B. Dickerson, K. H. Sandhage and J. C. Spain, *Small*, 2006, **2**, 640-643.

APPENDIX A: ROUGHNESS FACTOR CALCULATIONS

A.1 Derivation of Roughness Factor Calculation

The roughness factor or rugosity (f_r) of a surface is a commonly used to characterize surfaces, and is defined according to **Equation A.1**:[1]

$$f_r = \frac{A_r}{A_p} \qquad \text{(A.1)}$$

where A_r is the real (actual) surface area and A_p is the planar substrate (geometric) surface area. In DSSCs, the roughness factor is an estimate of the total internal surface area that is available for dye adsorption relative to its projected surface area. The real surface area can be measured (i.e., by Brunauer-Emmett-Teller surface area analysis) or estimated from measured dimensions. Roughness factor calculations for the synthesized aligned nanotube arrays synthesized were estimated based on geometric measurements obtained by SEM. From measurements of the nanotube wall thickness, outer diameter, length, and channel center-to-channel center spacing, both A_r and A_p can be calculated. An example of the measurements taken is shown in **Figure A.1.**

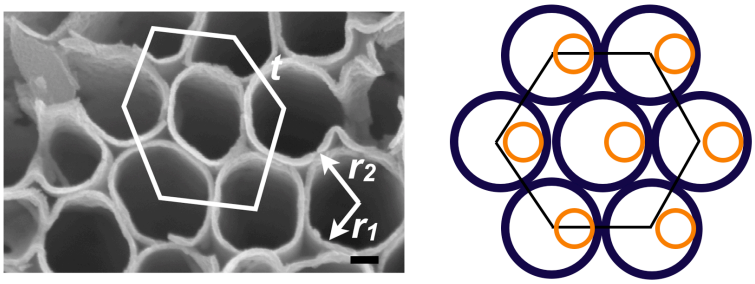

Figure A.1: Plan-view secondary electron microscopy (SEM) image of a peptide-enabled TiO_2 nanotube array demonstrating hexagonal packing of the nanotubes with tube-to-tube spacing, t, and inner- and outer-radii described by r_1 and r_2, respectively. The orange circles denote the second inner nanotube observed in multi-walled TiO_2 nanotube arrays. Scale bar: 100 nm.

Assuming the nanotube can be approximated as a smooth, symmetric, hollow cylinder with no porosity and negligible surface area at the top and bottom edges, the A_r is given by **Equation A.2**

$$A_r = 2\pi l(r_1 + r_2) \tag{A.2}$$

where l is the length of the cylinder and r_1 and r_2 are in the inner and outer radii of the cylinder (nanotube).

The planar substrate area is a two-dimensional area measurement of a three-dimensional object projected onto an arbitrary plane (in this case, the area per nanotube on the electrode surface). It was observed that, after dissolution of the anodic aluminum oxide (AAO) template, the nanotubes agglomerated in a near-hexagonal arrangement (**Figure A.1**). This arrangement allowed for the estimation of the area density of nanotubes for each electrode (i.e., assuming a regular hexagon with side-length, t_{space}, equal to the channel center-to-channel center spacing). The area of a regular hexagon is given by **Equation A.3**.

$$A_{hexagon} = \frac{3\sqrt{3}}{2} t_{space}^2 \tag{A.3}$$

For single-wall TiO_2 nanotube (SWTNT) and multi-wall TiO_2 nanotube (MWTNT) arrays, three complete nanotubes are within the hexagon (1 nanotube in the center and 6 nanotubes along the edges that contribute 1/3rd each). The areal density of nanotubes in the array, $A_{density}$ (nanotubes per unit area), was determined by dividing the number of nanotubes within the hexagonal area, n_{tubes}, by the area of the hexagon (**Equation A.4**).

$$A_{density} = \frac{2n_{tubes}}{3t_{space}^2\sqrt{3}} \quad \text{(A.4)}$$

$$A_p = A_{density}^{-1} = \frac{3t_{space}^2\sqrt{3}}{2n_{tubes}} \quad \text{(A.5)}$$

The inverse of **Equation A.4** yields the planar surface area per nanotube within the array (**Equation A.5**). Combining **Equations A.2** and **A.5** with **Equation A.1** provides an estimate for the roughness factor of the electrodes used in Chapters 1 and 2.

A.2 Example Calculations for Single-Wall and Multi-Wall Nanotube Arrays

In this section, a sample calculation of the estimated roughness factor is presented using measured geometric parameters obtained from single-wall and multi-wall TiO_2 nanotube arrays present in Chapter 2.

A.2.1 Example Calculation for Single-Wall TiO_2 Nanotube Arrays

Using the measured geometric parameters tabulated in **Table A.1**, a roughness factor was estimated for sol-gel-derived single-wall TiO_2 nanotube arrays using equations A.1, A.2, and A.5.

Table A.1. Measured parameters used to estimate the roughness factor for sol-gel derived SWTNT arrays.

Parameter	Symbol	Measured Value
Channel center-to-channel center spacing	t_{space}	398 ± 70 nm
Nanotube Length	l	13.2 ± 0.4 μm
Nanotube Wall Thickness	W_t	30 ± 10 nm
Nanotube Outer Radius	r_1	77 ± 20 nm

Subtracting the nanotube wall thickness (W_t) from the nanotube outer radius (r_1) yielded the value for the inner nanotube radius, r_2. These values were inserted into equation A.2. The calculation of A_r is shown, in full, from equations A.6 to A.9. The estimated value of A_r was 10 μm^2.

$$A_r = 2\pi \cdot (13.2\ \mu\text{m}) \cdot (0.077\ \mu\text{m} + 0.043\ \mu\text{m}) \quad \text{(A.6)}$$

$$A_r = 2\pi \cdot (13.2\ \mu\text{m}) \cdot (0.12\ \mu\text{m}) \quad \text{(A.7)}$$

$$A_r = 2\pi \cdot (13.2\ \mu\text{m}) \cdot (0.12\ \mu\text{m}) \quad \text{(A.8)}$$

$$A_r = 10.0\ \mu\text{m}^2 \quad \text{(A.9)}$$

To calculate the planar area (A_p) the channel center-to-channel center distance was entered into equation A.5 where n_{tubes} = 3. The results of the calculation are shown in equations A.10 to A.13 and yielded an estimated roughness factor of 75 ± 37 for SWTNT arrays.

$$A_p = A_{density}^{-1} = \frac{3(0.398\ \mu\text{m})^2\sqrt{3}}{2 \cdot 3} \quad \text{(A.10)}$$

$$A_p = \frac{0.823\ \mu\text{m}^2}{6} \quad \text{(A.11)}$$

$$A_p = 0.137 \mu\text{m}^2 \quad \text{(A.12)}$$

$$f_r = \frac{10.0\ \mu\text{m}^2}{0.137\ \mu\text{m}^2} = 73.0 \quad \text{(A.13)}$$

A.2.2 Example Calculation for Multi-Wall TiO_2 Nanotube Arrays

Using the measured geometric parameters tabulated in **Table A.2**, a roughness factor was estimated for sol-gel-derived single-wall TiO_2 nanotube arrays using equations A.1, A.2, and A.5.

Table A.2 Measured parameters used to estimate the roughness factor for MWTNT arrays.

Parameter	Symbol	Measured Value
Channel center-to-channel center spacing	t_{space}	398 ± 70 nm
Nanotube Length	l	13.2 ± 0.4 μm
Nanotube Wall Thickness	W_t	80 ± 13 nm
Nanotube Outer Radius	r_1	213 ± 38 nm

Subtracting the nanotube wall thickness (W_t) from the nanotube outer radius (r_1) yielded the value for the inner nanotube radius, r_2. These values were input into equation A.2. The calculation of A_r is shown, in full, from equations A.14 to A.17. The estimated value of A_r was 38.7 μm^2.

$$A_r = 2\pi \cdot (13.2\ \mu\text{m}) \cdot (0.077\ \mu\text{m} + 0.043\ \mu\text{m}) + 2\pi \cdot (13.2\ \mu\text{m}) \cdot (0.213\ \mu\text{m} + 0.133\ \mu\text{m}) \quad \text{(A.14)}$$

$$A_r = 2\pi \cdot (13.2\ \mu\text{m}) \cdot (0.12\ \mu\text{m}) + 2\pi \cdot (13.2\ \mu\text{m}) \cdot (0.346\ \mu\text{m}) \quad \text{(A.15)}$$

$$A_r = 9.95\,\mu\text{m}^2 + 28.7\,\mu\text{m}^2 \quad \text{(A.16)}$$

$$A_r = 38.7\ \mu\text{m}^2 \quad \text{(A.17)}$$

To calculate the planar area (A_p) the channel center-to-channel center distance was entered into equation A.5 where n_{tubes} = 3. The results of the calculation are shown in equations A.18 to A.21 and yielded an estimated roughness factor of 282 ± 99 for aligned MWTNT arrays. Error was calculated by using the geometric values that would lead to the greatest value for the estimated roughness factor (i.e., maximum length, smallest wall thickness, and largest nanotube diameter).

$$A_p = \mathrm{A}_{\mathrm{density}}^{-1} = \frac{3(0.398\ \mu\mathrm{m})^2\sqrt{3}}{2 \cdot 3} \tag{A.18}$$

$$A_p = \frac{0.823\ \mu\mathrm{m}^2}{6} \tag{A.19}$$

$$A_p = 0.137 \mu\mathrm{m}^2 \tag{A.20}$$

$$f_r = \frac{38.7\ \mu\mathrm{m}^2}{0.137\ \mu\mathrm{m}^2} = 282 \tag{A.21}$$

A.3 References

1. R. N. Wenzel, *The Journal of Physical and Colloid Chemistry*, 1948, **53**, 1466-1467.